GENERATION OF SUB-WAVELENGTH ACOUSTIC STATIONARY WAVES IN MICROFLUIDIC PLATFORMS: THEORY AND APPLICATIONS TO THE CONTROL OF MICRO-NANOPARTICLES AND BIOLOGICAL ENTITIES.

A Dissertation

Presented to the Faculty of the Graduate School

of Cornell University

in Partial Fulfillment of the Requirements for the Degree of

Doctor of Philosophy

by

Muhammet Kursad Araz

February 2010

GENERATION OF SUB-WAVELENGTH ACOUSTIC STATIONARY WAVES IN MICROFLUIDIC PLATFORMS: THEORY AND APPLICATIONS TO THE CONTROL OF MICRO-NANOPARTICLES AND BIOLOGICAL ENTITIES.

Muhammet Kursad Araz, Ph.D.

Cornell University 2010

Presented in this dissertation are the theoretical modeling and experimental results of a novel method for manipulating micro and nanoparticles in an acoustically actuated microfluidic glass capillary. Here, the PZT (Lead Zirconate Titanate)-glass capillary actuator mechanism performs bioanalytical methods such as collection, separation and mixing at microscale, at low voltage drives, enabling production of battery operated inexpensive portable microfluidic systems.

Analytical and finite element modeling of the vibrational modes of the fluid filled thick walled cylindrical capillary has been also studied. Torsional, longitudinal and flexural modes and their dispersion relationships are presented.

Through the excitation of the various vibrational modes of the silica capillary, sub-wavelength acoustic pressure modes in the microfluidic cavity are formed. More than 20 such sub-harmonic modes are generated harmonically in the 20kHz-2MHz regime whereas naturally occurring radial modes have a cut off frequency around 9 MHz. The amplitude of these stationary acoustic pressure fields are high enough to generate nonlinear acoustic forces and streaming effects for micro and nanoparticle manipulation. Theoretical models explaining the generation of the sub-wavelength modes and acoustic radiation forces are developed.

Generation of an effective macroscopic electric field as a result of the collection of charged colloidal particles under acoustic forces has been observed. This self

generated field causes fast collective diffusion of nanoparticles and can counterbalance the acoustic radiation forces, so a method for calibrating acoustic force field with respect to the collective electrostatic repulsion and the Zeta potential of particles is introduced.

A silicon bulk microfabricated actuator enabling different bioanalytical capabilities such as collection, separation and mixing of analytes on a single bulk-PZT-silicon microfluidic platform at low voltage drives is also demonstrated.

Presented experimental results include: collection of micro and nanoparticles, colloidal systems and biological entities such as bacteria and cells; separation of micro and nanoparticles with respect to acoustic contrast factor; planar chipscale centrifugation of blood; separation of microparticles with respect to size; and controlled oscillating bubble dynamics at the microscale, which are all obtained in the PZT-glass capillary actuator driven with a typical function generator at around 100 milliwatts of power consumption.

BIOGRAPHICAL SKETCH

Muhammet Kursad Araz received his B.S. degree in physics in 2001 from Bogazici University in Istanbul, Turkey and continued his graduate studies at the School of Applied and Engineering Physics Department at Cornell University. He received his Ph.D. degree in applied physics in 2009 with a minor in electrical engineering. During his Ph.D. studies, he focused on the theoretical modeling and applications of chipcscale novel acoustical methods for microfluidic control of micro and nanoparticles, and biological samples. His current and future research interests include acoustics, MEMS and microfluidics along with their applications in bioengineering, colloidal system characterization and renewable energy harvesting methods.

To

my parents, Rifat and Gulser Araz,

and

my wife Yasemin

ACKNOWLEDGEMENTS

During the preparation of this study, I got tremendous help from many people. While I may have missed a few due to my memory and the rush of the approaching deadline, I will really try my best to acknowledge everyone.

First of all, I would like to thank my thesis advisor, Prof. Amit Lal, for his endless trust, guidance and motivation during the course of this study. His curiosity and interest over many different scientific and engineering disciplines made this work very exciting. His wise and positive attitude in even the most awkward moments motivated me to become a more positive and more patient individual compared to what I was before. I cannot remember a single meeting with him after which I left his room without feeling energized. I also learned a lot from him about getting more professional in terms of my academic writing skills. His great motivation for providing enough resources for the development of his students is something I will remember if I have chance to be a faculty member someday. I would like to also thank Garima Goel Lal; with Prof. Lal, they always shared the warmth of their home environment and made me feel like a member of the family.

I would like to also thank my committee members Prof. Clifford Pollock and Prof. Michal Lipson for their, support, feedback and input throughout this study. Furthermore, I thank Prof. David Muller and Prof. Warren Zipfel for attending to my oral exams and providing constructive feedback. I also thank Prof. Sunil Bhave for the many fruitful discussions we had. It was very exciting and informative to be the teaching assistant of the MEMS class under his supervision.

I would like to thank my undergraduate advisors from Bogazici University: First Prof. Fahrunisa Neyzi for guiding me to do the right thing for myself, choosing physics as my undergraduate major; and to Prof. Levent Kurnaz with whom I started to get the real joy of doing scientific research. His easy way to approach

even very complex systems and starting all problems with the “assume a spherical horse” analogy helped me a lot not only in the course of this study but also throughout my life. I would like to also thank him for guiding me to apply for the Ph.D. program in Applied Physics Department at Cornell University, where I had really have found the study in which I am most interested.

I also would like to thank my group mates, SonicMEMS’ers: Serhan Ardanuc, Alper Bozkurt, Steven Tin, Norimasa Yoshimizu, Abhishek Ramkumar, Janet Shen, Siva Prasad, Hengky Chandrahalim, Kwame Amponsah, Yue Shi, Larry Lu, Manoj Pandey and former group members Chung-Hoon Lee, Xi Chen, Shankar Radhakrishnan, Rajesh Duggirala, Il-Seok Son, Abhijit Sathaye, Shi-Herng Kan, Ville Kaajakari and Hang Guo. Over the individual encounters or group meetings, I learned many new and exciting things from all of them. Special thanks go to Hoon for guiding me in the beginning of my research, and Xi for helping me during the design of the microfabrication steps and introducing the clean room environment. A special thanks also go to my dear friend Serhan, for our very fruitful discussions over acoustic problems, and other scientific, social and political matters and also for letting me know of Prof. Lal’s moving to Cornell.

I also thank Aaditya Khimani and staff members of Cornell Nanofabrication Facility and Cornell Nanobiotechnology Center for their help during the design and the fabrication of the silicon bulk actuator presented in the latter part of this thesis.

I would like to thank Scott Coldren, Kelli Hulslander, Susan Ferrara, Lisa Gould, Daniel Richter, William Bader, Carmen Blankinship, and all ISSO staff members, especially Sarah Hilsman and Elizabeth Shedd, for their help related to administrative matters. I would also like to thank my editor in the beginning and new friend at the end, Jill Marie, for editing my thesis and her strong passion over

improving my writing skills. I learned a lot from her and hope to learn more.

A Turkish proverb says "Tell me about your friends, I will tell who you are." I am not sure this would be true for me as I had really wonderful friends. I would like to thank my friends in Ithaca and elsewhere: Serhan Ardanuc, Alper Bozkurt, Hazer Inaltekin, Helena Silva, Engin Burgaz, Gokhan Arikan, Zeki Durak, Onur Tokel, Ekrem Cakmak, Omer Ilday, Ozhan Ozatay, Mahmut Aksit, Shaffique Adam, James van Howe, Abdurrahman Gumus, Arman Ajmuhanov, Abdullah Ozer, Ankush Gupta, Yildiray Yildirim, Mandy Esch, Murat Baday, Kadir Yavuz, Esref Dogan, Mehmet Sen, Askin Kocabas, Volkan Bilgili, Nuri Gokcek, Yasin Senbabaoglu, Jessie Childs and Oguzhan Vicil: and also my elder friends in Ithaca, Hatice Brenton, Mahbud and Henrike Burton, Fahri and Asu Unsal and Musaddak Ghaffur. I would like to specially thank my dear friend Ali Gokirmak and his parents Nevin and Hikmet Gokirmak for their welcoming support in my first year in Ithaca. I cannot forget the nice memories we had in their place in Maple Hill.

And my family; I do not know how to thank my parents Rifat and Gulser Araz, for everything they have provided for me and their trust in me. From them I learned the importance of social values such as sharing and caring for others. I would say most of my values are shaped positively by them. One of the earliest science discussions that I cannot forget is the one that my father told me at the age of 5, about the existence of a tremendously dynamic world of moving, rotating, oscillating atoms and molecules which we cannot see at all. That discussion still stays as the seed source of my enthusiasm over scientific research. I would like to say that his reflective attitude over nature spanning a broad range from stars in the sky to the cells in our stomach and strong belief in the importance of good education as a life long investment shaped my career interests. From him first, I learned if something exists, there is a purpose for it. I also would like to thank

my siblings Gulsum and Kadir Araz for their support and affection for me. I am really blessed with their presence. My deceased grandfathers Serafettin dede and Ali dede were my role models in terms of being a caring and understanding person. With their strong passion over education and a great hope for me, I so wish that they had the chance to see that I am finishing my Ph.D. I also would like to thank all of my relatives for their good wishes and support.

And my wife... Thank you very much for being with me during the most challenging and sometimes the most stressful part of my life while writing this thesis. You were always so supportive that I am not sure if this thesis would be completed without your compassionate coaching. Your endless inspirational and motivational comments "on accumulation of small steps" and "finishing things one by one with persuasion and patience" improved my productivity dramatically. You are making me a better and a more organized person! Please keep up the good work :-).

At the end, for all of the countless bounties and wonderful friends He has bestowed upon me, I would like to acknowledge the One who was pleased with the praise given by the king and prophet David. Like him I shall say, "How can I be fully thankful to You, since being able to 'thank You' is another favor of you that requires thankfulness...?" All praise be to You.

TABLE OF CONTENTS

LIST OF TABLES

LIST OF FIGURES

CHAPTER 1

INTRODUCTION

Acoustics in microfluidic systems, either man-made or naturally made, has been an active area of research for last two decades, providing significant advantages in microfluidic manipulation over competing techniques. Presented in this thesis are the theory of the generation of sub-wavelength acoustic stationary waves in a vibrating PZT-glass capillary coupled actuator as well as applications and experimental results on the collection and separation of micro-nanoparticles and microbiological entities. This introductory chapter plays a central role in presenting the principal ideas and organization of the rest of the chapters.

In the first and second parts of this chapter, a short review on the broad field of microfluidics and approaches utilizing acoustic interactions are given. Next, previous work which led to the present work and principal ideas are introduced. This chapter ends by briefly summarizing the other chapters and major contributions of the work presented here. The summary of the entire thesis can be found in pages 15 through 20, and a concise guide is given in Figure 1.5.

1.1 Microfluidics: A Short Review

The field of microfluidics dates back to the 1980s, the time inkjet printing became available, yet microfluidics has always been ubiquitous in nature. In the formation of a rain droplet or ice up in the sky; in the fall of rain or snow; in the absorption of water in the ground and then the absorption of same water by a plant root and the transference to leaves through capillaries in the stem; in the organization of channels on a leaf and the tremendous transport taking place through channels;

in the circulatory system of our body, and the uncountable interactions taking place within and between the cells therein; in the purification of soiled water in the underground; microfluidic effects has been everywhere from the beginning. Verily, nature is full of hidden secrets and signs for those of understanding. As humankind gets better in reflecting on nature, nature opens its secrets one by one. The concept of microfluidics is one such phenomenon. There are uncountable microfluidic phenomena taking place in the body of the author, right now as he writes this dissertation. Possibly on the same order of magnitude, microfluidic phenomena are taking place in the eyes, brain, vessels, cells, fingers and nervous system of the unaware reader.

Currently, the topic of microfluidics is a very interdisciplinary field, spanning the fields of physics, chemistry, biology, electrical engineering, mechanical engineering and systems engineering. In recent years, interest in microfluidics has been driven by the many potential benefits to current technological developments, especially in the field of biology and medicine. Small sample requirement, small device volume, less power consumption, and potential mass production using integrated-circuit fabrication, as well as the possibility of performing a large number of assays in parallel, make microfluidics attractive for portable and disposable diagnostic devices and research systems. More than the fabrication of small systems, controlling objects inside a microfluidic system is a challenging problem. Strongly statistical behavior at the micro scale, lack of precise mechanical tweezers, and high surface-to-volume ratio for analysis require new ways to manipulate particles. Only a small portion of the classical methods used in analytical biochemistry can be miniaturized to be able to work on a tiny chip. This is the main reason that microfluidics is still a developing field.

Breathtaking development in the field of integrated circuits enabled the replacement of conference room size computational machines manufactured to execute mathematical algorithms with hand held devices like the laptops, calculators and cell phones of today. While the big dream of "Lab-on-a-Chip" —in other words, miniaturization of a analytical biochemistry lab to a chip size— had been there for so long, the absence of physical steps enabling execution of this dream became a major research field for many scientists and engineers. While many researchers are keeping the aforementioned dream as their motto, many people are amazed about the complicated and expensive-to-manufacture but at the same time state-of-the-art microfluidics systems. However, the need is not for a state-of-the-art system but an inexpensive and easy-to-fabricate component which is either able to perform a necessary action in an easier, faster or cost-effective way, or to enable new directions to solve or deal with new unanswered questions.

Another challenge in the field of microfluidics is that, contrary to microfluidics in nature, most of today's microfluidic systems lack the necessary flexibility of integrability function with other systems performing other desired actions. Since many microfluidic actuation mechanisms depend on specific conditions or require other bulky mechanisms, an integrated approach becomes a nontrivial problem to solve.

An ideal Lab-on-a-Chip system may need to be able to perform sampling, separation, pumping, mixing, handling, detection of fluids and analytes which vary from a few nanometers to tens of micrometers in size. At the same time, this so called "Micro Total Analysis System (μTAS)" should not be expected to need a refrigerator-sizes host system to function or get powered up where neither of these components can fit on a "chip".

Today, many scientists and engineers work on various ways to manipulate or actuate fluids and micro-nano components through performing the specific actions mentioned above. A good review of these methods and the field in general can be found in [5, 6, 7]. Some of these methods include electro-osmotic and electrophoretic interactions, magnetic effects, pneumatic actuation, porous materials, fluid mechanics tricks, optical tweezers, modification of electrochemical properties or wettability of surfaces, and so on. The list is long and, as expected, all of these methods have advantages and disadvantages or certain limitations. For instance, electrical effects depend on certain electrolyte and enclosing microchannel surface properties; magnetic effects require paramagnetic beads and magnet sources; optical tweezers require bulky microscope and laser systems; et cetera. Many of these applications perform well enough in their area of usability or point of interest; however, at the same time, many of these methods lack applicability as an integrated component of a chipscale stand-alone microfluidic platform.

Nonlinear acoustic interactions are one example of a promising way for the manipulation of micro and nanoparticles in microfluidic systems. As these interactions predominantly depend on factors like size and material properties such as modulus and density, acoustic actuators are less dependent on electrical, ionic and pH concentration of the samples with respect to electro-osmotic or magnetic effects. One must especially consider that almost all Lab-on-a-Chip devices are aimed for biological sample detection or characterization; therefore, alternate methods that complement each other gain more importance. In addition, due to the possibility of manufacturing highly compliant micro structures with high vibration amplitudes, nonlinear acoustic interactions can be established in microfluidic systems even at a low electrical power drive. This process may eliminate the high power requirement as being one of the major challenges for the production of portable

diagnostic devices. In the next section, a brief review of acoustical methods for microfluidic applications will be given.

1.2 Ultrasonic Microfluidics

It has been known ever since the 19^{th} century that high amplitude acoustic waves have nonlinear interactions with the fluid medium they propagate and other suspended materials they encounter during the propagation. Two major types of interactions are known to be acoustic streaming and acoustic radiation forces stemming from acoustic radiation pressure. Since all materials have different elastic properties, their response in regards to propagation and absorption of a sound field is unique. In this way, acoustical effects at micro regime can be useful in terms of being applicable to a broader range of materials for implementing various desired functions. Acoustical interactions do not require any preprocessing, as they stem from the natural material properties of materials.

As will be shown later in Chapter 5, acoustic streaming and radiation forces are nonlinear effects, and quadratic functions of the of the acoustic pressure and velocity. In the macroscopic world, in many cases, observing these effects requires power hungry piezoelectric actuators, and usually the observed effects are weak. However, at the microscale, high amplitude oscillations can be generated at low power drives. Theoretically, this enables the generation of nonlinear acoustic effects at the micro regime even, at a low power drive.

While use of acoustics in microfluidics is a very promising field because it does not require any preprocessing of materials, and it does not delicately depend on electrostatic interactions, the major challenge comes with the design. This

is because acoustical fields and their effects depend on the boundary conditions, both at linear and nonlinear range. At the same time, in the case of acoustics, the nonlinear effects can change linear boundary conditions, and so that analytical modeling of an experimental result obtained by intuition is very challenging. The reason is that there are an abundant number of parameters to analyze that require some expertise in physics, fluid dynamics and nonlinear acoustics, contrary to the other methods used in microfluidics.[1] In fact, looking to developments in the history of acoustics, it is possible to say that, in many cases, interesting results obtained by experimenters led to the developments in the theory. This is also true at the microscale acoustics. In this sense, acoustics in microfludics is a very interesting field full of surprises for a curious researcher.

In recent years, there has been a tremendous increase in microfluidic applications which use acoustical interactions as the source of actuation. Methods of acoustical actuation can be categorized into several subgroups such as use of surface acoustic waves, use of flexurally excited plates and generation of standing waves in a microfluidic cavity. Depending on the design, specific actuators focus on either the streaming effects for pumping or mixing, or radiation force effects for the separation and manipulation of the micro-nanoparticles or biological entities. In most cases, designs enabling propagating elastic waves on the fluid structure boundary are used for pumping or mixing, and designs enabling standing waves on the cavity are used for capturing and manipulating particles.

Compared to the long and rich history of acoustics, recently, acoustic waves generated on a microfabricated silicon microfluidic platform have produced signifi-

[1]Due to the low Reynolds number limit, most viscous and related nonlinear effects can be ignored in most microfluidic devices. For microfluidic applications, dominant flow type is the laminar flow, and compared to macroscopic fluid dynamics problems, microscale flow dynamics can be relatively simpler. Unfortunately, when high amplitude acoustics is involved, second order terms cannot be ignored as the principle of operation depends on the second order effects.

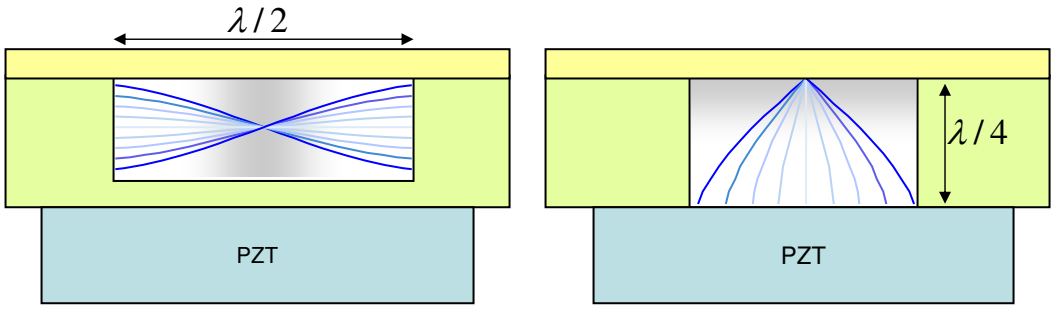

Figure 1.1: Standing acoustic waves generated in a microfluidic capillary. In such configurations, lowest frequency standing waves can be achieved when channel dimensions are equal to $\lambda/4$ or $\lambda/2$ depending on the configuration of the actuator mechanism.

cant progress. This platform is used to generate fluid flow [8] enabling microfluidic pumping due to acoustical effects. Kaajakari and his colleagues [9] demonstrated the use of streaming vortices generated by flexurally vibrating circular plates for capturing particles during a steady flow.

In terms of ultrasonic capture and manipulation of particles, acoustic radiation forces are widely used. The usual method to generate radiation forces is to form a standing acoustic wave field in a cavity [10]. As shown in Figure 1.1, this can be achieved by placing the actuator and reflector in parallel separated by a gap related to the wavelength. At the microscale, acoustic waves launched to a silicon chip body can also generate a standing wave in a cavity etched into the substrate if one of the dimensions of the cavity matches the half wavelength of the acoustic wavelength in the fluid [11]. By this classical method, similar to the macroscale methods (such as ultrasonic separation of fibers in a laminar flow used in the paper industry [12]), acoustic separation of materials had been miniaturized to separate biomaterials at the microscale. A limitation of this method is that because the wavelength is related to the channel dimensions as shown in Figure 1.1, shrinkage

in the channel dimensions leads to an increase in resonance frequency. For example, to be able to generate standing waves in a microchannel with a width of 100 μm filled with water, the frequency drive of the actuator will be around 10 MHz for the lowest frequency modes. Most relatively inexpensive piezoelectric materials, and driving circuitry targeted for ultrasonic transduction are produced to be driven between kHz and low MHz regime. Another limitation is that the whole actuator performance depends on the single resonance frequency of the structure or its harmonics. In addition, when the fluid medium changed to another fluid, resonance frequency for generating a standing mode will be different. Hence, geometry of the device, mixed boundary conditions due to packaging, and material properties of the microfluidics and the structure make performance control difficult. This thesis addresses these challenges by a novel actuation mechanism described in the following sections.

1.3 Microfluidic Capillary with Vibrating Walls

One ingenious way developed by Lee et al.[13] is to use high amplitude vibrations generated on a microfluidic capillary so that an acoustic field inside the capillary can be generated in an efficient way. In traditional acoustics, most guided systems are engineered in a way that actuators usually form a small portion of the system, and the rest of the system is designed to behave as a waveguide to confine the energy for specific purposes. In a system where whole walls behave like an actuator and at the same time act as a waveguide, the coupling of mechanical energy from the structure to fluid is maximized. The initial design of the actuator is given in Figure 1.2. As shown in the figure, a diced Lead Zirconate Titanate plate (PZT-4) is adhesively bonded from both sides to a bent silica capillary. Vibrations on

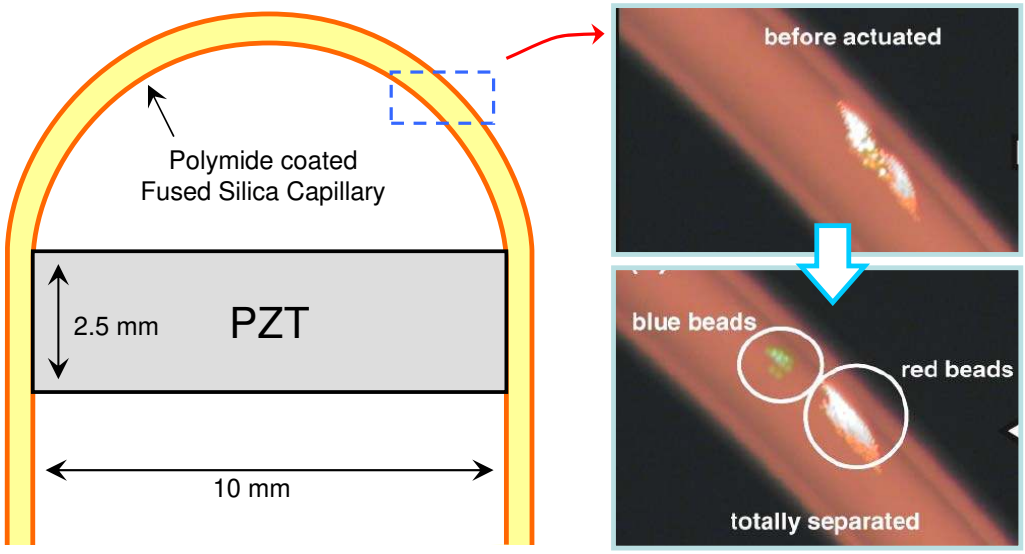

Figure 1.2: Schematic drawing of glass capillary PZT transducer and separation of polystyrene beads. 3 micron (red) and 10 micron blue beads (look green in the image due to filters) a re collected at a focal spot and then separated.

the PZT plate are coupled to the silica capillary so that acoustic modes can be generated inside. By this method, collecting and separating particles in a curved capillary-PZT coupled actuator had been achieved. The work presented in the rest of this dissertation is a continuing research effort based on the initial design presented in [13].

1.3.1 Sub-wavelength Acoustic Stationary Waves in a Vibrating Microfluidic Capillary

As shown in Figure 1.1, to be able to generate a standing wave field in a microfluidic capillary, capillary dimensions need to match half or quarter wavelength limits. One other way to create a stationary wave is to drive two sources in phase while

the gap between the two sources is much smaller than the wavelength. In such a configuration, no wave propagation can happen, and because of the boundary conditions, an oscillating pressure gradient forms. Figure 1.3 shows the formation of stationary waves under given conditions. When two walls oscillate in phase, and the gap is much shorter than a wavelength, a stationary pressure gradient forms in the enclosed fluid. When the walls are accelerating upwards, the pressure becomes maximum at point A and minimum at point B, which is denoted by the blue curve in the plot of acoustic pressure in the figure. When the walls are accelerating downwards, the gradient is reversed. During the cycle of oscillations, the slope of the pressure gradient between point A and B oscillates in a way that a pressure node is formed at the center of the enclosed fluid. By using this method, pressure nodes can be generated in extreme sub-wavelength cases. Here, generation of a stationary acoustic wave field does not depend on the gap of the capillary. In other words, acoustic wavelength and cavity dimensions are not related to each other for generating a stationary field. In this case, as long as two walls oscillate in phase and the gap is smaller than the acoustic wavelength, a stationary field can be generated inside in any frequency.

Now, the next problem is to make two walls oscillate in phase in a chip scale platform. This can be achieved by exciting flexural waves in a thick walled capillary. At lower harmonics, a thick walled capillary cross section moves up and down as a whole such that the top and bottom of the capillary moves in phase, meaning that, in *any harmonic of the flexural modes* of the capillary, pressure gradients at the capillary cross section can be generated. In addition, since the motion along the axis of the cylinder will also be a sinusoidal, periodic gradients along the central axis of the capillary will be present.

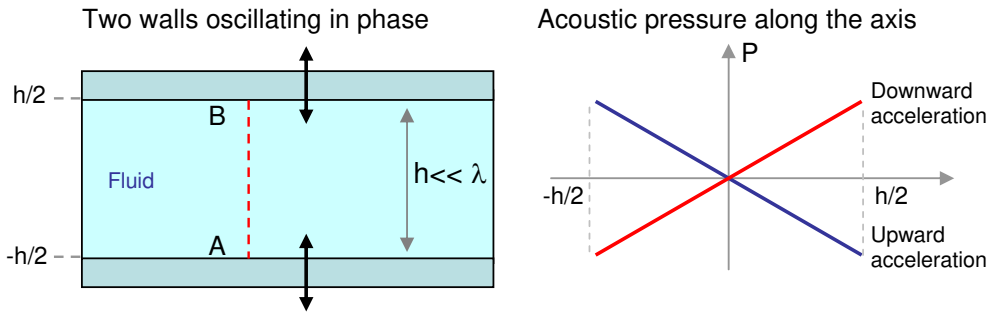

Figure 1.3: When two walls enclosing a fluid column oscillate in phase and the gap between them is much shorter than the acoustic wavelength, an oscillating stationary acoustic pressure field is generated. When walls accelerate in the upward direction, pressure at the bottom becomes maximum and the pressure at the top becomes minimum. When the walls accelerate in the downward direction, the pressure values are reversed. This leads to a pressure node at the center of the capillary.

Generating a high amplitude acoustic field depends on the particle acceleration at the fluid structure boundary level. If the forces applied to the fluid in terms of pushing and pulling are high, a higher amplitude acoustic field is generated. While Lead Zirconate Titanate (PZT) plates are one of the most reliable and efficient ways of electromechanical energy transduction, the maximum achievable particle velocity v_m is low. Given in [14], the maximum achievable particle velocity is limited by the maximum strain (S_m) a material can handle and the speed of sound c, such that $v_m = S_m c$. PZT is a ceramic material which cannot handle high strain. While PZT has a maximum achievable particle velocity of about 1 m/s, glass have about 620 m/s. In this case, by coupling mechanical energy generated by PZT into a glass capillary acting as a waveguide, much higher particle velocities can be achieved compared to the case of direct PZT-fluid coupling.

In this way, high amplitude vibrations can be generated in a glass capillary

driven by a PZT plate, which leads to the generation of high amplitude nonlinear acoustical effects in a micro-capillary at low voltage drives.

Need for New Actuator Mechanism

The PZT-glass capillary actuator mechanism presented in Figure 1.2 is an excellent way to generate flexural waves on a capillary. While the actuator displayed in Figure 1.2 has demonstrated an impressive achievement related to low power ultrasonic manipulation at the microscale, the folded structure of the capillary presents some challenges. First of all, because these preliminary devices are handmade, alignment of a folded capillary during bonding becomes a critical issue. Boundary conditions and dimensions are extremely important for standing wave acoustic systems and a slight variation during the simple assembly process may cause a significant change in device behavior. As the capillary folds around the PZT plate, it also defines length of resonating capillary section, which may vary from device to device due to the manual alignment procedure. In this case, the characterization of the device becomes difficult.

The second challenge is related to the polyimide coating. Silica capillaries, by themselves, are quite fragile. The polyimide coating enables flexibility so that it can be bent at 180° and dropped without generation of a fracture or breakdown. However, this coating layer may not always be desirable if high quality optical imaging in the capillary is required. As seen in Figure 1.2, under the UV light not only do fluorescent beads emit photons, which is the signal of interest, but polyimide also self fluoresces (glowing reddish under UV light), adding noise to the desired signal. When we are working with particles with a size of several microns and heavily doped with fluorescing molecules, this does not become a

critical issue. However, experiments in which samples may not emit as much photons as polyimide (as in case the of the platelets whose only surface membrane proteins are fluorescently tagged), emission from polyimide dominates the target signal coming from fluorescent markers. In short, polyimide not only absorbs and thus filters a part of UV light, but also dominates in the case of emission when the signal coming from the sample is low. While several methods for the nondestructive removal of polyimide coating are available (when the capillary is free of stress, i.e., straight), it is not straightforward when there is built-in-stress on the capillary due to its folded shape. As soon as the polyimide coating is removed, the glass capillary becomes extremely fragile and cannot support the stress built on by the folding. To overcome these challenges, a new actuator structure has been designed to eliminate the bending and associated problems mentioned above.

Fabrication

To generate standing waves on the capillary by coupling vibrations generated by an electrically excited PZT plate, symmetric boundary conditions are needed at the end of resonating capillary regimes where the capillary is bonded to the PZT plate. Instead of curling the capillary around the PZT, the structure is changed so that the capillary stays straight. For the following reason, the 0.5mm PZT-4 plates (available from EBL Products Inc.) are laser micromachined (with a Q-swithched Nd:YAG laser) into C-shaped structures. Trenches 250μm wide and 250μm deep are opened at the cantilever parts by laser micromachining to form bond grooves for better capillary bonding. A polyimide coated (polyimide thickness=12μm) silica capillary (PolyMicro Technologies) of ID=100 μm and OD=200μm is adhesively bonded to the C-shaped PZT plate via trenches mentioned above by 3M^{TM} instant glue. A low viscous glue is chosen so that no gaps remain for better coupling

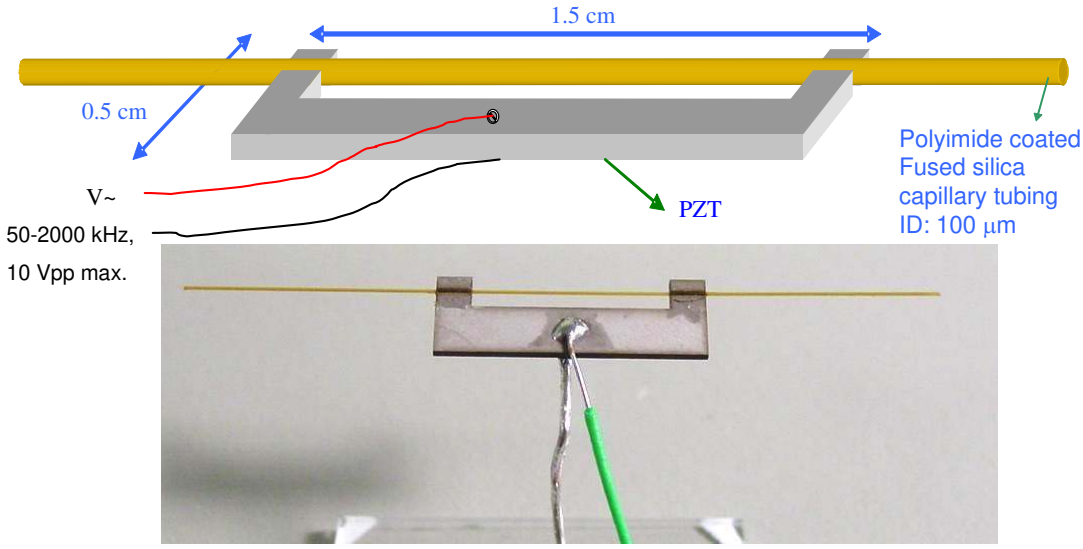

Figure 1.4: Schematic drawing of coupled C-shaped PZT capillary ultrasonic transducer (top) and picture of the actual device (bottom). The size of the PZT piece is 5mm by 15mm and the thickness is 0.5mm; the length of the capillary between the PZT cantilever ends is 11mm.

reasons. In some devices, for improved optical imaging sensitivity, the polyimide layer of the capillary between two cantilevers section is selectively ablated by using an open flame torch. The polyimide coating outside the PZT region is kept to enable robustness and flexibility for input-output connections. Finally, the actuator mechanism shown in Figure 1.4 eliminates all of the challenges mentioned before. Similar to the previous actuator design, two electrodes are soldered at the center of the PZT plate since a node of the displacement is at the center. The PZT plate is driven by a function generator in a frequency range of 35-2000 kHz and voltage drive range of 1-10 Vpp.

Estimated Cost of an Actuator

The total cost of a such actuator presented here is in the order of a few U.S. dollars. With automated mass production, the cost can be reduced further. With the low voltage drive factor included, cost efficient microfluidic actuators for point-of-care devices for the pharmaceutical and biomedical industry will be realized. A significant portion of the world population lives in underdeveloped regions where there is no access to bioanalytical laboratories or advanced hospitals. Unfortunately, every year millions of people, lose their lives because simple pathogenic diseases which could be treated with medicine only if the pathogen could be diagnosed correctly in a timely manner. In this case, cheap-to-fabricate, battery operated, portable point of care devices can help to save lives of millions of lives [15].

1.4 Guide to This Thesis

In Figure 1.5, a brief guide for the rest of this thesis is given. In Chapter 2, vibrational modes of the fluid filled thick walled silica cylindrical microcapillary are given. For the low frequency range, solutions of flexural, longitudinal and torsional modes are investigated from the elementary beam theory. It has been shown that for the flexural modes, elementary beam theory is not accurate enough. However, by including shear and rotary inertia effects through Timoshenko's approach and fluid loading, dispersion relation relating frequency and wave number can be found.

In Chapter 3, acoustical modes inside the microfluidic capillary, which vibrate in vibrational modes calculated in Chapter 2 are given. In particular, the acoustic field that results from the flexural motion of the capillary gets the most attention.

It has been shown that when the capillary vibrates in its flexural modes, in both subsonic and supersonic frequencies, acoustical modes can be generated inside the capillary efficiently because capillary dimension is much smaller than the acoustic wavelength inside the capillary. At subsonic frequencies, even the evanescent decay factor is large compared to the acoustic wavelengths. These factors enable sub-wavelength generation of acoustical radial modes inside the capillary. In Chapter 4, finite element modeling of the liquid filled cylindrical capillary is given. Analytically obtained dispersion relations and vibrational mode shapes match the simulation results excellently.

In Chapter 5, nonlinear acoustic interactions in a cylindrical micro capillary are investigated. First order acoustic pressure field, a necessary starting point for second order effects, is obtained from Chapter 2. Particularly, the acoustic radiation force field in a cylindrical capillary undergoing flexural vibrations is calculated in three dimensions. The analytical results achieved suggest that while pressure gradient plays an important role in terms of the acoustic force field, in the radial directions, the fluid particle velocity gradient plays the major role in the axial direction,. These two factors lead to particle collection and separation at specific locations. Force field and particle collection and separation locations are in excellent agreement with the experimental observations.

In Chapter 6, characterization of the PZT-glass capillary actuator and experimental results obtained on particle capture and focusing; separation of particles with respect to size; separation of particles with respect to acoustic contrast factors; planar chipscale centrifugation of processed and unprocessed fresh canine blood; eshceria-coli bacteria; and results on particle capture due to vibration of microbubbles are presented.

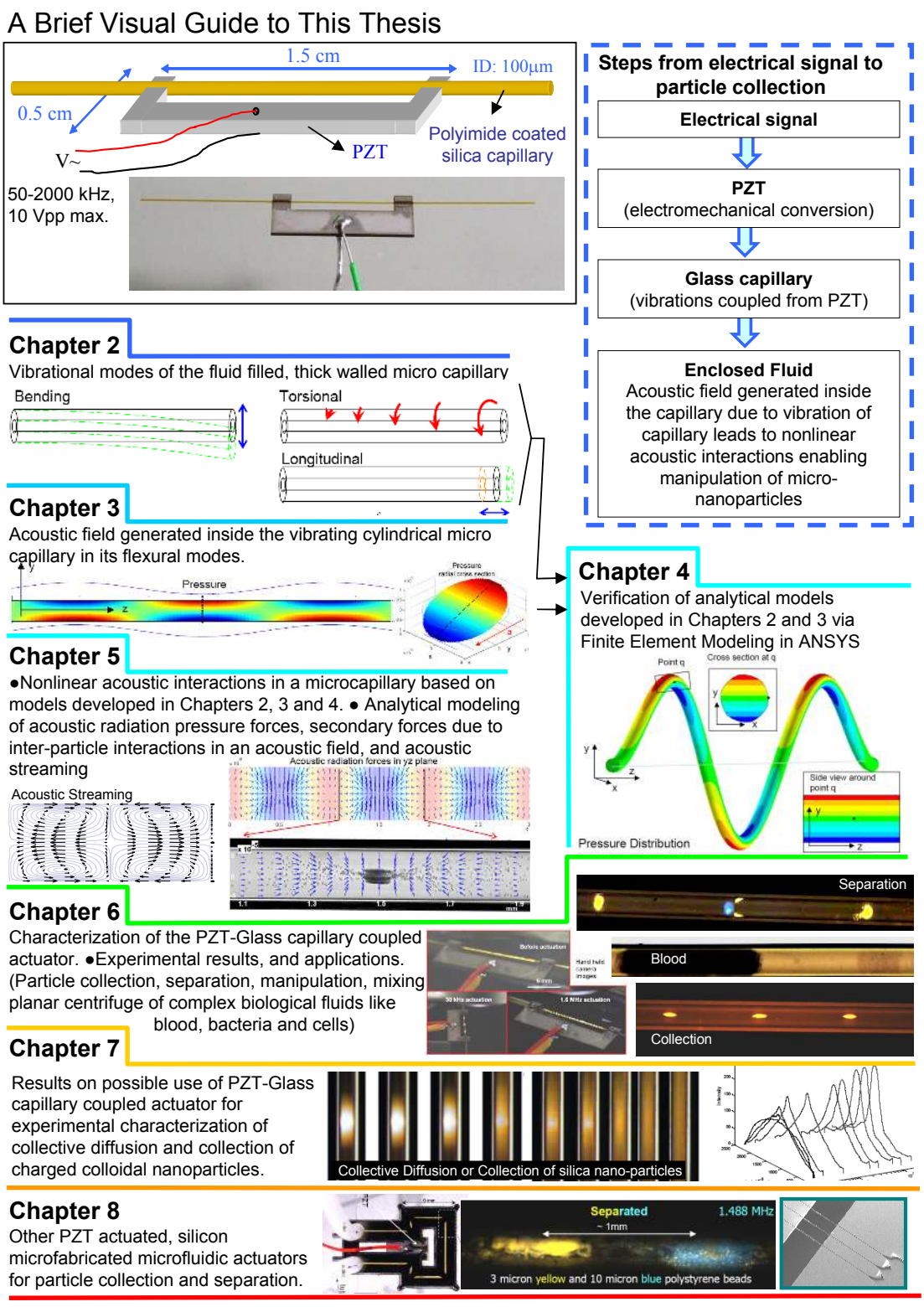

Figure 1.5: One page brief visual guide to this thesis. Details are described in Section 1.4

In Chapter 7, the application of the PZT-glass capillary actuator in terms of characterization of colloidal nanoparticles is demonstrated. It has been shown, under acoustic radiation force, that silica nanoparticles collect at particular locations. Due to the surface charge of the particles, modification of the distribution of the particles induces an electric field inside the channel. It has been shown, with the turning off the acoustic field, that particles undergo a collective diffusion, much higher than their normal diffusion. In this way, the device can be used to estimate surface charge related collective behavior of particles, and characterize the colloidal system. It has been also shown, after such a characterization, that it is possible to empirically estimate the acoustic force field because at equilibrium, acoustic forces counterbalance the acoustic radiation forces.

In Chapter 8, other types of acoustic microfluidic actuators fabricated and tested during the time of the doctoral study are shown. Similar to the PZT-glass capillary actuator, in the presented silicon bulk microfabricated actuator, acoustic separation is demonstrated. In this actuator mechanism, transverse vibrations on the silicon nitride membrane, vibrations on the silicon walls of the microfluidic chamber and acoustical modes inside the capillary lead to differential particle manipulation.

1.5 Summary of Major Accomplishments

The novel contributions of this research are:

1. Analytical calculation and Finite Element Modeling (in ANSYS^{TM}) of vibrational modes of a fluid filled thick walled cylindrical micro capillary have been shown.

2. Theoretical analysis and experimental demonstration of extreme sub-wavelength standing acoustic fields in a flexurally vibrating microcapillary at subsonic and supersonic frequencies are presented. In this way, sub-harmonic cavity modes are harmonically generated. For instance, by the method presented in this thesis, in between 30kHz–2MHz regime, more than 20 harmonic modes can be produced (all leading to particle manipulation), whereas the naturally occurring half wavelength cavity mode can be uniquely excited around 10MHz. Here, the harmonicity of sub-wavelength cavity modes depends on the harmonicity of the flexural modes of the enclosing micro capillary.

3. A three-dimensional analysis of acoustic radiation forces and secondary inter-particle forces in a cylindrical acoustic cavity is performed. A strong influence of fluid particle velocity gradient on the acoustic radiation forces, in addition to the acoustic pressure gradient, have been verified. Excellent agreement between theoretical models developed and experimental results have been achieved.

4. CMOS compatible low voltage collection of micro-nanoparticles, cells and bacteria has been demonstrated in a cheap and easy to fabricate microfluidic chip. Results on the separation of microparticles with respect to size; separation of particles with respect to acoustic contrast factors or density; planar centrifugation of blood in a capillary; and controlled bubble dynamics for capture of particles have been demonstrated.

5. Microscale characterization of colloidal nanoparticles under ultrasonic forces is performed. Formation of a macroscopic electric field by concentrating of charged nanoparticles in a confined region due to acoustic force field have been investigated.

6. Collective diffusion of charged nanoparticles after release of acoustic forces and related to that, a method for characterization of acoustic radiation forces in a microcapillary against interparticle electrostatic repulsion of colloidal nanoparticle system are presented.

7. Utilization of various vibrational modes excited in a silicon bulk microfabricated actuator for controlling and separation of microparticles in low voltage drive has been demonstrated, with integrated piezoresistive sensors.

CHAPTER 2

ON THE VIBRATIONS OF CYLINDRICAL CAPILLARY

Introduction

In this chapter, vibrational modes of a cylindrical capillary are analyzed. It is proven that cylinders have many different vibrational modes, and simple formula which define the eigenfrequencies of these modes easily do not exist. Depending on the aspect ratios and excitation frequencies many approximate shell theories have been introduced for specific cases. Some of these methods are described due to possible future relevance to capillary ultrasonic microfluidics. Many of these approximate modes work for the case of thin shells, in which thickness of the shell is small compared to its diameter.

We show that due to the aspect ratios of our cylindrical capillary (long cylinder with thick shell, $h = r_1 \ll \lambda < l$), some modes involving thickness, breathing or shear are not relevant, as frequency regime in which experiments are run is below the cutoff frequencies (<2.5 MHz). This is the reason in the great portion of this chapter, focus is mostly given to flexural, longitudinal and torsional modes. Particularly, flexural modes gets the highest attention as it is shown in the Chapter 3, that the flexural modes are responsible for subharmonic and subresonance generation of standing pressure waves inside the capillary.

In developing analytical approach of flexural vibrations, in this chapter it is shown that while for low frequency regime, the approximate Euler-Bernoulli beam theory explains well the behavior of the frequency response of the standing flexural vibrations, consideration of rotary inertia and shear corrections established by

Rayleigh [16] and Timoshenko [17] become necessary.

In the last part of the chapter, comparison of frequencies of modes are given for highlighting any coupling possibilities.

2.1 A Short Review of Exact Linear Elasticity Theory

Three dimensional theory of elasticity suggests that any elastic disturbance in an unbounded isotropic medium is propagated by two types of waves called dilatational and distortional. Dilatational waves are also called P-waves and propagate by restoring volume change by plane stresses. Distortional waves are mostly called S-waves and propagate by the transfer of shear deformation. Both wave types have distinct constant phase wave speeds which depend on material properties. In case of bounded mediums, reflection of wave from a boundary initiates other types of waves as well. In short, waves in bounded elastic medium are most often mixture of P and S waves. Speed of waves in bounded mediums are no longer constant but generally dispersive. This is why solution of wave propagation problems in bounded mediums by use of three dimensional theory of elasticity is extremely difficult. Solutions can be only obtained under certain conditions like semi infinite media, infinitely long plates or rods [18]. These solutions result in transcendental equations leading to infinitely many dispersion curves and results usually are obtained by numerical computing. With additional boundary conditions such as for finite media, superposition of infinitely many number of modes need to be included, which make analytical treatments very difficult.

For cylindrical structures, Pocchammer [19] and Chree [20] independently found solutions for infinitely long cylinders by using linear theory of elasticity. They

transformed fundamental equations and boundary conditions into cylindrical coordinates. While their solutions were not applicable for finite cylinders, they were still useful to understand the physics of wave propagation in cylinders. One can find a summary of their approach in classical text books such as [21, 22].

In case of hollow cylinders or cylindrical shells, most of the available theories ignore the transverse stress and strain components and this reduces the solution to only case of thin walled cylinders [1], which is why it is possible to find a great amount of literature for the case of thin walled shells. In order to find a solution for thick walled cylindrical shells by using three dimensional theory of elasticity, all six stress and strain components are needed, which makes the problem quite complex and not favorable to analytical analysis [23]. For cases where researchers were interested in the solution of thick walled cylindrical shells, studied certain cases of the problem such as: Mirsky and Herrmann, axially symmetric motion [24], non-axially symmetric motion [25]; Gazis, plane-strain vibrations [26]; Greenspon, flexural vibrations [27]. Gazis finally found the solution based on theory of elasticity by using Helmholtz potentials for the general case for the propagation of waves in infinitely long hollow circular cylinders [28]. He derived all 36 coefficients of the characteristic equation for the general case with stress free boundary conditions and derived dispersion relations for some cases. In the same year, Gazis published numerical solutions of his equations derived for thick cylinder for various shell thickness ratios and various vibrational modes [29]. This was a remarkable step since standing waves on simply supported finite shells is equivalent to the wave propagation in an infinite shell for the given mode and frequency. However, in cases of other boundary conditions such as free or clamped cases, various approximate shell theories are needed, otherwise infinite number of shell modes are

[1] In most cases thin walled cylinder theories require shell thickness to be at least 10 times smaller than the average shell radius.

required to be superimposed. Later Armenakas, Herrmann and Gazis published a booklet including the numerical results of frequency equations for hollow cylinders of various thicknesses and vibrational modes [30]. Singal and Williams [31] used energy method based on 3D theory of elasticity to analyze circumferential modes of vibrations of thick hollow cylinders.

As many approximate theories exist in literature regarding the topic, good comparisons of earlier methods can be found in the literature such as [32, 33].

Recently, Loy and Lam found a solution for finite cylinders with simply supported and clamped-clamped boundary conditions [23]. They analyzed the thick cylinder as a combination of many discrete thin cylindrical shells. From the principle of minimizing the stored energy, they found general eigenvalue equations from which they obtained numerical frequency values for various modes and cylinder thickness ratios. Another recent semi-analytical approach is provided by Mofakhami et al. [34], where they used techniques of variables separation on the basis of 3D theory of elasticity. Even their solution needed to satisfy special boundary conditions approximately. Their solution required a relatively smaller coefficient matrix and led to good convergence of the solution with moderate number of series terms.

2.2 Vibrational Modes and Their Frequency Spectrum for Liquid Filled Micro-Capillary

Most of the first harmonics of the various form of vibrational modes of a infinite cylindrical capillary are shown in Figure 2.1. For estimating the frequency range

roughly, it is possible to associate radial -thickness related modes of the cylinder with a plate having same thickness as the cylinder wall. The width of the plate can be the diameter of the cylinder and the length of the plate be the length of the cylinder. In this case we can associate breathing mode with the longitudinal-width mode of the plate, e.g. for cylinders having $r \ll l$ we expect two distinct frequency regimes for various types of vibrations. Modes which depend on the r or thickness would have much higher frequencies since frequency is inversely related to dimension along the vibration. In this case, bending, longitudinal and torsional vibrations would have low frequency values while modes involving thickness and radial modes and r-thickness related shear modes would have much higher frequencies.

For the PZT/capillary device, to be able to choose an analytical method, we need to reflect on aspect ratio of our cylindrical shell, and compare physical parameters of the cylindrical shell to wavelengths in the frequency range in which the actuator is run (Figure 2.1 is quite helpful in terms of visualizing this reflection). Length of the clamped-clamped part of the capillary (11mm) is much longer compared to its internal diameter (100μm). The shell wall (50μm) can be considered to be quite thick because it is half of the total diameter. Flexural wavelengths in the relevant frequency range (30kHz-2MHz) change from 10mm to 0.5mm. Hence, even for the smallest wavelength, the wavelength is about 10 times larger than the diameter or shell thickness of the capillary. Similarly, the circumference of the shell of the cylinder is also quite small compared to the wavelengths on the silica. By back of the envelope calculations using identity giving the wavelength $\lambda = c/f$ (where c is the speed of the elastic wave[2] and f is the frequency) we can estimate torsional, flexural and longitudinal modes would have modes at frequencies as low

[2]For silica speed of P and S waves are about 5760 m/s and 4000 m/s respectively

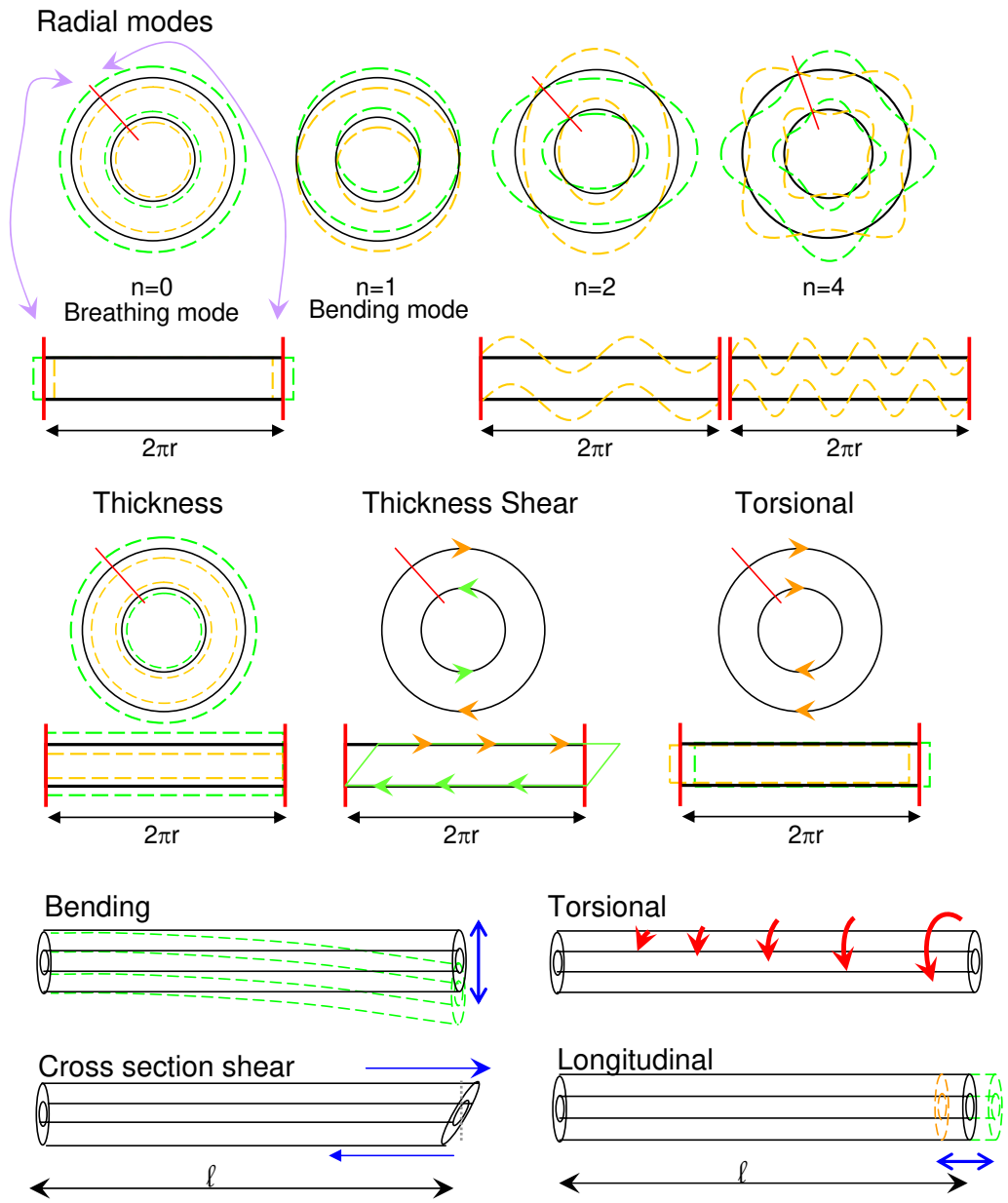

Figure 2.1: First harmonics of various vibrational modes of thick cylinder. To have a rough estimate of frequency range, radial and thickness modes of the cylinder cross section can be associated with a plate having the same thickness and its length is the diameter of the cylinder (the red line denotes the opening point). Here, the capillary has high aspect ratios ($r \ll l$).

as below 100 kHz, whereas thickness, radial and thickness modes would start at frequencies like 8-10 MHz range.

Frequency range in which the capillary has been actuated, covers the lower harmonics of vibrational modes such as flexural, longitudinal and torsional modes. In this range, use of simple approaches analyzing the force and displacement of the capillary elements, yields sufficiently accurate results. In [29] Gazis confirms this claim by comparing lower harmonics he calculated through the 3 dimensional linear theory of elasticity to the values given in [35], in which a Timoshenko-type shell theory has been used. In the following sections, we will introduce stress and strain, and from there analytically derive different types of vibrations present on the capillary, give dispersion relations for these vibrations and compare frequencies of modes of these vibrations with each other.

2.2.1 Stress, Strain and Hooke's Law

Elastic properties of materials strongly depend on their molecular structures. Here, the case of an isotropic solid will be investigated, where elastic properties are the same in all directions. This derivation can be found in many references related to elasticity or wave phenomena such as [36]. As shown in Figure 2.2 we start with a rectangular solid beam made up from an isotropic material. If we fix one end of the rectangular beam and apply a force to the other end of the beam, beam gets longer in the axis of the force applied. It is important to note that forces applied here stay in the regime such that no plastic or hysteresis deformation occurs in the beam, when the force is applied. Linear elastic theory dictates that:

1. When the applied force is increased, extension of the beam (δl) increases

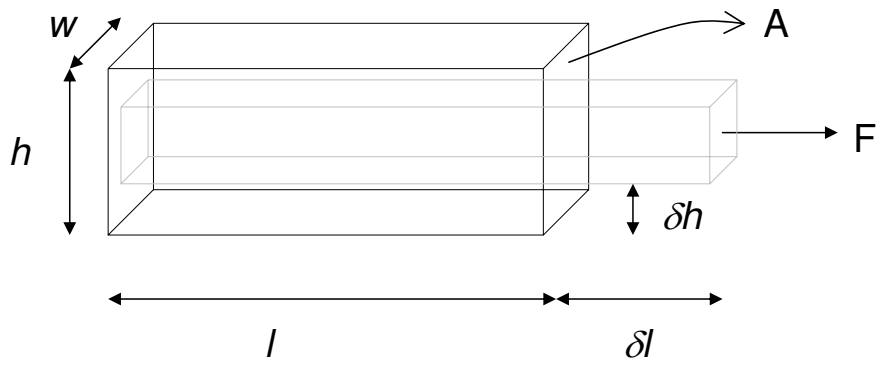

Figure 2.2: Linear deformation of a rectangular solid beam under a force applied in one dimension.

linearly with force.

2. When the area (A) of the beam is increased, extension of the beam (δl) decreases linearly.

3. Shrinkage in the height of the beam (δh) is proportional to the extension of the beam (δl).

Using these assumptions, linear elasticity gives:

$$\delta l \sim l\frac{F}{A} \tag{2.1}$$

Furthermore, δl depends linearly on the material property, Young's Modulus E,

$$\delta l = \frac{1}{E} l\frac{F}{A} \ . \tag{2.2}$$

Rewritten we have:

$$\frac{\delta l}{l} E = \frac{F}{A} \ . \tag{2.3}$$

The quantity $(\frac{\delta l}{l})$ is the ratio of extension to length and is known as strain (ε). Strain ε is proportional to force per unit area $(\frac{\delta F}{A})$, which is the stress (σ).

$$\varepsilon = E\sigma \tag{2.4}$$

This fundamental relation relating strain to stress is often called Hooke's Law and the general relationship between stress and strain is called the constitutive relationship.

The stress $\sigma = \frac{\delta F}{A}$ is the normal stress due to the force applied in normal to the surface A; however, solids can also be under other types of stress due to tangential forces. If one places their palm over a thick book placed on a surface and move the palm parallel to the surface, each page under the palm will slide with respect to the page just below it and the cross section of the book will transform to a parallelogram. Shear stress is defined by the ratio of tangential force (F_{xy}) applied to area (A) resisting this tangential force:

$$\sigma_{xy} = \frac{F_{xy}}{A} \ . \tag{2.5}$$

When shear stress is present, as shown in Figure 2.3, the block of material deforms and this deformation is called shear strain and is measured by the angle of deformation (γ) in radians,

$$\frac{\Delta x}{h} = \tan\gamma \approx \gamma \tag{2.6}$$

Similar to normal stress and strain, shear stress and shear strain are proportional to each other by a constant. This constant is called *shear modulus* or *modulus of rigidity* and is defined by,

$$G = \frac{\sigma_{xy}}{\gamma} \ . \tag{2.7}$$

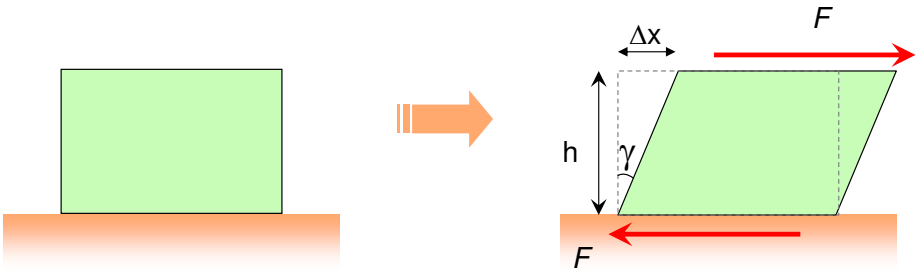

Figure 2.3: Deformation of a block of material under tangential forces.

Utilizing the information given above, and using classical analytical results in beam theory, elastic resonant response of the fluid-filled glass capillary driven by PZT plate is investigated in the following sections for the cases of flexural, torsional and longitudinal modes.

2.3 Flexural Modes of the Cylindrical Capillary

Here we now derive the beam bending theory from the linear Hooke's law. The theory of beam bending is dependent on beam cross section area with respect to length (A/l) as these effect not only the peak stress and strain but also the distribution of these across the beam cross section.

2.3.1 Euler-Bernoulli Beam

The Euler-Bernoulli approach to the bending of a beam is one of the more simpler theories that gives relatively good results for long thin beams. General assumptions related to this theory's derivation are:

1. Compared to beam length, lateral beam deflections are small.

2. Deformation of the shape is related to the pure bending, in other words as shown in part (a) of Figure 2.4 (dashed circle), all planes normal to the beam remains normal. This means that as shown in part (b) of Figure 2.4, the longitudinal strains (so the stresses) along the thickness of the beam vary linearly, which also means that shear deformations in the cross section are neglected.

From Figure 2.4 we can write

$$\Delta x' = (R - z)d\theta \tag{2.8}$$

$$\Delta x = Rd\theta \ . \tag{2.9}$$

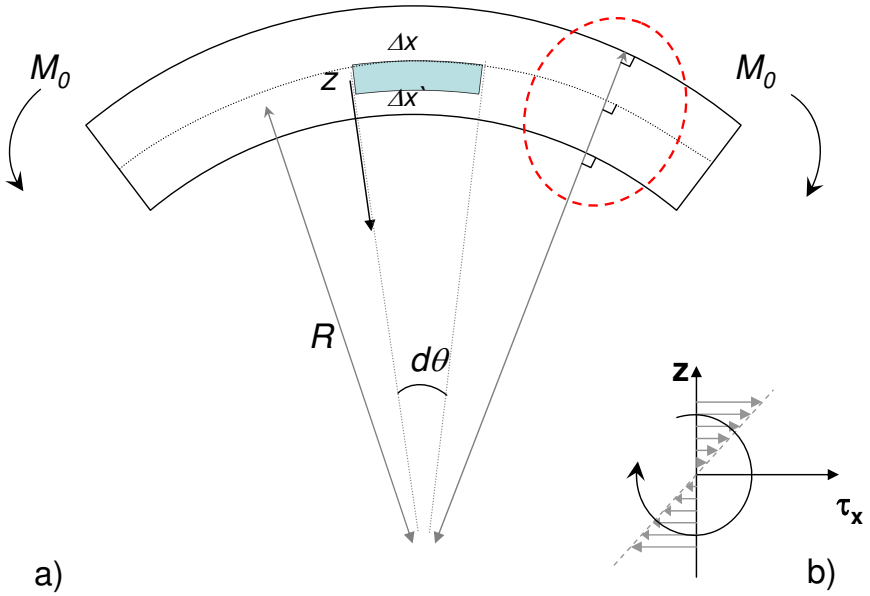

Figure 2.4: a) Bending of a beam element, b) stress in the z-axis

Strain on the small element is defined by,

$$\varepsilon(z) = \frac{\Delta x' - \Delta x}{\Delta x} \tag{2.10}$$

$$\varepsilon(z) = \frac{(R-z)d\theta - Rd\theta}{Rd\theta} = -\frac{z}{R} \tag{2.11}$$

since

$$\sigma(z) = E\varepsilon(z) \tag{2.12}$$

$$dF = -E\frac{z}{R}dA\ . \tag{2.13}$$

If we calculate the moment at point $z = 0$

$$M(x) = \int dF(x,z)dz \tag{2.14}$$

$$M(x) = -\int_{-h/2}^{h/2} \sigma(z) z dA \tag{2.15}$$

from Equation 2.12

$$M(x) = -\int_{-h/2}^{h/2} E\frac{z^2}{R}dA \tag{2.16}$$

$$M(x) = -\frac{E}{R}\underbrace{\int_{-h/2}^{h/2} z^2 dA}\ . \tag{2.17}$$

In this equation, the value of the integral is called *Second Moment of Inertia* or *Area Moment of Inertia* and is denoted by I. It should not be confused with the *Moment of Inertia* which is used for angular acceleration. Area moment of inertia defines how much a beam resists the bending. The equation above takes the form

$$M(x) = -\frac{1}{R}EI \tag{2.18}$$

where the quantity EI is called the flexural rigidity. This equation means that beam bends in a way that the internal moment cancels the external moment at point $x = 0$.

For the case of a thick hollow cylinder (although still $l >> A$),

$$I = \int_{r_2}^{r_1} z^2 dA \ . \tag{2.19}$$

In the case of a cylinder body $dA = 2\pi z dz$ so

$$I = \int_{r_2}^{r_1} z^2 2\pi z dz \tag{2.20}$$

$$I = \frac{\pi}{4}(r_2^4 - r_1^4) \ . \tag{2.21}$$

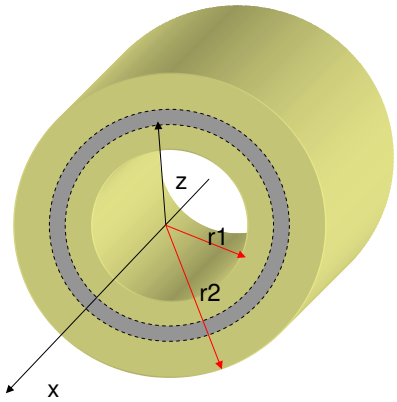

Figure 2.5: Cross section of the cylinder.

In Equation 2.18 the only item was left to be defined is $\frac{1}{R}$, which is the radius of the curvature. We would rather have a mathematical equivalent of this item, which would fit better in an equation.

As is shown in Figure 2.6, the length of the beam element ds can be related to radius of curvature R as,

$$ds = Rd\theta \ . \tag{2.22}$$

The relation between increase on the length of the beam ds and dx can be written as

$$ds = \frac{dx}{\cos\theta} \ . \tag{2.23}$$

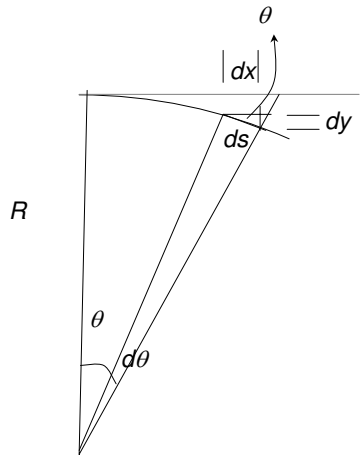

Figure 2.6: Radius of curvature in a bending beam.

Since the θ is small, $\cos\theta \cong 1$ and so $ds \cong dx$ On the other hand, for small angle θ

$$\frac{\partial y}{\partial x} = \tan\theta \cong \theta \tag{2.24}$$

from these we can conclude that for small angle θ

$$\frac{\partial^2 y}{\partial x^2} = \frac{1}{R} \tag{2.25}$$

replacing $1/R$ term in Equation 2.18 we reach to the relationship between the bending moment and the curvature,

$$M(x) = -EI\frac{\partial^2 y}{\partial x^2}\ . \tag{2.26}$$

2.3.2 Time Varying Flexural-Bending Waves in Thin Rods

In this section, we will analyze the transverse motion of the beam. Under the assumption of the Euler-Bernoulli beam theory, we will derive the equation of motion. We will neglect the shear and rotary effects, assuming the central axis remains vertical with respect to the motion of the beam as shown in Figure 2.7.

We start with the equation of motion for the beam element having cross sectional area A and density ρ shown in Figure 2.7. Bending moment M, shear force V and other external forces q act on the beam. Balancing these forces leads to the equation of motion:

$$-V + (V + \frac{\partial V}{\partial x}\, dx) + q\, dx = \rho A\, dx \frac{\partial^2 y}{\partial t^2} \tag{2.27}$$

which reduces to

$$\frac{\partial V}{\partial x} + q = \rho A \frac{\partial^2 y}{\partial t^2}\ . \tag{2.28}$$

If we write the equation for the moment of the beam element,

$$(V + (V + \frac{\partial V}{\partial x}\, dx))\frac{dx}{2} + M - (M + \frac{\partial M}{\partial x}\, dx) = 0 \tag{2.29}$$

assuming $\frac{\partial V}{\partial x}\,(dx)^2$ is small compared to the rest, we find

$$V = \frac{\partial M}{\partial x}\ . \tag{2.30}$$

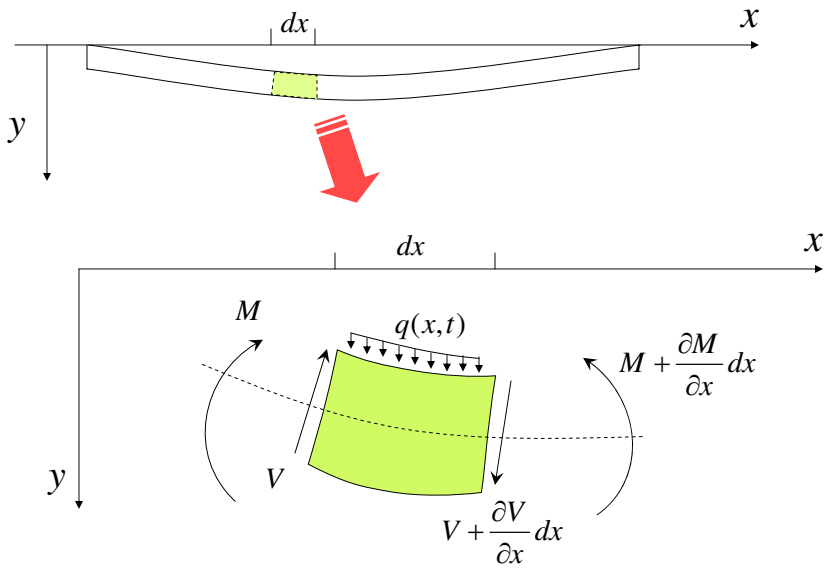

Figure 2.7: Transverse motion of the beam and the beam element.

If we substitute 2.30 in 2.28 we find

$$\frac{\partial^2 M}{\partial x^2} + q = \rho A \frac{\partial^2 y}{\partial t^2} \ . \tag{2.31}$$

Substituting Equation 2.26 for M, and noting that cross sectional area and physical parameters are constant along the beam we finally get

$$EI\frac{\partial^4 y}{\partial x^4} + \rho A \frac{\partial^2 y}{\partial t^2} = q \tag{2.32}$$

which represents the equation of motion for the beam element. This is not a usual wave equation as we see the 4^{th} order derivatives involved, however we will see that this formula will be the governing formula in analyzing the flexural waves in a beam. This is a 4^{th} order differential equation, and needs four boundary conditions to solve. These boundary conditions can include combinations of $y(x)$ and its derivatives related to the shear and the moment.

In case no external forces are involved, the equation of motion is reduced to

$$\frac{\partial^4 y}{\partial x^4} + \frac{1}{a^2}\frac{\partial^2 y}{\partial t^2} = 0, \qquad a^2 = \frac{EI}{\rho A} \ . \tag{2.33}$$

If we assume the propagation of harmonic waves,

$$y(x) = Ae^{i(\alpha x - \omega t)} \tag{2.34}$$

and substitute in 2.33 we find

$$\alpha^4 - \frac{\omega^2}{a^2} = 0 \tag{2.35}$$

$$\text{so} \qquad \alpha = \pm\sqrt{\frac{\omega}{a}}, \quad \alpha = \pm i\sqrt{\frac{\omega}{a}} \ . \tag{2.36}$$

Since $\omega = c_p\alpha$, where c_p is the phase velocity, we find the dispersion relation,

$$c_p = \pm a\alpha = \pm\sqrt{a\omega} \ . \tag{2.37}$$

Real roots of the α refer to traveling wave solutions, while the complex roots refer to nonpropagating, spatially decaying standing wave solutions; both are dispersive as they are related to ω by $\sqrt{\omega}$.

Equation 2.37 suggests that the phase velocity (c_p) of the wave increases with frequency. While this confirms with the experimentally observed results in low frequency regime, it creates an anomaly for higher frequencies since formula in its current case suggests there is no limit to the phase velocity and can diverge to infinity at high frequency limit. This is not a possible case for any type of wave and this anomaly will be discussed in a later part by including rotation and shear effects [16, 17]. Before proceeding to that part we will use the equations we derived here to get the mode shapes of a finite hollow cylinder and the approximate dispersion relation.

2.3.2.1 Natural Frequencies of a Fluid-Filled Finite Hollow Thick Cylinder

We may use the separation of variables technique here. Assuming the solution has the form

$$y(x,t) = Y(x)T(t) \tag{2.38}$$

and substituting in Equation 2.33 we find,

$$a^2 \frac{1}{Y}\frac{\partial^4 Y}{\partial x^4} = \frac{1}{T}\frac{\partial^2 T}{\partial t^2} = \omega^2 \ . \tag{2.39}$$

From this T and Y follow up as,

$$T(t) = Ae^{i\omega t} \tag{2.40}$$

$$Y(x) = C_1 \sin\beta x + C_2 \cos\beta x + C_3 \sinh\beta x + C_4 \cosh\beta x \tag{2.41}$$

where

$$\beta^4 = \frac{\omega^2}{a^2} \tag{2.42}$$

for the simplicity related to our boundary conditions a better equivalent of Y would be

$$\begin{aligned} Y(x) &= D_1(\cos\beta x + \cosh\beta x) + D_2(\cos\beta x - \cosh\beta x) \\ &\quad + D_3(\sin\beta x + \sinh\beta x) + D_4(\sin\beta x - \sinh\beta x)\ . \end{aligned} \tag{2.43}$$

In our case, the capillary is fixed at two points where grooves opened on the PZT plate. So for the regime we are interested we treat the ends as fixed boundary conditions as shown in Figure 2.8 as:

$$Y(x)\big|_{x=0} = \frac{dY(x)}{dx}\Big|_{x=0} = 0 \tag{2.44}$$

$$Y(x)\big|_{x=l} = \frac{dY(x)}{dx}\Big|_{x=l} = 0 \tag{2.45}$$

From the boundary condition at $x = 0$ we find $D_1 = D_3 = 0$, and from the fixed $x = l$ case we find the frequency equation

$$\cos(\beta l)\cosh(\beta l) = 1 \tag{2.46}$$

resulting in $\beta_n l = 4.73, 7.85, 11.00, 14.14, 17.279,$ ....., $\beta_n l - \pi,\ \beta_n l,\ \beta_n l + \pi,$ ..... After the 5^{th} mode, the incremental increase in the frequency parameter converges to π, as seen in Figure 2.9.The resulting wave function can be written as,

$$y_n(x,t) = \Big(D_2(\cos\beta_n x - \cosh\beta_n x) + D_4(\sin\beta_n x - \sinh\beta_n x)\Big)e^{i\omega t} \tag{2.47}$$

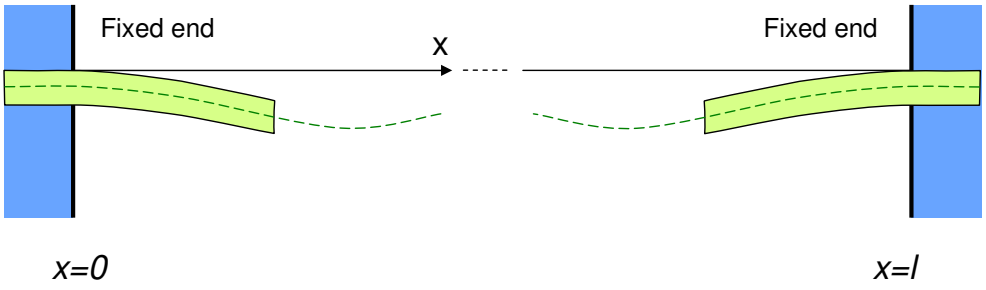

Figure 2.8: Boundary conditions for the capillary; both ends are fixed.

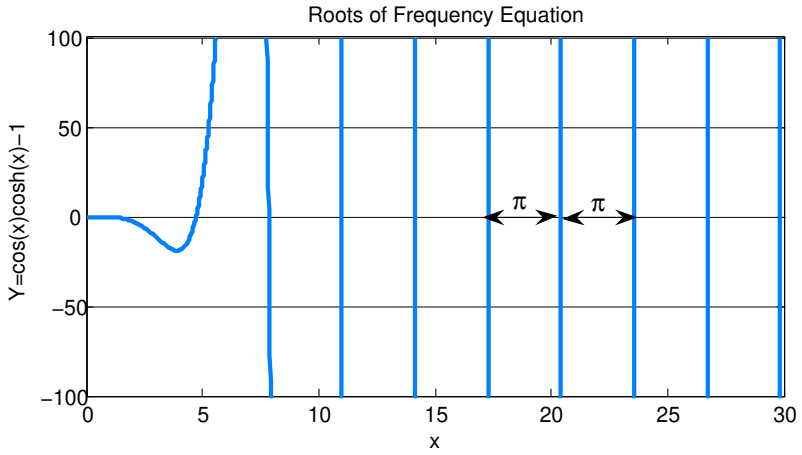

Figure 2.9: Roots of the frequency equation; the increase in the frequency parameter converges to π after the 5^{th} mode.

and the relation between D_2 and D_4 is

$$\frac{D_2}{D_4} = -\frac{\sin\beta_n l - \sinh\beta_n l}{\cos\beta_n l - \cosh\beta_n l} \tag{2.48}$$

$$= -1.018,\ -0.999,\ -1,\ -1,\ \text{.....(converges to -1 after n=3)} \tag{2.49}$$

From these, we can plot the mode shapes for the clamped clamped case. A few modes are plotted in Figure 2.10.

For quick and handy calculations for higher modes, $y_n(x,t)$ given in Equation

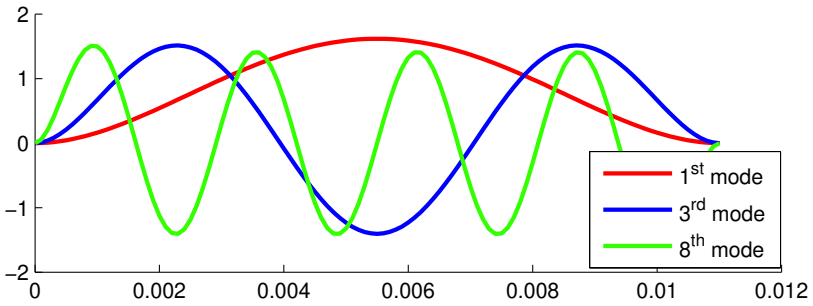

Figure 2.10: 1st, 3rd and 8th flexural mode shapes for the clamped-clamped case.

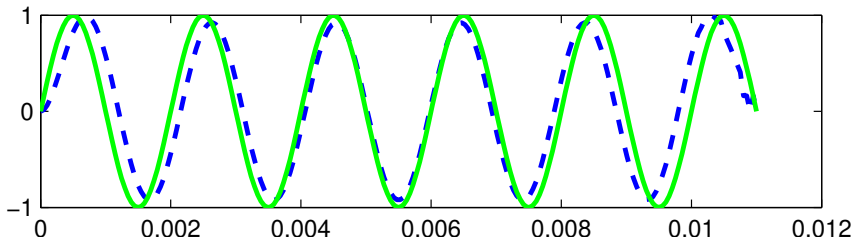

Figure 2.11: At higher modes, $y_n(x,t)$ given in Equation 2.47 approaches a simple sine function given in Equation 2.50.

2.47 can be approximated as

$$y_n(x) \approx A \sin\left(\frac{n\pi x}{l}\right) \tag{2.50}$$

where amplitude A should be re-normalized accordingly. As shown in Figure 2.11 for the 11th sine will give an approximate solution.

From 2.33 and 2.42 we find the final form of the dispersion relation,

$$f_n = \frac{(\beta_n l)^2}{2\pi l^2}\sqrt{\frac{EI}{\rho A}} \tag{2.51}$$

where I for the hollow cylinder is given in Equation 2.21, and $A = \pi(r_2^2 - r_1^2)$. In fact in this equation, the part included in the square root is nothing but the ratio of flexural rigidity over the mass per unit length. This equation can be generalized

for structures composed of different materials within this analogy and EI can be replaced by the total flexural rigidity of the composite structure and ρA can be replaced by the total mass per unit length of the composite structure.

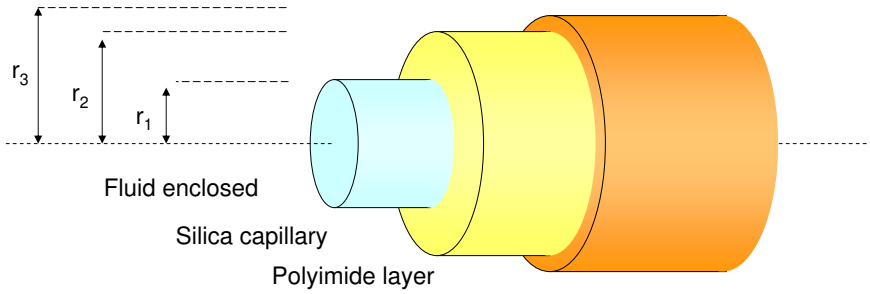

Figure 2.12: Drawing of silica capillary with the fluid enclosed and the polyimide coating.

As shown in Figure 2.12, in our case, the capillary is composed of a silica capillary and water, and in some cases, we also have a thin layer of polyimide coating on the capillary. In this case, we can generalize equation 2.51 as follows

$$f_n = \frac{(\beta_n l)^2}{2\pi l^2}\sqrt{\frac{E_1 I_1 + E_3 I_3}{\rho_1 A_1 + \rho_2 A_2 + \rho_3 A_3}} \tag{2.52}$$

where $E_3 I_3$ is the flexural rigidity of polyimide coating, $\rho_2 A_2$ is the mass of liquid enclosed per unit length and $\rho_3 A_3$ is the mass of polyimide coating per unit length. In Figure 2.13, frequency versus mode numbers for flexural modes are plotted for various cases *(i)* silica capillary, *(ii)* silica capillary including water, *(iii)* silica capillary including polyimide coating, and *(iv)* silica capillary including water and polyimide coating. As shown in Table 2.1, polyimide has much lower elastic modulus value compared to silica and also because it is a thin layer so it shifts the resonance frequencies by about 7%. Water, as a standard fluid characteristic, does not have any elastic modulus value and it only acts as a uniform mass load, decreasing the resonance frequencies by 7%. The polyimide coated capillary

including water case is plotted as the black curve showing about 13% decreased frequency.

Table 2.1: Material and geometrical properties for silica, polyimide and water.

	Water	Silica	Polyimide
Elastic Modulus (Gpa)	--	73-68	7.5-10
Shear Modulus (Gpa)	--	31	1-10
Bulk Modulus (Gpa)	2.2	41	<10
Density (kg/m^3)	1000	2200	1420
Poisson's Ratio	--	0.17	0.35
Inner Radius (μm)	0	50	100
Outer Radius (μm)	50	100	112

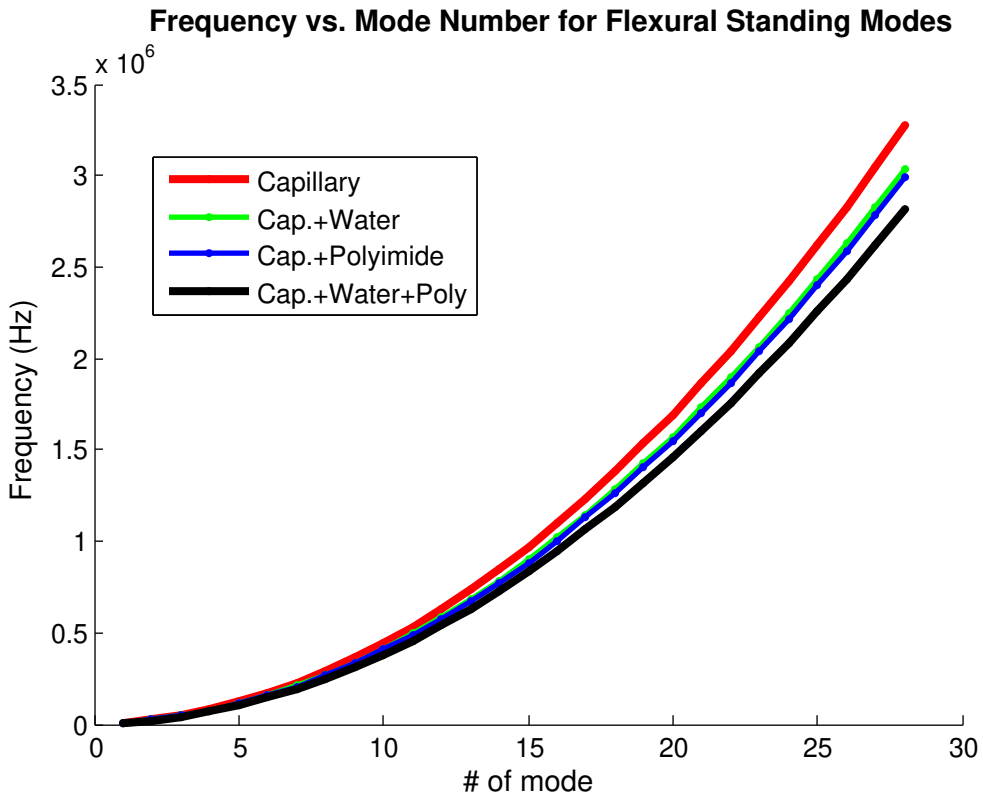

Figure 2.13: Frequency versus harmonic number of the flexural mode.

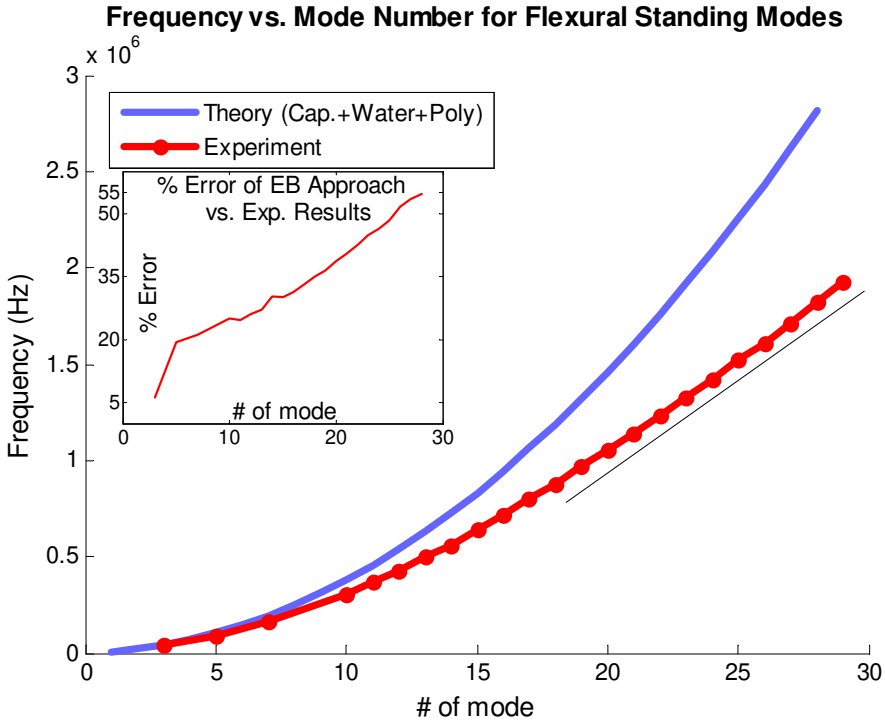

Figure 2.14: Frequency versus harmonic number of the flexural mode: Comparison of theoretical and experimental results.

2.3.2.2 Comparison of the Theory and Experimental Results

We can compare the theoretical dispersion relationship obtained in the previous section with the experimental results. Figure 2.14 shows the comparison of the frequency and mode number relationship we obtained from Euler-Bernoulli approximation with the experimental results. Experimental results were obtained through the frequency scan of the actuator, and visually monitoring the collection of particles under a microscope. At resonant frequencies the particles are collected at nodes, providing the wavelength of the standing wave. Hence, the umber of focusing locations gives the flexural mode number. While for low frequencies we see a relatively good match, for higher frequencies Euler-Bernoulli (EB) predicted mode number seems to diverge away from the experimental results. As shown in

subplot of Figure 2.14 we observe a systematic error which increases with increasing mode number and frequency. At the 28^{th} mode error goes up to 55%. We see that this discrepancy can be minimized by introducing a constant (0.75) to the dispersion relationship[3]

$$f_n = (\frac{3}{4})\frac{(\beta_n l)^2}{2\pi l^2}\sqrt{\frac{E_1 I_1 + E_3 I_3}{\rho_1 A_1 + \rho_2 A_2 + \rho_3 A_3}} \ . \tag{2.53}$$

With this correction, the results are plotted in Figure 2.15. The percentage error has been decreased, and although the theoretical and experimental values match within an order-of-magnitude, we still see a significant mismatch. This deviation is mostly related to the mismatch in the curve shape suggesting, additional terms might be needed for a better fit. While the EB approach suggests a quadratic

[3]This ambiguity will be re-touched in future sections.

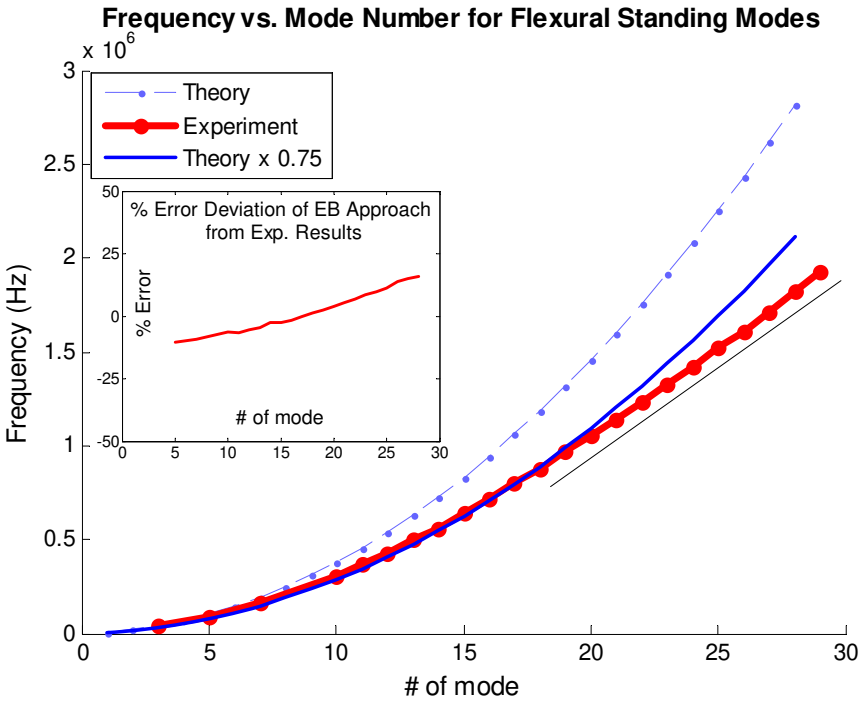

Figure 2.15: Comparison of theoretical and experimental results after introducing the constant.

tendency in frequency, experimental results show a linear increase at higher frequencies. This anomaly is due to ignored shear and rotary inertia effects in the EB approach, and will be estimated in the following section.

2.3.3 Corrections for the Shear and Rotary Inertia

The assumptions made to derive Euler-Bernoulli equations begin to fail at high frequencies. First correction to EB approach came from Rayleigh [16] as he included the effect of rotary inertia. When calculating total energy of the beam he included kinetic energy due to the angular velocity of infinitesimal sections. In Equation 2.24 it was shown that angle θ is given by $\partial y/\partial x$; in this case angular velocity $\dot{\theta}$ is

$$\dot{\theta} = \frac{\partial}{\partial t}(\frac{\partial y}{\partial x}) = \frac{\partial^2 y}{\partial x \partial t} \tag{2.54}$$

so the kinetic energy term due to the rotation is given as

$$K_r = \frac{1}{2}\int_0^l I_0(\frac{\partial^2 y}{\partial x \partial t})^2 dx \tag{2.55}$$

where I_0 is the mass moment-of-inertia about the central axis, per unit length, and is given by

$$I_0 = \rho I \tag{2.56}$$

where in the case of hollow cylinder, I is given by Equation 2.21.

From total energy and by using Hamilton's principle,[4] Rayleigh has found the equation of motion as

$$EI\frac{\partial^4 y}{\partial x^4} + \rho A\frac{\partial^2 y}{\partial t^2} - \rho I\frac{\partial^4 y}{\partial x^2 \partial t^2} = q \tag{2.57}$$

[4]More information about the Hamilton's principle can be found in many classical mechanics textbooks like [37], in particular in [38] Rayleigh's derivation is given as an elegant example of Hamilton's principle.

which reduces to EB case given in Equation 2.32, in the absence of rotary inertia.

Rayleigh's correction was good enough to predict that the phase velocities are bounded so that they can not diverge to infinity. However, they were not good enough to match the upper limit, and Timoshenko [17] included shear effects and obtained the closest approximation to the exact theory. As shown in Figure 2.16, beam elements not only have restoring force due to bending (springs k_b), but also due to the shear of the beam elements (springs k_s) [1].

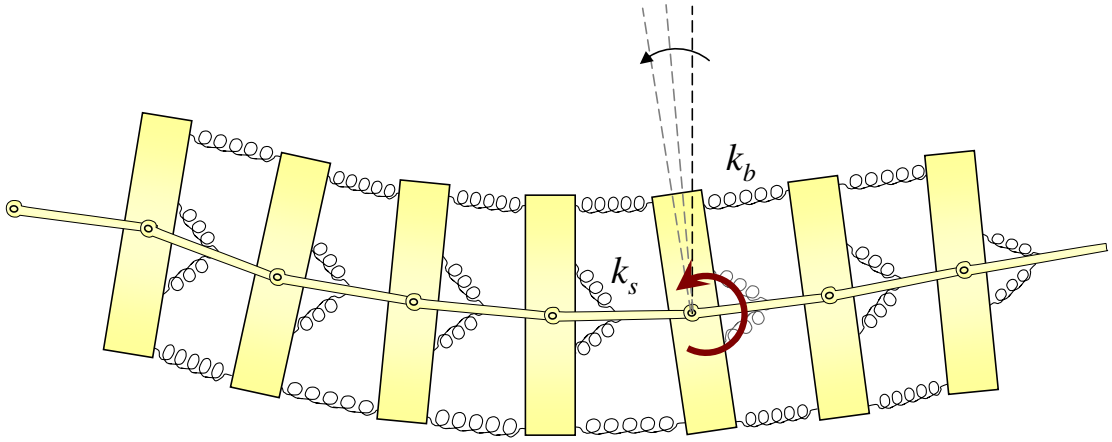

Figure 2.16: Lumped parameter modeling of Timoshenko model [1]. Energy can be stored in bending springs, shear springs and also in rotation of beam element around its central pivot. Total angle of deflection reflects the angle due to flexing of the beam element while remaining normal to its axis and angle due to shear-rotation around the pivot.

In this case, during the motion of the beam element, kinetic energy is stored in the vertical direction ($\dot{y}$), and rotation of beam element ($\dot{\theta}$). On the other hand, potential energy is stored in the bending of the beam (bending springs k_b), and shear stress on each beam (shear springs in the lumped system, k_b). While it is possible and easy to use Hamilton's principle to derive the equation of motion from

energy terms, here, for the sake of simplicity we will add the force related to shear effects to the Rayleigh's equation of motion and proceed from there as done by Timoshenko [17].

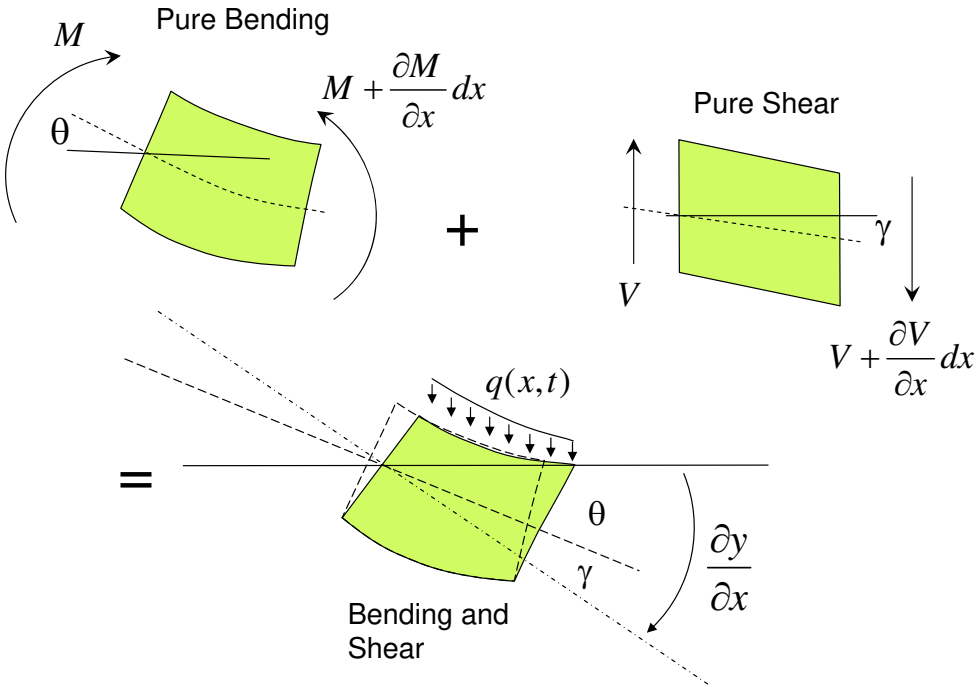

Figure 2.17: Beam element showing deflections due to pure bending; pure shear; bending and shear combined. Total angle of deflection includes distortion due to pure bending and the shear.

As shown in Figure 2.17 the angular deformation beam element undergoes, is not only due to angle of bending (θ) but also due to shear strain (γ). As shown in Figure 2.17 in this case, Equation 2.24 changes to

$$\frac{\partial y}{\partial x} = \theta + \gamma \ . \tag{2.58}$$

Related to the bending of the beam element, Equation 2.18 still holds where the radius of the curvature is R,

$$\frac{1}{R} = \frac{\partial \theta}{\partial x} \tag{2.59}$$

and

$$M(x) = -EI\frac{\partial\theta}{\partial x} \ . \tag{2.60}$$

Shear Force V can be calculated by

$$V = \int \sigma_{xy} dA \tag{2.61}$$

from Equation 2.7 we have

$$V = G\int \gamma dA = (G\gamma A)\kappa \tag{2.62}$$

where κ is defined by Timoshenko as shear coefficient and depends on the shape of the cross section of the beam. In [39] values of κ for various beam cross sections are given and in the case of a hollow cylinder we have

$$\kappa = \frac{6(r_2^2 + r_1^2)^2(1+\nu)^2}{7r_2^4 + 34r_2^2r_1^2 + 7r_1^4 + \nu(12r_2^4 + 48r_2^2r_1^2 + 12r_1^4) + \nu^2(4r_2^4 + 16r_2^2r_1^2 + 4r_1^4)} \tag{2.63}$$

where ν is the poisson ratio for fused silica. By using values given in Table 2.1, we find $\kappa = 0.63$ for our hollow cylinder.

Rephrasing Equation 2.58 and replacing γ we have

$$V = AG\kappa(\frac{\partial y}{\partial x} - \theta) \ . \tag{2.64}$$

Similar to Equation 2.27-2.29 from Figure 2.17, we can write equations of motion for rotation and translation. For the rotation we have

$$(V + (V + \frac{\partial V}{\partial x}\,dx))\frac{dx}{2} + M - (M + \frac{\partial M}{\partial x}\,dx) = \rho I dx\frac{\partial^2\theta}{\partial t^2} \tag{2.65}$$

where this equation is equivalent to Equation 2.29 except the right side equals to the angular acceleration due to the inclusion of rotary inertia in the calculation. Ignoring the square of small terms, equation of motion for rotation becomes

$$V - \frac{\partial M}{\partial x} = \rho I\frac{\partial^2\theta}{\partial t^2} \tag{2.66}$$

from Equation 2.64 and Equation 2.60 we have

$$EI\frac{\partial^2\theta}{\partial^2 x} + AG\kappa(\frac{\partial y}{\partial x} - \theta) - \rho I\frac{\partial^2\theta}{\partial t^2} = 0 \ . \tag{2.67}$$

Similar to Equation 2.28 for the case of pure translation, equation of motion follows as

$$-V + (V + \frac{\partial V}{\partial x}\,dx) + q\,dx = \rho A\,dx\frac{\partial^2 y}{\partial t^2} \tag{2.68}$$

$$\text{so,} \qquad \frac{\partial V}{\partial x} + q = \rho A\frac{\partial^2 y}{\partial t^2} \tag{2.69}$$

If we replace V From Equation 2.64 we have

$$\rho A\frac{\partial^2 y}{\partial t^2} - AG\kappa(\frac{\partial^2 y}{\partial x^2} - \frac{\partial\theta}{\partial x}) = 0 \ . \tag{2.70}$$

At the end, we have two coupled equations of motions; for any external force that is zero ($q(x,t) = 0$) we have

$$\rho A\frac{\partial^2 y}{\partial t^2} - AG\kappa(\frac{\partial^2 y}{\partial x^2} - \frac{\partial\theta}{\partial x}) = 0 \tag{2.71}$$

$$EI\frac{\partial^2\theta}{\partial^2 x} + AG\kappa(\frac{\partial y}{\partial x} - \theta) - \rho I\frac{\partial^2\theta}{\partial t^2} = 0 \tag{2.72}$$

Taking the partial derivative of Equation 2.72 with respect to x and eliminating θ and terms we find the equation of motion for the beam:

$$EI\frac{\partial^4 y}{\partial x^2} + \rho A\frac{\partial^2 y}{\partial t^2} - \rho I\Big(1 + \frac{E}{G\kappa}\Big)\frac{\partial^4 y}{\partial x^2\partial t^2} + \frac{\rho^2 I}{G\kappa}\frac{\partial^4 y}{\partial t^4} = 0 \tag{2.73}$$

or

$$a^2\frac{\partial^4 y}{\partial x^2} + \frac{\partial^2 y}{\partial t^2} - k^2\Big(1 + \frac{E}{G\kappa}\Big)\frac{\partial^4 y}{\partial x^2\partial t^2} + \frac{k^2\rho}{G\kappa}\frac{\partial^4 y}{\partial t^4} = 0 \tag{2.74}$$

where

$$a^2 = \frac{EI}{\rho A} \quad \text{and } k^2 = \frac{I}{A} \tag{2.75}$$

where k is defined as *radius of gyration*. Similar to Equation 2.38, we assume a solution by separation of a variable as

$$y(x,t) = Y(x)T(t) \tag{2.76}$$

where $Y(x,t)$ and $T(t)$ are given in Equation 2.43 and 2.42. Then,

$$\frac{\partial^2 Y}{\partial x^2} = -\beta^2 Y + \beta^2 e^{-\beta x} \cong -\beta^2 Y \ \text{(since for high } \beta,\ e^{-\beta x} \to 0) \tag{2.77}$$

$$\frac{\partial^4 Y}{\partial x^4} = \beta^4 Y \tag{2.78}$$

Since boundary conditions given in Equation 2.44 are the same, here, relationship between constants of Y and the relation giving values of $\beta_n l$ are the same. From Equation 2.74 we have

$$a^2\beta^4 - \omega^2 - k^2\Big(1 + \frac{E}{G\kappa}\Big)\beta^2\omega^2 + \frac{k^2\rho}{G\kappa}\omega^4 = 0\ . \tag{2.79}$$

Solving this equation for frequency gives two distinct solutions,

$$\omega_{1,2} = \frac{1}{\sqrt{2}}\sqrt{\frac{GA\kappa}{\rho I} + \Big(\frac{G\kappa}{\rho} + \frac{E}{\rho}\Big)\beta^2 \mp \sqrt{\Big[\frac{GA\kappa}{\rho I} + \Big(\frac{G\kappa}{\rho} + \frac{E}{\rho}\Big)\beta^2\Big]^2 - 4\frac{EG\kappa\beta^4}{\rho^2}}} \tag{2.80}$$

or

$$\omega_{1,2} = \frac{1}{\sqrt{2}}\sqrt{\Lambda \mp \sqrt{\Lambda^2 - 4\frac{EG\kappa\beta^4}{\rho^2}}} \tag{2.81}$$

where

$$\Lambda = \frac{GA\kappa}{\rho I} + \Big(\frac{G\kappa}{\rho} + \frac{E}{\rho}\Big)\beta^2 \tag{2.82}$$

This dispersion relation gives us information about the characteristics of the wave propagation. As $\beta \to \infty$ we have

$$\omega_1 = \sqrt{\frac{G\kappa}{\rho}}\beta \qquad \text{and} \qquad \omega_2 = \sqrt{\frac{E}{\rho}}\beta \tag{2.83}$$

which lead to limited wave speeds that are non-dispersive at high frequency limit

$$c_1 = \sqrt{\frac{G\kappa}{\rho}} \qquad \text{and} \qquad c_2 = \sqrt{\frac{E}{\rho}} \tag{2.84}$$

When we look to $\beta \to 0$ case, we observe,

$$\omega_1(0) = 0 \ \text{ as expected } \ \text{and} \qquad \omega_2(0) = \sqrt{\frac{GA\kappa}{\rho I}} \tag{2.85}$$

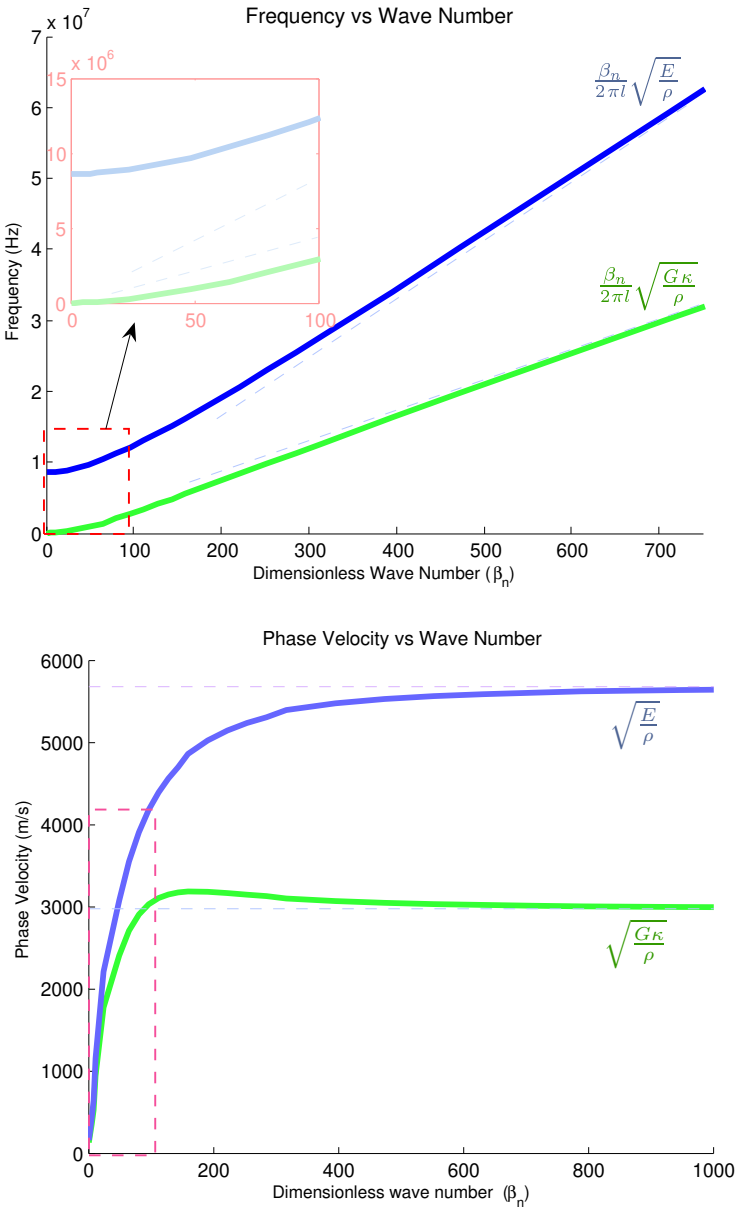

Figure 2.18: The figure on top shows the frequency values for given wave numbers. The first mode represents the flexural vibrations and it does not have a cut off frequency. The second mode represents the thickness shear mode which has a cut off frequency. The bottom figure shows the wave speed for two modes. While phase speeds tend to increase monotonically for low wave numbers, they are bounded from top by speed of shear waves and bulk waves. At high frequencies these curves converge to given values.

which indicates that the second mode we observe has a cut off frequency.

Dispersion curves obtained from above analysis are plotted in Figures 2.18. The speed c_1 is analogous to the flexural wave speed we obtained from the simple beam theory; this type of wave propagation is dispersive in the low β regime and converges to a nondispersive behavior with a limited wave speed. Quantity c_2 is not predicted by the simple bending beam theory, and it is the flexural thickness shear mode, also predicted by the exact theory [40]. At frequencies below its cut off, this mode has imaginary wave numbers which result in non-propagating decaying disturbances. However, when the wavelength of the shear mode becomes comparable to the value of the radius of gyration k, the thickness shear mode also starts to contribute to the wave dynamics of the capillary structure we have. From Equations 2.21 and 2.75, we calculate radius of gyration as 55 μm. This mode shows dispersive behavior in the beginning and c_2 starts from a low value and tends to increase with wave number or frequency; however, this increase is limited from above by the speed of bulk waves in the hollow cylinder. This means that contrary to low frequency regime, at high frequencies, speed of the wave becomes a constant of frequency and wave behavior becomes non-dispersive.

For parameters given in Table 2.1, high frequency limit values of c_1 and c_2 are 3063 m/s and 5502 m/s respectively. And the cut off frequency for the thickness shear mode is 8.62 MHz. This value is quite high compared to the frequency regime (20-2000 kHz), relevant to our experimental conditions. For this reason, we do not observe or expect any wave dynamics associated with this mode.

Frequency dispersion relationship given in Equation 2.80 is the exact solution of Equation 2.79; however, in our case we have a multilayered cylinder including a polyimide coating and enclosed liquid. In order to include this multilayered

configuration we are interested in such a formula:

$$f_n = H\frac{(\beta_n l)^2}{2\pi l^2}\sqrt{\frac{EI}{\rho A}} \tag{2.86}$$

where H is the desired correction from the Timoshenko theory. In such a configuration, we can switch to the multilayered case easily.

As we actuate the capillary below 10 MHz regime, the last term in Equation 2.79 is two orders of magnitude smaller compared to first three terms. Ignoring the last term, we find the frequency equation as

$$f_n = \frac{\frac{(\beta_n l)^2}{2\pi l^2}\sqrt{\frac{EI}{\rho A}}}{\sqrt{1+\frac{(\beta_n l)^2 k^2}{l^2}\left(1+\frac{E}{G\kappa}\right)}} \tag{2.87}$$

In fact, for low frequencies, one can use Taylor expansion and linearize the square root term in the denominator for simpler expressions. However, this results in a deviation at higher frequencies and does not help in our case.

As in Equation 2.53 when we include the effect of enclosed fluid and polyimide coating we have

$$f_n = \frac{\frac{(\beta_n l)^2}{2\pi l^2}\sqrt{\frac{E_1 I_1 + E_3 I_3}{\rho_1 A_1 + \rho_2 A_2 + \rho_3 A_3}}}{\sqrt{1+\frac{(\beta_n l)^2 k^2}{l^2}\left(1+\frac{E}{G\kappa}\right)}}\ . \tag{2.88}$$

As shown in Figure 2.19, if we compare f_n values obtained here with the experimental data we see that two curves have the same trend. Nevertheless, as in the previous case, there is a consistent error which increases as the frequency increase, in this case, again, a multiplier value is needed to fit the data exactly. This number in our case is 0.87 and final form of the frequency equation is given as

$$f_n = \frac{87}{100}\frac{\frac{(\beta_n l)^2}{2\pi l^2}\sqrt{\frac{E_1 I_1 + E_3 I_3}{\rho_1 A_1 + \rho_2 A_2 + \rho_3 A_3}}}{\sqrt{1+\frac{(\beta_n l)^2 k^2}{l^2}\left(1+\frac{E}{G\kappa}\right)}} \tag{2.89}$$

which gives an average deviation of less than 2% (Figure 2.20).

There are couple of reasons which may lead to 13% difference between theory and experiment. It will be shown in future chapters that the theoretical calculated values before introducing the correction factor is in very close agreement to the results obtained from finite element modeling. Boundary conditions and elements contributing to the motion are the same in two analysis. In these two analysis, boundary conditions are taken to be fixed through the circular cross section of the capillary at the ends. In experiments this is not the real case as capillary is adhered through its circumference, and in addition it does not end, but continues. Capillary in fact spans a longer regime compared to the PZT boundaries. Another

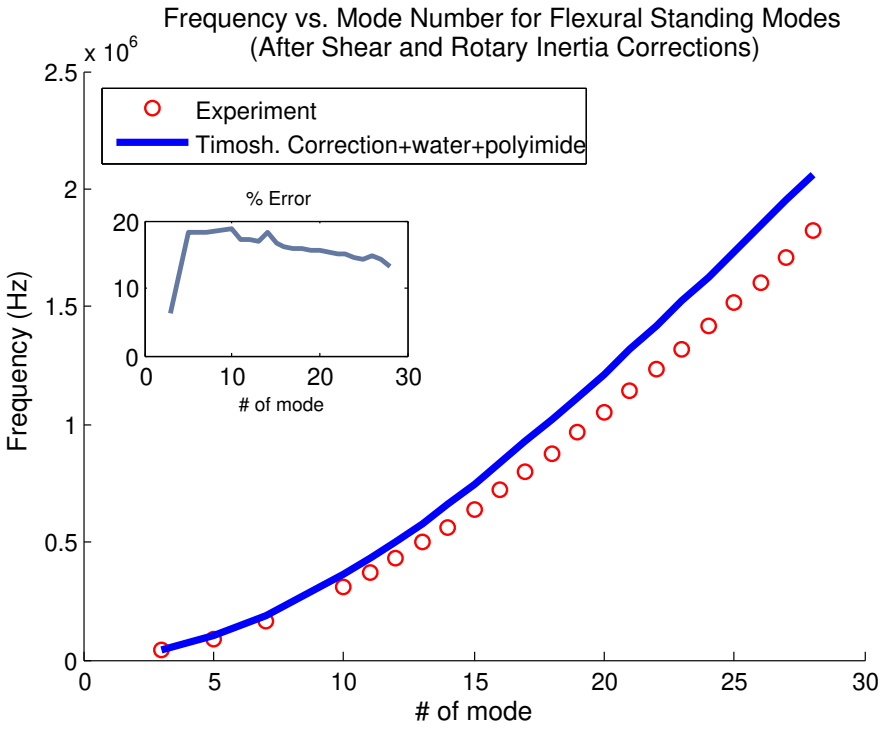

Figure 2.19: Correction by inclusion of shear and rotary inertia compared to experimental results.

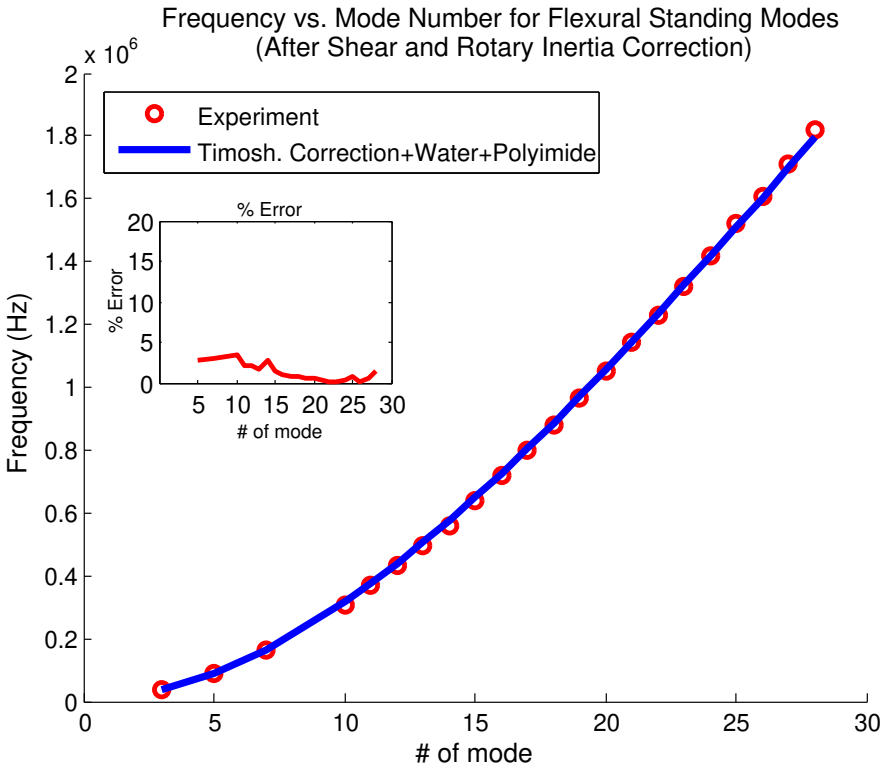

Figure 2.20: Theoretical fit including the multiplier compared to experimental data

factor which may lead to diminishing of frequencies is the adhesive. Capillary is adhesively bonded to the grooves on the PZT. And coupling between PZT and capillary happens through the adhesive bond. Most adhesives have very low elastic modulus which leads to softened boundary conditions.

Flexural waves are also heavily influenced by the surrounding fluid loading. In above derivation and finite element modeling, fluid enclosed had been included, however fluid present outside the cylinder, namely air, is ignored. Air outside will also have mass loading effect and reduce resonance frequencies. The energy coupling into air can potentially introduce damping as the energy is radiated away from the actuators.

2.3.4 Effect of the Density Variation of the enclosed Fluid

For our microfluidic actuator one of the components which may vary from device to device or sample to sample is the fluid enclosed inside the capillary. In this sense we need to further investigate the effect of density of fluid enclosed inside the capillary. From Equation 2.89, we can conclude that change in density will result in a shift in the dispersion curve or in a specific resonance frequency. Variation of dispersion curve versus density is plotted as a surface in Figure 2.21. Lines on the surface plot represent the variation of frequency versus density at a given mode. Black line represents the density dependency of the frequency in the 3^{rd} flexural mode and blue line represents for the 28^{th} flexural mode. It can be concluded from this plot that shift in the resonance frequencies gets bigger at higher modes. Variation of the resonance frequency versus density for the 28^{th} flexural mode is plotted in Figure 2.22. Two dots on the curve represent the density of water and mercury. Variation of frequency versus density around density of water is about 1 kHz per 10 g/m^3. In this case, typical frequency shift at 1.751 MHz (28^{th} mode) will be about 3 kHz when sea water (1027 kg/m^3) is used instead of pure water (1000 kg/m^3).

From Equation 2.86, it is possible to conclude that resonance frequencies of the flexural modes are inversely related to the square root of the fluid density such that

$$f_n(\rho_f) = A(\beta_n l)^2 (B + \rho_f)^{-1/2} \tag{2.90}$$

where A and B are constants and ρ_f is the fluid density. Then the change in the resonance frequency as a function of change in the fluid density becomes

$$d(f_n(\rho_f)) = -\frac{A}{2}(\beta_n l)^2 (B + \rho_f)^{-3/2} d(\rho_f) \ . \tag{2.91}$$

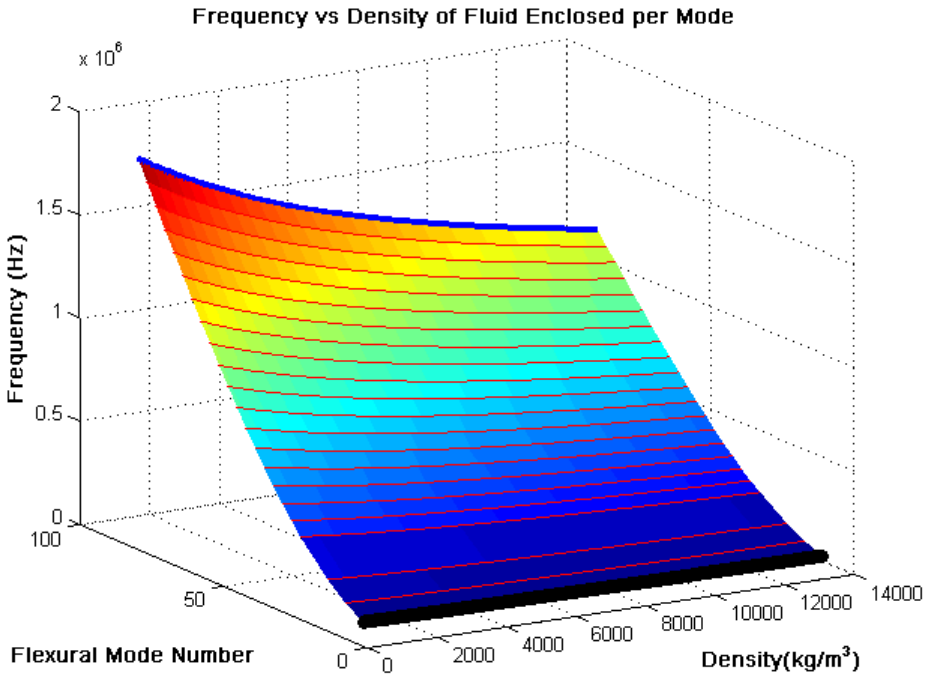

Figure 2.21: Variation of the resonance frequency with respect to the density of the fluid enclosed, for different modes.

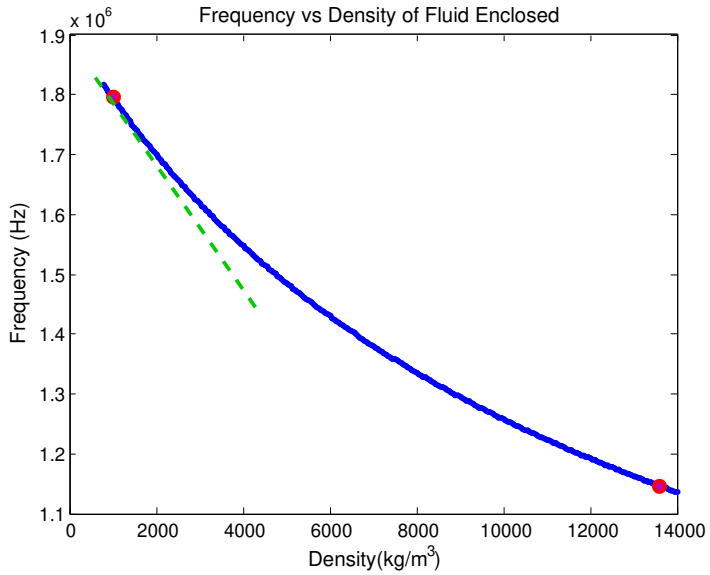

Figure 2.22: Variation of the resonance frequency with respect to the density of the fluid enclosed, for the 28^{th} mode.

Following these, the percent change in the frequency value ($\frac{d(f_n)}{f_n} \times 100$) becomes

$$-50(B+\rho_f)^{-1}d(\rho_f) \tag{2.92}$$

which is independent of the frequency. Here, it is possible to conclude that the percent change in the resonance frequencies are the same for all harmonics. In terms of device performance this means that, replacing DI water with the sea water, for example, would change the 28^{th} harmonic (at 1.751 MHz) by 3 kHz and the 5^{th} harmonic (at 90 kHz) by 0.1 kHz. As long as these changes are within the bandwidth of the resonance peak, device performance will not be altered significantly. However, as mentioned in [41] the quality factor for flexural vibrations of mechanical oscillators operated in air tends to increase at higher harmonics. Higher quality factor results in more sensitivity in the change of resonance frequency per given variables. As a result at higher harmonics, density variation may have a more sensible effect on the resonance frequencies. A more robust conclusion can be reached after the characterization of the actuator performance with various fluid samples.

2.3.5 Conclusions

In summary, flexural vibrations are the main reason behind the collection and separation mechanism and how they modify the acoustic pressure distribution inside the capillary will be further investigated in Chapter 3. However, before proceeding to those parts it is worth to describe the other types of vibrational modes in the frequency range of 10-2000 kHz, such as torsional and longitudinal modes. Matching frequencies of different modes may result in further interesting results to be analyzed in experiments.

2.4 Torsional Modes of the Cylindrical Capillary

In this section, torsional modes of the cylindrical capillary are described. While these modes do not play a significant role in particle collection; due to the tangential motion at the fluid structure boundary, they can contribute to streaming effects that may help in mixing in general or particle separation at particular harmonics which have matching frequency values with the flexural harmonics.

As shown in Figure 2.23, we can relate torque applied to the beam element, with the balancing shear stress on the body as

$$T = \int \tau_{\theta x} r dA \ . \tag{2.93}$$

Using the constitutive equation for shear modulus given in Equation 2.7 we have

$$T = \int G\gamma_{\theta x} r dA = \int Gr\frac{\partial \theta}{\partial x} r dA = G\frac{\partial \theta}{\partial x}\int r^2 dA \ . \tag{2.94}$$

The integral in the right hand side of the equation is defined as polar moment of inertia in the x axis.

$$J_x = \int r^2 dA \tag{2.95}$$

so the torque T is reduced to

$$T = G\frac{\partial \theta}{\partial x} J_x \ . \tag{2.96}$$

For the hollow cylinder in our case we find polar moment of inertia as

$$J_x = \frac{\pi}{2}(r_2^4 - r_1^4) \tag{2.97}$$

Similar to what was done in the case of flexural vibrations in previous parts, we can write the equation of motion for torsional motion of the beam element. As

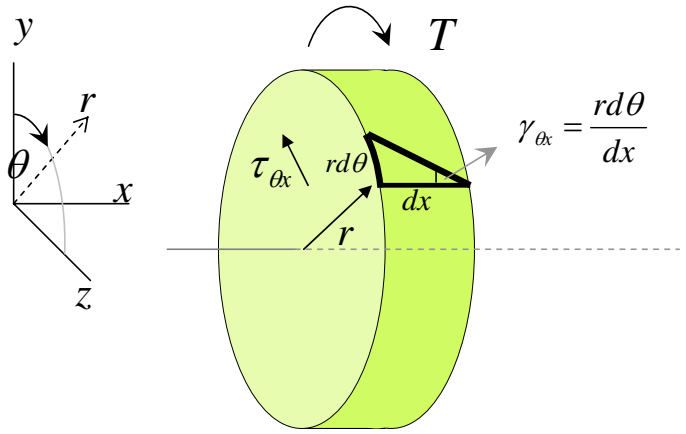

Figure 2.23: Equilibrium of applied torque and the shear stresses over the surface.

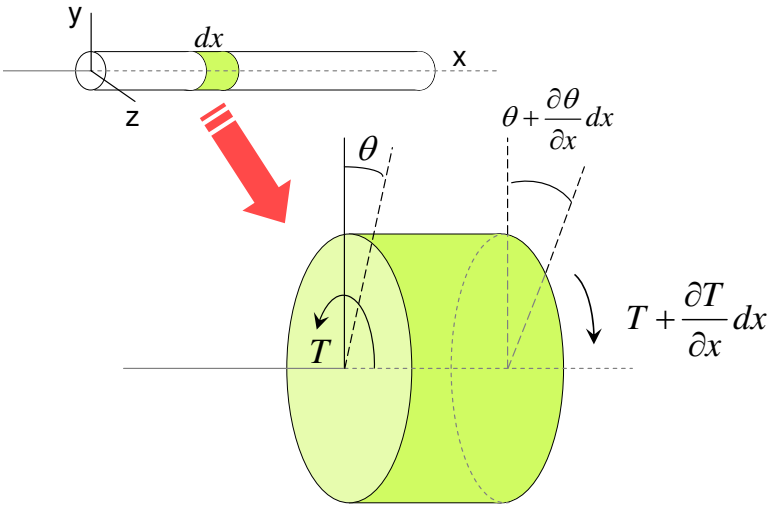

Figure 2.24: Beam element under differential torque.

shown in Figure 2.24, similar to the force acceleration relation we can relate torque with angular acceleration via polar moment of inertia (J).

$$-T + \left(T + \frac{\partial T}{\partial x}dx\right) = \rho J_x dx \frac{\partial^2 \theta}{\partial t^2} \ . \tag{2.98}$$

which reduces to

$$\frac{\partial T}{\partial x} = \rho J_x \frac{\partial^2 \theta}{\partial t^2} \tag{2.99}$$

Replacing T from Equation 2.96 we find the wave equation

$$\frac{\partial^2\theta}{\partial x^2} = \frac{1}{c_t^2}\frac{\partial^2\theta}{\partial t^2}, \quad \text{where} \quad c_t = \sqrt{\frac{G}{\rho}} \tag{2.100}$$

This result confirms that torsional waves on a rod are not dispersive and travel with the speed of shear waves. A general solution of the wave equation would have the form

$$\theta(x,t) = X_\theta(x)T_\theta(t) \tag{2.101}$$

where

$$X_\theta(x) = A_\theta \sin(\beta x) + B_\theta \cos(\beta x) \tag{2.102}$$

$$T_\theta(t) = e^{i\beta c_t t} \ . \tag{2.103}$$

Since we have clamped-clamped boundary conditions and beam length of l we have

$$B_\theta = 0 \quad \text{and} \quad \beta = m\pi/2l \tag{2.104}$$

resulting in,

$$\theta_m(x,t) = A_\theta \sin\frac{m\pi x}{2l} e^{im\pi c_t t/2l} \tag{2.105}$$

where m is the mode number.

The frequency equation can be given as

$$f_m = \frac{mc_t}{2l} \ . \tag{2.106}$$

Then for parameters given in Table 2.1, we expect to have torsional modes in frequencies given as

$$f_m = 171, 341, 512, 682, 853..., m \cdot 171, ... \ \ (kHz) \tag{2.107}$$

Results are also plotted in Figure 2.25, where we can see that first 13 modes fit in the 30-2000 kHz range. Torsional vibrations might help in mixing of fluids or suspensions. Due to the polyimide coating and liquid enclosure, there will be slight shift in the resonance frequencies however for now these results will be sufficient.

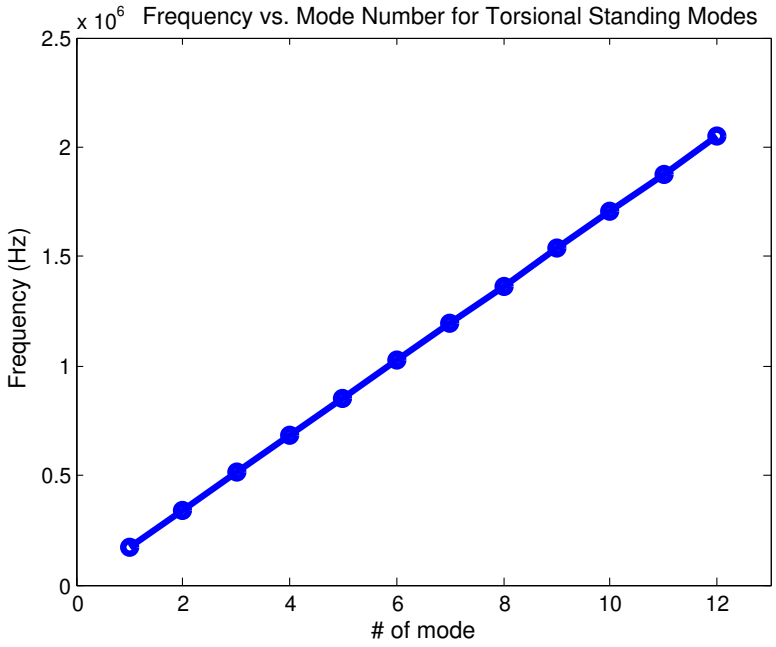

Figure 2.25: Dispersion relationship for torsional waves on the capillary in 0-2MHz range.

2.5 Longitudinal Modes of the Cylindrical Capillary

Related to longitudinal waves, we assume displacement, body displacement and wave propagation all happen in parallel to the central axis of the cylinder. When we consider the beam element shown in Figure 2.26 and write the force equation,

$$-\sigma(x,t)+\left(\sigma(x,t)+\frac{\partial\sigma(x,t)}{\partial x}dx\right)+q(x,t)Adx=\rho Adx\frac{\partial^2u(x,t)}{\partial t^2} \tag{2.108}$$

where A is the area, ρ is the density, $q(x,t)$ is the external body force per volume and $u(x,t)$ is the displacement of the beam element. Equation is reduced to,

$$\frac{\partial\sigma(x,t)}{\partial x}+q(x,t)=\rho\frac{\partial^2u(x,t)}{\partial t^2}\ . \tag{2.109}$$

From Equation 2.4 and definition of strain we have

$$\varepsilon=E\sigma(x,t)=E\frac{\partial u(x,t)}{\partial x}\ . \tag{2.110}$$

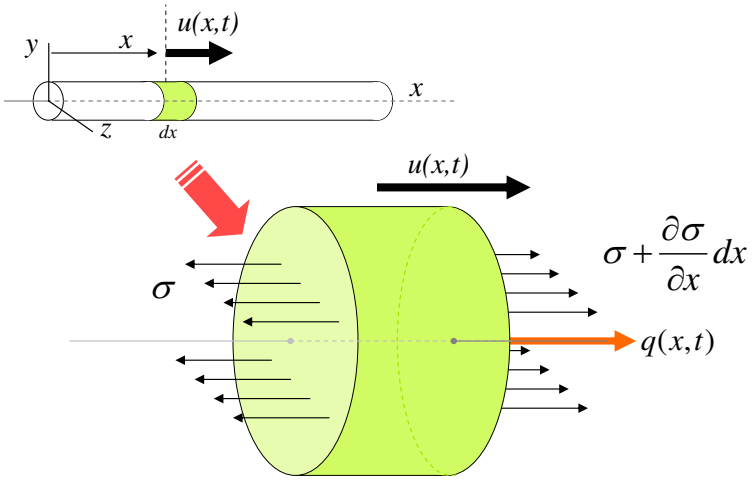

Figure 2.26: Force diagram for the beam element under longitudinal stresses; black arrows on the cylinder faces indicate body stresses and the red arrow indicates the external body force per volume applied everywhere. Displacement of the beam element is $u(x,t)$.

Using these in Equation 2.109 we have

$$E\frac{\partial^2 u(x,t)}{\partial x^2} + q(x,t) = \rho\frac{\partial^2 u(x,t)}{\partial t^2} \tag{2.111}$$

When there is no external forces we have the wave equation

$$\frac{\partial^2 u(x,t)}{\partial x^2} = \frac{1}{c^2}\frac{\partial^2 u(x,t)}{\partial t^2}, \quad \text{where} \quad c = \sqrt{\frac{E}{\rho}} \tag{2.112}$$

where c is the speed of longitudinal waves on the capillary. Since the capillary wall is relatively thick (just half of the capillary diameter) we do not need to worry about any major modification to the Equation 2.112. This equation is very similar to the we found in case of torsional waves, and the boundary conditions are also matching this is so one can just use results (Equations 2.105 and 2.106) from Section 2.4. We will replace G with E; $\theta_m(x,t)$ with $u_m(x,t)$; c_t with c; A_θ with A in Equation 2.105. Then we have,

$$u_m(x,t) = A\sin(k_m x)e^{j\omega t} \tag{2.113}$$

where

$$k_m = \frac{2\pi m}{\lambda} = \frac{\pi m}{l} \quad \text{and} \quad \omega = ck_m \tag{2.114}$$

and the frequency equation is

$$f_m = \frac{mc}{2l} \tag{2.115}$$

The results of the frequency equation is plotted in Figure 2.27, and the first 8 harmonics of longitudinal modes are in the range of less than 2 MHz regime and are given as

$$f = 258, 516, 775, 1033, 1291..., m \cdot 258, ... \ (kHz) \ . \tag{2.116}$$

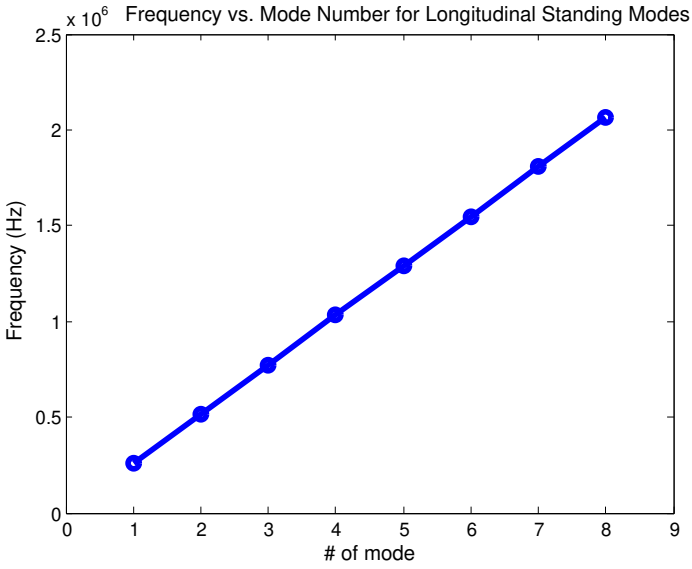

Figure 2.27: Dispersion relation for longitudinal waves on the capillary in 0-2MHz range

The existence of the enclosed fluid will also have some slight effect on the resonance modes, however, this will be only due to the boundary viscous-shear effect. Compared to the size and mass of the capillary, amount of fluid involved in this shear dissipation will be small, for simplicity we omitted that part of analysis.

We will further investigate validity of this assumption via finite element modeling in Chapter 4.

Table 2.2: List of frequencies of resonance modes of various vibrations of the capillary are given. Only modes having frequencies less than 2MHz are listed here. Frequencies having letters in parentheses indicate the mode shapes which have close frequency values.

Theoretical Frequency values of various vibrational modes

Mode Number	Flexural	Torsional	Longitudinal (Hz)
1	6877	170630 (a)	258220 (i)
2	18917	341250	(i*) 516450 (ii)
3	36967	(i*) 511880 (b)	774670
4	60840	682510	(ii*) 1032900
5	90407	853130	1291100
6	125470	(ii*) 1023800	(iii*) 1549300
7	165840 (a)	1194400	1807600 (iii)
8	211280	1365000	(iv*) 2065800
9	(i) 261530	(iii*) 1535600	
10	316360	1706300 (c)	
11	375460	1876900	
12	438600	(iv*) 2047500	
13	(iii) 505490 (b)		
14	575820		
15	649380		
16	725870		
17	805060		
18	886690		
19	970580		
20	1056500		
21	1144200		
22	1233500		
23	1324300		
24	1416400		
25	1509700		
26	1603900		
27	1699100 (c)		
28	(iii) 1795100		

2.6 Comparison of Vibrational Modes of the Capillary

We have found various transverse, torsional and longitudinal resonance modes of the capillary in previous parts. Some of these resonance frequencies of different vibrational modes are close to each other. This degeneracy might be useful in cases when a quick shift of actuator behavior is needed. In another way this degeneracy might be also useful for separation "tricks" and modalities. In Table 2.2, we have listed frequencies of resonance modes of the capillary for flexural, torsional and longitudinal modes (material properties and dimensions are listed in Table 2.1).

In Figure 2.28, the difference of resonance frequencies of flexural modes and torsional modes are plotted as a surface. Locations where surface gets a minimum value represent the resonance frequency matching regime for given modes. Similarly difference of frequency values of flexural modes and longitudinal modes are plotted in Figure 2.29, and torsional and longitudinal modes are plotted in Figure

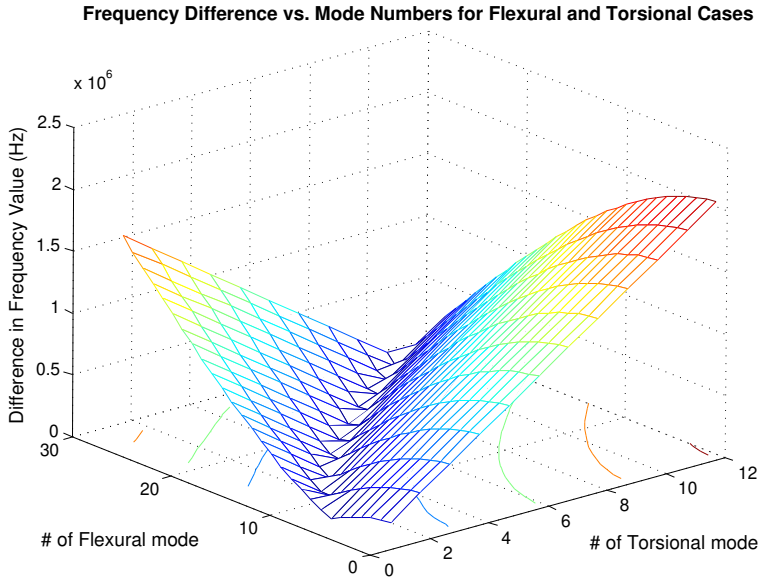

Figure 2.28: Frequency difference for given flexural and torsional modes.

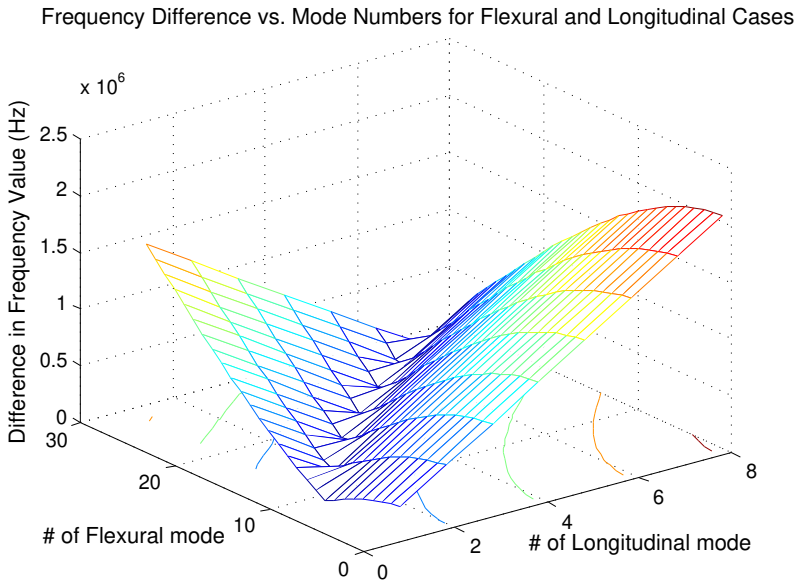

Figure 2.29: Frequency difference for given flexural and longitudinal modes.

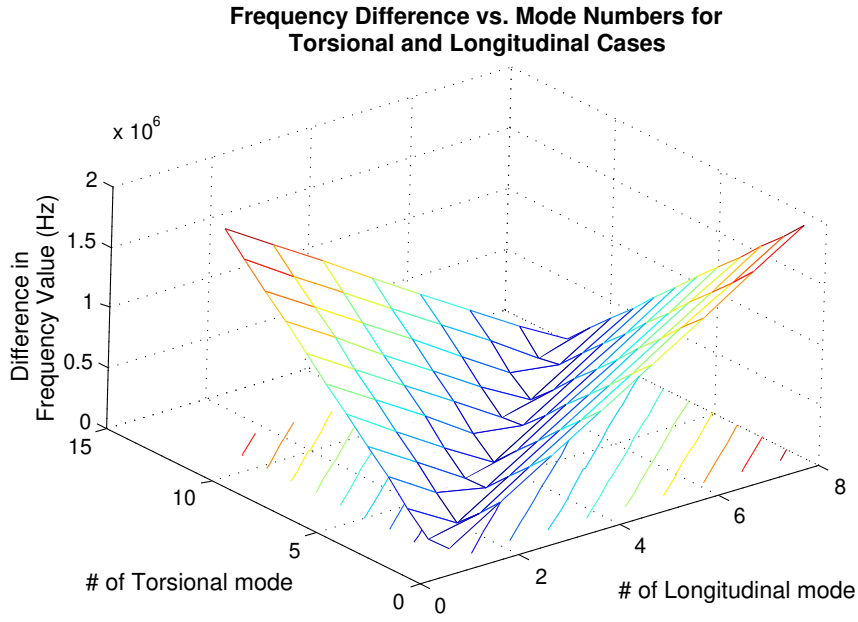

Figure 2.30: Frequency difference for given torsional and longitudinal modes.

2.30. Due to the dispersive behavior of flexural modes, minimum lines on flexural-longitudinal and flexural-torsional difference surfaces tend to be quadratic, while the minimum line on torsional-longitudinal difference surface tends to be linear, as neither of them are dispersive.

From these plots we can analyze and correlate the close values. In Table 2.2, we have indicated modes of different vibration types which are closer to each other with differences being smaller than 20 kHz.

CHAPTER 3

ACOUSTIC PRESSURE WAVES INSIDE THE GLASS CAPILLARY

Introduction

In this chapter dynamics of acoustic pressure waves inside the cylindrical glass capillary is investigated. Acoustic waves in unbounded fluids is first introduced. Next the narrow channel effect reducing the speed of sound in a cylindrical capillary is presented. Following that, inside the capillary is treated as a bounded cylindrical cavity and natural the acoustic modes of this cavity are derived.

In the second part of this chapter, the coupling of flexural waves in an elastic medium to the fluid at the boundary is analyzed. A focus on the capillary case and conditions for radiation are investigated. It is proven that by utilizing harmonic flexural vibration of the capillary, subharmonic acoustic pressure standing waves in fluid can be generated inside the cavity. In this case standing waves can be generated at frequencies as low as 30 kHz while naturally occurring cavity modes are expected to appear at least at 8.26 MHz. It is also shown that harmonicity of these acoustic standing pressure wave modes depend on the harmonicity of flexural modes.

In the final part of this chapter, acoustic pressure distribution due to quasi-longitudinal vibration of the capillary will be investigated. It will be shown that due to the finite thickness of the capillary, radially symmetric transverse velocity distribution is also present, although they are two orders of magnitude smaller than the axial capillary motion. It is shown that, similar to the flexural motion case, this radially symmetric transverse velocity couples acoustic pressure waves

inside the cavity.

3.1 Acoustic Modes inside the Capillary: Cylindrical Cavity Problem

In this part, we will derive propagation behavior of sound waves in bulk fluids, and fluids confined in a narrow channel. Later inner part of the capillary will be modeled as a cylindrical cavity and we will investigate the acoustic modes inside capillary.

3.1.1 Sound Waves in Nonviscous Fluids

Compared to wave propagation in solids analysis of acoustic wave propagation in fluids tends to be simpler. In case of nonviscous ideal fluids, there are no restoring forces against any shear disturbances.[1] The only stress component in a fluid is the scalar pressure. When a time dependent oscillating pressure variation or force is introduced to the fluid, individual elements of the fluid move back and forth along the direction of forces applied and series of compression and decompression effect is introduced. This compression and decompression is also felt by the adjacent fluid element which enables propagation of the wave. This propagation is identical to longitudinal waves in solids.

[1]No fluid in real life is an ideal fluid and exhibits some shear effects due to its viscosity. This property is important in case of nonlinear or second order acoustic phenomenon. However, for simply deriving propagating sound waves, these effects are ignored as these shear interactions cannot form any kind of restoring force to generate a propagating transverse wave as in the case of solids.

While the acoustic wave equation for nonviscous fluids is derived here, we will assume that acoustic pressure p is much smaller than the equilibrium P or instantaneous P_0 pressure of the fluid element which can be formulated as

$$p = P - P_0 \text{ and } \; p \ll P, P_0 \; . \tag{3.1}$$

Taking a fluid element of volume V into consideration, the equation of continuity can be found by equating the change in the total mass of this given volume per time with the net mass flow through the whole surface of the volume. In differential form this relation is given as

$$\frac{\partial \rho}{\partial t} + \nabla \cdot (\rho \mathbf{v}) = 0 \tag{3.2}$$

where ρ is the density of the fluid and $\mathbf{v}$ is the fluid particle velocity.

The momentum equation for nonviscous fluids can be found by using Newton's law for the fluid element having volume V. Change of momentum for volume V per unit time should be equal to the sum of all external forces (such as gravity etc.), and the net momentum flow through the surface of the volume V carried by the fluid.

$$\frac{\partial (\rho \mathbf{v})}{\partial t} + \nabla (\rho \mathbf{v}) \cdot \mathbf{v} + \nabla p = \rho \mathbf{B} \tag{3.3}$$

where $\mathbf{B}$ is the body force per unit mass.

Since the temperature change in the volume element due to its compression or expansion, the temperature gradient within the neighboring fluid elements and the thermal conductivity are all small, acoustical interactions for linear regime are mostly treated as adiabatic and reversible processes. For the perfect gas under these conditions, pressure values can be associated with density values through

$$\frac{P}{P_0} = (\frac{\rho}{\rho_0})^{\gamma} \tag{3.4}$$

where γ is the ratio of heat capacities. Having $\delta\rho = (\rho - \rho_0)$, if we take the Taylor's expansion of Equation 3.4 we get

$$P = P_0 + \Big(\frac{\partial P}{\partial \rho}\Big)_{\rho_0} \delta\rho + \frac{1}{2}\Big(\frac{\partial^2 P}{\partial \rho^2}\Big)_{\rho_0} (\delta\rho)^2 + ... \tag{3.5}$$

The first term gives

$$p = P - P_0 = \Big(\frac{\partial P}{\partial \rho}\Big)_{\rho_0} \delta\rho = ß\frac{\delta\rho}{\rho_0} \tag{3.6}$$

where ß is the adiabatic bulk modulus relating the density change[2] with the pressure change

$$ß = \rho_0 \Big(\frac{\partial P}{\partial \rho}\Big)_{\rho_0} \tag{3.7}$$

Now we can proceed to the next step for deriving the wave equation. If we take the divergence of the momentum equation (Equation 3.3) for linear case and ignoring all external body forces we have

$$\nabla \frac{\partial(\rho \mathbf{v})}{\partial t} + \nabla^2 p = 0 \tag{3.8}$$

We can take the time derivative of the continuity equation, we get

$$\frac{\partial^2 \rho}{\partial t^2} + \frac{\partial}{\partial t}\Big(\nabla \cdot (\rho \mathbf{v})\Big) = 0 \tag{3.9}$$

The second term of Equation 3.8 and first term of Equation 3.9 are equivalent which leads to

$$\frac{\partial^2 \rho}{\partial t^2} = -\nabla^2 p \tag{3.10}$$

From Equation 3.6 we can relate pressure and density variation and also noting that the time derivative of $\delta\rho$ will be equal to the time derivative of ρ (since ρ_0 is constant). Taking the second time derivative of Equation 3.6 and replacing density terms in Equation 3.10, we find the acoustic wave equation for fluids given as,

$$\nabla^2 p = \frac{1}{c^2}\frac{\partial^2 p}{\partial t^2} \tag{3.11}$$

[2]Reminding conservation of mass, this is equivalent to replace density with volume and say bulk modulus is nothing but relating volume change with pressure change.

where c is the speed of the sound wave in the fluid, which is given by

$$c^2 = \frac{ß}{\rho_0} \tag{3.12}$$

For a time harmonic plane wave given as

$$p(\vec{r}, t) = Ae^{-j(\vec{k}\vec{r}-\omega t)} \tag{3.13}$$

equation 3.11 takes the form of the Helmholtz equation

$$\nabla^2 p + k^2 p = 0 \tag{3.14}$$

where

$$k = \frac{\omega}{c} \tag{3.15}$$

is the wave vector.

3.1.1.1 Speed of Acoustic Waves in Narrow Channels

It has been known that acoustic waves do not exhibit same propagation characteristics that they show in infinite bulk, when they are confined. Especially in the case of layered media, different acoustic properties and the geometry of the structure define the propagation characteristics. For example, in the case of a plate immersed in a fluid, when the propagating waves are incident on the boundary at an angle, such that total internal reflection occurs, then waves can couple into and propagate in the solid layer. However, when the angle of incidence is less then the critical value, then some part of the incident wave is refracted to the fluid enclosing the solid layer. In this case, propagation is affected by the boundary, and even could be leaky in case of an infinite or absorbing boundary.

This topic draws attention of geologists and seismologists as there are many naturally occurring multilayered waveguides in nature, such as earth's crust, ice

layers on lakes or oceans, etc. Scientists and engineers, working on projects related to fluid transport pipelines or tubing systems like in reactors where tubes or pipes are subject to vibration, also have to take this topic into consideration. Recent technological advancements in the field of MEMS and microfluidic systems also deal with elastic and acoustic properties of materials at microscale as well as acoustic wave propagation.

In general analysis of multilayered waveguides, different combinations might be investigated separately such as, finite-finite media, finite-infinite media, infinite-infinite media.

In cases of fluid-fluid or fluid-thin solid interfaces solving wave equation considering boundary conditions are enough. However, in cases of fluid-solid or solid-solid media, the problem formulation is more complex and a more detailed investigation through the general theory of elasticity is needed.

In our case, we are interested in propagation of internal waves in liquid enclosed in a thick hollow cylinder. Early observations regarding this topic dates back to the 1800s. Working on organ pipes, Wertheim observed his calculations on wave dynamics of organ pipes deviate when air filling is replaced with water [42]. In 1848 Helmholtz [43] first showed how to predict such phenomenon theoretically, and commented on Wertheim's experiments. While for gases, this effect is not very significant; in case of liquids enclosed in a channel, change is considerable. Later, in 1878, Korteweg [44] published a more comprehensive mathematical derivation. Following Korteweg, in 1898, Lamb [45] confirmed Korteweg's analysis, and included the solution for the case of a thick cylinder.

Following the calculations in [46], in Appendix A, speed of sound in a cylin-

drical capillary for the cylindrical capillary case is calculated. During the analysis pressure inside the capillary is assumed to be constant, and displacement of the capillary due to this pressure is taken to be axis-symmetric. The length of the capillary is long enough compared to the radius or thickness so that shear or moment related edge effects are negligible, and deformation of the capillary remains normal to the radius (so all displacement is in plane). Lastly, the wavelengths are much larger compared to cylindrical radius and thickness. It is also assumed that due to the pressure normal to the capillary-fluid boundary, both displacements in fluid and solid structures are only in radial ($\mathbf{r}$) direction. Following these equations, pressure inside the channel is equated to the normal stresses on the solid structure at the internal boundary. In addition from non slip boundary conditions, the displacement in the fluid and the displacement of solid structure at the boundary are also equal. Finally, the speed of acoustic plane waves in a cylindrical cavity is obtained as

$$c \;=\; c_0 \,\frac{1}{\sqrt{1+2M\lambda_1}} \tag{3.16}$$

where c is the speed of sound in bulk fluid and M is given by

$$M = \frac{r_1^2}{2(\lambda_2+\mu_2)(r_2^2-r_1^2)} + \frac{r_2^2}{2\mu_2(r_2^2-r_1^2)} \tag{3.17}$$

Following the values in Table 2.1, at room temperature we find speed of sound in bulk water (c_0) to be 1485 m/s. In the fluid filled silica cylindrical capillary with inner radius 50 μm and the outer radius 100 μm, the speed of sound in the fluid core (c) is found to be 1410 m/s from Equation 3.16, which results in a 5% lower value than the value in the bulk. In the calculations in the following sections, this value (c) given above will be used in place of speed of sound in bulk water (c_0).

3.1.2 Solution of Wave Equation for a Cylindrical Cavity

As shown in Figure 3.1, acoustic modeling of fluid enclosed in a cylindrical capillary can be modeled through solution of wave equation for a cylindrical cavity. In our case, due to the glass capillary, the cylinder walls are rigid and the ends of the channel are open.

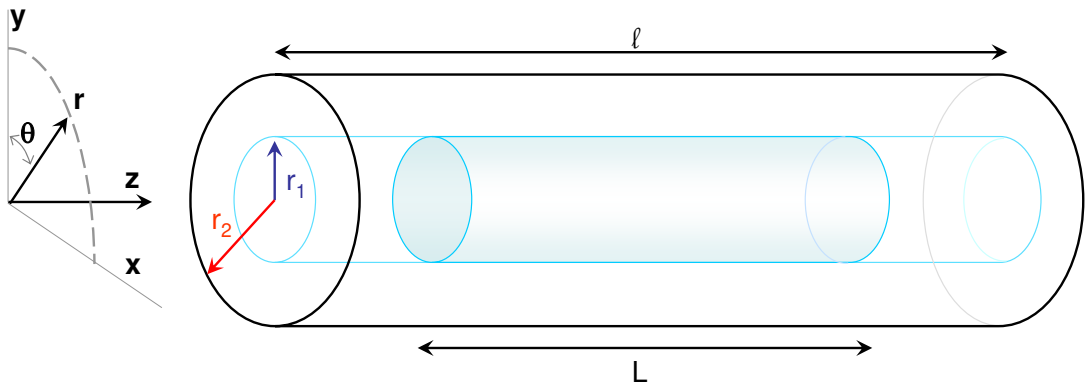

Figure 3.1: Fluid column of length L enclosed in a silica capillary of length l.

The problem will be first investigated by treating the capillary as a waveguide and then propagating modes and cut off frequencies will be extracted. Furthermore, limiting the length of the capillary, the modal frequencies and wave functions will be investigated. Rephrasing the wave equation given in Equation 3.11in cylindrical coordinates, we have,

$$\Big(\frac{\partial^2}{r^2}+\frac{1}{r}\frac{\partial}{\partial r}+\frac{1}{r^2}\frac{\partial^2}{\theta^2}+\frac{\partial}{\partial z^2}\Big)p=\frac{1}{c^2}\frac{\partial^2 p}{t^2} \tag{3.18}$$

As we are seeking harmonic solutions, the standard approach is the method of separation of variables.

$$p(r,\theta,z,t)=R(r)\Theta(\theta)Z(z)e^{j\omega t} \tag{3.19}$$

If we place the $p(r,\theta,z,t)$ value in Equation 3.19 in Equation 3.18 we find

$$\frac{1}{R}\frac{\partial^2 R}{\partial r^2}+\frac{1}{R}\frac{1}{r}\frac{\partial R}{\partial r}+\frac{1}{r^2}\frac{1}{\Theta}\frac{\partial^2\Theta}{\partial\theta^2}+\frac{1}{Z}\frac{\partial^2 Z}{\partial z^2}=-\frac{\omega^2}{c^2}\ . \tag{3.20}$$

Starting with components depending on z, θ and r values, we have the following equations

$$\frac{\partial^2 Z}{\partial z^2}+k_z^2 Z=0 \tag{3.21}$$

$$\frac{\partial^2\Theta}{\partial\theta^2}+m^2\Theta=0 \tag{3.22}$$

$$\frac{\partial^2 R}{\partial r^2}+\frac{1}{r}\frac{\partial R}{\partial r}+\big(k_r^2-\frac{m^2}{r^2}\big)R=0 \tag{3.23}$$

$$\frac{\omega^2}{c^2}=k^2=k_r^2+k_z^2\ . \tag{3.24}$$

The z dependent part gives the solution

$$Z(z)=\begin{pmatrix}\cos k_z z\\ \sin k_z z\end{pmatrix} \tag{3.25}$$

and the θ part

$$\Theta(\theta)=\begin{pmatrix}\cos m\theta\\ \sin m\theta\end{pmatrix}\ . \tag{3.26}$$

As given in Equation 3.23, r dependent part is known as Bessel's equation of order m. The solutions to Bessel's equation can be found in many applied mathematics or physics books [47, 48] and are given as,

$$R(r)=\begin{pmatrix}J_m(k_r r)\\ N_m(k_r r)\end{pmatrix}\quad\text{or}\quad\begin{pmatrix}H_m^{(1)}(k_r r)\\ H_m^{(2)}(k_r r)\end{pmatrix} \tag{3.27}$$

The first set of solutions J_m and N_m are called ordinary Bessel and Neuman functions, and are used particularly for interior problems such as radiation into a cavity (which applies to our case). Neuman functions go to infinity as r approaches to

zero, this is not a likely situation in our case so Neuman functions are not a possible solution case in our experiments (and generally in most experiments). The second set of equations H_m are the the Hankel functions and they are used in the case of exterior problems such as a cylindrical structure radiating to free space. As a result, having arbitrary constants A and B, we have the general solution of acoustic waves in a cylindrical cavity,

$$p(r,\theta,z,t) = \begin{pmatrix} A \\ B \end{pmatrix} \begin{pmatrix} J_m(k_r r) \end{pmatrix} \begin{pmatrix} \cos m\theta \\ \sin m\theta \end{pmatrix} \begin{pmatrix} \cos k_z z \\ \sin k_z z \end{pmatrix} \begin{pmatrix} \cos \omega t \\ \sin \omega t \end{pmatrix} \quad (3.28)$$

In our case acoustic cavity or waveguide is surrounded by rigid cylinder walls and in such cases, due to the nonslip fluid-solid interface the radial velocity (v_r) of fluid particles at fluid-solid boundary ($r = r_1$) is zero,

$$v_r(r_1) = 0 \quad (3.29)$$

In the case of harmonic waves, we can write Equation 3.8 (known as *Euler's equation*), as

$$\mathbf{v} = -\frac{1}{j\omega\rho}\vec{\nabla}p \ . \quad (3.30)$$

Then the velocity ($\mathbf{v}$) becomes

$$\mathbf{v}(r,\theta,z,t) = -\frac{k_r J'_m(k_r r)}{j\omega\rho} \begin{pmatrix} A \\ B \end{pmatrix} \begin{pmatrix} \cos m\theta \\ \sin m\theta \end{pmatrix} \begin{pmatrix} \cos k_z z \\ \sin k_z z \end{pmatrix} \begin{pmatrix} \cos \omega t \\ \sin \omega t \end{pmatrix} \quad (3.31)$$

where $J'_m(k_r r)$ is the first derivative of $J_m(k_r r)$ with respect to r.

For generalized k_r values related to our solution, the boundary condition given in Equation 3.29 can be written as

$$v_r(k_r r_1) = 0 \quad (3.32)$$

where k_r values can be chosen as

$$k_r = \alpha'_{mn}/r_1 \tag{3.33}$$

and α'_{mn} is the n$^{\text{th}}$ zero of J'_m. The first few values of α'_{mn} can be found in Table 3.1.

Table 3.1: Roots of the first derivative of Bessel functions.

$J'_{mn}(x)=0$	m					
n	0	1	2	3	4	5
1	0	1.8412	3.0542	4.2012	5.3175	6.4156
2	3.8317	5.3314	6.7061	8.0152	9.2824	10.5199
3	7.0156	8.5363	9.9695	11.3459	12.6819	13.9872
4	10.1735	11.706	13.1704	14.5858	15.9641	17.3128

For waves propagating in the z direction, from Equation 3.24, the frequency equation is found as,

$$k_z^2 = \frac{\omega^2}{c^2} - k_r^2 \tag{3.34}$$

following

$$k_{z,mn}^2 = \frac{\omega^2}{c^2} - \frac{{\alpha'_{mn}}^2}{{r_1}^2} \ . \tag{3.35}$$

Since the phase velocity is given by

$$c_{ph} = \frac{\omega}{k_{z(mn)}} \tag{3.36}$$

we have,

$$c_{ph} = c\frac{1}{\sqrt{1 - \left(\frac{\alpha'_{mn}c}{\omega r_1}\right)^2}} \tag{3.37}$$

from which we find cut off frequencies as

$$f_{mn} = \frac{\alpha'_{mn}c}{2\pi r_1} \ . \tag{3.38}$$

For a fluid column of finite length (L), we expect to observe modes in z direction as well. Depending on the end locations of the fluid column, frequency harmonics

of standing modes can be calculated. Boundary conditions for end locations in our case, are open to air and so pressure value can be treated as zero. In this case from Equation 3.28 we have

$$p_{(z=0)} = 0 \;\Rightarrow\; \sin 0 = 0 \quad \text{and} \quad p_{(z=L)} = 0 \;\Rightarrow\; \sin k_z L = 0 \tag{3.39}$$

from which we have,

$$k_z = \frac{N\pi}{L} \; . \tag{3.40}$$

Then from the frequency equation given in Equation 3.24, and value of k_r we defined in Equation 3.33 we find the modal frequencies as

$$f_{mnN} = \frac{c}{2}\sqrt{\left(\frac{\alpha'_{mn}}{\pi r_1}\right)^2 + \left(\frac{N}{L}\right)^2} \tag{3.41}$$

and wave function as

$$p_{mnN}(r,\theta,z,t) = A_{mn} J_m(\frac{\alpha'_{mn}}{r1} r) \sin m\theta \sin \frac{N\pi z}{L} \sin \omega t \tag{3.42}$$

Interpreting the results we have, from Table 3.1 for $m = 0$, $n = 1$, we have $\alpha'_{01} = 0$. Since $J_0(0) = 1$ we have a mode which is independent of r and θ. This is the simple longitudinal plane wave mode, and the time harmonic wave function is given as

$$p_{01N}(r,\theta,z,t) = A \sin \frac{N\pi z}{L} \sin \omega t \tag{3.43}$$

Here, A depends on the driving forces. The phase velocity c is given in Equation 3.37. This mode is not dispersive and does not have any cut off frequency; the frequency relationship is given as,

$$f_N = \frac{cN}{2l} = N f_1 \tag{3.44}$$

As shown on the top sketch of Figure 3.2, this mode is due to the fundamental plane wave propagating through the cavity inside the capillary. An important aspect of

this mode is that it is independent of the source location and geometry which means that except for locations close to the source, wave propagation is uniform. Figure 3.2 also shows two other radial modes. Radial pressure and displacement variation inside the capillary for various modes are computed and graphed in Figure 3.3. As seen on the top of the figure, in the plane wave mode, no radial or angular variation exists. This is the axial in plane mode inside the capillary and only variation is through the z axis. All other modes plotted in Figure 3.3 are radial and/or angular modes, and due to this radial and angular variation, we have velocity trajectories guided by the pressure variation.

Table 3.2 shows the cut off frequencies of the modes. Since the next smallest

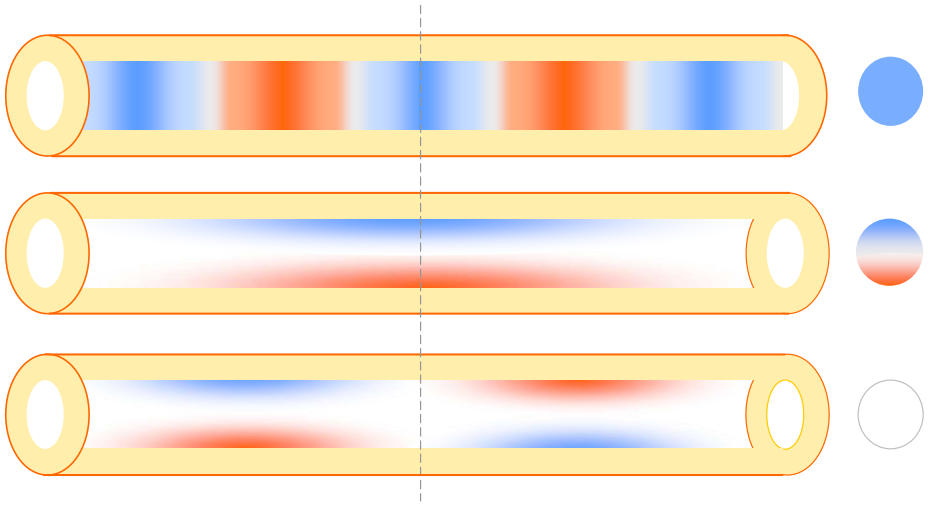

Figure 3.2: Several capillary modes are sketched. On the side cross section view of the middle of the capillary is shown. Top: m=0, n=1, N=5 mode, f=320 kHz. Middle: m=1, n=1, N=1 mode, f=8.27 MHz. Bottom: m=1, n=1, N=2 mode, f=8.29 MHz. The relatively small difference between frequencies of middle and bottom modes is due to the high aspect ratio of the capillary. Due to the small radial distance, radial modes have high cut off frequencies. From Equation 3.41, it is possible to see that the contribution of N modes (z axis) is small compared to high values of radial modes.

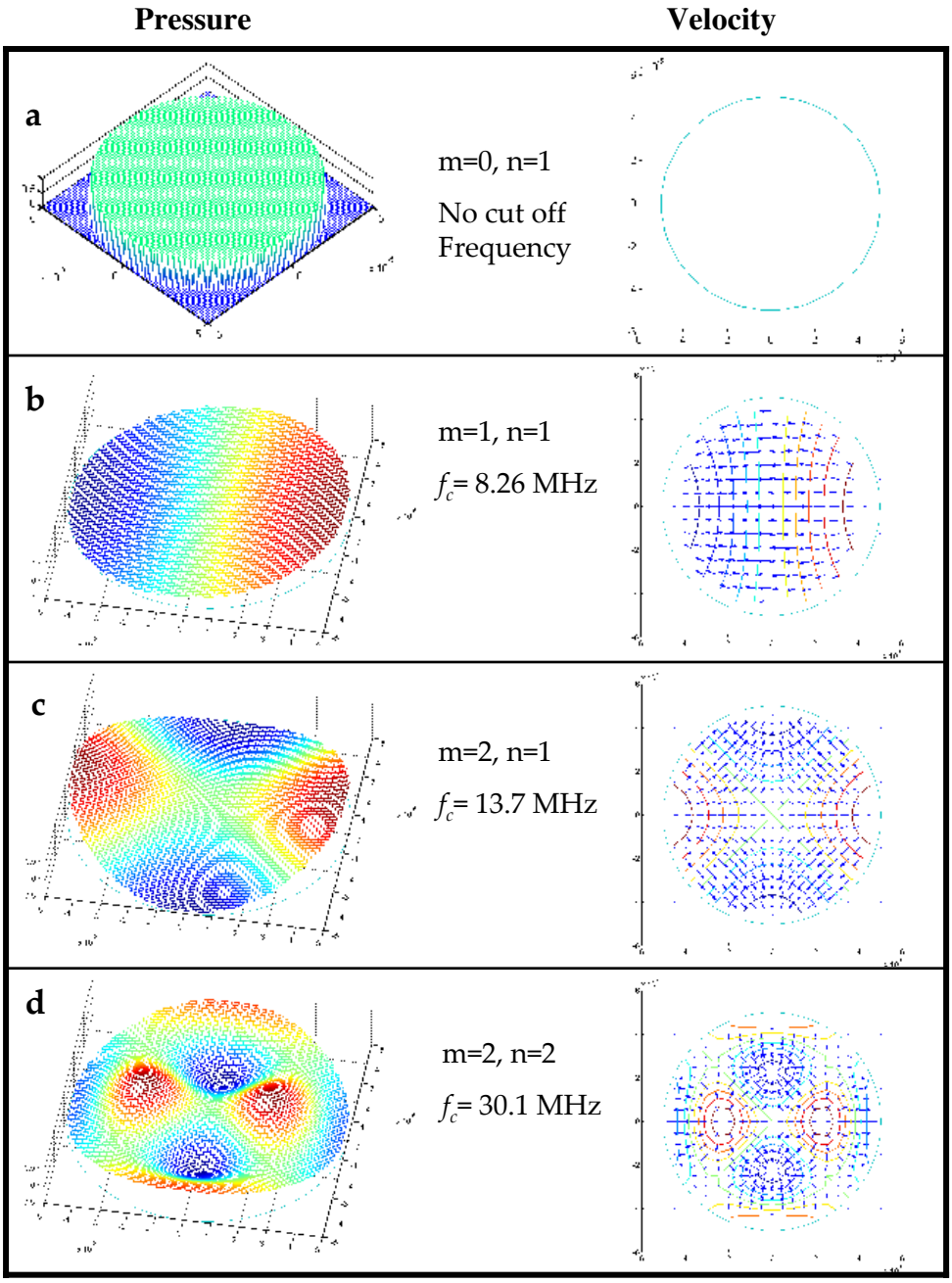

Figure 3.3: Cavity cross section pressure values and corresponding fluid velocity distributions are plotted for various modes. As expected the plane mode plotted on the top does not have any radial or angular variation and this is why this mode does not have any angular or radial component for the fluid velocity. This mode has velocity variation in z direction which is not plotted here. All of the other three modes given have radial and angular variation of pressure and velocity components in these axes.

Table 3.2: Cut off frequencies of various modes are computed from Equation 3.38. All values are in MHz.

		Cut off Frequencies (MHz)					
n	**m**	**0**	**1**	**2**	**3**	**4**	**5**
1		0.0	8.3	13.7	18.9	23.9	28.8
2		17.2	23.9	30.1	36.0	41.7	47.2
3		31.5	38.3	44.8	50.9	56.9	62.8
4		45.7	52.6	59.1	65.5	71.7	77.7

value of α'_{mn} is 1.84 from Table 3.1, next mode of propagation is expected to appear at frequencies higher than 8.27 MHz (Equation 3.38). This is much higher than the drive frequency range in our experiments (20kHz–2MHz). Since all other α'_{mn} values and their cut off frequencies are higher, we can conclude that in the frequency regime in which the capillary is actuated, only the axis symmetric plane waves can propagate through the channel. Other modes at low frequencies are evanescent and cannot propagate. However, they exist in the local neighborhood of the actuation. While these higher modes do not exhibit any importance for the naturally occurring cavity modes, we will see in the following sections that they are important because of the localized excitation of the cavity through the flexural modes of the enclosing capillary.

3.2 Interaction of Flexural Waves with the Fluid Medium

During the propagation of flexural waves, the surface of the elastic medium moves harmonically normal to the surface. In the presence of a fluid boundary, these periodic displacements are coupled to the fluid and may cause sound to be emitted from the surface and carried in the fluid medium. In depth details of structure borne sound can be found in references [49, 50, 51], which are used by the author

for derivations and comments made in this section.

For a plate (which might be also infinite) analysis usually is done through a selection of a strip from the plate. In our case, we have a vibrating cylinder vibrating transversely. As shown in Figure 3.4, we can approximately[3] treat the bottom and the top part of the inner part of the cylinder as two long strips (moving in phase with the cylinder flexural mode), and approach problem similar to the plate case. Waves on these strips will have the same frequency and wavelength of the entire capillary, which is already modeled in Chapter 2.

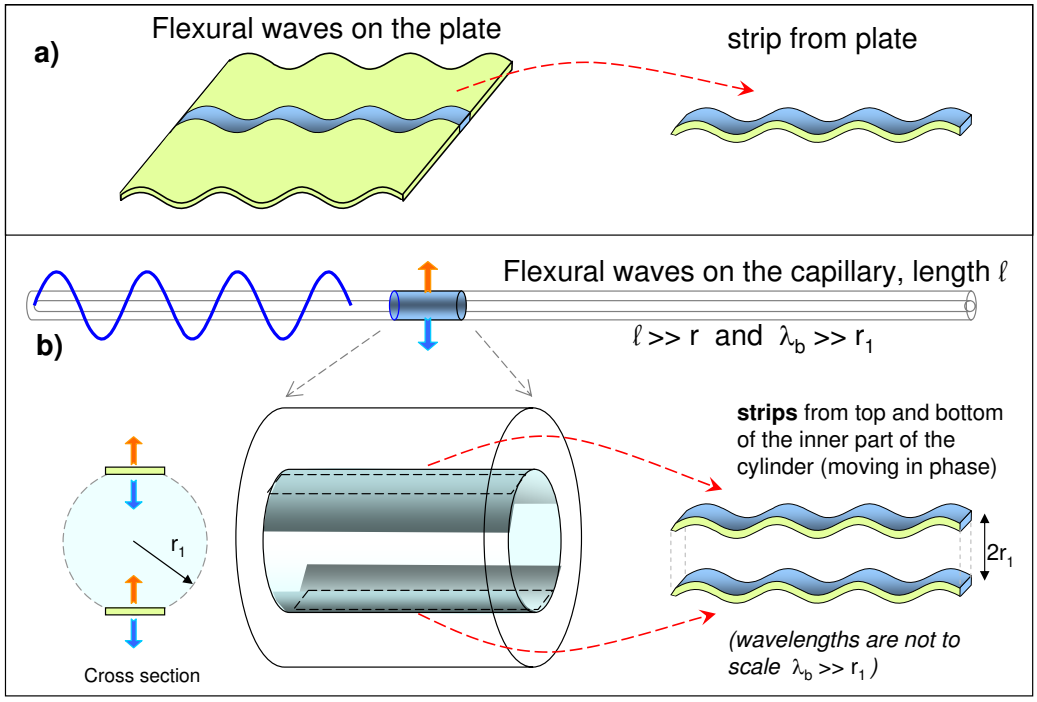

Figure 3.4: Similar to the strip taken from a plate, the top and the bottom of the inner capillary can be treated as two strips away from each other by $2r_1$ and moving in phase. Please note that wavelength of the strips taken from the cylinder's inner surface are not to scale. In fact we have $\lambda_b \gg r_1$ and $l \gg r_1$.

[3]It will be confirmed in later sections that resulting derivation of pressure inside the capillary related to this approximation gives a reasonably good match with FEM modeling and experimental results.

3.2.1 Case of Infinite Plate Loaded with Fluid Medium above

For far field acoustic radiation analysis, finiteness of the plate length is very important as there will be two distinct region on the plate, places where there is harmonic motion and places that do not move at all. A far field point will be able to feel the contribution of all moving locations. However, as shown in Figure 3.5, in the case of near field –especially thinking of the regime which is much smaller compared to the length of the beam (or plate or capillary in our case)– a fluid particle will only be able to feel pressure and displacement differences mostly due to its close boundary. From this we can conclude that as long as $l \gg d$, treatment of the problem as finite or infinite in z axis will not create any major difference. Since treatment of a finite case involves more steps of algebra and numerical integration of the radiation field, we will choose the infinite approach, which has a more straightforward analysis.

First, we will start with one strip and after we find the solution we will include the other. As shown in Figure 3.6, flexural wave propagating in z direction generates a propagating plane wave in fluid in the direction of wave vector ($\mathbf{k}$). In such a configuration, the direction of wave propagation in fluid is determined by the angle such that $\lambda_{fluid} = \lambda_{flex} \sin\theta$.

Related to our case, interaction of a standing flexural wave with the fluid medium will be investigated. Here, length of the elastic medium vibrating in flexural mode is infinite and the fluid medium is also infinite. Assuming a flexural

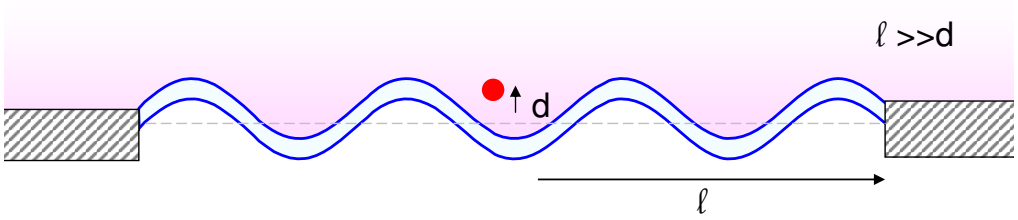

Figure 3.5: The Red dot indicates the fluid volume in the close neighborhood of the vibrating medium. Since $l \gg d$ pressure and displacement variations of this fluid volume will be mostly controlled by the close neighborhood vibrations of its location. So an finite or infinite case will not bother this particle at all. This will be different for the far field and also the end locations. This ambiguity related to end locations will be clarified in later sections.

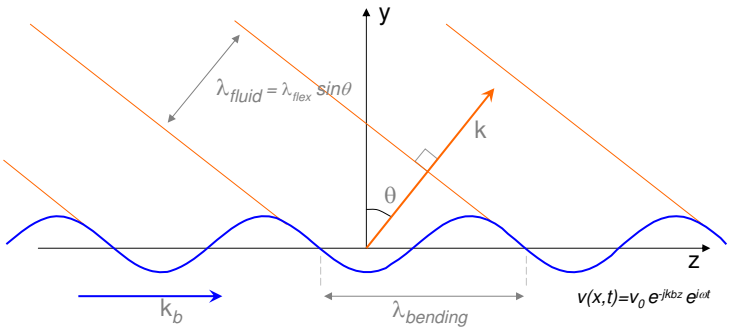

Figure 3.6: Acoustic radiation from a flexural wave propagating on an infinite plate.

standing wave having the velocity profile (just normal[4] to the strip),

$$\mathbf{v}(z,t) = v_0 \sin(k_b z) e^{j\omega t} \hat{\mathbf{y}} \tag{3.45}$$

Please note that, since final results will be interpreted in cylindrical coordinates, in order not to cause any ambiguities, horizontal axis is taken to be the z direction.

[4]For a strip of very small thickness, the tangential component of the velocity will be very small compared to the normal velocity and can be ignored. In this case, the shear effects in the fluid at close boundary is also neglected. We will further examine in future sections that if negligibility of shear associated tangential velocity is valid, as the strip or plate thickness gets higher. These shear effects might have some influence on some second order acoustic streaming effects.

We would like to find pressure waves in the fluid medium. Conditions which will guide us through the investigation can be listed as;

1. Pressure, p, has to satisfy Helmtholtz's differential equation given in 3.14.
2. Due to the continuity of the boundary, instantaneous normal velocity of the elastic surface should be in phase and equal to the normal velocity of the fluid.

Following conditions given above, we can guess a general form for pressure such as

$$p(y,z,t) = p_0 \sin(k_b z) e^{-jk_y y} e^{j\omega t} \ . \tag{3.46}$$

Now, we have to find k_y and p_0 in agreement with the given conditions above. Inserting this pressure value into the Helmholtz equation in 3.14 we find

$$k_y = \sqrt{k^2 - k_b^2} \tag{3.47}$$

where

$$k = \frac{\omega}{c} \tag{3.48}$$

where c is the speed of waves in fluid. From Euler's equation given in 3.30 we find normal velocity of the fluid as

$$v(y,z,t) = \frac{p_0 k_y}{\rho_f c k} \sin(k_b z) e^{-jk_y y} e^{j\omega t} \tag{3.49}$$

from boundary conditions mentioned above at $y = 0$, normal components of the fluid and flexural velocities should be the same, from which we find the unknown p_0,

$$p_0 = \frac{v_0 \rho_f c k}{k_y} \ . \tag{3.50}$$

Then we find the pressure waves in the fluid

$$p(y,z,t) = \frac{v_0 \rho_f c k}{k_y} \sin(k_b z) e^{-jk_y y} e^{j\omega t} \tag{3.51}$$

or using 3.47

$$p(y,z,t) = \frac{v_0 \rho_f c}{\sqrt{1-\frac{k_b^2}{k^2}}} \sin(k_b z) e^{-j\sqrt{k^2-k_b^2}y} e^{j\omega t} \ . \tag{3.52}$$

Commenting on the result we have; as long as $k > k_b$ or equivalently $\lambda_b > \lambda$ square root term in the denominator is always real and positive. This means that as long as wavelength of flexural waves are longer than wavelength of fluid waves, pressure waves will be propagating in the fluid and sound radiation will occur. Since $\lambda_{fluid} = \lambda_{flex} \sin\theta$, and $\lambda = 2\pi/k$ we have

$$\frac{k_b}{k} = \sin\theta \quad \text{and} \quad \sqrt{1-\frac{k_b^2}{k^2}} = \cos\theta \tag{3.53}$$

then pressure can be written as,

$$p(y,z,t) = \frac{v_0 \rho_f c}{\cos\theta} \sin(k_b z) e^{-j\sqrt{k^2-k_b^2}y} e^{j\omega t} \quad \text{for} \quad \lambda_b > \lambda \tag{3.54}$$

In the above equation, the only parameter that changes with the frequency is the $\cos\theta$ term. This means that amplitude of pressure depends highly on the relationship of wavelengths. As the difference between wavelength values of fluid and flexural medium gets smaller, we observe that amplitude of pressure waves tends to increase. Interestingly, as $k = k_b$, the amplitude of the pressure tends to infinity. At this value, the angle of propagation becomes 90°. This condition is used in endfire sonar radiators to radiate high sound energies in very select directions. While the derivation above suggests an infinite amount of pressure amplitudes, this will not be the case in experiments as everything will be limited by the energy supplied to the flexural beam. However, it is possible to say that compared to other frequency ranges in this range, energy transfer to fluid will be drastically higher.

We still have not looked to the regime where wavelength of the flexural waves is lower than the fluid waves ($k_b > k$ or equivalently $\lambda > \lambda_b$). The frequency value

where the k value is equal to k_b is called *critical frequency*. Below the critical frequency k_y will be imaginary. Rearranging Equation 3.52, we have

$$p(y,z,t) = \frac{jv_0\rho_f c}{\sqrt{\frac{k_b^2}{k^2}-1}}\sin(k_b z)e^{-\sqrt{k_b^2-k^2}y}e^{j\omega t} \quad \text{for} \quad \lambda > \lambda_b \ . \tag{3.55}$$

However, this is not a propagating wave, rather it decays exponentially in y direction, so this is an evanescent wave, periodic in z direction following the flexural wave. Decay rate $\sqrt{k_b^2-k^2}$ increases as the k_b and k difference increases, which means we expect a stronger decay in y direction at lower frequencies. Furthermore, this pressure value is $\frac{\pi}{2}$ out of phase with the velocity of flexural wave. Since power radiated is related to the real part of pv product, no net power is radiated to the far field. All power remains reactively in the close neighborhood of the flexural displacements. Results of equations obtained above are plotted in Figure 3.7.

Critical Frequency

In the previous section, it was demonstrated that wave dynamics in fluids due to flexural vibrations depend on the wavelength of the plane waves in fluid, and the wavelength of flexural waves on the elastic medium at a given frequency. Related to our case, we need to further investigate if there exists a frequency where the wavelength match occurs. It is a logical guess to expect such a frequency since, as shown in Section 2.3.2, flexural waves exhibit dispersive behavior and their wavelength frequency relationship is not a linear one.

Since this critical frequency value strongly depends on material and geometrical properties, we will specifically check for the critical frequency for the our capillary cylindrical actuator. For our fluid filled capillary structure, dispersion relationship was given in Equation 2.89. Using this equation, frequency values of harmonics of

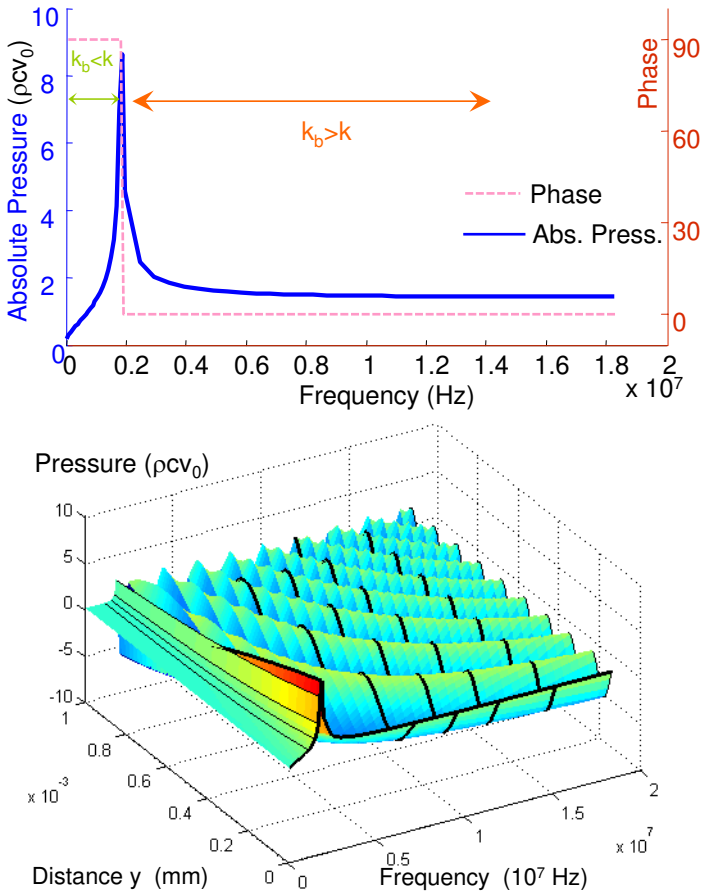

Figure 3.7: Pressure values in fluid are plotted. In the top graph, absolute value of the pressure and phase are plotted respectively against frequency. It can be clearly seen that below critical frequency phase is $\pi/2$ so that only imaginary pressure values exist. In other words, pressure is out phase with the velocity of flexural beam, or in phase with acceleration. At frequencies higher than critical frequency, pressure is pure real, and it decays from a maximum value at critical frequency as the frequency increases (reminding one over cosine factor). In the bottom graph, the behavior of the top graph in y direction is examined. Range of depth is 1 mm. Above critical frequencies propagating waves exist and their wavelength (inversely related to k_y) tends to decrease with increasing frequency. This trend can be seen from the thick black lines; each line corresponds to a wave at a given frequency. Below the critical frequency, no wave propagation can be observed because of the evanescent behavior of the pressure value. The decay rate increases as $k_b - k$ difference increases.

flexural waves can be found, and corresponding wavelengths are given as

$$\lambda_{fn} = \frac{2l}{n} \tag{3.56}$$

where l is the length of the capillary and n is the number of harmonics. The wavelength frequency relationship for plane waves in fluid is simpler and given by the formula

$$\lambda_n = \frac{c}{f_n} \tag{3.57}$$

where c is the speed of sound in a fluid medium enclosed in a channel, given in Equation 3.16.

Plotting frequency values against wavelengths in Figure 3.8, we can see the critical frequency to be 1.83 MHz. Below the critical frequency regime is defined as the subsonic regime in which flexural waves on the strip or capillary cannot generate propagating acoustic waves in fluid rather generate evanescent waves which are out of phase with the normal velocity of the elastic medium. Similarly above the critical frequency is defined as supersonic regime in which flexural waves on the strip or capillary will able to generate propagating waves in the fluid medium.

Critical frequency value we found (1.8 MHz) is quite meaningful for our case since it resides in the 30 kHz-2 MHz regime in which we excite the capillary. This means that it is possible to observe subsonic and supersonic regime in the given frequency range.

Another important parameter whose behavior over the frequency variation is also needed to be investigated is the value of $(k_b^2 - k^2)$. Reminding the equation giving pressure distribution;

$$p(y,z,t) = \frac{v_0 \rho_f c}{\sqrt{1 - \frac{k_b^2}{k^2}}} \sin(k_b z) e^{-j\sqrt{k^2 - k_b^2}\, y} e^{j\omega t} \ .$$

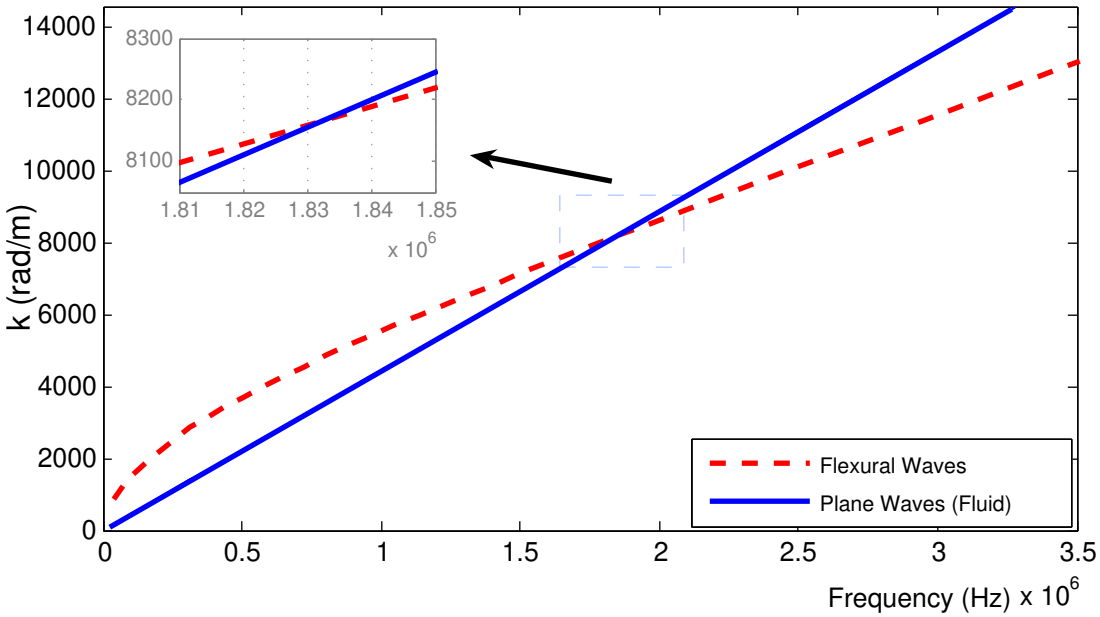

Figure 3.8: Graph of frequency values against wavelength for flexural waves on the elastic body and plane waves in enclosed fluid. Wavelengths become equal at 1.83 MHz. For frequencies smaller than this value we have $\lambda_b > \lambda$.

In this equation, exponent of the term representing y variation becomes real and negative in the subsonic regime. In this case, as the $(k_b^2 - k^2)$ value gets higher, the decay rate gets higher. From Figure 3.9 we find that the $(k_b^2 - k^2)$ value gets its highest in subsonic regime at 813 kHz. As shown in Figure 3.7b, the magnitude of pressure value gets higher with frequency at $(y = 0)$. However, for the subsonic regime its decay rate becomes maximum around the 600-1000 kHz regime which is denoted as regime II in Figure 3.9. In the next section, pressure distribution from various frequency regimes mentioned in roman numerals in Figure 3.9 will be compared.

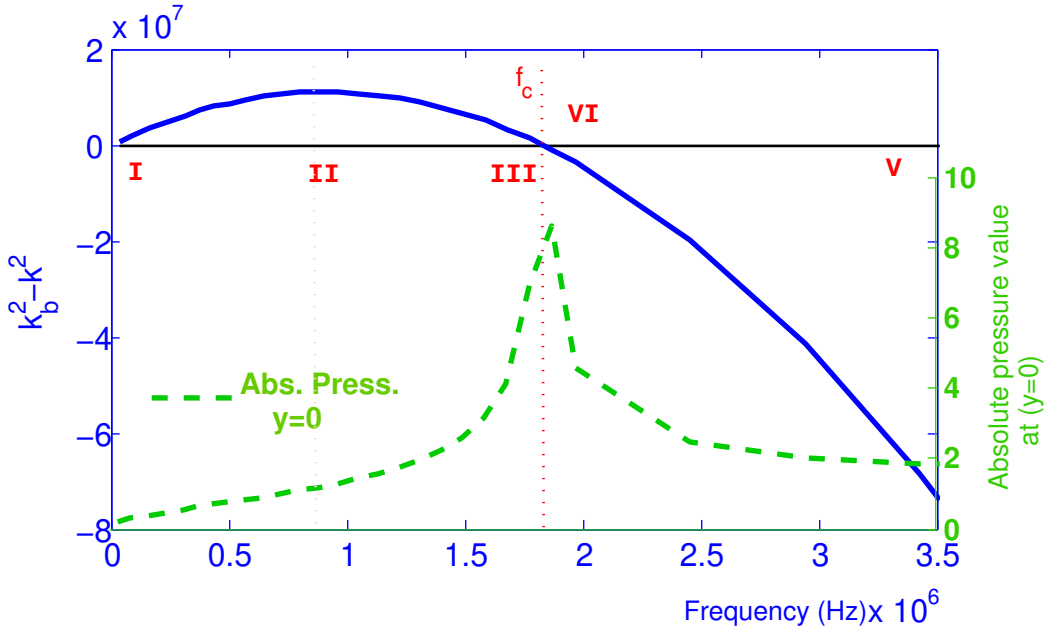

Figure 3.9: In this graph, $(k_b^2 - k^2)$ value and absolute value of pressure at $y = 0$ are plotted against frequency. In regime I, II, and III, waves are evanescent. Amplitude of pressure increases till the critical frequency (red dotted line), decay rate of this evanescent behavior is controlled by $\sqrt{k_b^2 - k^2}$. In this case, we expect a quite low decay rate in regime I and III. However, in regime II the decay rate reaches its maximum. Regime III has high amplitude and low decay rate. In regime III, pressure value is still in phase with the velocity of the flexural strip. Regime IV is in in the supersonic region, and there is no decay factor anymore; however, $\sqrt{k^2 - k_b^2}$ value defines the magnitude of the wave vector in y direction. Amplitude of pressure decreases and stabilizes at a nominal value as the frequency gets higher than the critical value.

Coupling in Subsonic and Supersonic Regimes

Since our capillary actuator has a very high aspect ratio ($r_1 = 50 \times 10^{-6}$m and $l = 1.1 \times 10^{-2}$m), before proceeding to the capillary case, we rather give the picture for a case in which we have more reasonable aspect ratios. In Figure 3.10, an infinite strip vibrating at a standing mode is bounded by fluid (water in this case) from the top. In Figures 3.12 and 3.13, wave dynamics of the dashed region is plotted

at sample frequencies from ranges in Figure 3.9 that are indicated with roman numerals.

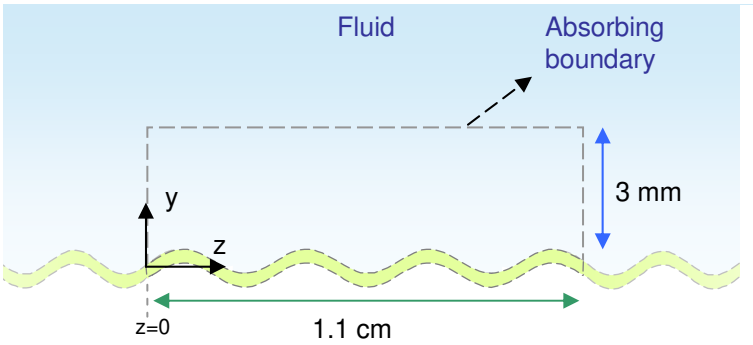

Figure 3.10: Sketch of standing flexural wave on the strip, loaded with fluid from top.

Figure 3.12 shows pressure and velocity distribution for frequencies below the critical value. In this range as given in Equation 3.55, pressure is purely imaginary. Which means that velocity of the plate and pressure distribution are out of phase by $\pi/2$. From Euler's equation given in Equation 3.30 we find velocity distribution to be

$$u_y(y,z,t) = v_0 \sin(k_b z) e^{-\sqrt{k_b^2 - k^2}\, y} e^{j\omega t} \tag{3.58}$$

$$u_z(y,z,t) = -\frac{v_0}{\sqrt{1-\frac{k^2}{k_b^2}}} \cos(k_b z) e^{-\sqrt{k_b^2 - k^2}\, y} e^{j\omega t} \,. \tag{3.59}$$

As we can see, contrary to pressure values, velocity components of the fluid are all real. Power intensity is given by the formula

$$\vec{I} = \frac{1}{T} \int_0^T p(t)\vec{u}(t) dt \tag{3.60}$$

where T is the period of the wave, or in frequency domain

$$\vec{I} = \frac{1}{2} Re\left[p(\omega)\vec{u}(\omega)^*\right] \tag{3.61}$$

where $(*)$ represents the complex conjugate. In this case, for below critical frequencies we do not have any power radiation since pressure values are purely imaginary and velocity values are purely real, in other words, they are out of phase by $\pi/2$. This is shown in the plots in Figure 3.11.

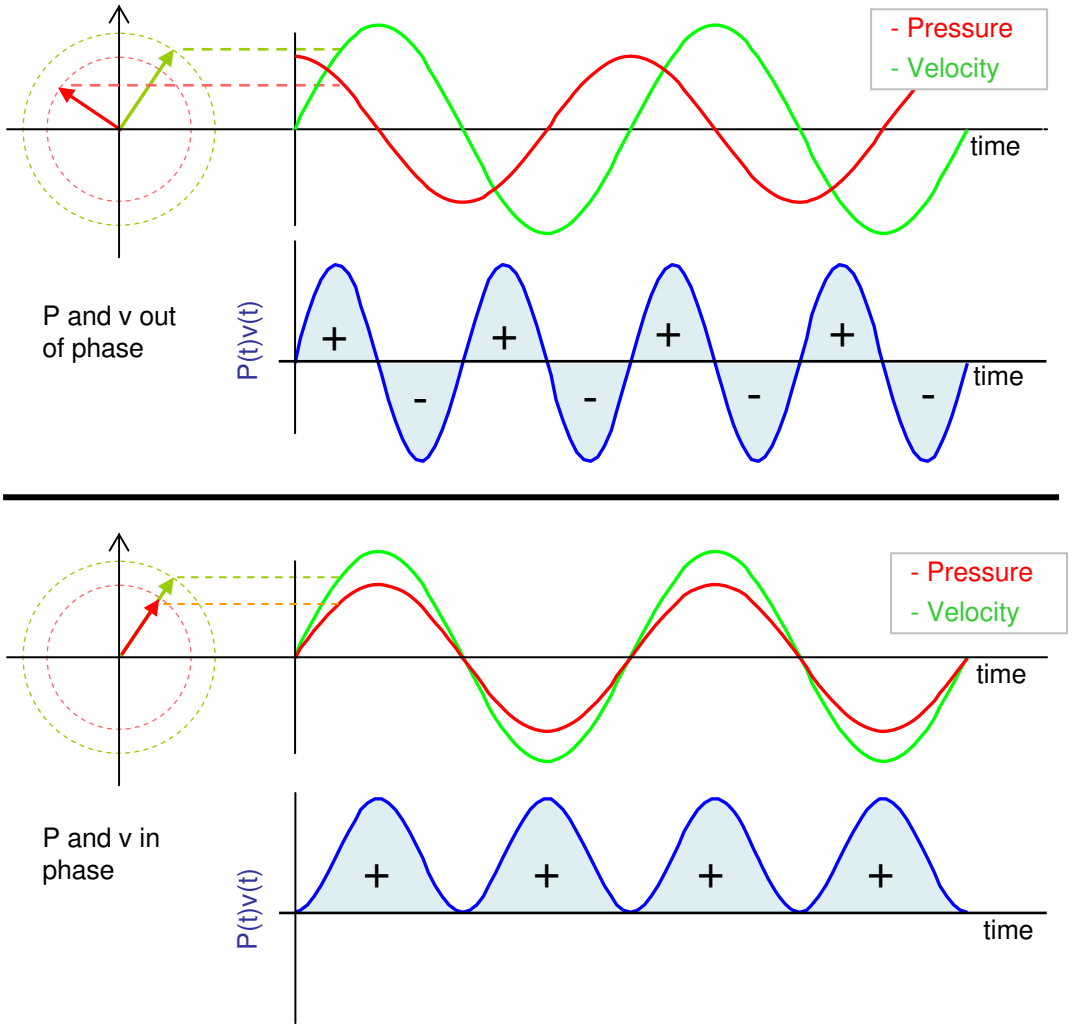

Figure 3.11: Instantaneous power plotted for cases pressure and velocity are in and out of phase. Total radiation is the sum of area below the instantaneous power over a period. When p and v are out of phase, area sums to zero, so that no power radiation takes place. When p and v are in phase, area is always positive in other words there is total power radiation.

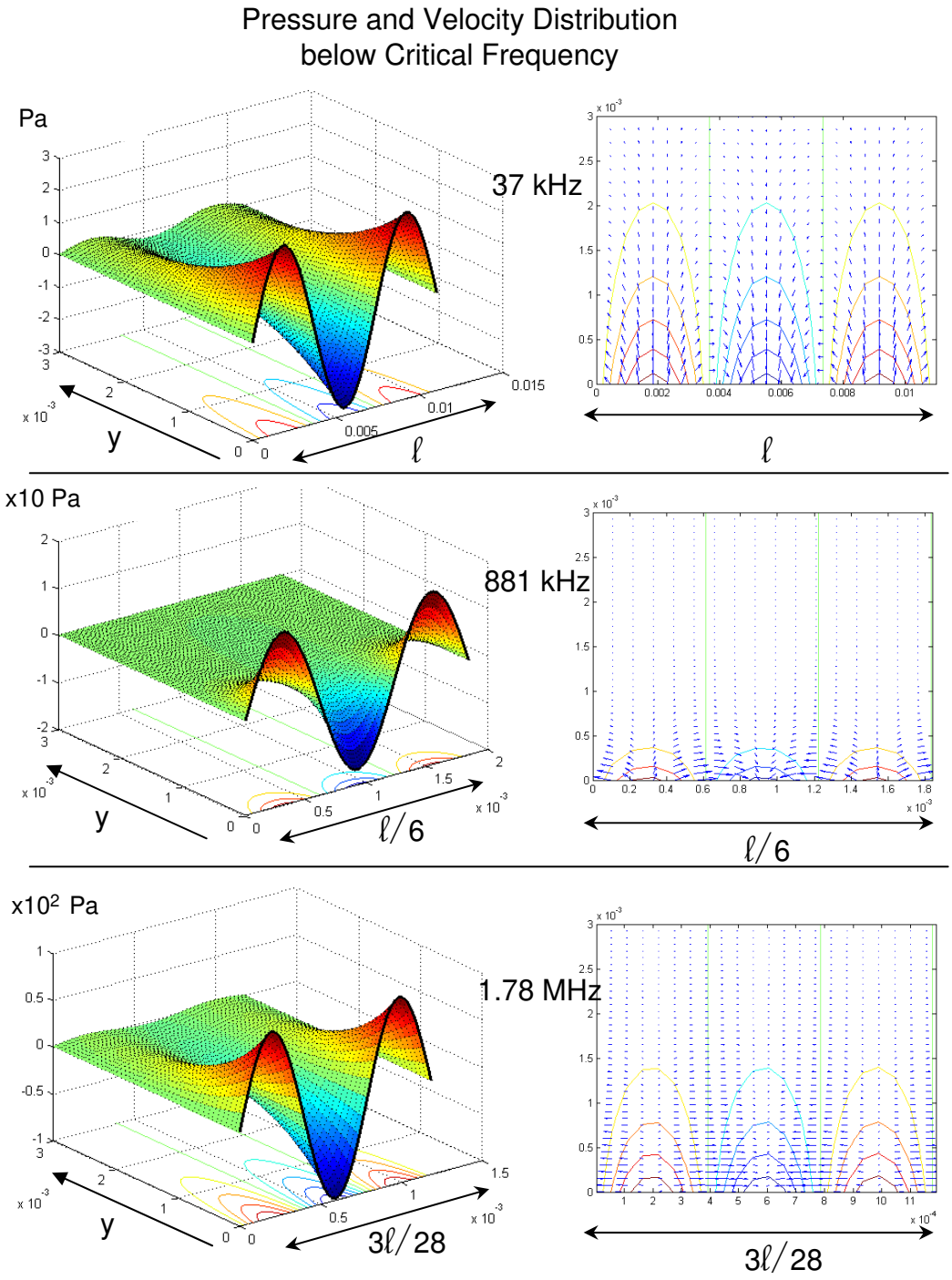

Figure 3.12: Pressure (left column) and velocity (right column) distributions are plotted for various frequencies below the critical frequency. The amplitude of the strip is taken to be $1\mu m/s$. For the sake of comparison, only 3 wavelengths (in z) are plotted. Comments related to these graphs are given in the text on Pages 94-97.

What happens here, below the critical frequency, fluid in the near boundary moves with the plate in phase (similar to the case of a mechanical harmonic oscillator driven under resonance). Since movement on the boundary is a sinusoidal wave, fluid in the boundary regime where displacement is upward, is pushed towards the regime that is moving down. This is an hydrodynamic short circuit effect. Since energy transferred to the fluid during the push is absorbed in the next half cycle as a pull, no net power is radiated to the fluid. This can be clearly seen through the arrows in velocity distribution graphs on the right column of Figure 3.12. As seen in velocity distributions, as the frequency gets higher (and wavelength in z direction gets lower) most of fluid particles move back and forth mostly in z direction.

The graphs on the top in Figure 3.12 represent the frequency regime marked as I in Figure 3.9. In accordance with the amplitude of the pressure variation with frequency, we have relatively low amplitude of pressure in this regime. However, since $(k_b^2 - k^2)$ is small, the decay rate is also small. The middle section of the same figure shows pressure distribution at section II of Figure 3.9. We observe larger amplitude at the boundary but a faster decay since $(k_b^2 - k^2)$ value gets its maximum at the below critical frequency regime. Lastly, in the bottom part of Figure 3.12 we have pressure distribution plotted for regime III of Figure 3.9. In this range, frequency is very close to the critical value, and the amplitude of the pressure gets close to its maximum value (two orders of magnitude higher compared to regime I: upper graph). In addition, the decay rate is low compared to regime II, as expected.

For the frequency regime above the critical frequency, Equation 3.52 represents the pressure distribution in the fluid. In this case, pressure value has both real

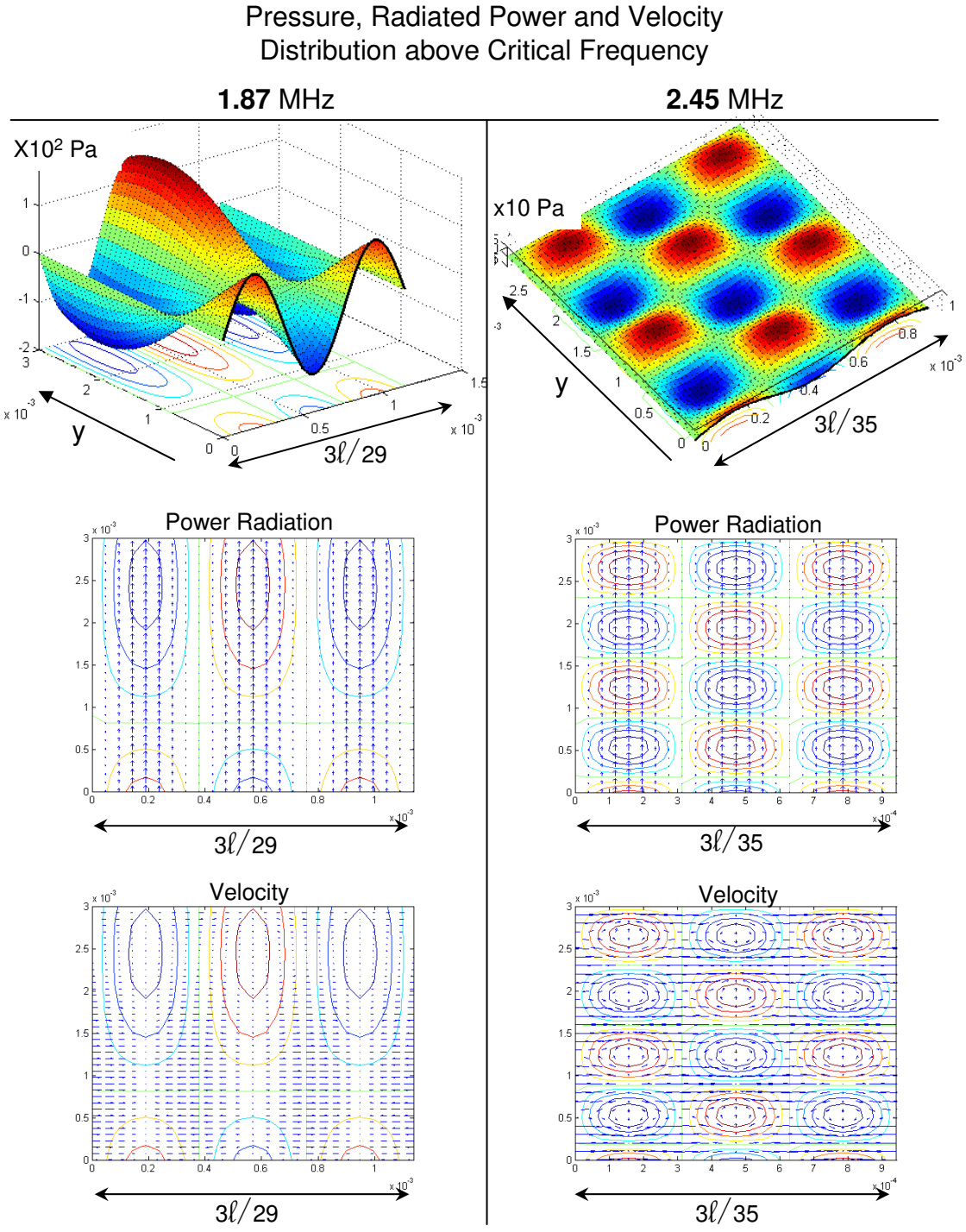

Figure 3.13: Pressure, radiated power and velocity distribution of two sample frequencies above the critical frequency values are plotted. In z direction three half wavelengths are shown. Comments related to these graphs are given on Pages 97-99.

and imaginary terms, indicating a traveling wave. From Euler's equation given in Equation 3.30 we find velocity distributions to be

$$u_y(y,z,t) = v_0 \sin(k_b z) e^{-j\sqrt{k^2-k_b^2}y} e^{j\omega t} \tag{3.62}$$

$$u_z(y,z,t) = j\frac{v_0}{\sqrt{\frac{k^2}{k_b^2}-1}} \cos(k_b z) e^{-j\sqrt{k^2-k_b^2}y} e^{j\omega t} \tag{3.63}$$

From Equation 3.61 we can find the power radiated as,

$$I_y(y,z,t) = \frac{v_0^2 \rho c}{\sqrt{1-\frac{k_b^2}{k^2}}} \sin^2(k_b z) \tag{3.64}$$

$$I_z(y,z,t) = 0 \tag{3.65}$$

since the plate vibrates in a standing mode, there is no power radiated in z direction[5]; however, there is fluid sloshing back and forth between displacement maxima.

The results obtained above for above the critical frequency regime is shown in plots in Figure 3.13. Pressure, velocity and power radiation are plotted for two frequencies from the regions marked as IV and V in Figure 3.9. From the pressure distribution, we observe traveling waves in y direction. Wavelength in y direction and absolute power decreases with increasing frequency. Quiver plots in the middle show the power radiation is only in y direction and gets maximum at locations where plate displacement has antinodes. In frequencies close to critical frequency, most of the fluid particle velocity is in z direction and it is oscillating locally but is not propagating. At much higher frequencies (such as 2.45 MHz), particle velocities in z direction can be observed as well. However, this does not contribute to an increase to the radiated power since amplitude of pressure decreases with increasing frequency.

[5]Standing wave is the superposition of two waves propagating in opposite directions. If we rather had a traveling wave then we would also find a real value for I_z. In such a case, the angle of propagation would be found from the ratio of y and z components of power radiated, or directly from Equation 3.53.

3.2.2 Pressure Distribution inside Capillary Vibrating in Flexural Mode

In the light of the analytical experience we acquired in the previous section, here, pressure and velocity distribution inside the capillary will be investigated. In section 2.3.2.1 of Chapter 2, we had found the displacement equation for the flexural vibrations of the capillary. Due to clamped-clamped boundary ends hyperbolic sin terms contributing to end locations will be ignored here, so we will simply assume sinusoidal variation of capillary velocity. The capillary will be vibrating in a standing flexural mode with a velocity in y direction given as

$$\mathbf{v}(z,t) = v_0 \sin(k_b z) e^{j\omega t} \hat{\mathbf{y}} \ . \tag{3.66}$$

Compared to this vibration velocity, variation of velocity inside the capillary wall will be negligible. In this case, as shown in Figure 3.14, velocity of a capillary element at any angle θ at the boundary ($r = r_1$) in cylindrical coordinates, will be

$$\mathbf{v}(r,\theta,z,t) = v_0 \sin(k_b z) \sin\theta e^{j\omega t} \hat{\mathbf{r}} + v_0 \sin(k_b z) cos\theta e^{j\omega t} \hat{\theta} \tag{3.67}$$

For the fluid cavity in cylindrical coordinates, we had found the possible solutions of Helmholtz Equation (3.14) such that, a general form of the solution was given in Equation 3.28

$$p(r,\theta,z,t) = \begin{pmatrix} A \\ B \end{pmatrix} \begin{pmatrix} J_m(k_r r) \end{pmatrix} \begin{pmatrix} \cos m\theta \\ \sin m\theta \end{pmatrix} \begin{pmatrix} \cos k_z z \\ \sin k_z z \end{pmatrix} \begin{pmatrix} \cos \omega t \\ \sin \omega t \end{pmatrix}$$

For a boundary value problem, the desired function can be a combination of various orders of modes. In this case the general form can be written as

$$p(r,\theta,z,t) = \sum_{m=0}^{\infty} \sum_{n=0}^{\infty} J_m(k_{mn} r) \sin(k_n z)(A_{mn} \sin m\theta + B_{mn} \cos m\theta) e^{j\omega t} \ . \tag{3.68}$$

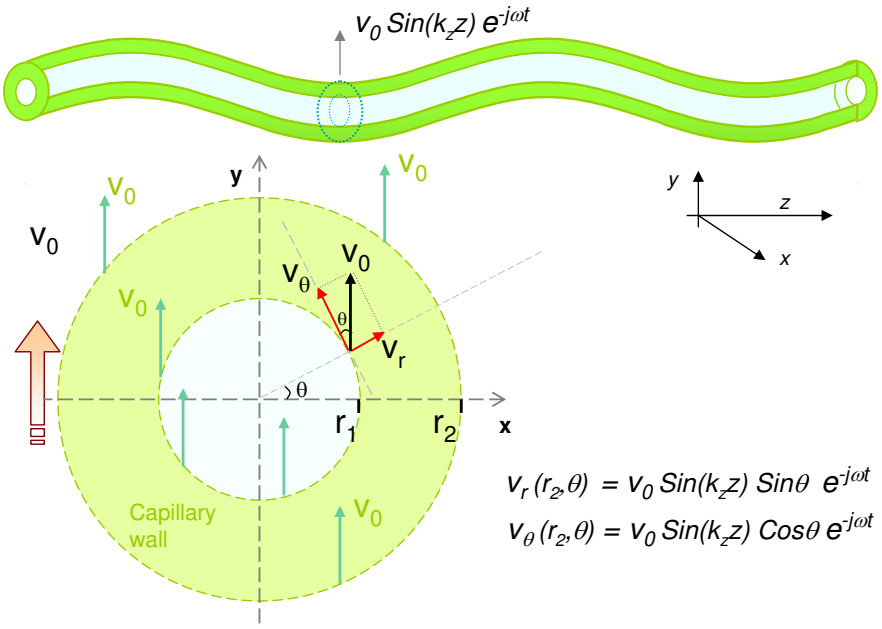

Figure 3.14: Boundary conditions for the capillary vibrating in a flexural mode. The entire capillary wall moves up and down with the same velocity amplitude v_0 in y direction. At the fluid capillary wall interface radial and tangential components of velocity v_0 are shown on the capillary cross section.

A_{mn} and general behavior of the series will be determined by the boundary conditions. From Figure 3.14, it can be seen that radial component of the fluid particles at $r = r_1$ have to be equal to the radial component of the capillary elements.

$$v_r(r_1, \theta, z, t)_{fluid} = v_r(r_1, \theta, z, t)_{capillary} \ . \tag{3.69}$$

Since no fluid can pass through the capillary or no fluid can emerge from the capillary wall, this is trivial. Then the boundary condition for the fluid elements at $r = r_1$ becomes

$$v_r(r_1, \theta, z, t) = v_0 \sin(k_b z) \sin\theta e^{j\omega t} \ . \tag{3.70}$$

Since the normal velocity at the fluid capillary interface $v_r(r_1)$ is a function of z, θ and t we have a nonhomogeneous boundary condition.

Fluid particle velocity at any point can be found by inserting Equation 3.68 into 3.30. At $r = r_1$, the radial part gives

$$v_r(r_1, \theta, z, t) = -\sum_{m=0}^{\infty}\sum_{n=0}^{\infty} \frac{A_{mn} k_{mn} J'_m(k_{mn} r_1)}{j\omega\rho} \sin(k_n z) \sin(m\theta)\ e^{j\omega t}\ . \tag{3.71}$$

Since we know the left hand side of the above equation from Equation 3.70, this is nothing but a Fourier series [48] in θ and z. Then A_{mn} values can be found from the integral

$$A_{mn} = -\frac{j2\omega\rho}{\pi l k_{mn} J'_m(k_{mn} r_1)} \int_0^{2\pi} \int_0^{l} \sin(k_n z)\ \sin(m\theta)\ v_r(r_1, \theta, z)\ d\theta dz \tag{3.72}$$

inserting $v_r(r_1, \theta, z)$ from Equation 3.70

$$A_{mn} = -\frac{j2v_0\omega\rho}{\pi l k_{mn} J'_m(k_{mn} r_1)} \int_0^{2\pi} \sin(m\theta)\sin(\theta)\ d\theta \int_0^{l} \sin(k_n z)\sin(k_b z) dz \tag{3.73}$$

This is an interesting result as two integrals have nonzero values only for the cases $m = 1$ and $k_n = k_b$; for other values other than these, A_{mn} becomes zero. Then we do not have a series solution, due to the single non zero A_{mn} value left in hand. Then for $m = 1$ and $k_n = k_b$ we have

$$A_{mn} = -\frac{jv_0\omega\rho}{k_r J'_m(k_r r_1)} \qquad \text{if} \quad m = 1, \quad k_n = k_b \tag{3.74}$$

$$= 0 \qquad \text{for others} \tag{3.75}$$

where k_r is used instead of k_{mn} due to the single value at a given frequency.

Using identity $\omega = ck$ from Equation 3.24, and for pressure inside the fluid, p, we find

$$p(r, \theta, z, t) = -\frac{jv_0 ck\rho}{k_r J'_1(k_r r_1)} J_1(k_r r) \sin(k_b z) \sin(\theta)\ e^{j\omega t} \tag{3.76}$$

where from Equation 3.24, k_r is given by

$$k_r = \sqrt{k^2 - k_b^2} \tag{3.77}$$

and $J_1'(k_r r_1)$ can be written[47] in terms of ordinary Bessel functions from the identity,

$$J_1'(k_r r_1) = \frac{1}{2}(J_0(k_r r_1) - J_2(k_r r_1)) \ . \tag{3.78}$$

The results given above are in agreement with the ones estimated in [52] by using Green's function approach.

One point that needs to be recalled is that, the above solution is valid when $k_r = \sqrt{k^2 - k_b^2}$ is real, which is only true when $k > k_b$ in other words above the critical frequency (supersonic regime). For below the critical frequency, in other words in the subsonic regime, k_r will be imaginary and can be written as

$$k_r = \mp j k_r' \tag{3.79}$$

where k_r' is real (for below critical frequencies) and given by

$$k_r' = \sqrt{k_b^2 - k_r^2} \ . \tag{3.80}$$

In this case, Bessel functions of k_r turn out to be $J_m(ik_r' r)$. This is equivalent to the modified functions which are the solutions of the Helmholtz equation in cylindrical coordinates when k_r is imaginary. They are related to ordinary Bessel functions with the relationship [48],

$$J_m(jx) = j^m I_m(x) \tag{3.81}$$

Plugging this to Equation 3.76, we find the pressure values below the critical frequency.

$$p(r, \theta, z, t) = -\frac{j v_0 c k \rho}{I_1'(k_r' r_1)} I_1(k_r' r) \sin(k_b z) \sin(\theta) \ e^{j\omega t} \tag{3.82}$$

where k_r' is real and given by 3.80. As shown in Figure 3.15, in the range $k_r' r < 0.5$ $I_1'(k_r' r)$ can be approximated as follows:

$$I_1'(k_r' r) = \frac{k_r'}{2} \sqrt{I_0(k_r' r)^2 + I_1(k_r' r)^2} \tag{3.83}$$

in our case, for below critical frequency, we have $k_r'r$ is limited from the top such that $k_r'r < 0.5$. Equation 3.82 is already defined to be valid only in this regime so this approximation is very accurate and no further comments are necessary.

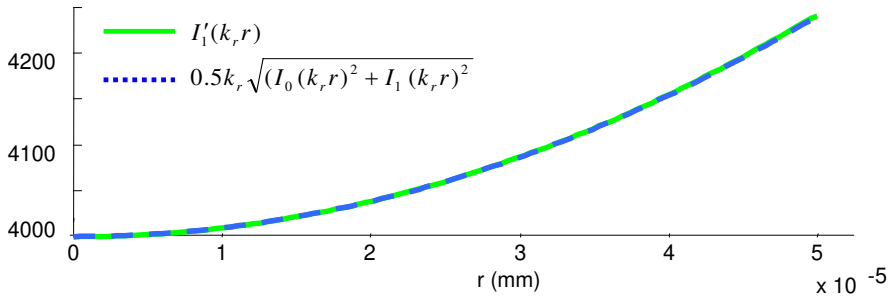

Figure 3.15: Visualization of approximation done for the derivative of the modified Bessel function of order 1 in the range $k_r'r < 0.5$. For this range, the two curves look indistinguishable.

In contrast to Bessel functions, modified Bessel functions take an exponential form and they go to infinity for larger values. This can be interpreted as a decay of pressure from the capillary wall in a way that its value becomes zero at $r = 0$. However, as shown in Figure 3.16, below critical frequencies, absolute value of $k_r r2$ is always less than 0.3. In this range we do not expect I_1 to exhibit any exponential behavior. Even though $J_1(x)$ and $I_1(x)$ have completely different asymptotic ends, in the range $-0.4 < x < 0.4$ they are almost identical and they can be approximated as

$$J_1(x) \approx I_1(x) \approx \frac{x}{2} \quad \text{for} \quad -0.4 < x < 0.4 \tag{3.84}$$

which can be seen clearly in Figure 3.17. In our case, for frequencies below 2.5 MHz, we have $|k_r r| < 0.3$ and since critical frequency of 1.8 MHz is below 2.5 MHz, it is safe to use one equation given in 3.76. This due to so small value of radius (r) compared to the fluid and structural wavelengths. For cylinders of larger r,

this approximation cannot be made. For the sake of accuracy capability in hand, in our calculations we used two separate equations for below and above critical frequencies. However for this range, the approximation given in Equation 3.84 could also be used conveniently.

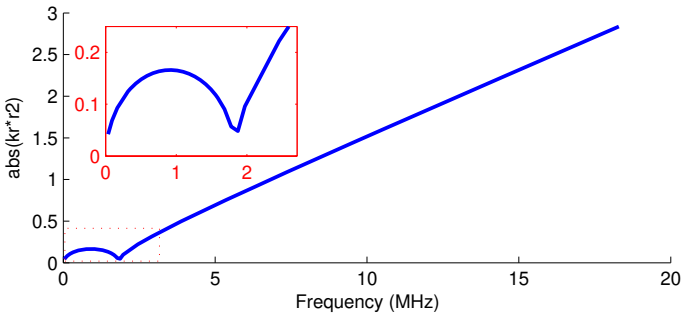

Figure 3.16: Absolute value of $k_r r_1$ value is plotted against frequency. It gets minimum at critical frequency. For below 2.5 MHz regime it is always smaller than 0.3.

3.2.2.1 Frequency Dependence of Pressure Amplitude

In calculating critical frequency on Page 89, since we used the frequency equation derived in Equation 2.89 for the capillary, the critical frequency obtained in Figure 3.8 is the critical frequency for the capillary fluid actuator, having the value $f_c =$ 1.83 MHz.

For structures vibrating in a flexural mode, when the same amount of energy is supplied to the system for different frequencies, it is expected to have the velocity amplitude of the vibrations will remain unchanged[6]. This is due to energy is related to velocity square. From this, assuming the same amount of energy is supplied to

[6] In reality this is not very practical in our case since actuating mechanism -PZT here- has impedance dependence on frequency. In addition it is expected so that coupling of different modes of PZT to the capillary would also be different

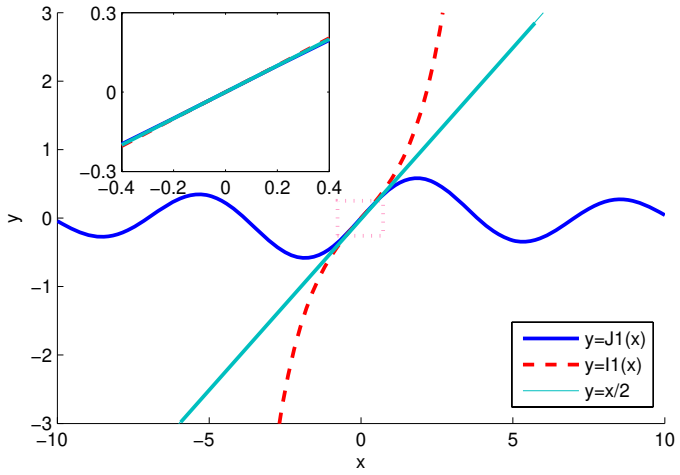

Figure 3.17: Bessel function of the first order; the modified Besssel function of the first order and $y = x/2$ are plotted together. As can be seen in the zoomed in section in the range $-0.4 < x < 0.4$, all three of these functions are almost identical and can be used interchangeably. This small range is due to the small radius of the channel compared to its length and fluid and structural wavelengths.

the capillary fluid system, it is possible to monitor amount of pressure variation over the frequency range. In fact, this is simply the specific acoustic impedance since the specific acoustic impedance is given by pressure divided by velocity, which is given by

$$z = \frac{p}{v} \tag{3.85}$$

In this case, assuming a constant velocity value $v_0 = 1m/s$, in Figure 3.18 the pressure amplitude at $\theta = \pi/2$ and $r = r_1$ is plotted against frequency (reminding k is also a function of frequency) using Equations 3.76 and 3.82.[7] Contrary to the case of strip-fluid coupling shown in Figure 3.7, we do not observe any major change at the critical frequency (green dotted line in Figure 3.18). This is because while the

[7]The author would like to mention again that PZT related impedance and geometric factors are not included here. These factors can be obtained via experimental measurements of the capillary vibration at various frequencies at a constant power supplied to the PZT. These measurements are given in Chapter 6.

$k_r = \sqrt{k^2 - k_b^2}$ value in the denominator goes to zero at critical frequency, $J_1(k_r r)$ also goes to zero, which limits any blow up in the pressure value. Pressure stays rather stable at critical frequency. However, pressure peaks around 9 MHz, which represents the first half wavelength resonance of the capillary in radial mode. As expected the phase also changes 180^o at resonance. Before resonance frequency pressure (and thus the acoustic impedance) is imaginary and negative, and above the resonance frequency it happens to be positive and imaginary. Below the resonance frequency fluid acts as a mass load and gives inertial response to the push and pull from the capillary. However, after resonance frequency compressibility of the fluid starts to become dominant so that fluid acts as a spring. This is comparable to the impedance variation of a forced harmonic oscillator (of mass and spring attachment) around the resonance frequency spectrum. In a mass-spring system oscillating below the critical frequency, system acts more inertial such that mass moves inertially in phase with the driving force. However, passing resonance frequency we observe mass moves out of phase with the driving force. Different from the harmonic oscillator, in acoustics, acoustic impedance maxima and minima may both denote the resonances depending on the boundary and conditions and actuating mechanism. At an impedance maximum, pressure is high for low particle velocity, and at a minimum, particle velocity is maximum for a limited pressure. For a closed system maxima are the resonances, and for an air open system, minima denote the resonances. This is an important factor for musical instruments; for example, while a flute operates at minima, a clarinet operates in maxima [53]. This can be explained as follows, when the cavity is closed maximum velocity is controlled by the velocity of the cavity. Then value of pressure is important related to interior acoustics. However in an open air system, at the opening, pressure is set to air pressure, and air flow is important for the acoustic

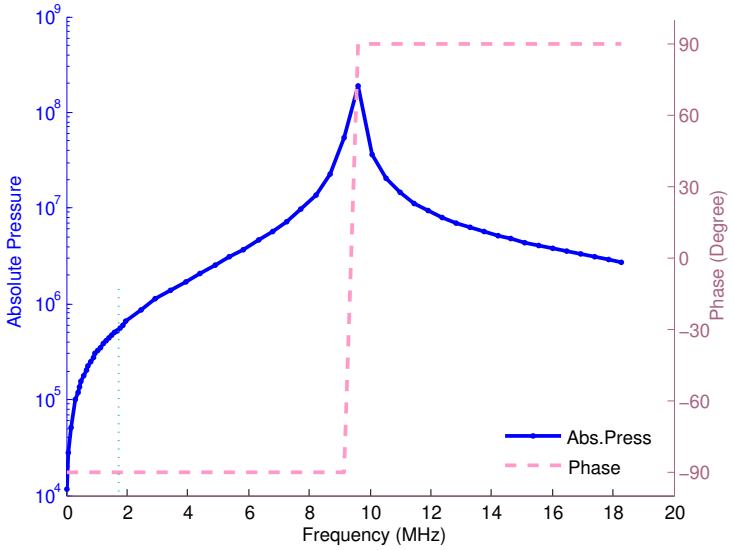

Figure 3.18: Variation of the acoustic pressure amplitude and the phase at the capillary wall versus frequency in the 0-20MHz regime. Critical frequency defining the subsonic-supersonic transition is at 1.8 MHz and indicated by the green dashed line. Resonance half wavelength cavity mode occurs around 9 MHz (acoustic pressure peak).

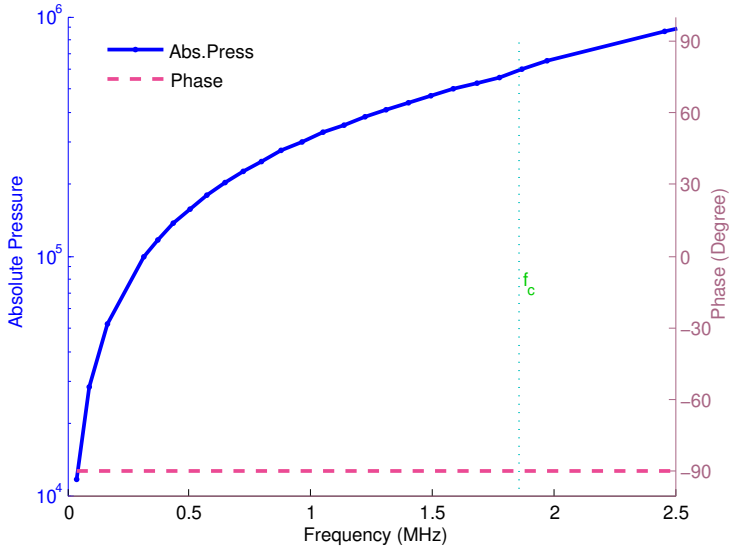

Figure 3.19: Variation of the acoustic pressure amplitude and the phase at the capillary wall versus frequency in the 0-2.5 MHz regime. Critical frequency is indicated by the green dashed line.

energy transfer.

In a typical cavity or waveguide ultrasonic transducer, this resonance frequency mentioned above is the first possible resonance frequency to obtain a standing mode in radial direction. And most of the micro or macro scale acoustic capture and manipulation devices work with this principle; and they are designed and actuated so that half or quarter wavelength acoustic modes can be generated in the cavity. In our case, we eliminate this requirement. Details of this claim will be mentioned in details in the next section.

Since the glass capillary actuator presented here is run mostly in the 30kHz-2MHz region, the variation of the pressure over frequency focused at this region is also plotted in Figure 3.19. In this section, we clearly see no major happening or change around critical frequency which defines the transition from subsonic to supersonic regime (indicated by green dotted line).

3.2.2.2 Acoustic Pressure Variation inside the Capillary due to Flexural Vibrations

In this section, radial and side view pressure distribution for above and below critical frequency cases are investigated. Equations 3.76 and 3.82 give the pressure distribution inside the capillary due to flexural vibrational modes that were derived in the previous section. Figure 3.20 shows the acoustic pressure distribution inside the capillary in the y-z plane. We observe that pressure distribution follows flexural movement of the capillary, suggesting that as the frequency –and so the number of harmonics of the flexural modes of the capillary– increases, number of transverse pressure variations along z axis increases accordingly.

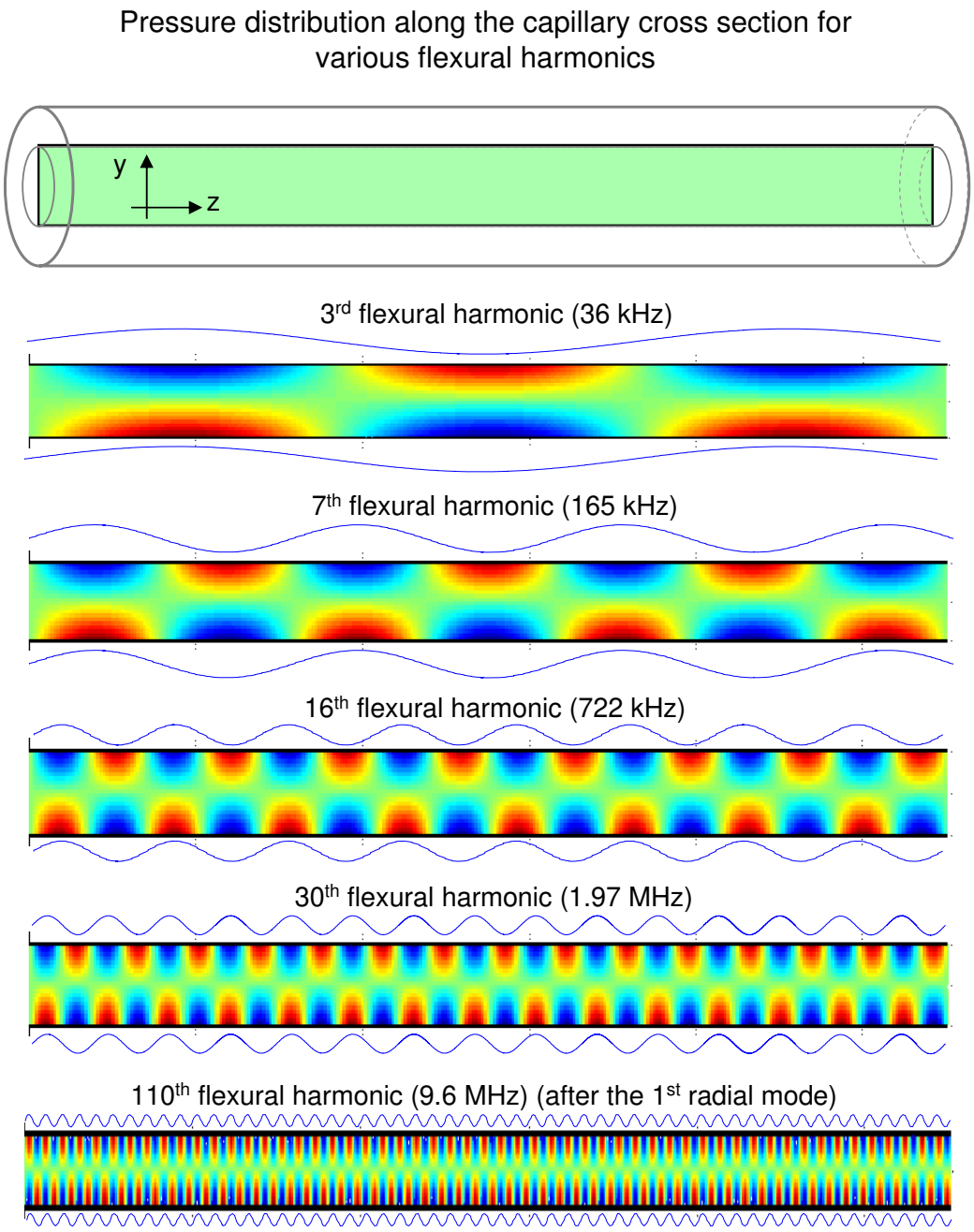

Figure 3.20: Variation of pressure inside the capillary in the y-z plane. Blue sinusoidal lines represent the top and bottom acceleration of the capillary. For all these plots, pressure and acceleration are in phase since all are below the resonance frequency. Please note that 30^{th} mode is above the critical frequency (1.83 MHz); however as found in the previous section, phase shift occurs after the frequency of the first radial capillary mode (around 9 MHz).

A detailed analysis of a sample particular flexural harmonic (3^{rd} harmonic) of the capillary is plotted in Figure 3.21. Part a) of this figure shows three radial pressure variations along the capillary since this is the third flexural mode. The blue sinusoidal curve on top represents the distribution of the acceleration of the capillary. We observe that capillary acceleration and the pressure variation are in phase. Part b) and d) shows pressure variation in the y-z and x-y planes respectively. Part c) and e) show the fluid particle velocities due to pressure variations shown in part b) and d). We observe that particles tend to flow (escape) from high pressure regimes to low pressure regimes as expected. Fluid particle flow exists only in one dimension, parallel to the vibration axis of the capillary. At the frequency regime described here, fluid moves inertially with the push or pull of the capillary, as we see the pressure variation is in phase with acceleration a. From velocity distribution plots it can be seen that this is a strong hydrodynamic short circuit effect. In the z axis, fluid particle velocity gets maximum in vibration maxima. Part f) shows the radial pressure variation. Dotted lines shown in Part a), b), d), and f) all represent the same line in different views. Graph f) shows that standing wave pattern is a triangular wave.[8] This is an interesting result, which confirms that even at frequencies much lower than the radial resonant cavity modes, we observe standing waves of triangular form. In Chapter 3, we will show that these standing waves are responsible for generating radiation force fields to capture and manipulate micron scale particles. In the 30kHz-2.5MHz regime, the characteristics of the pressure and velocity variations are almost same as this sample case given in Figure 3.21, only the number of repetitions in the z direction increases with the frequency. As the frequency gets higher, major change happens with radial variation of the pressure. Radial distribution of the pressure starts to

[8]We already mentioned about this in the previous section, as for small $(k_r r)$ values, $J_1(k_r r)$, $I_1(k_r r)$ are almost the same and can be approximated as $k_r r/2$ (Figure 3.17).

look more like the $J_1(k_r r)$ function.

Similar to Figure 3.21, in Figure 3.22, pressure and velocity distribution at the 110^{th} flexural harmonic (at 9.6 MHz) is analyzed in a detailed manner. In fact, this harmonic is not in the range in which we perform our experiments; however, it is included to highlight the differences at high frequencies. This frequency is above the frequency corresponding to the peak value of pressure given in Figure 3.19, which denotes the first radial resonance. After this resonance frequency, phase of the pressure value gets a 180^{o} of shift. Pressure is still reactive (imaginary) and 180^{o} out of phase with the acceleration (Graph a). Accordingly, phase of the fluid particle flow is also affected and gets reversed.

A physical explanation could be as follows; before the resonance frequency fluid volume acts as a inertial mass (like the neck of a Helmholtz resonator). Any acoustic disturbance is answered by an inertial motion (flow). Since wavelength is much larger than the fluid volume dimensions, compressibility of the fluid volume is quite low. However, when dimensions of the fluid volume start to become comparable with the wavelengths, fluid volume starts to be compressible and acts as a spring (like the cavity part of Helmholtz resonator). At the point where these effects become equal in magnitude is the resonance in the cavity. In our case this happens when the denominator of pressure equation, becomes zero $J_1'(k_r r) = 0$, which is the first maximum of $J_1(k_r r)$.

In fact, we can also see this in Part f) of Figure 3.22, as the pressure variation looks more like the Bessel function from first minimum to first maximum. In this case the $k_r r/2$ approximation is no longer valid. In the figure, the dotted lines in parts a), b), d) and f) are all represent the same line.

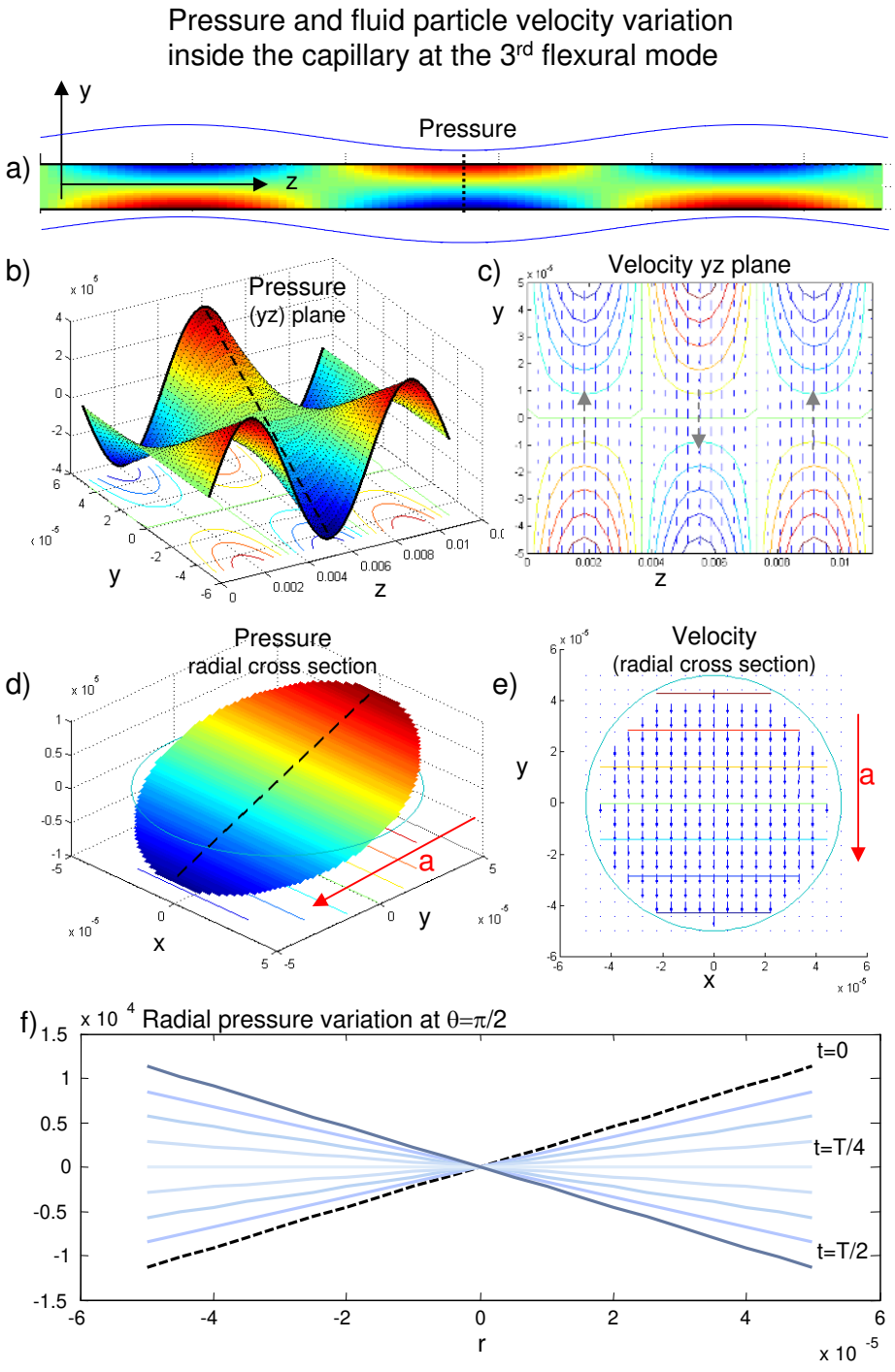

Figure 3.21: Pressure and fluid particle velocity distribution for the 3rd flexural mode of the capillary is given. All length scales are in meters. And T in Figure f) is the period of flexural vibration. Comments on figures given here can be found on pages 109-112.

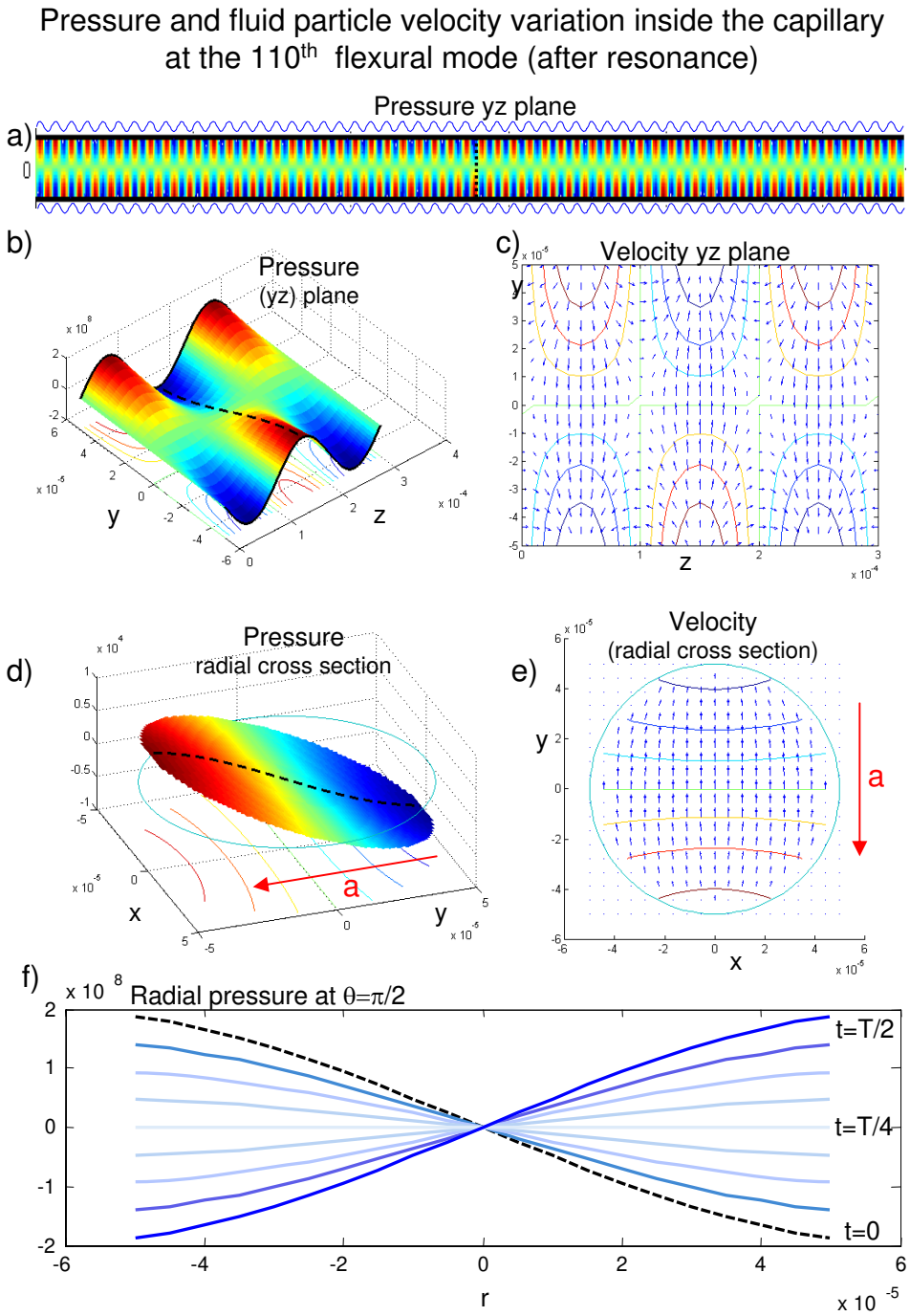

Figure 3.22: Pressure and fluid particle velocity distribution for the 110th flexural mode of the capillary (after resonance) is given. All length scales are in meters. And T in Figure f) is the period of flexural vibration. Comments on figures given here can be found on page 112.

Another observation from this figure is that, in part c) fluid particle velocities are not all parallel with the capillary motion. Since the wavelength in z direction is diminished and its value gets close to the radius of the capillary, hydrodynamic short circuit is no longer occur only in y direction (top-bottom) but also in z direction. In this case, neighboring maxima and minima in z direction start to interact as their separation gets close to the r_1 value.

Regarding power radiation, in our microcapillary case, for the frequency regimes <2MHz, pressure and fluid particle velocities due to flexural waves are found to be always out of phase by 90º. From Equation 3.61, we find that no power is radiated. The physics of this motion can be explained as follows: In the first half acoustic cycle, kinetic energy is transferred to the fluid by the capillary motion, and is received by the capillary as a push from the fluid in the next half cycle. All the instantaneous power transmitted to fluid is received in the next cycle. This does not mean that the presence of fluid does not have any effect. We already included mass loading of the capillary when we calculated the dispersion relation for the flexural waves of the fluid filled cylinder in Section 2.3.3, and we found that the presence of fluid lowers the frequencies of harmonics significantly.

Before we conclude this section, tracking the life cycle of a specific fluid particle at the boundary during an acoustic cycle might be helpful for a better understanding. As shown in Figure 3.23, assuming that at $t = 0$ capillary is at the minimum displacement, its velocity will be zero; at the same time acceleration will be at its maximum value. At this point, since the acceleration towards the top is maximum, fluid particle will be feeling the strongest force during the cycle which makes the acoustic pressure at this point to be maximum. At $t = T/4$, the capillary will have its maximum velocity towards the upward direction and acceleration will be zero;

thus the fluid particle will not be sensing any pressure momentarily. At $t = T/4$, the fluid particle would be interested to move upward with the momentum it gained during the previous quarter cycle, however in the $t = T/4 - T/2$ range, since the neighboring capillary wall is slowing down, it will sense a negative pressure.

At frequencies higher than the resonance frequency, since the compressibility of the fluid dominates, effect mentioned above is reversed. This can be understood easily with the help of the lumped parameter mechanical analogy shown in Figure 3.24. Since the stiffness coming from the compressibility of the fluid is much higher compared to flexural stiffness of the capillary (the capillary is very long compared to its diameter), at low frequencies, any periodic motion will be controlled by the

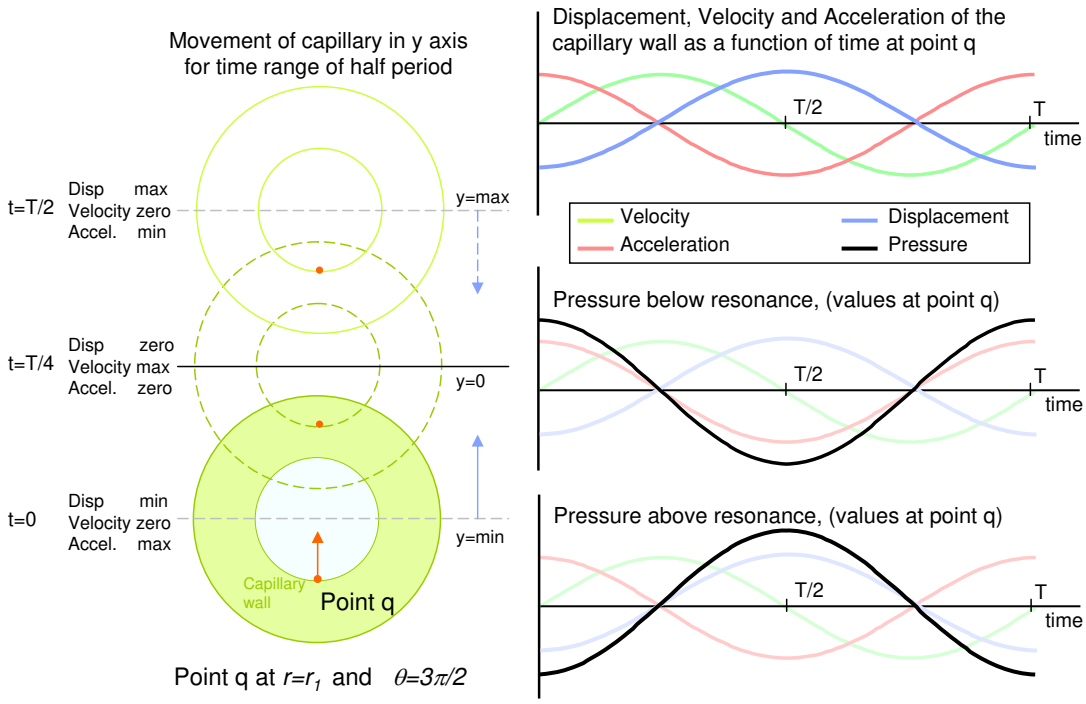

Figure 3.23: Displacement, velocity, acceleration and pressure plots as a function of time for the fluid particle located at point q. Black curves on the middle and bottom graphs show pressure for below and above resonances respectively.

weak spring. In this case, the big spring will not compress or expand at all but just move with the fluid mass attached to the other end. In higher frequencies, however, this large spring will start to absorb some of the displacement, depending on the frequency. As we already have the solution in hand, further analysis of the lumped parameter model will be skipped here.

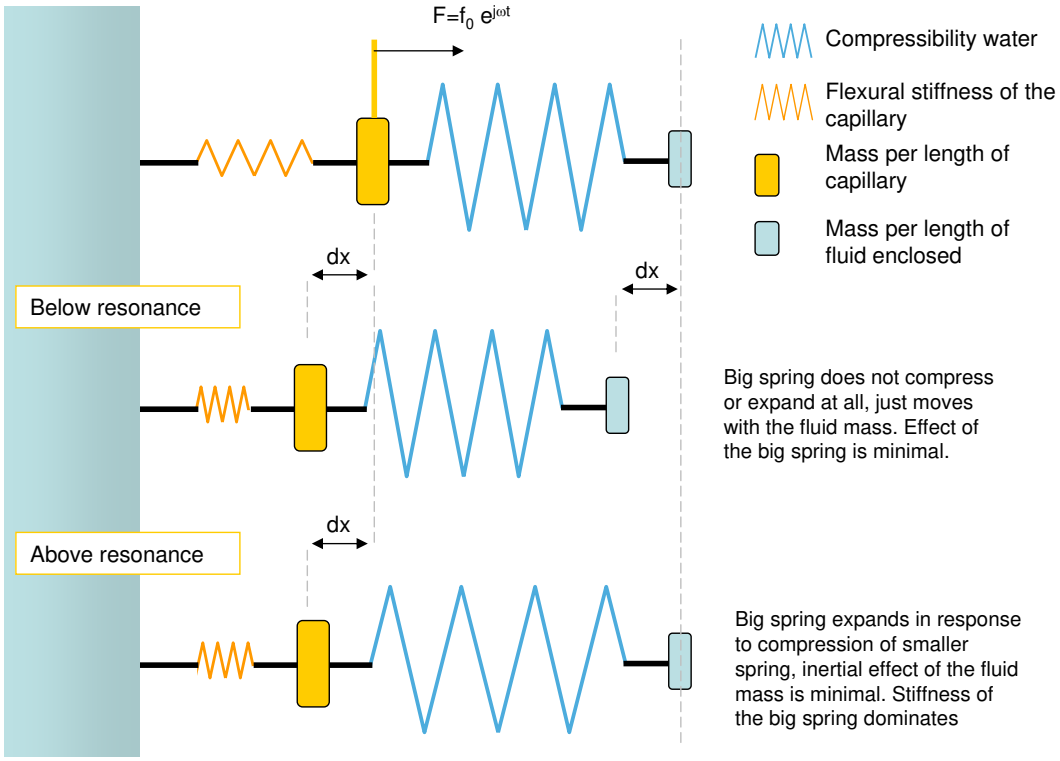

Figure 3.24: Mechanical lumped parameter modeling of the fluid filled capillary. The big stiff spring denotes the compressibility of the fluid, and the small and soft spring represents the flexural stiffness of the capillary.

3.2.3 Conclusions and Summary

As shown in Figure 3.25, in most acoustic applications for particle capture or streaming, resonators are designed in a way that standing waves can occur in

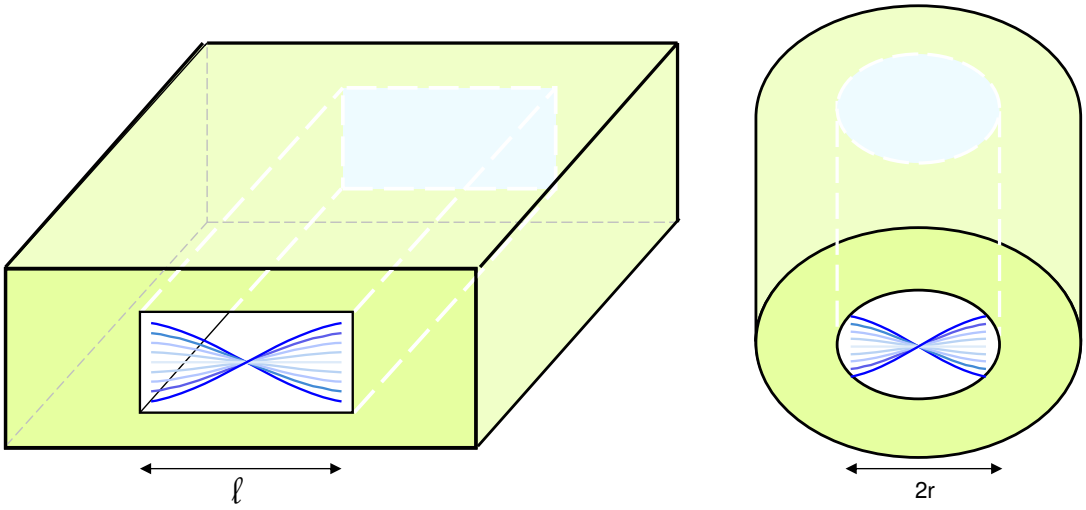

Figure 3.25: Standing modes in rectangular and cylindrical cavities. Frequency of the first standing pressure mode inversely depends on the capillary

the fluid cavity. In microfluidic applications, as the size of the cavity diminishes, frequency value required to generate a standing mode also increases. For example, for a rectangular microfluidic channel filled with water and having width of 100µm, the first standing wave mode appears at 7 MHz. In our case for the capillary of inner diameter 100µm this value was calculated as 8.26 MHz in Section 3.1.2. However, due to axis antisymmetric motion of the flexural vibrations, it is possible to generate subharmonic stationary modes in a harmonic way. In this case, harmonicity of the acoustic pressure standing modes depend not on the fluid wave dynamics but the harmonicity of the flexural motion of the capillary or the structure containing the fluid. In this way, for example, we can observe about 100 standing acoustic pressure modes before the actual expected resonance around the 100^{th} flexural mode. This means that below the naturally occurring cavity modes, 100 early standing modes can be generated. This lowers the frequency required to form the first standing mode significantly. In our case, theoretically, it is possible

to generate the first standing mode as low as 20 kHz via the first flexural mode of the capillary. In experiments, this is demonstrated as low as around 30 kHz via the 3^{rd} flexural harmonic, (whereas the naturally occurring standing modes start around 8.26 MHz). This enables a broad range of frequency applicability and gives a strong trade off capability in terms of designing other parameters such as performance dependence related to PZT impedance and vibration coupling, and dimensions or geometry of PZT itself. By utilizing this method the cavity dimension requirements are no longer that strict.

3.3 Interaction of Longitudinal Waves with the Fluid Medium

The coupling of structural motions with the fluid to generate sound waves only happens through the displacements normal to the fluid-structure interface. Any other displacements do not create any pressure variation (though they contribute via second order streaming effects).

In the case of dilatational waves in bulk, compression and expansion only happens in normal to the propagation direction. However, in the case of plates and beams of finite thicknesses, due to compressibility and volume preservation, some compression and expansion also occurs in the cross section, which is why in many references longitudinal waves in beams and plates are named as quasi-longitudinal waves.

Amplitude of transverse strain is related to axial strain through the well known Poisson's ratio ν.

Assuming the solution given in Equation 2.113, for the longitudinal mode we will have velocity distribution in z direction as follows:

$$v_z(z,t) = v_0 \sin(k_l z) e^{j\omega t} \tag{3.86}$$

where

$$k_l = \frac{2\pi}{\lambda} = \frac{\pi n}{l} \tag{3.87}$$

where n is the harmonic mode number of the longitudinal mode of the capillary.

Due to radial symmetry, there will not be any angular (θ) dependence. Velocity in transverse direction at the inner surface of the capillary is given by [54]

$$v_r(z,t) = \frac{\nu(r_2 - r_1)}{2(1-\nu)} \frac{\partial v_z}{\partial z} \tag{3.88}$$

from which we can find v_r in our case,

$$v_r(z,t) = v_0 \left(\frac{k_l \nu (r_2 - r_1)}{2(1-\nu)} \right) \cos(k_l z) e^{j\omega t} \ . \tag{3.89}$$

The value of the items inside the brackets is 3×10^{-3} in our case, which means that radial velocity will be about two orders of magnitude smaller than velocity in z direction.

In the case of longitudinal waves on the capillary, boundary conditions at the fluid capillary interface are given in Figure 3.26. Solution method will be exactly the same as given in Section 3.2.2. Due to boundary conditions, since there is no angular dependence value of m given in the general solution in Equation 3.68 will be zero. In this case, the radial solution will be the Bessel function of the zeroth order (J_0). Since $k_l > k$ always, there will not be any subsonic regime which requires other types of solutions like the modified Bessel functions. Continuing to follow the same steps given in Section 3.2.2, we find the pressure inside the

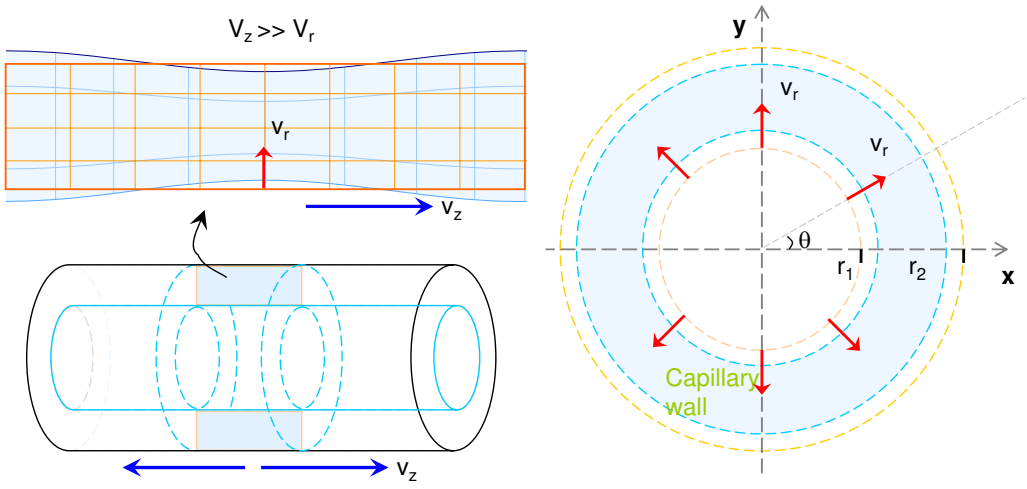

Figure 3.26: During the longitudinal motion of the capillary, due to the Poisson effect a slight motion in the transverse radial directions also occurs. These normal displacements modify the acoustic pressure distribution inside the cavity and generate periodic plane waves with the periodicity of the longitudinal capillary modes.

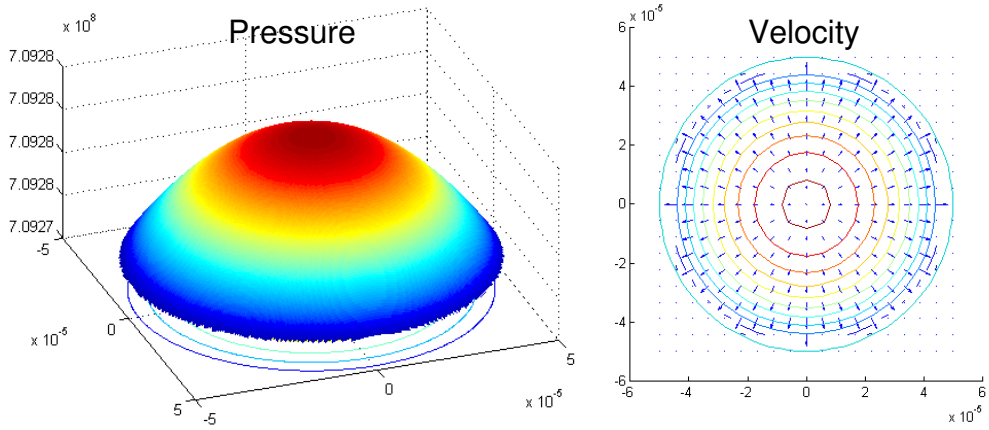

Figure 3.27: Radial pressure and velocity distribution inside the cavity due to longitudinal vibration of the capillary is plotted. Due to the radially symmetric boundary conditions no angular dependence is present. Radial variation of the pressure from the capillary walls to the center of the capillary is one part in ten thousand. In this case, it is possible to conclude that all pressure variation happens along the capillary in the z direction.

capillary due to longitudinal waves on the capillary as

$$p(r,\theta,z,t) = -\frac{jv_0ck\rho}{k_rJ_0'(k_rr_1)}\left(\frac{k\nu(r_2-r_1)}{2(1-\nu)}\right)J_0(k_rr)\cos(k_bz)\ e^{j\omega t}\ . \tag{3.90}$$

The radial pressure distribution is plotted in Figure 3.27.

Since the k_rr_2 value is low, radial variation of acoustic pressure will be reasonably small. In this case, most of the pressure variation will be in the z axis. From this, we can conclude that pressure waves will be in the form of plane waves as given in the top sketch of Figure 3.2, with small radial dependence. Please note that periodicity in z will follow the periodicity of longitudinal waves of the capillary, not the periodicity of plane waves in fluid. However, if there is a mode coincidence at a given frequency, observation of superposition of two plane waves with different wavelengths is expected.

CHAPTER 4

FINITE ELEMENT MODELING OF THE ACTUATOR

Introduction

In this chapter, Finite Element Modeling (FEM) of the actuator is presented. The complexity of the problem is diminished in terms of dividing problem into sections. Here, results of a modal analysis for the fluid filled capillary clamped from the ends are presented. Vibrational modes, displacement variations and pressure distribution inside the capillary due to structural vibrations are congruent with the results of theoretical analysis given in Chapters 2 and 3.

4.1 Finite Element Modeling

Introduction to FEM

While we developed an analytical model of the capillary actuator in the previous chapter, computer simulations help further to analyze and improve the actuator design and performance. Especially in such a case where many different components are gathered and with relating vibration and acoustics at the microscale, it is not possible to generate a comprehensive analytical model. One of the major and most powerful tools to fill this gap in engineering research is finite element modeling. Here, we have a complex system having piezoelectric material serving as the source of actuation, capillary structure for amplification of the vibration and acoustic cavity and the fluid sample enclosed in this capillary cavity. In our

model, we also need to consider solid fluid boundary conditions and interactions. For the FEM we particularly used the ANSYS^{TM} multiphysics edition.

The modal analysis of the fluid filled capillary is investigated to extract possible harmonics of vibration modes in the given frequency range. During the analysis, fluid filled and empty capillary cases are also compared.

As the capillary geometry is cylindrical and some of the vibrational modes are expected to be axis antisymmetric, modeling have been done in 3D. In order to make the results meaningful, element sizes after meshing kept to be much smaller than $1/10^{th}$ of the shortest wavelength possible. In fact, element size-wavelength ratio becomes the limiting factor for higher frequency simulations; one possible solution to this would be to simulate a smaller portion of the actuator for higher frequencies.

4.1.1 Simulation of the Capillary/PZT Device

In this part, details and results of finite element modeling of the capillary will be given. For the capillary, only the part which is clamped between the PZT plate is modeled. As shown in Figure 4.1, the capillary is clamped to the PZT plate from two points, which will be the end locations of the modeled part of the capillary. Boundary conditions for the end locations are taken to be clamped so that first and second order derivatives of displacement with respect to the central axis is zero. The length of the capillary is 11 mm, and the inner and outer diameter are taken as 50μm and 100μm. For the simulations, in which fluid enclosed in the capillary is also included, static pressure values at the end openings are taken to be zero so that any pressure variation inside the capillary related to alternating

motion of the capillary will be centered around zero value.

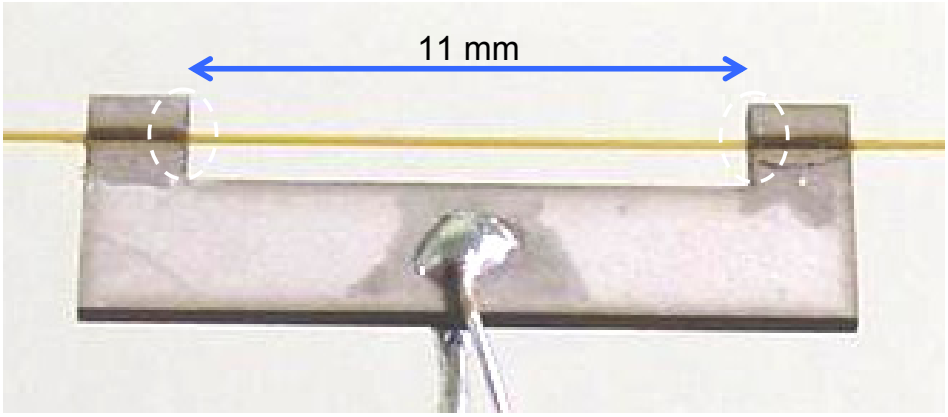

Figure 4.1: Part of the capillary clamped between the PZT is modeled. For the boundary conditions, as seen in the dashed circles clamped-clamped case would be the best option.

For the modeling of the capillary part in ANSYS, Solid45 element has been chosen, which is used in 3D modeling of solid structures. The cubic structure of the element enables 8 nodes each having 3 degrees of freedom for translations in 3D. Solid45 element encompasses critical capabilities such as large deflection, plasticity and large strain. Out of the many output capabilities that the Solid45 element has, we are most interested in displacement, stress, strain and pressure load on the surfaces and the capillary structure. Figure 4.2 shows the end of the meshed capillary structure.

For the modeling of the fluid part, we are interested in acoustic properties. Fluid30 element is used for acoustic modeling and fluid structure interaction problems. Fluid structure interaction is modeled by the coupling of the acoustic pressure of the fluid with the structural motion at the interface. The Fluid30 element has 8 nodes, each having 4 degrees of freedom; 3 translation and 1 pressure. The key output variables in which we are interested are pressure and pressure gradient.

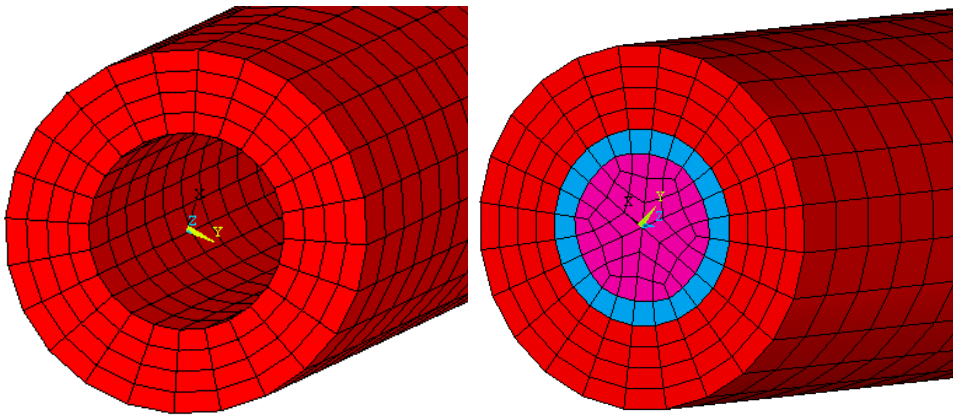

Figure 4.2: The end section of the meshed capillary is shown for the empty and fluid filled capillary. Red elements (Solid45) represent the capillary structure, the pink and blue elements represent the fluid (Fluid30). The layer colored with blue shows the fluid elements which enable coupling at fluid structure interface.

More information about elements used in the simulations can be found in ANSYS Reference Manual [55]. As mentioned in the Coupled Field Analysis Guide in the ANSYS manual [55], fluid structure interface (FSI) loads are specified on the fluid elements. In Figure 4.2, blue colored fluid elements next to solid boundary indicates the fluid structure interaction regime.

After meshing, the total number of elements modeled is 55440. Simulation is run in the frequency range 10-700 kHz. Modal analysis is done in order to obtain the resonance modes of the capillary actuator.

4.1.1.1 Simulation Results

In this section, individual vibration types and influence of these vibrations on the capillary structure will be mentioned. As expected in the theory part, modal analysis of the capillary in ANSYS showed the existence of eigenmodes in the form

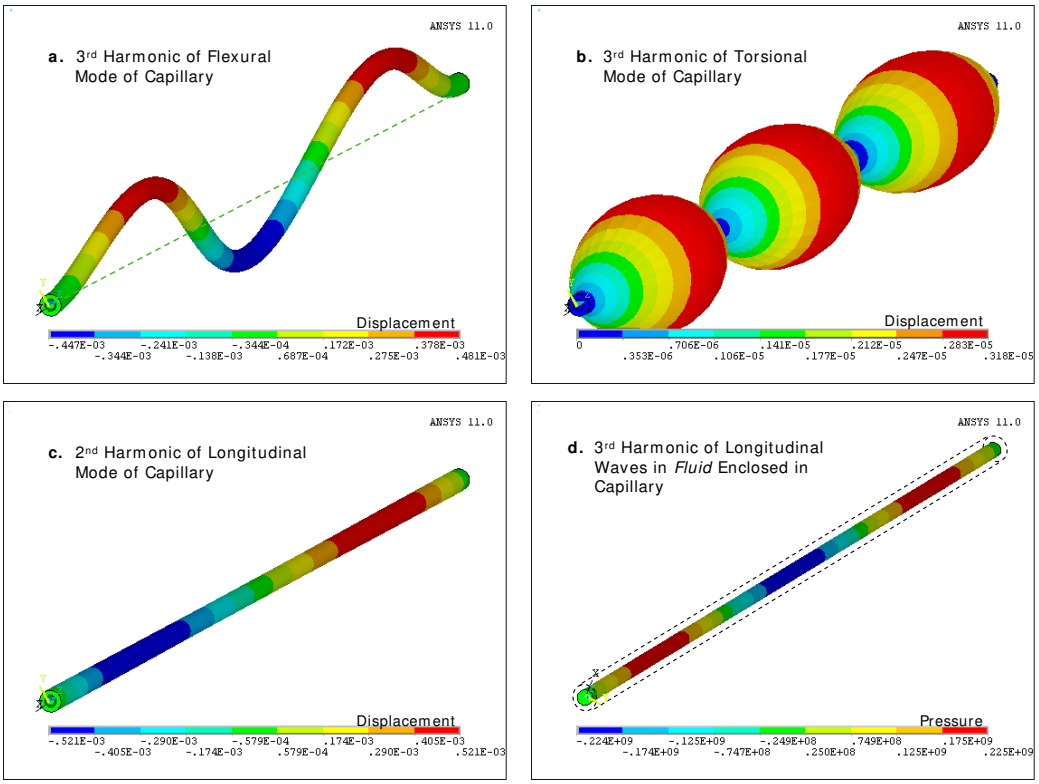

Figure 4.3: Types of vibrational modes are listed as follows: a) 3rd flexural mode, b) 3rd torsional mode, c) 2nd Longitudinal mode of capillary, d) Internal pressure variation for the 3rd mode of standing longitudinal waves in enclosed fluid. In figures a, b, c, the mode shapes are color coded to show displacement as they are the vibrational modes of the capillary. In figure d however, the color code shows the pressure variation, as this case is not a fundamental vibrational mode of the capillary and imaginary lines show the capillary.

of flexural vibrations, torsional vibrations, longitudinal vibrations of the capillary and longitudinal modes of the fluid enclosed inside the capillary. A sample harmonic from each set of different vibrational modes is shown in Figure 4.3. Each vibration type has specific effects on the pressure variation inside the capillary. In the following sections, we will investigate details of a sample harmonic from each vibration type.

ANSYS FSI elements approach acoustic problems related to the normal displacement of the boundary. This is why only the first order variation of pressure due to these vibrations are analyzed. Nonlinear acoustic effects such as acoustic and boundary layer streaming effects due to tangential and axial displacements are not calculated. However, tangential and axial velocities calculated in this analysis will be the guide in Chapter 5 calculating the streaming effects for various vibrational modes.

Figure 4.4 shows the dispersion curves for the vibrational and cavity modes of the actuator. As expected from the theory, only the flexural mode shows dispersive behavior. In the next sections, results obtained from ANSYS simulations will be compared with the theoretical and experimental values.

4.1.2 Cavity Modes:

Plane Waves in Fluid Enclosed in the Capillary

As mentioned in section 3.1.2, the capillary acts as a waveguide or cavity for propagating waves within the enclosed fluid. Out of various possible guided modes, only longitudinal waves can propagate inside the capillary in the given frequency range. All other modes exist at frequencies higher than the cut off frequency and the lowest value is found to be 8.26 MHz in Section 3.1.2. Depending on the boundary conditions, the capillary may act as a cavity and in this case longitudinal waves form resonance modes in terms of standing waves inside the capillary. Pressure variation only happens in the axis parallel to the capillary (z direction in cylindrical coordinates). It is completely uniform through the radius of the fluid volume and does not have any angular dependence. Pressure variation for the 3rd

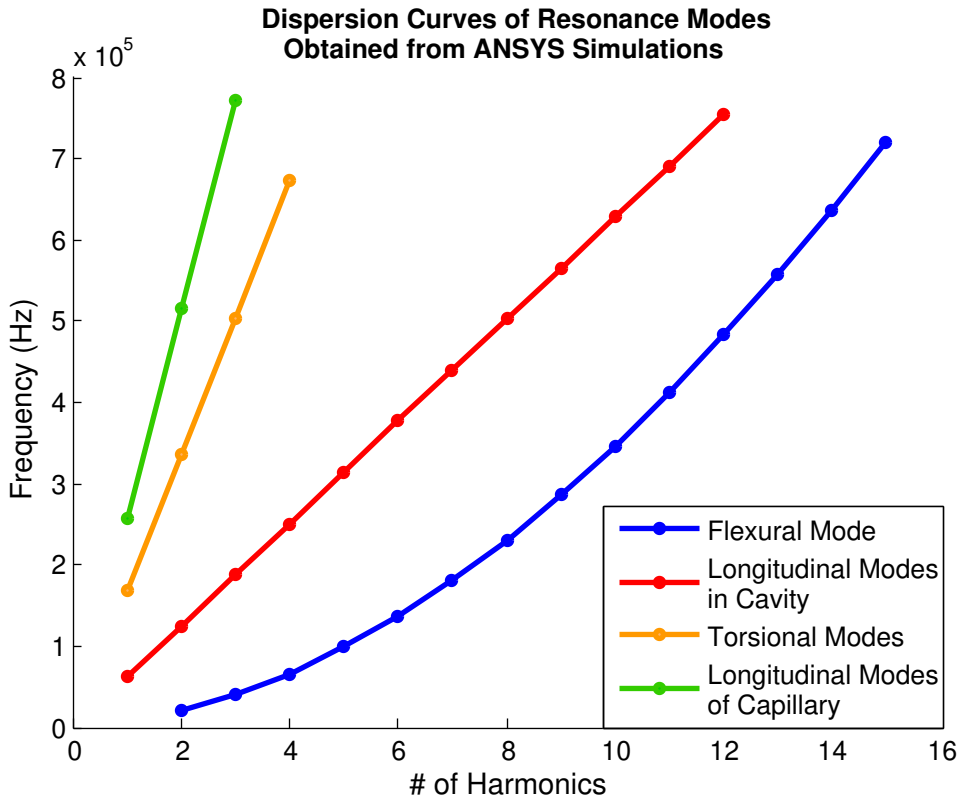

Figure 4.4: Dispersion curves for each mode are shown. As expected from the theory part, only the flexural mode is dispersive.

harmonic mode is plotted in Figure 4.1.2.

The dispersion relationship for this mode is presented in Figure 4.4. In the 1-800 kHz frequency range, we have about 12 harmonic modes and it can be seen that frequency is linearly dependent on the harmonic mode number. Since, for standing waves, half of the wavelength has to be a multiple of the cavity length, the slope of the dispersion relation could be used to find the speed of acoustic pressure waves in the cavity by the formula,

$$slope = \frac{f_n - f'_n}{n - n'} = \frac{c}{2l} \tag{4.1}$$

where f_n is the frequency of n^{th} mode, l is the length of the cavity and c is the

speed of the wave. From this relationship and simulation results, speed of acoustic waves in this case is found to be 1380 m/s. In the simulation parameters speed of sound in water in bulk was 1460 m/s. This 5% difference is due to the decrease of speed of sound in narrow channels. This effect was already mentioned in Section 3.1.1.1, and a 5% decrease found from simulation results matches well with the 5% decrease suggested from the analytical methods.

Frequencies of harmonics of this mode strongly depend on the length of the fluid column. In experiments, it is possible to control the length of the capillary end locations and structural vibrations of the capillary. However, the end locations of the fluid column inside the capillary are not as controllable. In this case, for the longitudinal pressure waves, a shift in the resonance frequencies from one experiment to another is unavoidable.

4.1.3 Longitudinal Vibrations of the Capillary

In the case of longitudinal vibrations, the entire crossectional area of the capillary moves back and forth only in an axis parallel to the center of the capillary. Figure 4.6 shows the 2^{nd} harmonic of the longitudinal mode at 514 kHz. Due to the Poisson effect, a minimal displacement in radial direction also exists. As shown in Section 3.3, the amount of radial displacement is two orders of magnitude lower than the displacement along the central axis. Displacements in z, x, and y directions are plotted in Figure 4.6. As predicted from theory, it can be seen from the figures that displacements in x and y directions (u_x,u_y) are almost 3 orders of magnitude smaller than the displacement in z direction (u_z). Variation of u_z is a function of sine as expected from theory. In this case, radial displacement is expected to be a cosine, from Equation 3.88. Displacement in y direction, (u_y), seems to be a

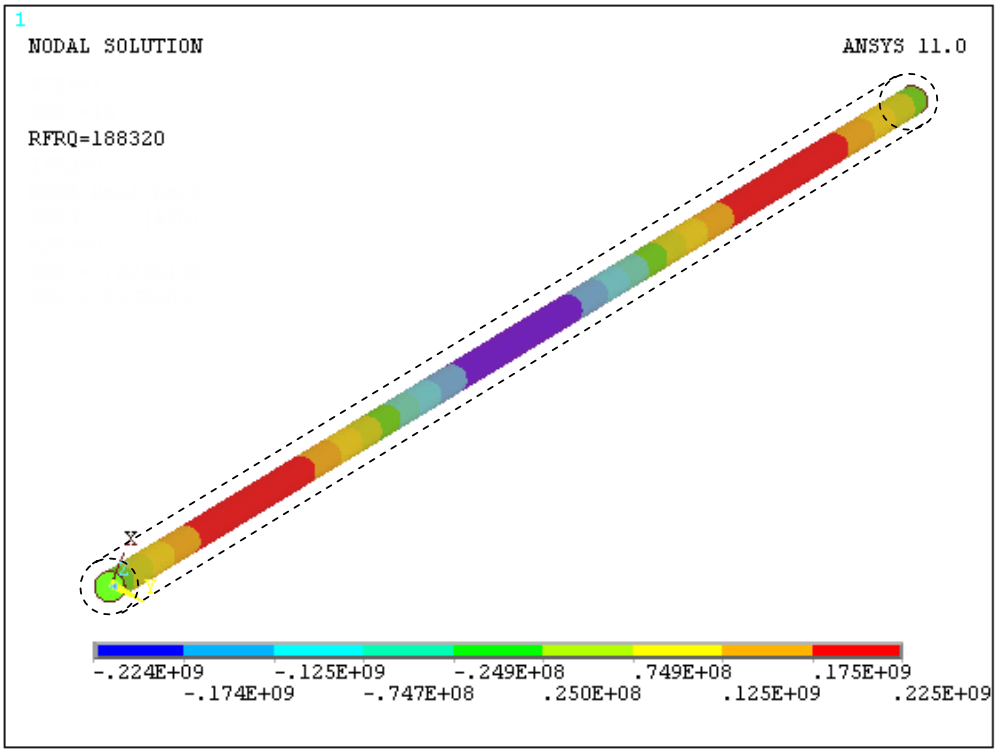

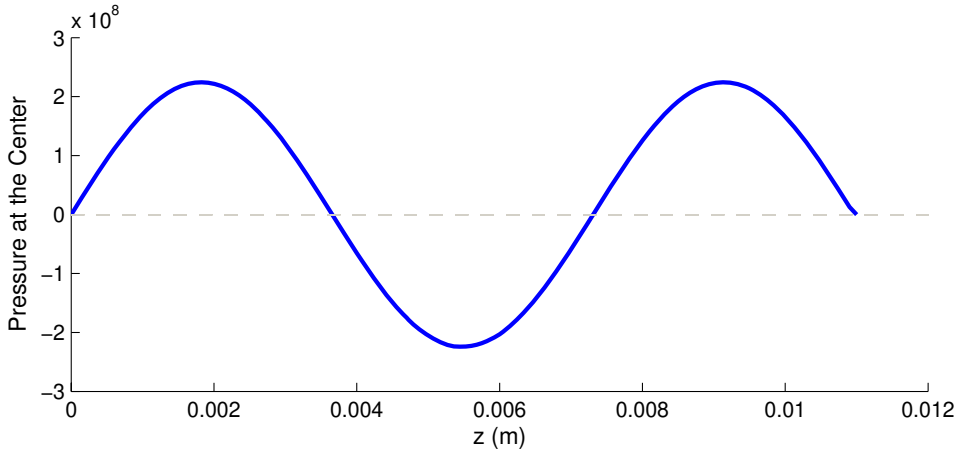

Figure 4.5: Top: 3rd harmonic of longitudinal pressure waves inside the capillary plotted in 3D. Bottom: Pressure variation along z axis is plotted for the same mode.

function of cosine; however, the completely unrelated behavior of u_x needs further investigation and explanation.

The wave number of u_x is 5, however this plots are for the second longitudinal

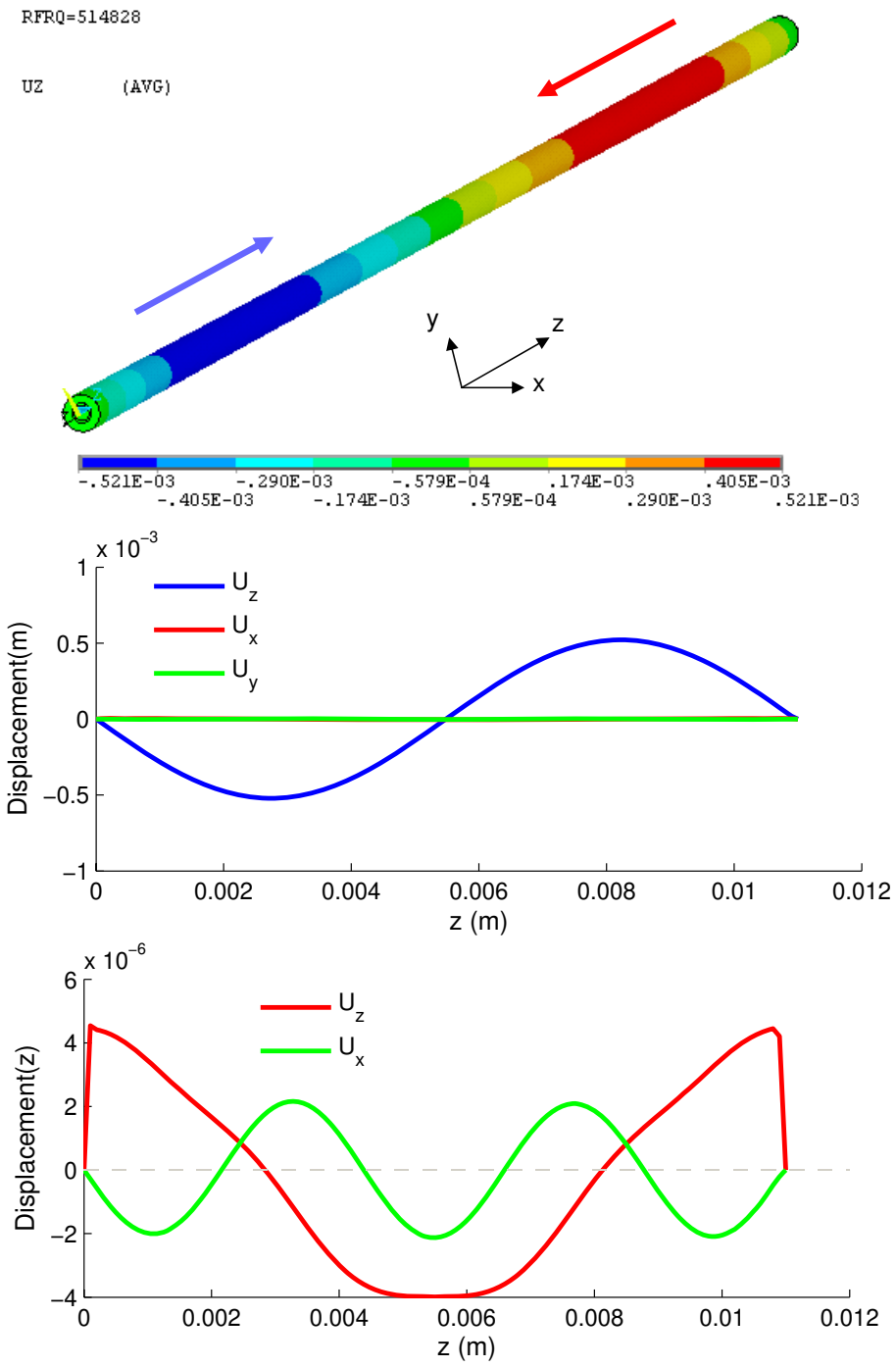

Figure 4.6: 2nd Longitudinal mode of the capillary is shown on top. Displacements on the top of the capillary are plotted. Radial u_y and tangential u_x displacements are 3 orders of magnitude lower than the axial displacement u_z

mode and there should be another wave coupled at this frequency.

One way to explain what happens here is if a particle follows a trajectory on a cylinder parallel to its axis, it just travels the length of the cylinder. However, when a slight angle is present, particle trajectory changes from a straight line to a helix around the cylinder. What happens here is that the particle will keep rotating around the cylinder however while its every turn, it will also proceed in z direction depending on the angle.

Waves work similarly. What we observe in Figure 4.7 is that, in z direction, the second mode of longitudinal mode is present. If we open the cylinder in an axis parallel to its circumference to be as a plate, we can extend the number of plates depending on the angle of the wave vector. Here we observe 5 modes in the circumferential direction. In this case, it means that wavelength in the circumferential direction is two circumferences $2\pi r'$, where r' is a value between r_2 and r_1, approximately. In this case, we expect the speed of waves in this direction to be approximately between 300-600 m/s. From Equation 2.37, we find this value is in the range of phase speed of flexural waves for a plate with a thickness around $(r_2 - r_1)$ at this frequency.

In short, as shown in Figure 4.7, this is a superposition of two different modes of vibration. Axial length (l) of the capillary is a multiple (2) of wavelength of longitudinal modes. And in the circumferential direction, we have the 5^{th} flexural "plate" mode from the beginning to the end of the capillary. It is important to note that displacements due to the helical flexural mode are 3 orders of magnitude lower than displacement variation in u_z, which is due to longitudinal mode.

In Figure 4.8, a comparison of dispersion relationship for the longitudinal mode

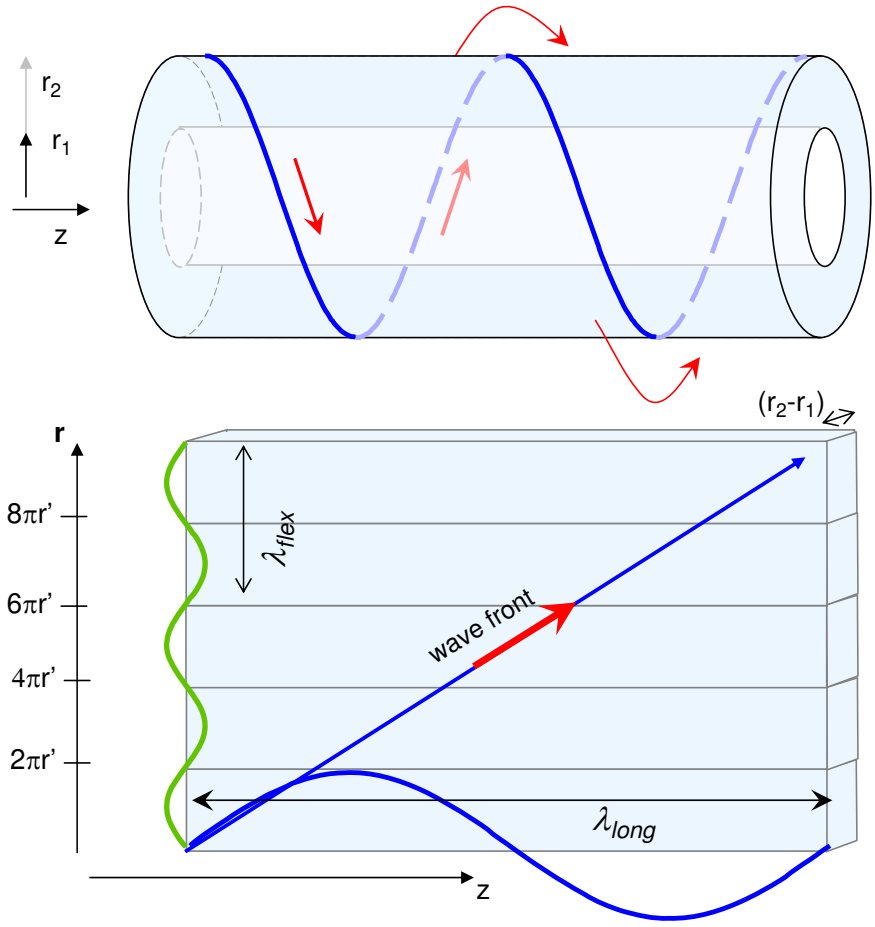

Figure 4.7: Assuming the cylinder thickness as a plate, circumferential modes also contribute to wave dynamics. Shifting of the wave vectors from the axial direction results in helical waves.

is presented for two different cases. One curve represents the empty capillary and the other represents the capillary filled with water. We observe almost no shift in the frequency values. This means that fluid loading is negligible in the case of longitudinal modes. This is expected since most of the displacements are in parallel to the fluid column enclosed, and fluid loading becomes effective in the case where normal displacements are dominant.

From the dispersion relationship sketched in Figure 4.8, it is possible to find

phase speed of the longitudinal waves on the capillary by using Equation 4.1, given in the previous section. The phase speed found from this dispersion relationship is 5664 m/s, which is less than 1% close to the theoretical expectation of 5648 m/s given in Equation 2.112 in Chapter 2.

4.1.3.1 Cavity Pressure due to Longitudinal Modes

It was mentioned in Section 3.3 of Chapter 3 that the acoustic pressure variation due to longitudinal vibrations only happen because of small transverse displacements due to the Poisson effect. In this case, acoustic pressure variation inside the cavity should follow the distribution of the radial (transverse) displacements in z, and that is why most of the periodic variation is expected in z direction, whereas radial variation of pressure inside the cavity can be neglected. Acoustic pressure distribution found from the FEM analysis is shown in the top graph of Figure 4.9. We observe no radial variation, as pressure distributions at the fluid-capillary boundary ($r = r_1$) and center of the cavity are indistinguishable from each other. However, distribution of pressure variation is different than the expected transverse displacement distributions given in the bottom graph of Figure 4.6.

If we take Fourier transform of this data, we observe that the pressure variation is a superposition of two distinct modes inside the cavity. As shown in the bottom graph of Figure 4.9, one mode (orange color) has a wave number of 2, matching the expected distribution from the longitudinal case and makes sense. The other mode is the natural acoustic pressure mode of the cavity. If one observes the dispersion graphs shown in Figure 4.4, around 500 kHz, there also exists the 8th harmonic of the cavity modes. Since two frequencies are close to each other, we observe two distinct modes are coupled to each other in a way to match the boundary

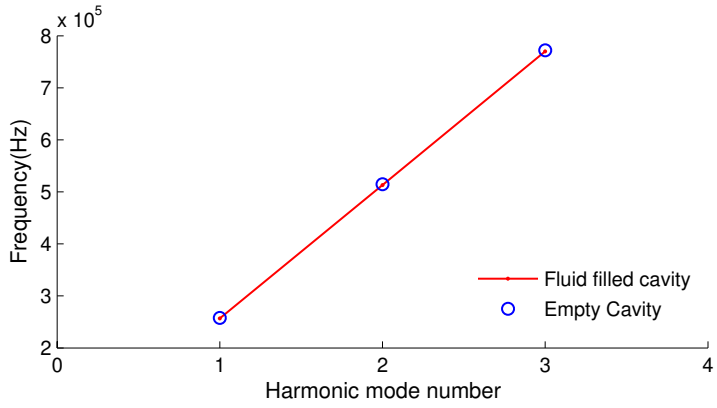

Figure 4.8: Longitudinal mode dispersion relationship. The presence of fluid inside the cavity does not cause any loading, so that the dispersion relationship is almost the same for the case of an empty cavity and a water filled cavity.

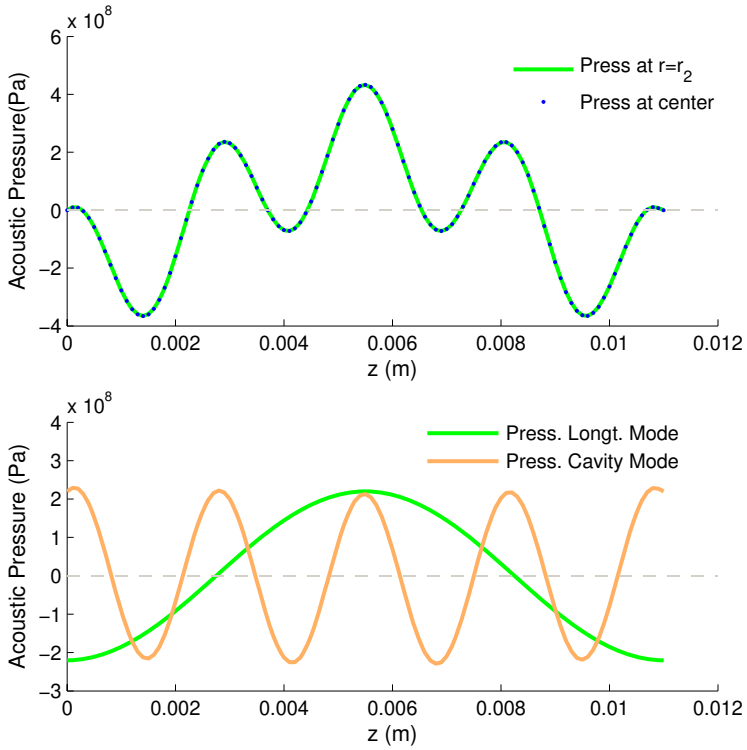

Figure 4.9: The figure on top shows that there is no radial variance of pressure, as expected. While a trend due to longitudinal mode in axial direction is present, superposition with another mode exists. The bottom figure shows the decomposition of two waves, which demonstrate the strong coupling of cavity modes due to close frequency values.

conditions (pressure of being zero at the ends). We would like to mention that since this is a modal simulation, we believe ANSYS makes a normalization so that pressure amplitudes are the same for the cavity mode and the longitudinal mode. This requires further analysis and can be done through running the simulation in harmonic analysis mode; however, locations for driving forces and amplitudes should be pre-defined.

As a verification of what is observed above, it is noteworthy to mention that while figures are not included here, in the experiments, the same coupling is observed in the first harmonic of the longitudinal mode. At that frequency (257 kHz), pressure variation due to the 1st harmonic of the longitudinal modes and 4^{th} harmonic of the cavity modes are coupled to each other.

4.1.4 Torsional Vibrations of the Capillary

In the case of torsional modes, the circular cross section of the capillary rotates back and forth. As a sample, 3rd flexural mode displacement around 500 kHz is shown in the top sketch of Figure 4.10. In this case, most of the displacement is in the tangential direction in the cylindrical coordinates. Displacements in tangential, radial, and axial (z) directions are plotted in Figure 4.10. Tangential displacement can be easily distinguished from radial and axial displacements. Under normal conditions for pure torsional mode, no radial or axial displacements are expected. However, in this case, while being low in amplitude compared to tangential, there are radial and axial displacements. These are, in fact, due to coupling of other modes and before further explaining these displacements, it may be helpful to look into pressure distribution inside the capillary.

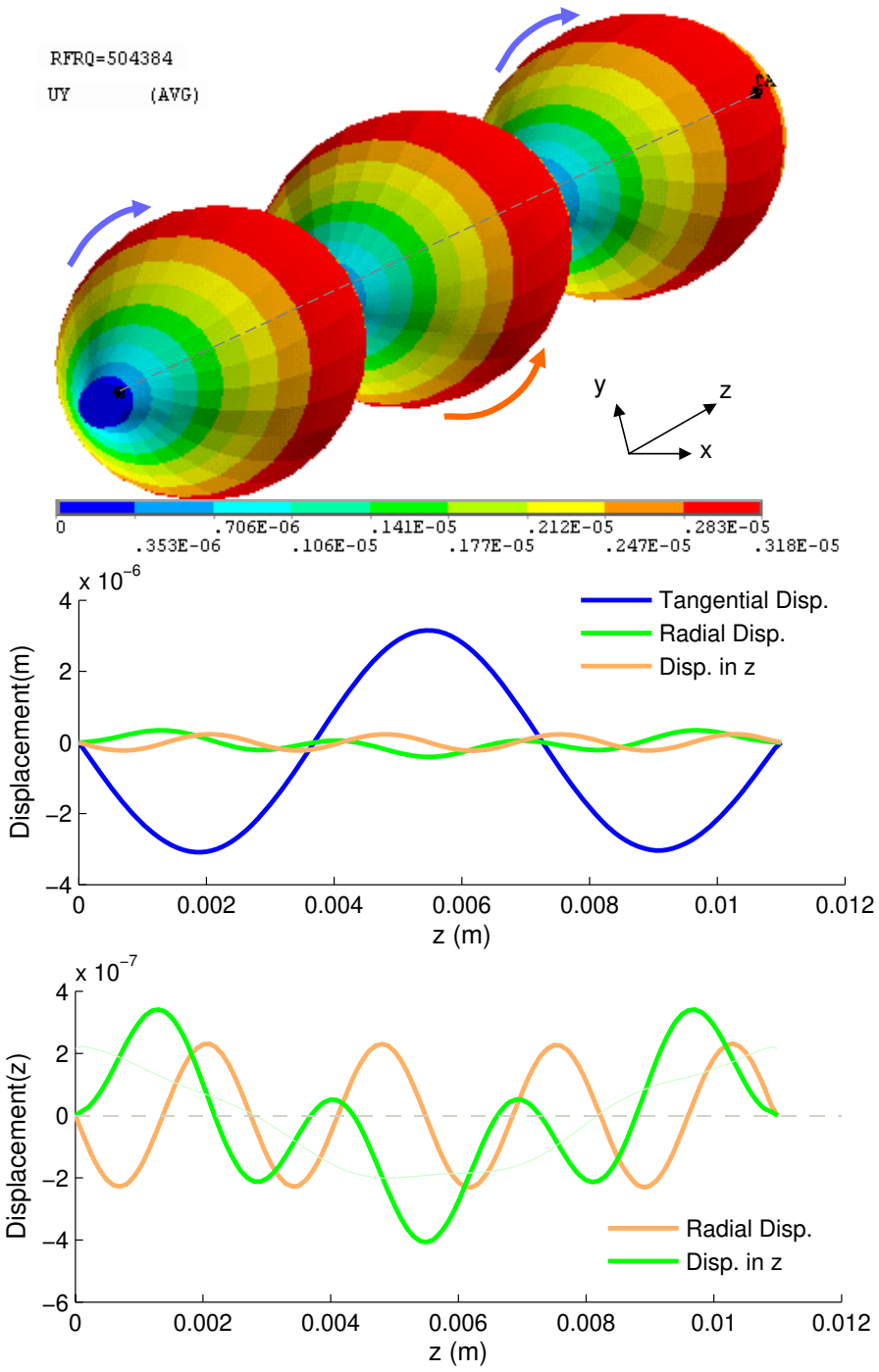

Figure 4.10: The tangential displacement distribution for the 3rd torsional mode of the capillary is shown on top. As expected, radial and axial displacements are much lower than the tangential displacements. Periodic radial displacement is due to the presence of 8th cavity pressure mode which has almost the same frequency.

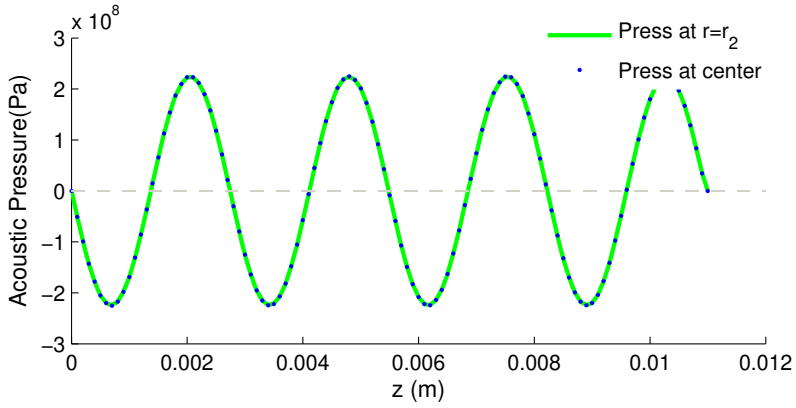

Figure 4.11: Variation of acoustic pressure inside the capillary around 500 kHz. Since most of the torsional displacement is tangential, no effect of the 3rd torsional mode can be observed. Pressure variation is due to the 8th cavity mode around 500 kHz.

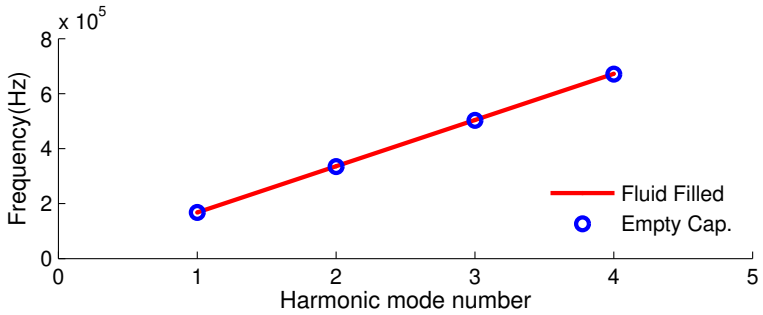

Figure 4.12: Dispersion relationship for the torsional modes. Presence of fluid inside the cavity does not cause any loading, so that the dispersion relationship is almost the same for the case of empty and water filled capillary.

Figure 4.11 shows the acoustic pressure distribution along the axial direction (z) inside the cavity. Two curves representing pressure distribution at the center and the fluid-capillary wall boundary are indistinguishable. As shown in Figure 4.4 around 500 kHz, the 8th harmonic of the cavity modes is also present. Since two distinct modes have very close frequencies, internal pressure is fully managed by the cavity mode. In this case, on the capillary, a radial displacement due to internal pressure variation might be expected; however, this will be really low and in reality

hard to observe. For the torsional mode, all displacements except the tangential one can be ignored. In addition, since there is no normal displacement present, there will not be any contribution of torsional modes to inside pressure variation. However, these modes have much to contribute through forming streaming vortices inside due to boundary layer streaming. This effect will be treated in detail in Chapter 5.

Similar to the previous section, for the empty and fluid filled capillary, dispersion relations for the torsional mode are plotted in Figure 4.12. Since presence of fluid does not cause any loading, there is no change in the dispersion curve. As mentioned in Section 2.4, restoring force for the torsional waves is the pure shear on the the circular cross section of the capillary and they are not dispersive. This is also confirmed by the FEM analysis. From the slope of the curve in Figure 4.12, by using the method given in Equation 4.1, we find the phase speed of shear waves to be 3698 m/s. This is less than 1% close to the value 3693 m/s, predicted by the formula given in Equation 2.100.

4.1.5 Flexural Vibrations of the Capillary

Flexural vibrations happen due to restoring of transverse, bending displacements by the stiffness of the structure. Of the all vibrational modes mentioned above, related to our case, flexural modes are the most important in terms of acoustic pressure variation inside the fluid. Flexural vibrations enable relatively high normal velocities, which contribute to generation of pressure variation. As an example, 3^{rd} flexural mode of the capillary structure is shown in Figure 4.13. As can be seen from the mode shape and the graph given below, displacement is mostly in y direction, normal to the z axis. Mode shape is identical to the theoretical

prediction given in Equation 2.47 in Chapter 2.

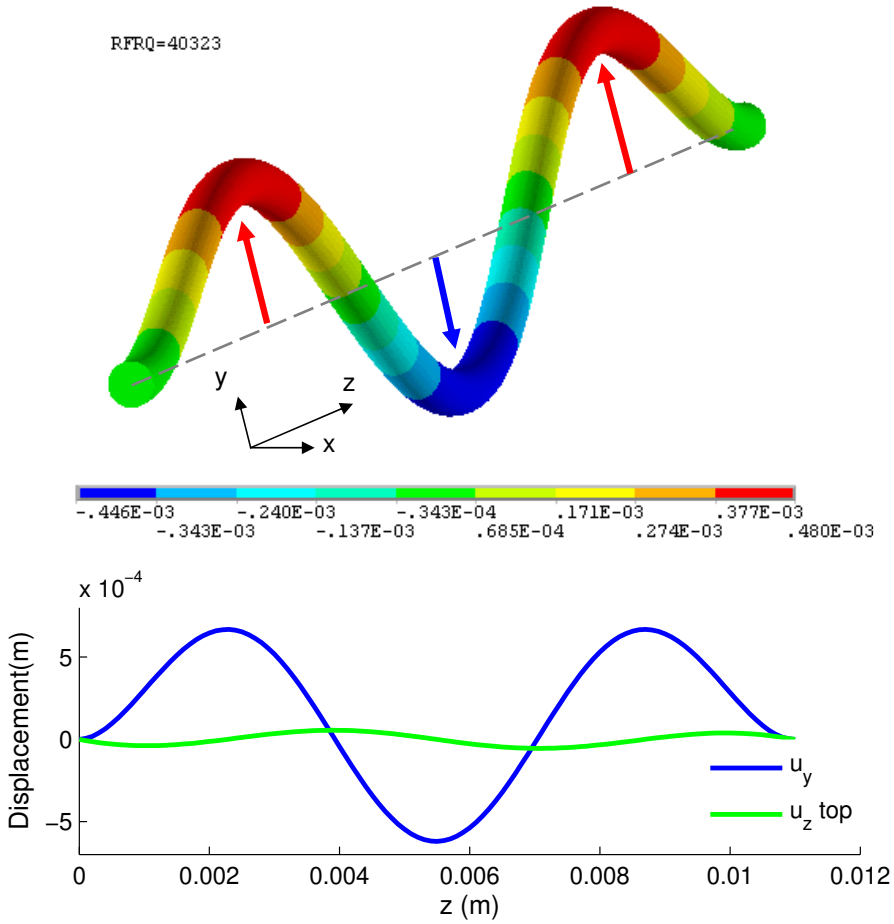

Figure 4.13: 3rd flexural mode of the capillary is shown on top. As expected, most of the displacement occurs in y axis. Since the capillary bends, some axial strain occurs symmetrically around the central axis. This strain causes displacement in axial direction which is related to the first derivative of the normal velocity.

In cartesian coordinates, the entire capillary circular cross section moves up and down in y axis. If the coordinate system is switched to the cylindrical coordinates, it will be seen that radial displacement will have angular dependence as shown in Figure 3.14 of Section 3.2.2.

During the displacement of the capillary in y direction, due to the stress distri-

bution, there will be a slight displacement (u_z) in z direction. This is shown by the green curve in Figure 4.13. However, since in the case of flexural waves, stresses in y direction are symmetric around the z axis, distribution will be reversed for the bottom half of the capillary.

Analytical approach: displacement in z direction due to displacements in y are given by

$$u_z = -r\phi \ . \tag{4.2}$$

In section 2.3.1, it was shown that[1]

$$\phi = \frac{\partial y}{\partial z} \tag{4.3}$$

for small displacements.

Writing u_y given in Equation 2.47, in cylindrical coordinates, we have

$$u_y(r,\theta,z) = A\Big(\frac{D_2}{D_4}(\cos\beta_n z - \cosh\beta_n z) + (\sin\beta_n z - \sinh\beta_n z)\Big)\sin\theta \tag{4.4}$$

where A is the amplitude and the relation between D_2 and D_4 is given by

$$\frac{D_2}{D_4} = -\frac{\sin\beta_n l - \sinh\beta_n l}{\cos\beta_n l - \cosh\beta_n l} \tag{4.5}$$

Combining all of the above, for u_z we find,

$$u_z(r,\theta,z) = A\beta_n r\Big(\frac{D_2}{D_4}(\sin\beta_n z + \sinh\beta_n z) + (\cos\beta_n z - \cosh\beta_n z)\Big)\sin\theta \tag{4.6}$$

where D_2/D_4 ratio is given by Equation 4.5. In this back of the envelope derivation we assumed a full cylinder; however, this is a hollow cylinder, which means that actual u_z will be slightly different than given above. By intuition, a 10-20% difference is expected.

[1] θ was used instead of ϕ in Section 2.3.1. Since θ is used as an axis of cylindrical coordinates here, ϕ represents the bending angle of the cylinder off the z axis.

In Figure 4.15, for normalized value of $A = 4.45\ 10^{-4}$m, we see that u_y given in Equation 4.4 exactly matches the shape of FEM result. By using the same amplitude in Equation 4.6, we find the expected displacement in z. Expected and simulation results are given in Figure 4.15. As mentioned above, there is an expected difference between simulated value and theoretical value for the whole cylinder. This difference matches the expectations due to the hollow core of the cylinder.

One important point regarding u_z is that u_z depends on θ. In cylindrical coordinates, at $\theta = \pi/2$, u_z gets its maximum value, becomes zero at $\theta = 0$ and $\theta = \pi$ and gets reversed between 0 and π. This is shown in Figure 4.14: while the top part of the capillary moves in one direction in z axis, the bottom part moves in the negative direction. So this tangential displacement distribution is different compared to the longitudinal displacements in z direction.

4.1.5.1 Dispersion of Flexural Modes

As mentioned in Section 2.3.2, flexural waves show dispersive behavior. At low frequency regime, phase velocity of the wave is related to the square root of the frequency. As shown in Figure 4.16, since most of the displacement is normal to the fluid-structure boundary, flexural waves are considerably influenced from fluid loading. In each cycle of upward and downward motion, the capillary has to move fluid enclosed with the same displacement amount. In this case fluid, acts as a mass load. While contributing to the load, since most fluids does not exhibit any shear or stiffness related restoring forces, the capillary remains single in terms of restoring any displacement happening off the axis. In Section 2.3.2.1, influence of the fluid loading was about a 7% decrease in the resonance frequencies. ANSYS

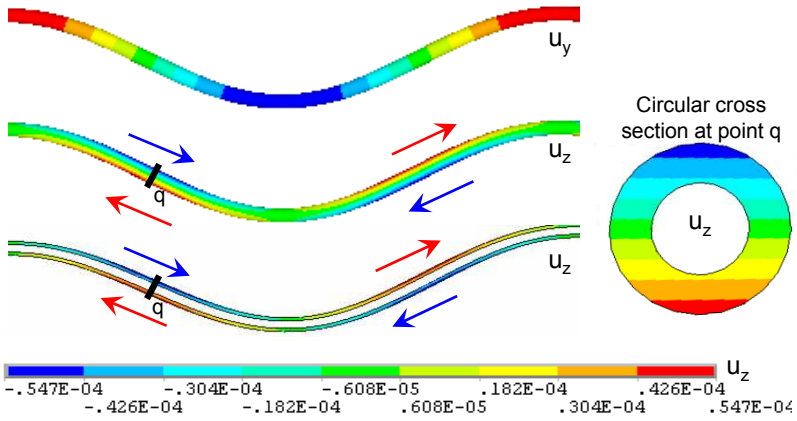

Figure 4.14: Normal (u_y) and axial (u_z) displacement distributions are compared. From the circular cross section, radial and angular dependence of the axial distribution can be seen.

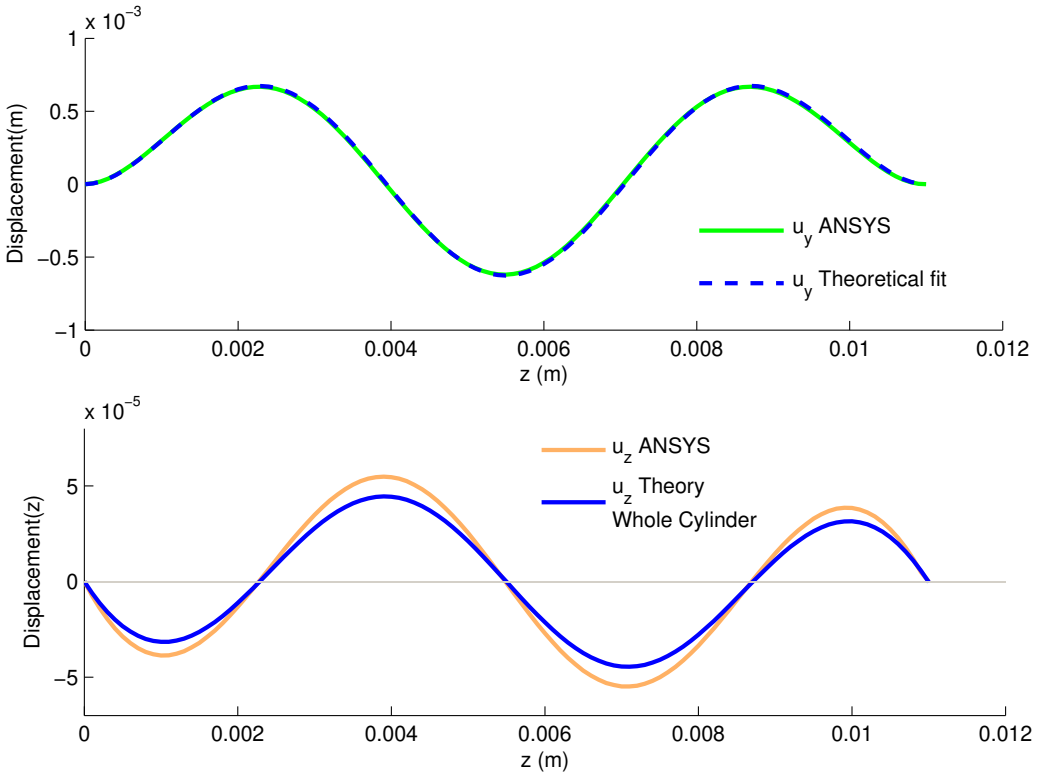

Figure 4.15: The top figure shows the exact matching of the mode shape calculated by ANSYS with the theoretical one given in Equation 2.47. Axial displacements calculated for the whole cylinder in Equation 4.6 show a similar trend to the ANSYS result for the hollow cylinder case.

FEM results plotted in Figure 4.16 show the similar reduction of frequency values about 8-10% in the case of fluid loading compared to empty cylinder.

In Figure 4.17, the dispersion curve obtained from FEM is compared with the theoretical value given in Equation 2.88 (without the 0.87 factor). Both results are in agreement with each other since both curves are in the 3% neighborhood of each other.

Figure 4.17 shows all dispersion relations obtained from ANSYS, theory and experiments. As mentioned before good agreement between ANSYS and theory is present. However, dispersion relation obtained from experiments have about 10% and 13% lower values than ANSYS and theoretical results respectively. There are couple of reasons for the mismatch. First of all, in theoretical analysis and simulations, boundary conditions in which the capillary is adhered to the PZT plate is assumed to be clamped through the all circular cross section. However, in experiments, this is not the case. The space between the PZT and the capillary is filled with thin adhesive material. Adhesive material fixes the capillary through the circumference, rather than through the cross section. In addition, most glue materials (including the 3M superglue we use) have very low modulus, which enables softness in the case of high frequency vibrations. Another parameter not included in theoretical analysis or FEM is that the capillary does not end at the point where it is attached to the PZT plate. As shown in Figure 4.1 after PZT, outside the resonating regime, capillary continues. The last item to be mentioned is the loading of air. In flexural motions, as fluid inside the capillary happens to be a mass load for the system, in a similar manner outside fluid which is air, is also a mass load for the capillary actuator. This should not be confused with damping. Damping reduces the amplitude of vibration; however, its effect on frequency

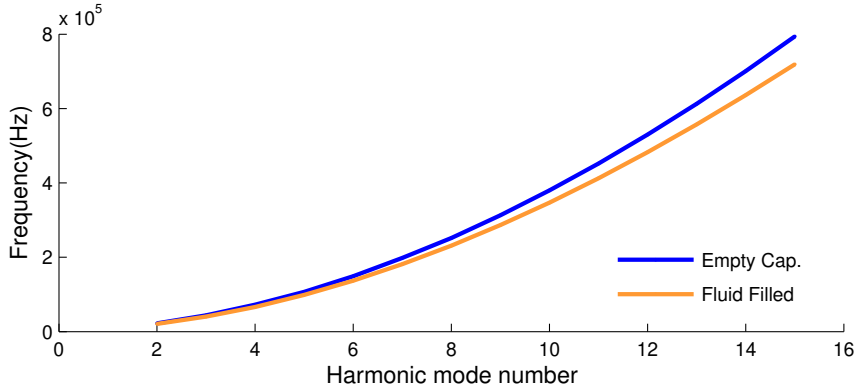

Figure 4.16: Comparison of dispersion curves for the fluid filled and empty capillary cases. Different than other vibrational modes, frequency values of flexural modes are significantly affected by the fluid loading.

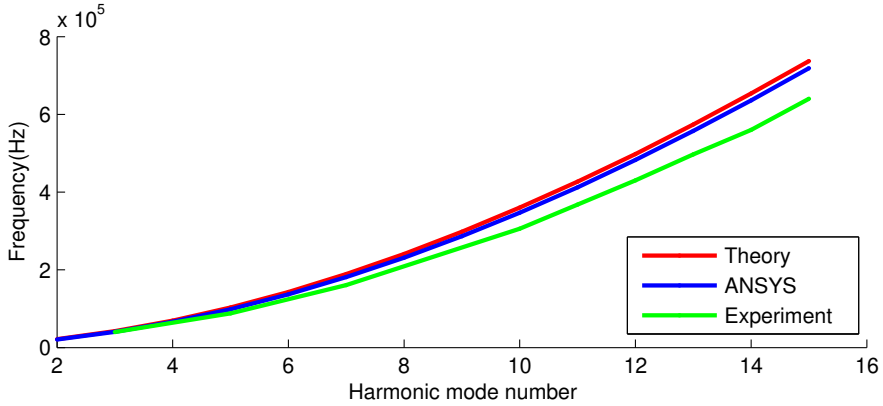

Figure 4.17: Comparison of the dispersion curves obtained by ANSYS, theory and experiments. ANSYS and theoretically expected results match very well. Frequency values obtained from experiments show about a 10% decrease due to neglected factors such as, softer boundary conditions and air loading from outside of the capillary.

values is not that high.

All these effects mentioned above contribute to lowering the resonance frequencies. Within these conditions, a 10-13% difference matches the reduction expected due to the factors mentioned above.

4.1.5.2 Acoustical Pressure Variation due to Flexural Modes

It was shown in Section 3.2 that flexural motions generate high normal displacements which generate pressure variations inside the cavity following the distribution of the normal displacements. Different from all other modes mentioned above in this chapter, pressure variation due to flexural motion not only exists in z direction but also in the radial direction. Axis anti-antisymmetric motion of the capillary generates alternating pressure variances in the radial direction. ANSYS results presented in Figure 4.18 shows the mode shape and the pressure variation of the fluid column. The fluid column is enclosed with the capillary (not shown here) having the same displacement. Pressure distribution plotted in cylindrical z and r axes is shown as the bottom graph of Figure 4.18. Distribution shown here matches the expected distribution from the theoretical approach given in Section 3.2.2.2.

Since energy distribution is related to the square of the velocity, similar to what we had done in Section 3.2.2.2, ANSYS also performs modal analysis with a constant velocity amplitude. From displacement results found by ANSYS we can find the normal velocities. From this, we can extract the velocity and pressure relationship. For 1 m/s normal velocity values, the theoretical and ANSYS simulation results for the frequency dependence of the internal pressure due to flexural waves are the same. This confirmation is plotted in Figure 4.19.

In summary, we have transverse acoustic pressure standing fields along the capillary, and variation in z axis follows exactly the variation of u_y. In the case of constant energy supply, amplitude of the pressure increases linearly with the frequency. ANSYS simulation results does not span the frequency regime where we observe change in this trend, as shown in Figure 3.19. This why Figure 4.19

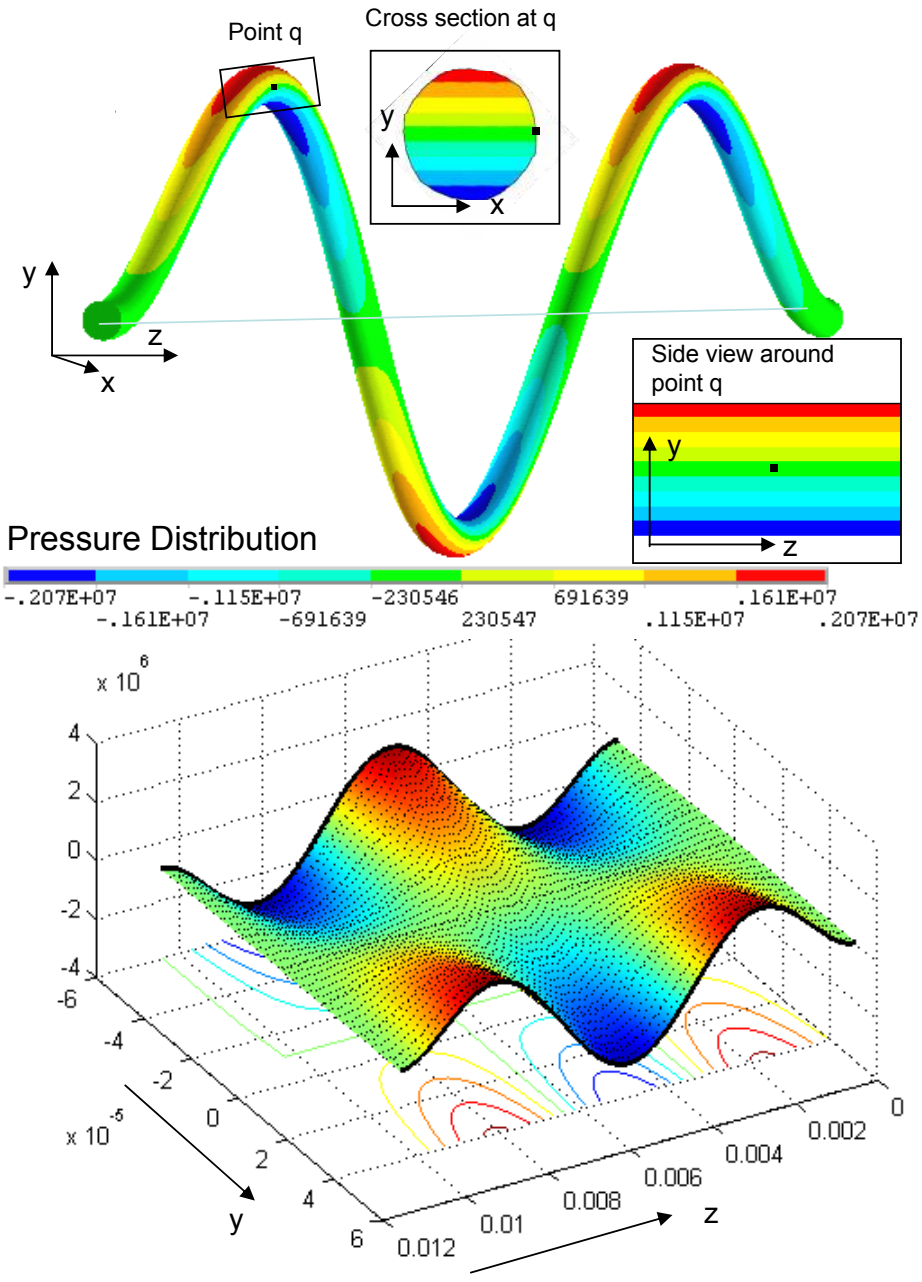

Figure 4.18: Pressure distribution along the fluid column is shown on the flexural mode shape. The enclosing capillary is not shown. Cross sectional views show the radial and angular pressure variation. In each oscillating cycle, variation of pressure changes sign, generating a radial standing wave mode. Distribution of the pressure in yz plane is the same as the theoretical distribution shown in Figure 3.21.

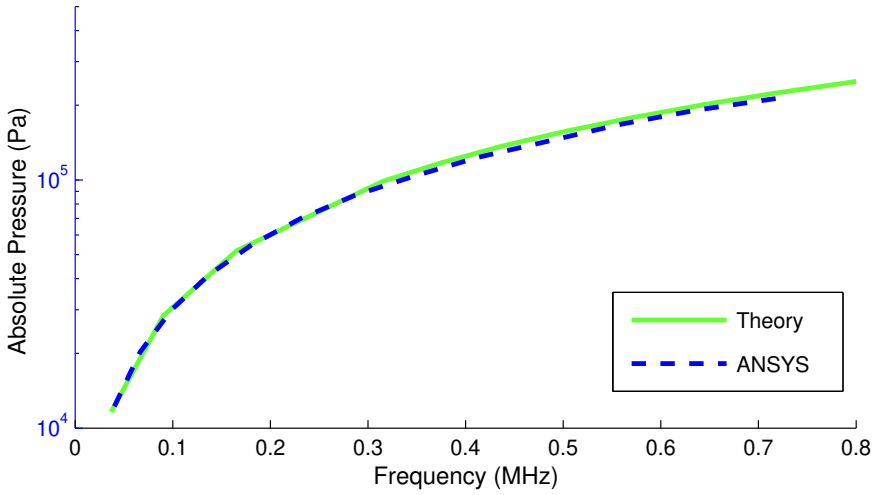

Figure 4.19: Variation of absolute pressure value with frequency. Theory and ANSYS results are the same for normal velocities taken to be 1m/s.

axes are left in linear scale rather than logarithmic scale.

CHAPTER 5

NONLINEAR ACOUSTIC INTERACTIONS INSIDE THE CYLINDRICAL CAPILLARY

Introduction

In this chapter, nonlinear acoustic interactions inside the capillary will be examined. Particularly, manipulation of micro and nanoparticles with the acoustic field generated by the flexural vibrations of the capillary gets the highest interest.

The first part discusses acoustic radiation forces in a acoustic field generated inside a microfluidic capillary due to the flexural motion of the capillary. Analytical results for forces are in excellent agreement with the experimental results.

The second part examines secondary forces which occur due to the inter-particle interactions in an acoustic field. It has been shown that, band formations observed in some experiments can be explained by the inter-particle secondary forces present in an acoustic field.

In the last part, acoustic streaming effects in a flexurally vibrating capillary are shown. While acoustic radiation forces are more influential in our experiments, streaming effects help particles or fluids to mix. In addition, in small particle limits, streaming effects influence the particle collection as the radiation force gets smaller.

5.1 Acoustic Radiation Forces on Micro and nanoparticles

5.1.1 Introduction: Acoustic Radiation Pressure

The concept of "acoustic radiation pressure" was first introduced by Lord Rayleigh, with the idea, similar to the electrodynamics waves, that acoustic waves should also exhibit a nonzero average pressure on the medium. While this effect had been verified experimentally for long time, various researchers came up with different analytical explanations of the phenomenon. In [56] Robert Beyer gave a review of four different approaches to the topic. These can be listed as Eularian radiation pressure, Lagrangian radiation pressure, Rayleigh's radiation pressure and Langevin's radiation pressure. A quote from the abstract of the article summarizes the complexity of the topic:

> It might be said that radiation pressure is a phenomenon that the observer thinks he understands -for short intervals, and only everynow and then.

Another quote from the conclusion part of the same article is a good indicator of the long-run debate over the topic:

> "It takes nerve as well as ability to criticize Lord Rayleigh successfully, and Brillouin had both. But as we have seen even a Brillouin can make a *faux pas*. On the other hand so can I, and so can any of you. I've already made plenty on my part; now it's someone else's turn."

There exist a couple of reasons for the different results available in the literature. First of all, since this effect is completely non-linear, approaches in Eulerian and

Lagrangian coordinates give different results. In addition, unfortunately, not everyone's understanding of "acoustic radiation pressure" is the same. For instance, in the case of Rayleigh and Langevin, physical understandings of the concept are different. Rayleigh defines acoustic radiation pressure as the difference between the mean pressure at the neighborhood of the reflecting or absorbing structure and the ambient pressure present in the fluid, whereas Langevin takes the unperturbed pressure on the other side of the structure as the reference ambient pressure.

A comprehensive review of the topic can be found in references [57, 58, 59, 60, 61]; curious readers may refer to these references. In this section, focus is given to the force on the particles due to the acoustic radiation pressure. In this case, using the Eulerian approach would be meaningful and a brief derivation of the radiation pressure is introduced.

5.1.1.1 Acoustic Radiation Stress Tensor

From Newton's second law, momentum is conserved for a sample fluid volume. For an arbitrary volume equation governing momentum, conservation can be written in tensor notation as,

$$\rho\Big(\frac{\partial v_i}{\partial t} + v_j\frac{\partial v_i}{\partial x_j}\Big) = -\frac{\partial P}{\partial x_i} \tag{5.1}$$

where v_i is the i component of the fluid particle velocity, ρ is the density and P is the net pressure and is given by

$$P = P_0 + p \tag{5.2}$$

where P_0 is the ambient pressure and p is the acoustic pressure.

Since the mass is also conserved, the continuity equation can be written as,

$$\frac{\partial \rho}{\partial t} + \frac{\partial(\rho v_i)}{\partial x_j} = 0\ . \tag{5.3}$$

Multiplying the continuity equation with v_i and combining with the momentum equation, they give;

$$\frac{\partial(\rho v_i)}{\partial t} + \frac{\partial(\rho v_j v_i)}{\partial x_j} = -\frac{\partial P}{\partial x_i} \ . \tag{5.4}$$

Taking the time average over a cycle leads to

$$\frac{\partial\langle\rho v_j v_i\rangle}{\partial x_j} + \frac{\partial\langle P\rangle}{\partial x_i} = 0 \tag{5.5}$$

which can also be written as

$$\frac{\partial}{\partial x_j}\Big(\langle\rho v_j v_i\rangle + \langle P\rangle\delta_{ij}\Big) = 0 \ . \tag{5.6}$$

Since

$$\frac{P_0}{\partial x_j} = 0 \ , \tag{5.7}$$

Equation 5.6 can be written as,

$$\frac{\partial}{\partial x_j}\Big(\langle\rho v_j v_i\rangle + \langle P - P_0\rangle\delta_{ij}\Big) = 0 \ . \tag{5.8}$$

Focusing the items inside the parentheses a new term is introduced:

$$S_{ij} = -\langle\rho v_i v_j\rangle - \langle P - P_0\rangle\delta_{ij} \ . \tag{5.9}$$

S_{ij} is called the acoustic radiation stress tensor and was first derived by Brillouin in 1938. Since the change in the density over a cycle is zero,

$$\langle\rho\rangle = \langle\rho_0 + \rho(t)\rangle = \rho_0 \ . \tag{5.10}$$

Then the final expression for S_{ij} becomes

$$S_{ij} = -\langle P - P_0\rangle\delta_{ij} - \rho_0\langle v_i v_j\rangle \tag{5.11}$$

where the quantity $\langle P - P_0\rangle$ is called the mean excess pressure.

5.1.1.2 Mean Excess Pressure

In the first order approximation, mean excess pressure becomes zero, however the inclusion of second order terms reveals non zero terms. Here the second order approximation to the mean excess pressure in Eularian coordinates will be included due to its relevance. Original derivation can be found in [62].

The first assumption is that fluid is taken to be nonviscous. In this case, all effects of sound will be irrotational which makes the curl of a possible velocity potential always zero. This results in $\mathbf{v} = \vec{\nabla}\phi$ where ϕ is the velocity potential. Plugging the above identity into Equation 5.1, the momentum equation becomes,

$$\vec{\nabla}\Big[\frac{\partial\phi}{\partial t} + \frac{1}{2}|\vec{\nabla}\phi|^2\Big] = -\frac{\vec{\nabla}P}{\rho} \ . \tag{5.12}$$

Change in the enthalpy per unit mass, dw, as a function of change in the entropy, ds, and change in the pressure, dP, can be written as,

$$dw = Tds + \frac{1}{\rho}dP \tag{5.13}$$

where T is the temperature. For an adiabatic process, change in the entropy is zero. This reduces the enthalpy change to

$$dw = \frac{1}{\rho}dP \tag{5.14}$$

which can be written in generalized coordinates as

$$\vec{\nabla}w = \frac{1}{\rho}\vec{\nabla}P \ . \tag{5.15}$$

Equating the above equation with the Equation 5.12, enthalpy becomes formulated as a function of velocity potential,

$$w = -\frac{\partial\phi}{\partial t} - \frac{1}{2}|\vec{\nabla}\phi|^2 + C' \tag{5.16}$$

where C' is a constant.[1]

Taylor expansion of the pressure as a function of the enthalpy at constant entropy and equilibrium can be written as,

$$P = P_0 + \Big(\frac{\partial P}{\partial w}\Big)_s w + \frac{1}{2}\Big(\frac{\partial^2 P}{\partial w^2}\Big)_s w^2 + \cdots \tag{5.17}$$

where partial terms in parentheses needs to be found. From Equation 5.13, at constant entropy $ds = 0$, we get,

$$\frac{\partial P}{\partial w} = \rho \tag{5.18}$$

and

$$\Big(\frac{\partial^2 P}{\partial w^2}\Big)_s = \Big(\frac{\partial}{\partial w}\Big(\frac{\partial P}{\partial w}\Big)\Big)_s = \Big(\frac{\partial \rho}{\partial w}\Big)_s = \Big(\frac{\partial \rho}{\partial P}\Big)_s \Big(\frac{\partial P}{\partial w}\Big)_s = \rho\Big(\frac{\partial \rho}{\partial P}\Big)_s. \tag{5.19}$$

Newton derived the speed of sound relating pressure variance of a gaseous compressible medium to the change in the density; the fundamental result he found for small acoustic amplitudes was,

$$c^2 = \frac{\partial \rho}{\partial P}\ . \tag{5.20}$$

Using this fundamental formula, we find

$$\Big(\frac{\partial^2 P}{\partial w^2}\Big)_s = \frac{\rho}{c^2}\ . \tag{5.21}$$

Plugging the values found in Equations 5.18 and 5.21 into the Taylor expansion given in Equation 5.17 leads to,

$$P = P_0 + \rho_0\Big(-\frac{\partial \phi}{\partial t} - \frac{1}{2}|\vec{\nabla}\phi|^2 + C'\Big) + \frac{1}{2}\frac{\rho}{c^2}\Big(-\frac{\partial \phi}{\partial t} - \frac{1}{2}|\vec{\nabla}\phi|^2 + C'\Big)^2 + \cdots \tag{5.22}$$

where C' is a second order quantity and becomes zero for linear acoustics. Since time average of first order terms give zero, only second order terms are the point of

[1] From the derivation it can be concluded C' is constant of spacial distribution. However, it may be a function of time.

interest. Combining all second order terms, mean excess pressure takes the form,

$$\langle P - P_0 \rangle = \frac{1}{2}\frac{\rho_0}{c_0^2}\left\langle \left(\frac{\partial \phi}{\partial t}\right)^2 \right\rangle - \frac{1}{2}\rho_0 \langle |\vec{\nabla}\phi|^2 \rangle + C \tag{5.23}$$

where C is defined as, $C = \rho_0 \langle C' \rangle$. Since $(\vec{\nabla}\phi = \mathbf{v})$ and $(\partial\phi/\partial t = -p/\rho_0)$, mean excess pressure in Eulerian coordinates can be written as,

$$\langle P - P_0 \rangle = \underbrace{\frac{1}{2\rho_0 c_0^2}\langle p^2 \rangle}_{\langle U \rangle} - \underbrace{\frac{1}{2}\rho_0 \langle \mathbf{v} \cdot \mathbf{v} \rangle}_{\langle K \rangle} + C \tag{5.24}$$

$$= \langle U \rangle - \langle K \rangle + C \tag{5.25}$$

where U and K are the potential and kinetic energy densities respectively.

5.1.2 Acoustic Radiation Forces on a Particle

When an object is placed in an acoustic field, the wave field is modified depending on the size of the object. As shown in Figure 5.1, if the size of the particle is larger than the wavelength ($kr \gg 1$), then the particle significantly scatters the wave incident on it. In addition, depending on the elastic properties, the object may generate some acoustic radiation due to its vibrations excited by the absorbed acoustic energy from the present ambient radiation. If the particle size is comparable to the wavelength ($kr \sim 1$), then diffraction is expected in addition to the radiation due to the vibrations generated by the absorbed energy. If the particle size is much smaller than the wavelength ($kr \ll 1$), then the scattering is very small, but it is large enough to generate a small decaying field in its neighborhood. At this scale, contribution of the compressibility of the particle will be smaller compared to the large cases. Here, these definitions are made on a single particle. Modification of the sound field under many particles case will be obviously different.

Interaction of particles with the acoustic field was first studied by Kundt [63].

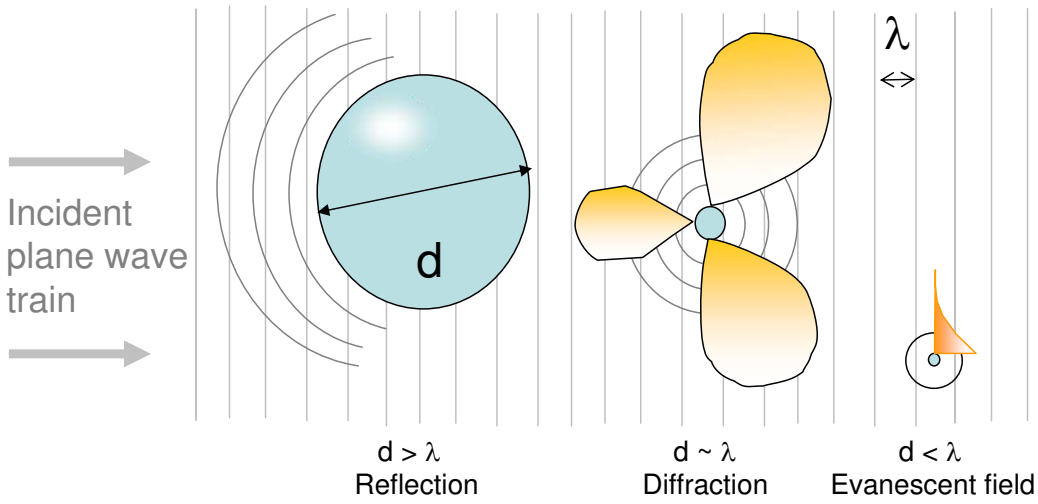

Figure 5.1: Effect of the particle size on the pressure field. Large particles act as reflectors, particles having sizes comparable to wavelength of the acoustic waves cause diffraction, and small particle generate an evanescent field

Kundt studied displacement of randomly dispersed sand particles inside a tube with the acoustic field generated inside the tube. In his experiments, he found that sand particles tend to collect where the standing acoustic pressure distribution has minima. From the measurement of the periodicity of the sand collections,[2] he successfully calculated speed of sound in different materials.

5.1.2.1 Non-compressible Spherical Particle in a Gaseous Medium

Compared to the theoretical models proposed on the general case of acoustic radiation pressure, there is less debate on the resulting forces of acoustic radiation pressure on a spherical particle. First, the theoretical explanation of the acoustic radiation forces on a small particle was presented by King [64] in 1934. In his paper,

[2]In a Kundt's tub experiment while a major collection at nodal points is observed, fine striations also occur when the acoustic field is present. Those fine striations are not related to the acoustic radiation force but is related to the streaming effects.

King studied solid and liquid particles in a gaseous medium. Since compressibility of liquids and solids are very low compared to the gases, in his analysis he took the particles as rigid and not compressible. Assuming the presence of a known acoustic pressure field incident on the particle, a secondary acoustic field due to the scattering from the particle can be obtained from the boundary condition that the fluid particle velocity at the rigid particle surface will be zero (since particle is not compressible). In this case, total acoustic pressure around the particle can be calculated as a summation of these two acoustic fields. As the resulting acoustic pressure field around the particle is known, King calculated the force on the sphere by integrating the normal component of the radiation stress tensor given in Equation 5.11 over the surface S:

$$F_z = \int_S S_{ij} n_j dS \tag{5.26}$$

where S_{ij} is given by Equation 5.11 and mean excess pressure is given by Equation 5.24. Since the compressibility of the particles is ignored, normal velocity is zero. Then only the mean excess pressure contributes to the integral such that,

$$F_z = -\int_S \langle P - P_0 \rangle \cos\theta dS \tag{5.27}$$

where θ is the angle between the radial vector of spherical coordinates and z axis of cartesian coordinates. From the approach mentioned above, for a standing acoustic radiation field ($p_{i0} = A \sin kz$), King found the acoustic radiation force on the particle

$$F_z = -\frac{5\pi}{6} \frac{A^2 k R^3}{\rho_0 c_0^2} \sin 2kz \tag{5.28}$$

where A is the amplitude of acoustic radiation pressure, k is the wave vector and R is the particle radius. The force in this case is always towards the pressure nodes. At the nodal points, the force reduces to zero and around the nodal points, the force field acts as a spring force balancing the particles at the nodal point. For the

case of a progressive wave, the radiation force on the particle is

$$F_z = -\frac{11\pi}{8}\frac{A^2k^4R^6}{\rho_0 c_0^2}. \tag{5.29}$$

Force by the progressive waves is $(kR)^3$ times the force generated by the standing waves. Since $kR \ll 1$, the forces generated by the progressive waves are very low compared to the forces generated in a standing wave field.

Experimental verification of the theoretical force values calculated by King in 1934 are reported in 1977 [65] and 1981 [66].

5.1.2.2 Compressible Spherical Particle in a Liquid Medium

In a gaseous medium, compressibility of the particles compared to the medium can be easily ignored. However, in the case of a liquid or solid particles suspended in a in a liquid medium, compressibility of the particles and liquid medium has close values which fails the above assumption. In 1955, Yosioka et al. [67] generalized King's theory by including the compressibility of the particles. There were two main fundamental differences in their approach. First, the boundary condition at the medium-particle surface boundary changed. In King's theory, since the particles were not compressible, pressure was taken to be zero at the boundary; however, in the compressible case, this is not required and since the boundary can move because of the compressibility, normal particle velocity has to be continuous. The second update was the method of integration. Force field was calculated in terms of far field relations using the Gauss' theorem. In the compressible sphere case, since the normal velocity terms in the integral given in Equation 5.26 are non zero, the force calculated included terms related to the material properties of the material such as density and compressibility. Following the method summarized

above, the acoustic radiation force on a compressible spherical particle is found as

$$F_z = -f(\varrho,\sigma)\frac{\pi A^2 k R^3}{\rho_0 c_0^2}\sin 2kZ \tag{5.30}$$

where $f(\varrho,\sigma)$ is named as the acoustic contrast factor, and given by

$$f(\varrho,\sigma) = \Big[\Big(\frac{3\varrho-2}{3+6\varrho}\Big) - \frac{1}{3\varrho\sigma^2}\Big] \quad \text{where} \quad \varrho = \frac{\rho_1}{\rho_0} \quad \text{and} \quad \sigma = \frac{c_1}{c_0}\ . \tag{5.31}$$

Here ρ_1 and c_1 are the density of the particle and the speed of the sound in the particle. The first term of $f(\varrho,\sigma)$ in the square brackets is the contribution of the scattered pressure field from the particle in terms of a dipole radiation. This dipole radiation stems from the oscillatory motion of the particle along the incident field. The second term, however, is related to the monopole radiation which stems from the the compressibility of the particle. In the case of a gaseous medium, the above formula converges to King's formula.

While King's formula predicted radiation forces to be always towards the pressure nodes, Yosioka's formula the leaves decision to the sign of the acoustic contrast factor. In the above formula, $f(\varrho,\sigma)$ can be either negative or positive depending on the material properties of the particles and the medium. If $f(\varrho,\sigma)$ is positive, the forces are towards the pressure nodes, and if $f(\varrho,\sigma)$ is negative, then the forces are towards the antinodal locations. Figure 5.2 shows the $f(\varrho,\sigma)=0$ curve in the ϱ-σ plane. Materials which fall above the curve tend to collect at pressure nodes, and materials that fall below the curve tend to collect at antinodes.

In 1962, Gor'kov [68, 58] calculated the total potential energy for the particle in an acoustic radiation field in terms of the local incident pressure wave field such that,

$$U = 2\pi R^3\Big[\ \frac{f_1}{3\rho_0 c_0^2}\langle p^2\rangle - \frac{f_2\rho_0}{2}\langle \vec{v}\cdot\vec{v}\rangle\ \Big] \tag{5.32}$$

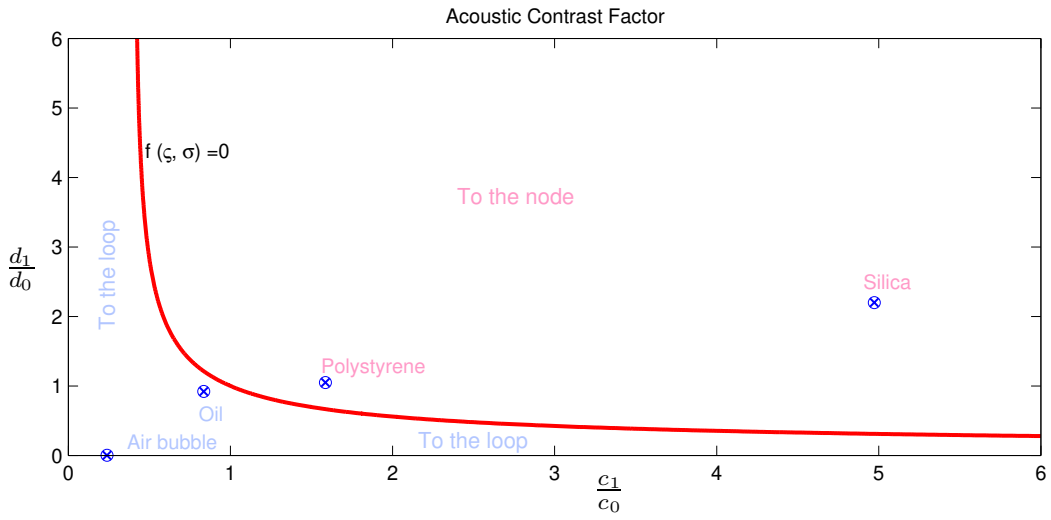

Figure 5.2: Particles that remain above the $f(\varrho, \sigma) = 0$ curve feel acoustic radiation force towards the acoustic pressure nodes, and on the other hand, materials of particles that remain below the curve feel the force towards at loops.

where

$$f_1 = 1 - \frac{\rho_0 c_0^2}{\rho_1 c_1^2} \quad \text{and} \quad f_2 = \frac{2(\rho_0 - \rho_1)}{2\rho_0 + \rho_1} \quad . \tag{5.33}$$

Once the potential energy for the particle is calculated through the above relationship, radiation forces can be found in 3 dimensions using the relationship,

$$\vec{F} = -\vec{\nabla} U \ . \tag{5.34}$$

For the conditions of Yosioka et al., forces calculated by the Gor'kov's method give very close values to Equation 5.30. The major advantage of the Gor'kov's approach is that, since it is a scalar quantity, it is easier to calculate potential energy, especially for 3-dimensional systems. And after potential energy is found, force can be calculated through the gradient in a particular direction.

5.1.3 Acoustic Radiation Forces on Particles in a Flexurally Vibrating Cylindrical Micro-Capillary

Gor'kov's formula method can be used to calculate radiation forces in a vibrating cylindrical capillary; however, distribution of the pressure field (p) inside and velocity components needs to be known. In Section 3.2.2 of Chapter 3, pressure distribution inside the capillary due to flexural vibrations of a micro-capillary was derived. Pressure generated for subharmonic frequency range was given by the relationship,

$$p(r,\theta,z,t) = -\frac{jv_0ck\rho_0}{I_1'(k_r'r_1)} I_1(k_r'r)\sin(k_bz)\sin\theta\ e^{j\omega t} \tag{5.35}$$

where v_0 is the normal velocity of the flexurally vibrating capillary, which can be measured by an interferometric scan of vibrating surface.

Velocity components of the fluid particles inside the capillary can be found from pressure distribution via the relationship,

$$\vec{v} = -\frac{1}{j\omega\rho_0}\vec{\nabla}p \tag{5.36}$$

where gradient in cylindrical coordinates is given by

$$\vec{\nabla} = \frac{\partial}{\partial r}\hat{r} + \frac{1}{r}\frac{\partial}{\partial\theta}\hat{\theta} + \frac{\partial}{\partial z}\hat{z}\ . \tag{5.37}$$

Then, velocity components in cylindrical coordinates are given by

$$v_r = \frac{v_0}{I_1'(k_r'r_1)}\ I_1'(k_r'r)\ \sin(k_bz)\ \sin\theta \tag{5.38}$$

$$v_\theta = \frac{v_0}{rI_1'(k_r'r_1)}\ I_1(k_r'r)\ \sin(k_bz)\ \cos\theta \tag{5.39}$$

$$v_r = \frac{v_0k_b}{I_1'(k_r'r_1)}\ I_1(k_r'r)\ \cos(k_bz)\ \sin\theta \tag{5.40}$$

where $I_1'(k_r'r)$ is the first derivative of $I_1(k_r'r)$ with respect to r.

In this case, $\langle \vec{v} \cdot \vec{v} \rangle$ is found to be[3]

$$\begin{aligned} \langle \vec{v} \cdot \vec{v} \rangle = \frac{1}{2} \frac{v_0^2}{\left(I_1'(k_r' r_1)\right)^2} \Bigg[& \Big(I_1'(k_r' r) \ \sin(k_b z) \ \sin\theta \Big)^2 \\ & + \Big(\frac{1}{r} \ I_1(k_r' r) \ \sin(k_b z) \ \cos\theta \Big)^2 \\ & + \Big(k_b \ I_1(k_r' r) \ \cos(k_b z) \ \sin\theta \Big)^2 \Bigg] . \end{aligned} \tag{5.41}$$

Plugging formulas given in Equations 5.38 and 5.41 in Equation 5.32, the radiation force potential on a particle suspended in a fluid column in the flexurally vibrating cylindrical capillary can be found as

$$\begin{aligned} U = \frac{\pi R^3 \rho_0 v_0^2}{\left(I_1'(k_r' r_1)\right)^2} \Bigg[& \frac{f_1}{3} \Big(k I_1(k_r' r) \sin(k_b z) \ \sin\theta \Big)^2 \\ & - \frac{f_2}{2} \Big[\Big(\ I_1'(k_r' r) \ \sin(k_b z) \ \sin\theta \Big)^2 \\ & + \Big(\ \frac{1}{r} \ I_1(k_r' r) \ \sin(k_b z) \ \cos\theta \Big)^2 \\ & + \Big(\ k_b I_1(k_r' r) \ \cos(k_b z) \ \sin\theta \Big)^2 \ \Big] \Bigg] \end{aligned} \tag{5.42}$$

where f_1 and f_2 were defined in Equation 5.33. Using the potential given above and Equation 5.34, it is possible to find force fields. In fact, for calculation and modeling purposes after the calculation of potential in 3D, force field in specific directions can be calculated numerically through the gradient of the potential field in a specific direction.

Acoustic radiation potential given in Equation 5.42 consists of 4 terms which –distinctly from each other– depend on the spatial location, various wave vectors (k_r', k_b, k), and material properties. If forces were calculated directly from this equation, three force equations in three dimensions would have still four distinct terms coming from the potential. In this case, to be able to conclude which terms

[3] $(\frac{1}{2})$ comes from the time averaging of the time dependent sine and cosine squared terms.

dominate at what direction and at a given frequency range, analysis of 16 surface plots per given mode would be necessary, which requires a lot of time and space. Since the potential equation is very long and does seem to be very practical, some meaningful approximations may increase its functionality. In section 3.2.2, it was shown that in the range of $-0.4 < k_r'r < 0.4$, $I_1(k_r'r)$ and $J_1(k_r'r)$ can be approximated as

$$I_1(k_r'r) = J_1(k_r'r) = \frac{k_r'r}{2} \quad \text{for} \quad -0.4 < k_r'r < 0.4 \tag{5.43}$$

and this was visually demonstrated in Figure 3.17. In this case, their derivatives become,

$$I_1'(k_r'r) = J_1'(k_r'r) = \frac{k_r'}{2} \quad \text{for} \quad -0.4 < k_r'r < 0.4 \tag{5.44}$$

For below 4 MHz frequency regime, it is always true that $-0.4 < k_r'r < 0.4$. Since in our case experiments are run in a 30kHz-2MHz range, the approximate values given above can be used safely. Calculations show that these approximations only contribute error in the order of 1%. Another benefit of these approximations is that, by this way, both subsonic and supersonic cases are governed with the same spatial function.

Replacing $I_1(k_r'r)$ and $I_1'(k_r'r)$ terms with their approximations given in Equations 5.43 and 5.44, radiation force potential becomes surprisingly independent of k_r' and much simpler:

$$\begin{aligned} U = \ \pi R^3 \rho_0 v_0^2 \Bigg[& \frac{f_1}{3}\Big(kr \sin(k_b z)\ \sin\theta\Big)^2 \\ & - \frac{f_2}{2}\Big[\ \Big(\sin(k_b z)\Big)^2 + \Big(k_b r\ \cos(k_b z)\ \sin\theta\Big)^2\ \Big]\Bigg] . \end{aligned} \tag{5.45}$$

The negative of the gradient in z direction gives F_z:

$$F_z = \ \pi R^3 \rho_0 v_0^2 k_b \sin(2k_b z)\left[\frac{f_2}{2} - (\sin\theta)^2\Big(\frac{f_1}{3}(kr)^2 + \frac{f_2}{2}(k_b r)^2\Big)\right] . \tag{5.46}$$

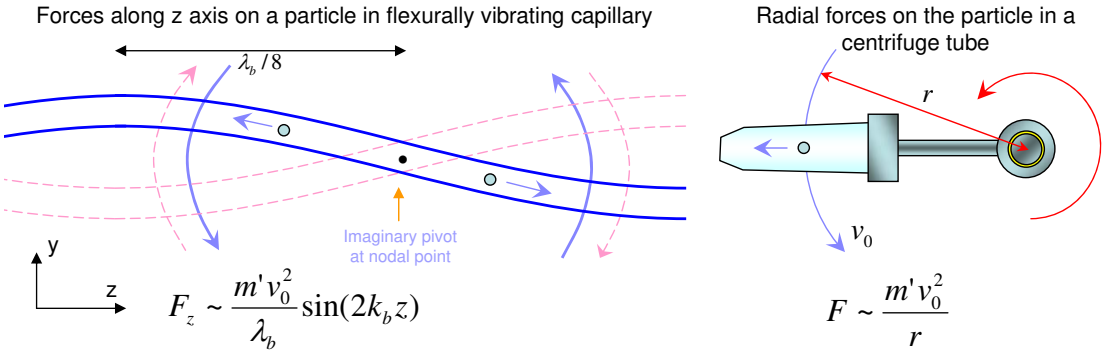

Figure 5.3: Similarity between the force on the particle in a traditional centrifugal setup, and the force on the particle in a capillary vibrating in a flexural mode. While in centrifugal setup tangential v_0 increases with radius, in a capillary case, variation of the v_0 is more complex and corrected by some sinusoidal terms.

Force in z direction, F_z, depends on many parameters; however a broad way of looking reveals that it is kind of analogous to the centrifugal force ($\frac{m' v_0^2}{r} \sim \frac{m' v_0^2}{\lambda_b}$ since $k_b = \frac{2\pi}{\lambda}$ and $f_2 \pi R^3 \rho_0 \sim m'$). A physical explanation would be as follows: as shown in Figure 5.3, during the flexural motion of the capillary, over a half cycle capillary segment rotates around a nodal point, and in the next cycle it rotates around the same point in the reverse direction. Here, having an imaginary pivot at a nodal point, v_y becomes a component of the tangential velocity with respect to this point. Since v_y is not constant but increasing over the half wavelength till the maximum point, particles suspended in this segment feel a kind of centrifugal field. Since the curvature decreases the increase in the v_y as a function of z, v_y does not linearly depend on the length of the wavelength i.e., radius in the centrifugal concept, in fact the sine term complements this factor. In this regard, acoustic actuator presented here works as a non-rotating, micro-centrifuge.

Having the gradient of Equation 5.45 in radial and tangential directions, forces

in these directions are found as,

$$F_r = 2\pi R^3 \rho_0 v_0^2 r \sin\theta \left[\frac{f_2}{2} (k_b \cos(k_b z))^2 - \frac{f_1}{3} (k \sin(k_b z))^2 \right] \sin\theta \quad (5.47)$$

$$F_\theta = \underbrace{2\pi R^3 \rho_0 v_0^2 r \sin\theta \left[\frac{f_2}{2} (k_b \cos(k_b z))^2 - \frac{f_1}{3} (k \sin(k_b z))^2 \right]}_{} \cos\theta \ . \quad (5.48)$$

It is easy to see that F_r and F_θ have the same terms until the sine and cosine of θ terms at the end. Combining these and the $rsin\theta = y$ relationship result elegantly in F_y and F_x in cartesian coordinates. Then we have

$$F_x = 0 \quad (5.49)$$

$$F_y = 2\pi R^3 \rho_0 v_0^2 y \left[\frac{f_2}{2} (k_b \cos(k_b z))^2 - \frac{f_1}{3} (k \sin(k_b z))^2 \right] \quad (5.50)$$

$$F_z = \pi R^3 \rho_0 v_0^2 k_b \sin(2k_b z) \left[\frac{f_2}{2} - \left(\frac{f_1}{3} (ky)^2 + \frac{f_2}{2} (k_b y)^2 \right) \right] \quad (5.51)$$

where y is the axis parallel to the flexural motion of the capillary and $y = 0$ is the radial center of the capillary.

Commenting on the final form of the forces, it can be noted that force on the particle depends on many parameters such as densities (f_1) and acoustical properties of the materials (f_2), frequency drive (k and k_b), vibrational velocity of the capillary (v_0) and the particle size ($\sim R^3$). Out of these parameters, particle size and the vibrational velocity draw more attention. An order of magnitude reduction in the particle volume decreases the net force a thousand times. Vibrational velocity of the capillary can be measured interferometrically and is related to the voltage drive of the PZT plate. In this case, an order of magnitude increase or decrease in the voltage drive causes the force field to change a hundred times.

Direction of the forces depend on the spatial location and material properties. In z direction, the first term in the square brackets is the dominating term since

kr and $k_b r$ terms are squared and less then 1. In this case f_2, which is the density relation given in Equation 5.33, defines the direction of the force. For particles denser than the liquid medium, force is attractive towards points where there exist a displacement-vibration maximum ($\sin 2k_b z = 0$). Due to the sinusoidal distribution, at these locations force field will behave as a spring holding particles in balance. When particles are in these locations, force will be zero. It is also true that F_z will gets its maximum value at the y=0 plane due to the $\sin\theta$ term. For the particles less dense with respect to the fluid, collection point will be the displacement nodes. For either case, along the z axis, force gets maximum in the exact middle location of the nodal and maximal displacement points. It is mathematically possible that at a specific frequency and material selection, terms in square brackets will cancel each other so that F_z becomes zero, independent of the spatial location. This situation needs to hold the condition,

$$f_2 = \frac{2f_1(kr)^2}{3(1-(k_b r)^2)} \ . \tag{5.52}$$

For silica particles in water, this equation can hold true around frequencies in the range of gigahertz, which is way above the frequency regime in which this actuator is driven.

For the force in y direction, the magnitude of F_y increases linearly in y direction, getting maximum at the boundaries and zero at the center where $y = 0$. Direction of the force field depends on the location of the z axis. For silica particles in water, for example, at locations $\sin(k_b z) = 0$, force acts as a spring causing particles to concentrate at the center, and at nodal points where $\cos(k_b z) = 0$, direction of the forces is away from the center.

The results in Equation 5.50 show $F_x = 0$. While F_x is expected to be orders of magnitude smaller compared to F_z and F_y, in reality a small value is expected due

to scattering from the collected particles. The net acoustic field will be modified so that there will be some interaction between the particles themselves and also the modified field. In experiments, it has been observed that particles tend to be collected in a plate-like platform, which reveals that forces in y direction are superior compared to forces in x direction.

Since the radiation potential and the force field values depend on material properties and specific frequency, plots of these values can only be done for specific conditions. To give a general idea, some examples will be shown in the next section.

It is observed that the forces in y and z directions are functions of the spatial location, and they become zero at the center of the capillary where also a maxima of the flexural vibration exists. In this case, as shown in Figure 5.4, radiation forces act as springs trying to hold particles in a balance. Taking the negative gradient of the force fields, spring constants in y and z directions at the center of the capillary ($y = 0$ and $z = n\lambda_b/2$) can be found as,

$$k_y = \frac{2}{3} f_1 \pi R^3 \rho_0 v_0^2 k \tag{5.53}$$

$$k_z = f_2 \pi R^3 \rho_0 v_0^2 k_b^2 \cos(2k_b z) \; . \tag{5.54}$$

It can be seen that while the spring constant in y direction is linear, the spring constant in z direction (k_z) is nonlinear and even gets negative values, for dense particles k_z becomes a real spring around a vibrational maxima pulling particles to the vibrational maxima center, and around vibrational nodal points, it acts as a negative spring pushing particles away.

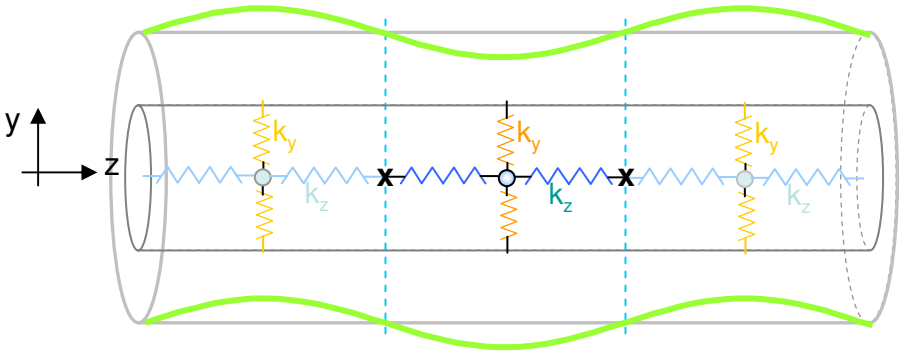

Figure 5.4: Forces about the center of the capillary and vibration maxima act as springs which hold particle at the prescribed locations in balance. Net force on the particles at the collection points is zero.

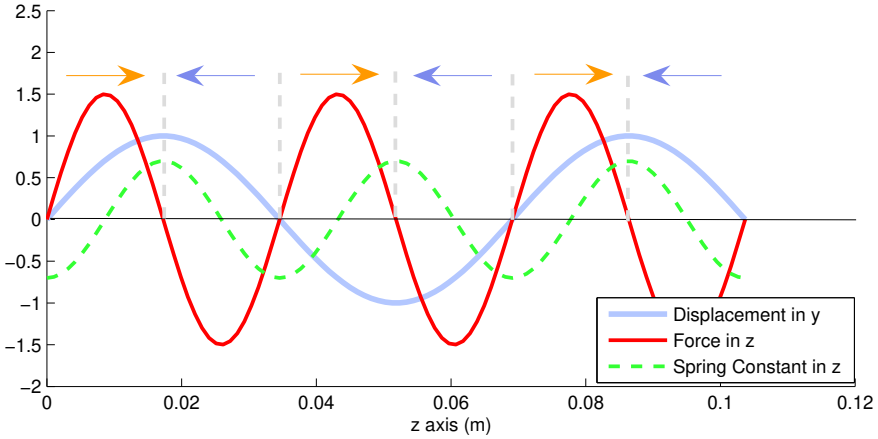

Figure 5.5: Force and spring constant in the z direction and the displacement of the capillary along the central axis. Forces on the particles get maximum in the middle of a displacement node and maxima. Arrows on top show the direction of the force on the particle in z axis. All magnitudes are arbitrary.

5.1.3.1 Acoustic Radiation Force Fields for Polystyrene Microbeads in Water

In this section, acoustic radiation potential and radiation forces will be shown for a 2 micrometer polystyrene bead suspended in water, which is enclosed in a silica capillary vibrating in one of its flexural modes. Results shown in this section

will be similar for other type of materials which are in the same category as the polystyrene with respect to the curve shown in Figure 5.2. The silica beads, most types of cells, most types of bacteria, metallic micro and nanoparticles all fall into this category. While the shape of the curves will be similar, magnitudes will be different due to the change in the density and the particle size of the sample.

The top schematic given in Figure 5.6 shows the 5^{th} flexural mode of the capillary vibrating up and down in y-z plane. Acoustic pressure field -due to the flexural motion- is also plotted along the channel. Part (b) of this figure shows the pressure distribution on the y-z plane for 3 half flexural wavelengths along the z direction. Part (c) shows the pressure variance at the cross sectional area shown in the schematic given in part (a). Part (d) is the surface plot of the acoustic radiation force potential obtained from the Equation 5.45. In this figure, most of the variation appears along the z axis; however, the reader should be reminded about the high aspect ratios ($y \ll z$). In this case, since the space in y direction is much shorter, at low frequencies where ($r_1 \ll \lambda_b$), some slight variation in y direction may lead to equivalent or even larger forces in magnitude in y direction compared to z direction. Part (e) shows the acoustic radiation force potential at the cross section of the capillary shown in part (a). Parts (f) and (g) of this figure show the quiver plots revealing the direction of the forces in the yz plane and the indicated cross section. In all graphs of this figure, locations marked with 'A' indicate the center of the capillary where there exist a flexural displacement maxima. Part (h) shows the microscope image of the collection of polystyrene particles inside the capillary vibrating in its 5^{th} flexural mode at 88.7 kHz and the computed force field (arrows). Location of the particle collection and motion of the particles towards the collection point are in excellent agreement with the force field derived analytically (arrows in the picture). At this particular frequency, for polystyrene

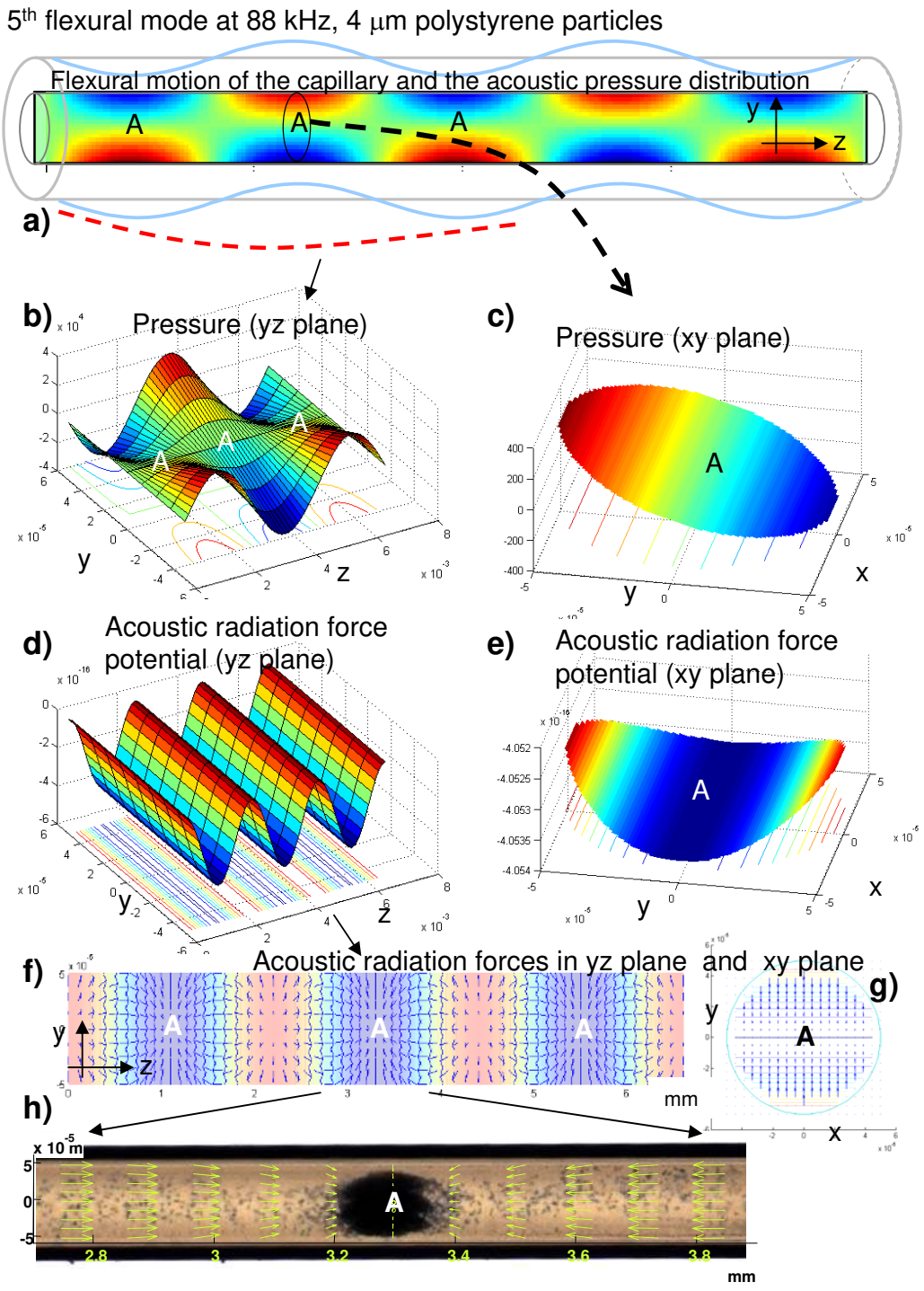

Figure 5.6: Acoustic pressure and radiation force potential distribution, and the acoustic radiation forces for the 5th flexural mode. For the explanation, see page 170 (Units: Pressure in Pascal; spatial coordinates in meters; and potential energy is Joules).

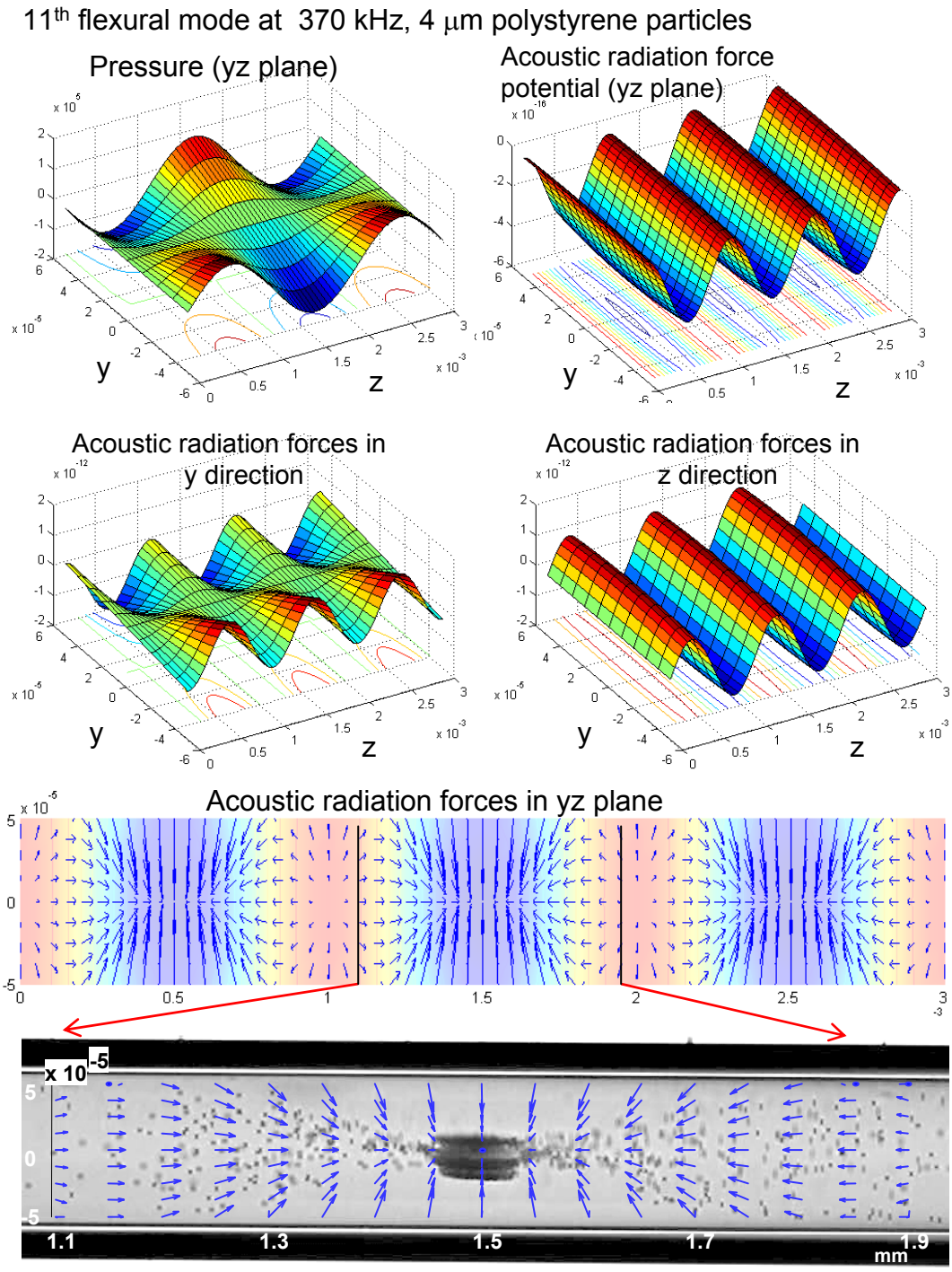

Figure 5.7: Acoustic pressure and radiation force potential distribution, and the acoustic radiation forces for the 11th flexural mode. For the explanation, see page 173 (Units: Pressure in Pascal; spatial coordinates in meters; Force in Newton; and potential energy is Joules).

beads suspended in water and at 1 m/s flexural vibration velocity, the maximum value of the force in y direction is 3×10^{-13}N and the maximum value of the force in z direction is 8×10^{-13}N. Both forces act as spring forces pulling particles to the collection spot. Force values in y and z directions reach zero at the collection spot, which means that once the particles are focused, force acting on them is close to zero. This is an important point for biological or other type of delicate samples. Forces act mainly during the collection process, which may take seconds to minutes depending on the sample, size and voltage drive.

Figure 5.7 shows details for the 11^{th} flexural mode. In this figure, surface plots for the acoustic radiation forces in y and z directions are also included. The major difference observed at this frequency is that maximum force in y direction and in z direction have the same value of 1×10^{-12}N. As shown in the microscope image of the particles while they moving to the collection spot, forces in y direction at the vibration maxima push all particles to the center. In other locations, particles still float and move along the z axis as at those locations where F_y is zero. At the nodal locations, F_y changes sign, which implements particles tending to move away from the center which can be observed in the microscope image. Results presented here confirm that the derived analytical force field explains experimental observations at this frequency very well. As it was mentioned above, force field depends on many parameters including the material properties; for example, if particles suspended here were made up of silica instead of polystyrene, in this case F_{zmax} would still be higher than F_{ymax} and the collection mechanism would be still similar to the one presented in Figure 5.6.

As frequency gets higher, y variance of acoustic radiation potential gets more dominant. Figure 5.8 shows the radiation potential at 1.7MHz. At this frequency,

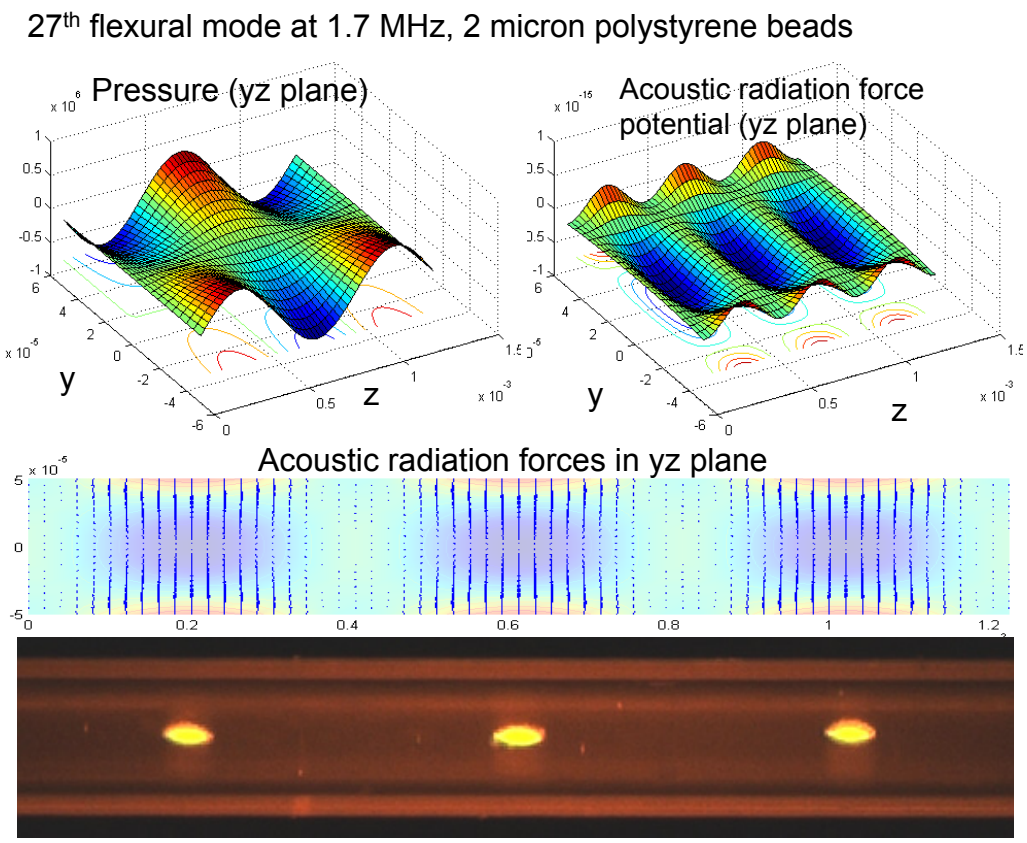

Figure 5.8: Acoustic pressure and radiation force potential distribution, and the acoustic radiation forces for the 27th flexural mode. For the explanation, see page 173 (Units: Pressure in Pascal; spatial coordinates in meters; and potential energy is Joules).

F_{zmax} is around 2×10^{-12}N and F_{ymax} is around 2×10^{-11}N. Also at this frequency, maximum force in y direction is an order of magnitude higher, which can be seen from the microscope fluorescent image which shows the disc shape collection of particles at the center of the capillary.

5.1.3.2 Frequency Dependence of the Radiation Forces for Various Materials

As it can be seen from Equations 5.50–5.51, F_y gets its maximum value at the capillary wall where $y = r_1$ and F_z gets its maximum value at $y = 0$, $z = \frac{(2n+1)\pi}{4k_b}$ which is the mid point between a vibration node and vibration maxima at the center of the capillary. Under these conditions, F_{ymax} and F_{ymax} can be written as,

$$F_{ymax} = \frac{2f_1}{3}\pi R^3 \rho_0 v_0^2 k^2 r_1 \tag{5.55}$$

$$F_{zmax} = \frac{f_2}{2}\pi R^3 \rho_0 v_0^2 k_b \ . \tag{5.56}$$

It can be seen that F_{ymax} depends on the k^2 where F_{zmax} depends on the k_b. In this case, forces in y direction increase faster compared to the forces in z direction, which confirms the observations mentioned in the previous section. It is important to note that an increase in the force values is not limitless. In other words, the forces are not monotonically increasing indefinitely with the frequency. Reader should be reminded that force values found above are valid in the $-0.4 < k_r' r < 0.4$ region. When $k_r r$ value gets higher than 0.4, $J_1(k_r r) \sim k_r r/2$ approximation does not hold. In this case, as $J_1(k_r r)$ is bounded and forces will be function of bessel functions, they will have a upper bound at the first maxima of the $J_1(k_r r)$, which happens around 10 MHz.

Figure 5.9 shows the maximum forces in y and z directions for 2 micrometer silica, polystyrene particles and oil droplets as a function of frequency. Here, frequency regime is within the $-0.4 < k_r' r < 0.4$ region. It should be noted that since the acoustic contrast factor for the oil droplets have opposite sign compared to the silica and polystyrene, in fact, forces will be negative; however, here, the absolute value is plotted to be compared with other samples side by side. It can

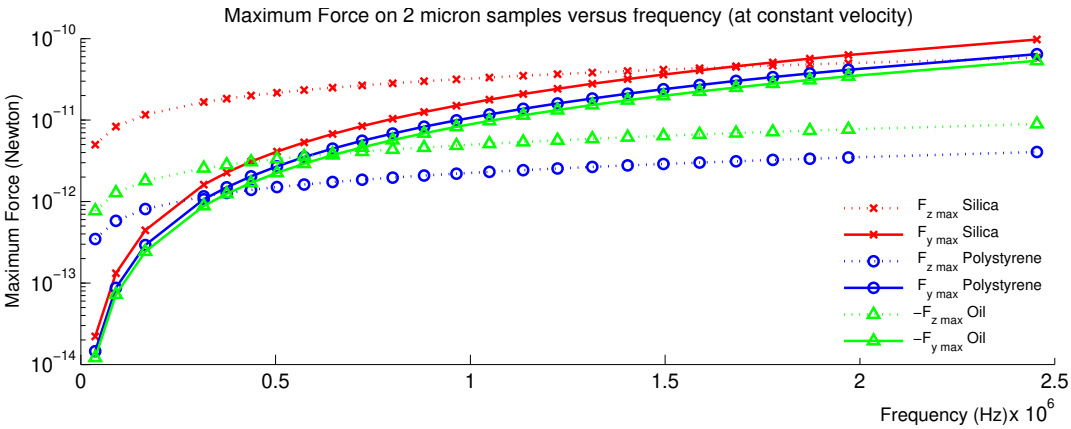

Figure 5.9: Variation of the maximum force in z and y directions against frequency for silica, polystyrene and oil. Particle size is taken to be 4 micrometers, and v_0=1 m/s.

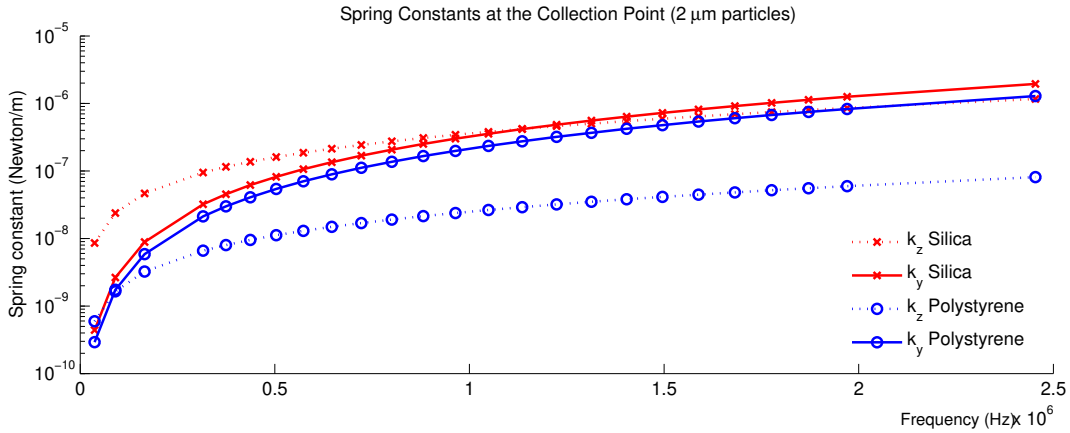

Figure 5.10: Variation of the spring constants in z and y directions (k_z and k_y) at collection spots against frequency for silica, polystyrene and oil. Particle size is taken to be 4 micrometers, and v_0=1 m/s.

be seen that due to the material properties for silica particles, forces are higher. Forces in z direction increase as a function of frequency; however, it can be seen that due to the square term, forces in y direction increase faster.

Figure 5.10 shows the frequency dependence of the spring constants for silica,

polystyrene and oil samples. Again, velocity of the capillary is taken to be constant at 1 m/s. It can be seen that spring constants reach to values about 10^{-6} N/m which is comparable to a typical optical tweezer trapping spring constant. Comparing the bulky setup and powerful laser requirements, the silica capillary actuator serves as a low power portable replacement to such systems. It may be a point of interest that in this configuration, the force field spans a much greater field so that all particles in the field are affected by the force field rather than a single particle in the case of optical tweezers.

It is important to mention that here in the above figures, the velocity of the capillary vibration is taken to be constant (v_0=1 m/s). In real experiments, due to the change in the impedance of the actuator over the frequency, v_0 is also a nontrivial, but an experimentally measurable function of the frequency.

5.1.3.3 Acoustic Radiation Force Fields for Air Microbubbles in Water

In previous sections, force fields and acoustic radiation potentials were calculated for silica and polystyrene particles. Both of these materials have higher speed of sound and density values compared to the water, resulting positive values for f_1 and f_2 (Equations 5.33). In this case, forces were always towards the center of the capillary and locations where vibration maxima exist. However, materials that are less dense and have lower speed of sound (or lower compressibility) compared to the water, will have negative values for f_1 and f_2. In this case, forces will be reversed. This means that such materials will move in opposite directions and end up accumulating in a different location. Oil droplets, fats, air bubbles and most of the materials which exhibit creaming effects will be in this category.

Figure 5.11 shows the analytical approach and the experimental result for the

5th flexural mode at 88 kHz,
Separation of 500 nm silica nanoparticles and air bubble

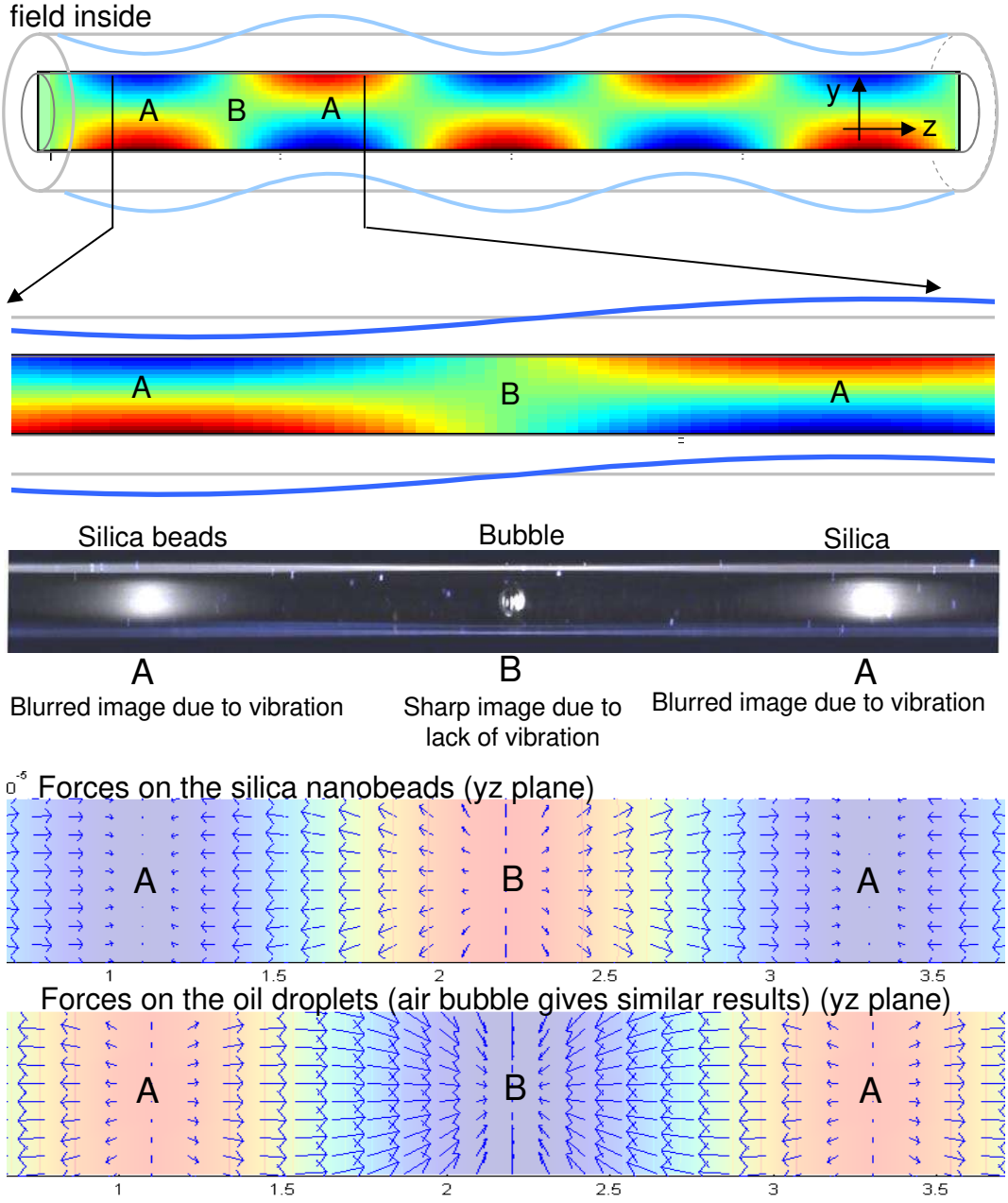

Figure 5.11: Separation of 500nm silica nanoparticles and air bubbles. Acoustic radiation forces for silica and air bubbles generated from the same acoustic field are different such that two materials are collected at different locations inside the capillary. For a further explanation, see page 177.

air bubble silica nanoparticle mix. At 88 kHz, the capillary vibrates in its 5^{th} flexural harmonic. It is experimentally observed that at this frequency, silica beads are collected at locations where vibration maxima exist. These locations are marked by "A" in the figure. Computed forces for the silica nanoparticles match with the microscope image. In the case of air bubbles, as shown in the bottom figure, forces[4] act differently and they are towards nodal locations which are marked by "B" in the figure. It can be seen that the image is blurred at locations marked by "A", which is due to the vibration of the capillary at these locations. Whereas at location "B" image is clear and no blurring effect is observed. This is where the air bubble is pushed. In Chapter 6, it will be shown that in a similar way blood can be separated into its components and device can be used as a planar, non rotating, portable micro-centrifuge.

5.1.4 Dependence of the Force on the Size of the Particles

Both of the acoustic radiation forces in y and z directions are a cubic function of particle radius, which means that an order of magnitude decrease in the particle size results in three orders of magnitude reduction in the radiation forces. Here, one may ask a valid question about the bottom limit for the particle size, or in other words, what is the smallest particle size which enables particle to be manipulated by the acoustic radiation forces?

All micro and nanoparticles exhibit Brownian motion. Detailed information about Brownian motion and its relation to this work are given in Chapter 7. This motion stems from the momentum transfer by the randomized collisions of the fluid

[4]In the given figure, computed force field is calculated for oil droplets rather than air bubbles. This is only due to the fact that since air has 3 orders of magnitude lower density compared to water, force values blow up and does not look understandable in the quiver plots.

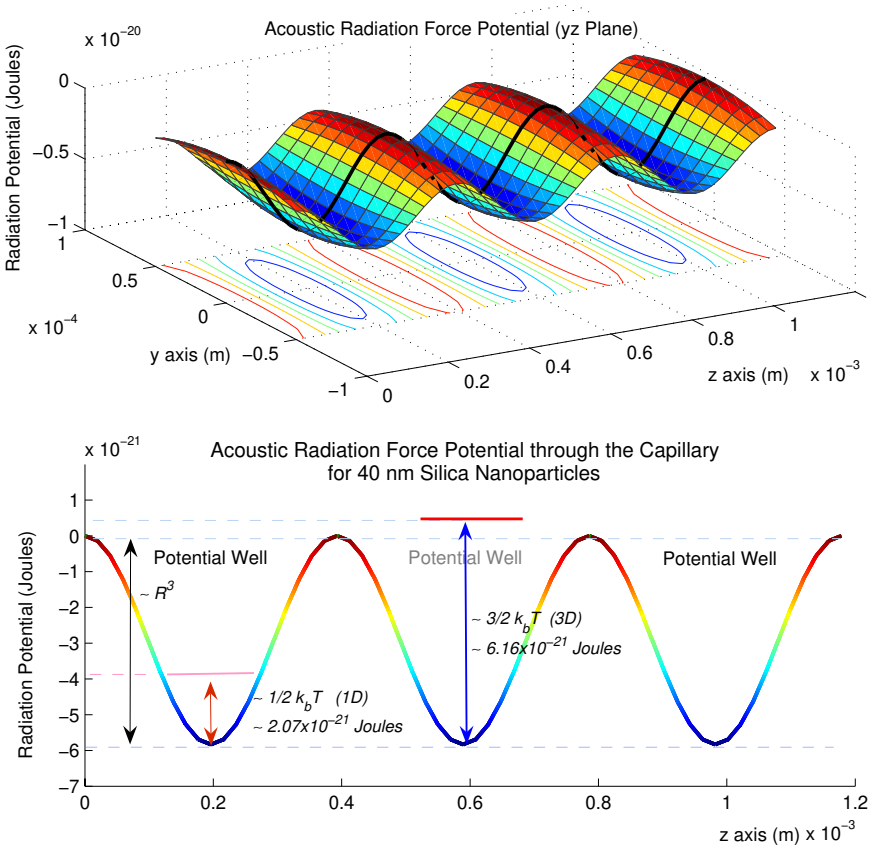

Figure 5.12: Top: Acoustic radiation potential for 40nm silica nanoparticles at 1.7 MHz (27th flexural harmonic) and v0=1 m/s. Bottom: Acoustic radiation potential along the central axis of the capillary. Depth of the potential well is not enough to hold particles which have thermal kinetic energy of $\frac{3}{2}kT$.

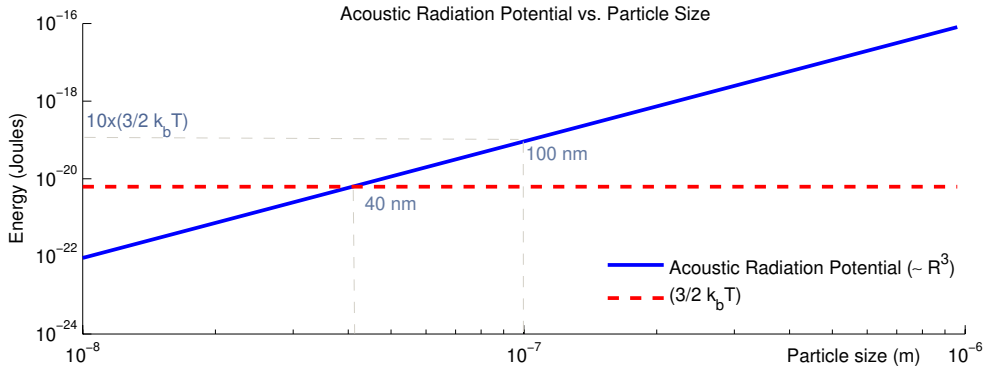

Figure 5.13: Acoustic radiation potential well depth versus particle size. For particle sizes below about 40 nm, Brownian motion completely takes over.

molecules with the particle. As molecules have a distribution of energies, at the end at a given short time scale particle will feel a net momentum gain in a particular random direction. The equipartition theorem suggests that all degrees of freedom in a system shares the energy in an equivalent way. In thermal equilibrium, energy value for each degree of freedom becomes $\frac{1}{2}kT$, where k is the Boltzmann constant[5] and T is the temperature in Kelvin. In the case of a micro or nanoparticle since particle is free to move in 3 dimensions, total translational average kinetic energy for this particle will be $\frac{3}{2}kT$.

Through Gor'kov's analysis, we can conclude that acoustic radiation pressure generates potential wells which leads to the capturing of particles. Depth of the potential wells depends on the cube of the particle size. As the particle size gets smaller, the depth of the potential wells gets smaller. At a certain limit depth of the potential becomes shallow enough so that the thermal kinetic energy of the particle ($\frac{3}{2}kT$) will be enough to overcome this potential well. Figure 5.12 shows such a configuration. The top graph of this figure shows the acoustic radiation potential for 40 nm size silica particles (v_0=1 m/s at f=1.7 MHz). The bottom graph of this figure is the variation of acoustic radiation potential at the center of the capillary along the capillary (also the black bold line in the top figure). In this graph, it can be seen that the depth of the potential well is smaller than the $\frac{3}{2}kT$ value. For this case, statistically, most of the particles will not feel the existence of the potential wells and Brownian motion will completely dominate. Figure 5.13 shows the variation of the depth of the potential well versus particle size. It can be concluded that for a capillary actuator vibrating at 1.7 MHz with a vibrational speed of 1 m/s, Brownian motion takes over for particles smaller than 40 nm.

[5]This phenomenon is only true for this particular section. In the rest of this chapter, k denotes wave vector for the acoustic waves in fluid and should not be confused with the Boltzmann constant.

To be able to get meaningful forces and collect most of the particles, potential wells having a depth of around $15kT$ would be reasonable, which corresponds to the particle size 100nm. This size range is in agreement with the experimental observations.

Here, particles are assumed to be non interacting. In most cases, this is not valid as most micro and nanoparticles bear surface charges and depending on the solution and particle material type, electrostatic interactions may add a few tens of kT energy to the particle kinetic energy. In this case, the size limit gets higher.

It is possible to increase vibration velocities with some power amplification. In this way, particle size limit may be reduced to sub 100 nm. However, it should not be forgotten that when nonlinear acoustic interactions are present, not only the acoustic radiation forces are present but also the acoustic, Rayleigh and boundary layer streaming effects are observed. While the effect of radiation forces gets lower with the particle size, the influence of streaming effects does scale down in a similar way. In this case, it can be concluded that unless streaming effects are engineered to be eliminated, it may not be very trivial to manipulate particles below 100–200 nm size.

5.1.5 Effect of Viscosity

Acoustic radiation force equations calculated by King, Yosioka and Gor'kov are related to the cube of the radius of the particle and these equations are considered to be valid for the nonviscous cases. In fluid dynamics, if the length scale is larger than the boundary thickness shear layer (δ), the system can be treated as nonviscous, which leads to the fact that all approaches mentioned above are valid

in the $\delta/R \gg 1$ limit, where δ is given by,

$$\delta = \sqrt{\frac{2\eta}{\rho\omega}} \, . \tag{5.57}$$

Here, η is the viscosity of the fluid, ρ is the density of the fluid and, ω is the angular frequency of the acoustical waves. Figure 5.14 shows variation in the thickness of the boundary shear viscous layer over the frequency. For samples suspended in water at room temperature, the thickness of the boundary layer take values between 3μm-0.4μm in the 30kHz-2MHz range.

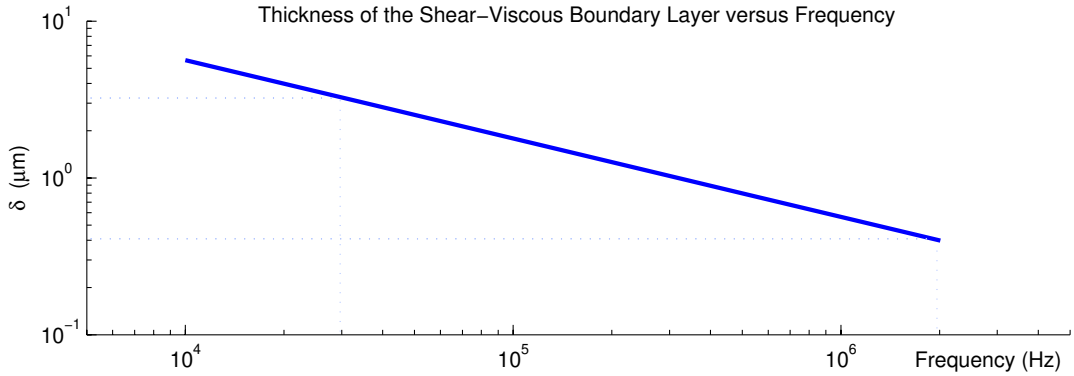

Figure 5.14: Thickness of the shear viscous layer versus frequency. In the 30kHz-2MHz region, the thickness of the viscous boundary layer has values between 3μm-0.4μm.

Westervelt [69, 70] has shown that both the experimental and theoretical results he reached confirm that viscous effects are negligible in a case where $\delta/R \gg 1$ holds. However, comparing the size range of particles we have (300nm-10μm) with the range of viscous boundary layer thickness range (400nm-3μ), it is clear that the effect of viscosity cannot not be fully eliminated and should be kept under consideration.

More recently, Doinikov [71, 72, 73] had calculated the contribution of the viscous and thermal effects on the radiation force for the cases of plane progressive

and plane standing waves. Later, Danilov and Mironov [74] showed that viscous effects cannot be ignored for $\delta/R \leq 1$ cases. His major conclusion is that, as the particle size gets smaller compared to the thickness of the boundary layer, forces that result from streaming effects start to dominate.

While experimental verification for the above methods is still not available, an experimental study by Yasuda and Kamakura [75] shows the size dependence of the acoustic radiation forces on particles in a planar standing wave field excited at 500 kHz. Their data show that for the particles larger than 5 μm, $F \sim R^3$ relation predicted by the general theory (by Yosioka or Gor'kov) holds reasonably well. However, their results show a significant deviation from the $F \sim R^3$ theory for the particles smaller than 5 μm. For the particle size range in the 300nm– 3μm region, rather than $F \sim R^3$, they suggest an empirical relation such that

$$F \sim (R + \chi)^3 \tag{5.58}$$

where χ is found to be 1.5μm from the fit. Their result suggests that as R gets smaller, the force does not go to zero but a finite value of χ^3. Their findings suggest an important result: because the acoustic forces do not scale down with R^3, manipulation of particles smaller than thought might be possible. In their paper, the researchers mention that χ =1.5 μm value can be attributed to two possible effects. One possibility is the viscous boundary layer effects as the thickness of the shear-viscous layer at 500 kHz is about 0.8 μm, and the other possibility is the ionic diffuse layer around the particle, which has a thickness value of about 1 μm for pure water at pH 7. It is not very trivial to trace back the origin of the modification in fact, because the force field is not measured directly. Rather, they measured the velocity of the particle, from which the force is calculated using Stoke's law. In this case, there is no way to guarantee that the force calculated is only due to radiation pressure. As mentioned in [74], the force might be a

summation of radiation forces and streaming forces for the viscous regime.

In short, here we conclude that while the effect of viscosity on the radiation force does not change everything, and the calculated force fields agree reasonably well with our experimental results, viscous effects still cannot be fully ignored in the $\delta/R \leq 1$ regime. From the experimental results presented by Yasuda and Kamakura [75], it is possible to conclude that the effect of viscosity appearing in the low particle size limit may influence the device performance in a positive way.

In Chapter 6, it will be shown that possible competition between streaming and radiation forces may be used to separate particles with respect to their sizes by applying some frequency hopping tricks.

5.2 Secondary Forces on Particles in an Acoustic Field

When acoustical waves and vibrations are present in a particle-suspended-in-fluid system, there are other interactions which lead to secondary forces in addition to acoustic radiation forces. In this section, such forces will be briefly introduced.

5.2.1 Bjerknes Forces

As it was already mentioned in this chapter, acoustic radiation forces on small spherical particles are generated due to the modification of the incident acoustic field by the scattering from the particle and the compression of the particle. When two particles are close enough, this scattered field is also felt by the secondary particles. Due to their high compressibility, these forces are dominant in the case

of bubbles present in an acoustic field and first introduced by Bjerknes [76]. A detailed analytical and experimental investigation of Bjerknes forces on bubbles in a stationary acoustic force is given by Crum [77]. The general time averaged value for the Bjerknes force is given by

$$F_b = -\langle V(t)\nabla p(r,\theta,z,t)\rangle \tag{5.59}$$

where $V(t)$ it the volume of the particle as a function of time, and $p(r,\theta,z,t)$ is the acoustic pressure as a function of time and location. As shown in Figure 5.15, Bjerknes forces are always attractive and given by the formula[78]:

$$F_b = -\rho\omega^2 \frac{[V_0 p\beta(1-\beta^*/\beta)]^2}{4\pi D^2} \tag{5.60}$$

where V_0 is the volume of the particle, β is the compressibility[6] of the fluid, β^* is the compressibility of the particle, ω is the angular frequency, ρ is the density of the fluid and D is the distance between the center of the particles. For 1μm silica particles in water with acoustic pressure values around 1 MPa, the Bjerknes force between two particles separated by 3μm is in the order of 10^{-10}N. This value will be reached at a pressure antinode.

When particles are away from each other, Bjerknes forces can be ignored due to the inverse square relationship with separation. Bjerknes forces are influential when particles are close in the order of couple of micrometers. In addition, since Bjerknes forces are related to the amplitude of the pressure, at pressure nodes Bjerknes forces will be low, which means that after particles find their stable collection locations, similar to the acoustic radiation forces, Bjerknes forces will be small as long as particles stay in their stable collection locations at the pressure nodes.

[6]Compressibility is the inverse of the bulk modulus.

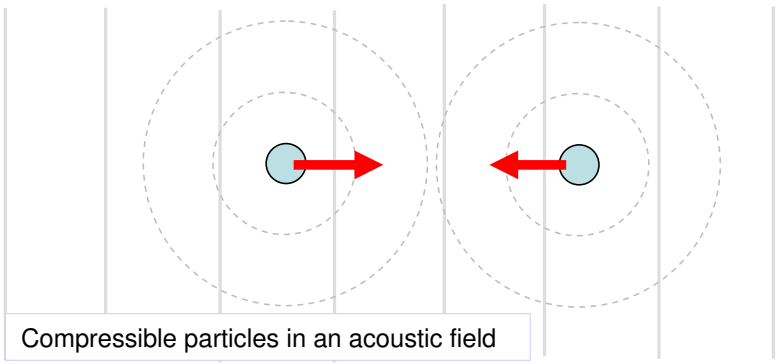

Figure 5.15: Bjerknes force between two compressible spherical particles in an acoustic field.

Away from the collection spots, Bjerknes forces will be higher; however, particles will not able to come close. At these locations, particles are moving towards collection spots due to the acoustic radiation forces. In addition, because of the motion of the particles, hydrodynamic-viscous effects will dominate.

5.2.2 Secondary Acoustic Field Forces

When two particles are present in the acoustic field, independent of the compressibility, particles will modify the acoustic field due to the scattering effects. In this case, similar to the Bjerknes forces, there will be an interaction among the particles. This interaction force is calculated by Zheng and Weiser [79, 78] through kinetic and potential energy of the particles due to this secondary field as,

$$F_i = \frac{2\pi(\rho^* - \rho)^2 v_0^2 R_1^3 R_1^3}{3\rho D^4}(3\cos^2\theta - 1) \tag{5.61}$$

where θ is the angle between propagation direction of the acoustic field and the direction in which particles are lined up. This force gets maximum at pressure nodes, where the acoustic pressure is minimum and the acoustic velocity of the

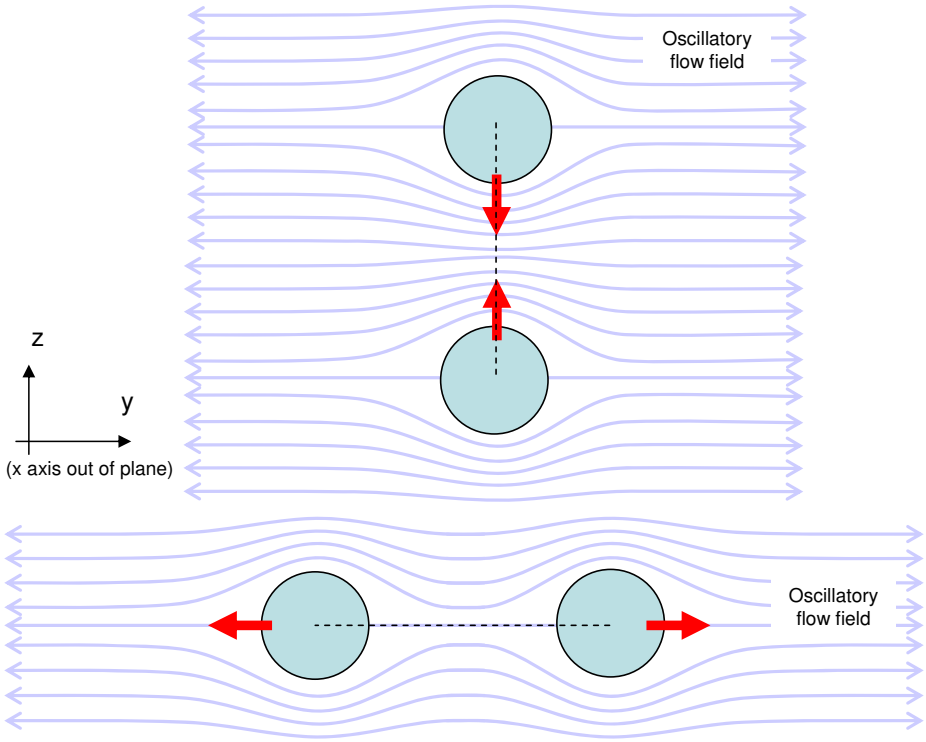

Figure 5.16: Hydrodynamic forces between two spherical particles in an oscillating fluid medium. These forces get maximum at pressure nodes; in other words, where particles collect.

fluid elements are maximum. In fact, the same problem was treated by Konig in 1891 just using the hydrodynamic interactions. By just taking the oscillating fluid term around the particles into consideration, Konig reached an equation which is very similar to Equation 5.61. Details of his approach can be found in [16].

When particles are lined up in normal direction to the propagation of the field and so parallel the oscillating flow direction, angle θ will be $\pi/2$ and the force will be negative, which means the particles will be pulling each other. As shown in the top schematic of Figure 5.16, this can be explained by the hydrodynamic interactions; when the particles are in proximity, the net flow between the particles will be higher and so the pressure will be lower. This means that particles will be sucked towards

the center between them. When the angle is zero, so the alignment of particles is parallel to the oscillating flow (in other words normal to the propagation of the field), due to the Stokes flow, the net flow between the particles will be diminished and so the pressure between the particles will be higher and particles will push each other away, as shown in the bottom schematic of Figure 5.16.

When the particles are aligned at an arbitrary angle, the net force on the system of particles will apply a torque about the center of mass of the particle system. If particles are attached to each other, this torque will cause the two-particle system to be aligned with the direction of the field.

For 1 μm silica particles which are a few micrometers apart from each other, the force given in Equation 5.61 becomes in the order of 10^{-11}N for a fluid particle velocity of 1 m/s. This value is comparable to the primary acoustic radiation force magnitude which means, as will be shown in Section 5.2.5, that this secondary force has a considerable effect on the collection style of the particles.

5.2.3 Viscous Drag Forces

As shown in Figure 5.17, when a flow is present around an object at low Reynolds numbers, creeping flow about the object generates a drag force directly related to the magnitude of the relative velocity of the flow. This is called Stokes law and the drag force is given by,

$$F_d = 6\pi\eta R v_f \tag{5.62}$$

where η is the fluid viscosity, R is the particle radius and v_f is the fluid velocity.

In an acoustic field, flow is oscillatory and this leads to an oscillating motion of

the particle. At low frequencies, due to the low effect of inertia of the particle, the difference between the particle and fluid velocity, and the phase difference between the oscillation of particle and the fluid are low. However, at higher frequencies, viscous effects get diminished and inertia of the particle becomes more dominant. In this case, some difference between particle and fluid velocity and a phase difference between oscillation of particle and fluid are expected. For $v_f = v_0 \sin \omega t$, the frequency dependent formula relating particle motion to the fluid motion is given by [80],

$$v_p = \frac{v_f}{\sqrt{1 + \left(\frac{4p\rho_p f R^2}{9\eta}\right)^2}} = \kappa v_f \tag{5.63}$$

where v_p is the amplitude of the oscillatory particle velocity, p is the pressure, ρ_p is the density of the particle, f is the frequency and κ is the one over square root term. The phase difference is given by,

$$\phi = \tan^{-1}\left(\frac{4p\rho_p f R^2}{9\eta}\right) . \tag{5.64}$$

In this case, the instantaneous viscous drag force will be

$$F_d = 6\pi\eta R(v_f - v_p) = 6\pi\eta R v_f(\sin(\omega t) - \kappa \sin(\omega t + \phi)) . \tag{5.65}$$

This force is a pure oscillatory, and the time average gives zero. It can be concluded that viscous drag forces in an acoustic field does not result in any steady net force. For 1 μm particles suspended in water where the magnitude of the oscillatory fluid velocity is 1 m/s, the amplitude of the oscillatory force will be in the order of 10^{-8}N. While the average of this force is zero, instantaneous values seem to reach couple of higher order of magnitude compared to the acoustic radiation forces. So the effect of this force is zero except for the case of streaming driven flow.

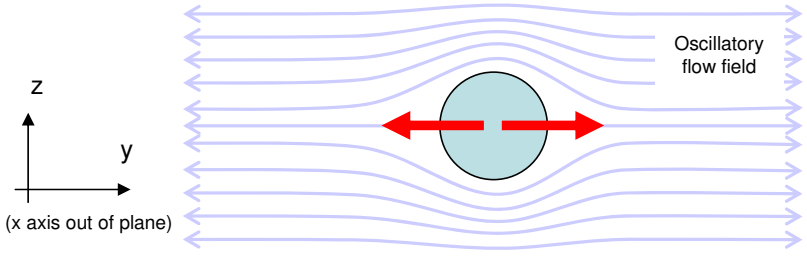

Figure 5.17: Viscous forces occur due to drag of fluid particles oscillating around the particle.

5.2.4 Oseen Forces

When a steady flow is present, the vibration of the particle in the acoustic field generates an asymmetry around the particle along the direction of the flow [2]. This asymmetry in the flow field causes a force between the particles, depending on the location of the particles. Oseen forces are observable in fluidic systems where the Reynolds number is greater than 1. Since most acoustic systems involve water as the fluidic medium, Oseen forces are taken to be negligible compared to other interactions mentioned before in this section.

5.2.5 Total Forces on the Microparticles Collecting at the Pressure nodes

At the pressure nodes, due to the low p value, Bjerknes forces will be very small and can be ignored. In this case, at pressure nodes, only two force fields are present. Primary acoustic radiation forces F_y and F_z given in Equations 5.50, 5.51 and secondary acoustic field-hydrodynamic forces given in Equation 5.61. In the flexurally vibrating capillary case, oscillatory flow of the fluid particles and the

propagation of acoustic field are parallel to the y axis. In this case, the secondary forces in z direction are attractive forces on the particles themselves. Since the x axis is also normal to the direction of the propagation-vibration, secondary field-hydrodynamic forces will be acting in the x-z plane. In this case there will be no balancing force[7] terms in the x-z plane so that all particles are expected to come close to each other in the x-z plane at the nodal points at y=0.

At the y axis, the primary acoustic field is attractive towards the pressure node and particles will start to collect. As particles start to collect and come into closer proximity, particles which line up parallel to the y axis will feel the repelling force due to secondary field-hydrodynamic interactions. In other words, in y direction, two force fields will be competing each other: one is effective in a broad range and the other is dominant in the proximity of particles. In this case, formation of band structures are expected. This phenomenon is sketched in Figure 5.18. The gap between the particle bands depends on where the primary field force cancels the secondary field force. Assuming two symmetric bands around $y = 0$ at a stable point, the net force will be zero such that,

$$\frac{4\pi(\rho^* - \rho)^2 v_0^2 R_1^3 R_1^3}{3\rho D^4} - \frac{2\pi}{3} f_1 R^3 \rho_0 k^2 v_0^2 D = 0 \quad . \tag{5.66}$$

From this formula, for 1μm polystyrene particles the gap between the bands is expected to be about 25μm. Due to the viscous effects at this particle size limit, the acoustic radiation force is expected to be higher (since $F \sim (R + \sigma)^3$) which leads to a smaller gap than 25μm.

Band formations observed in some of our experiments can be explained with this approach. Such formation of bands at various frequencies for silica and polystyrene

[7]Here only acoustic forces are meant. Related to DVLO theory, depending on the surface charge of particles, particles may or may not stick to each other.

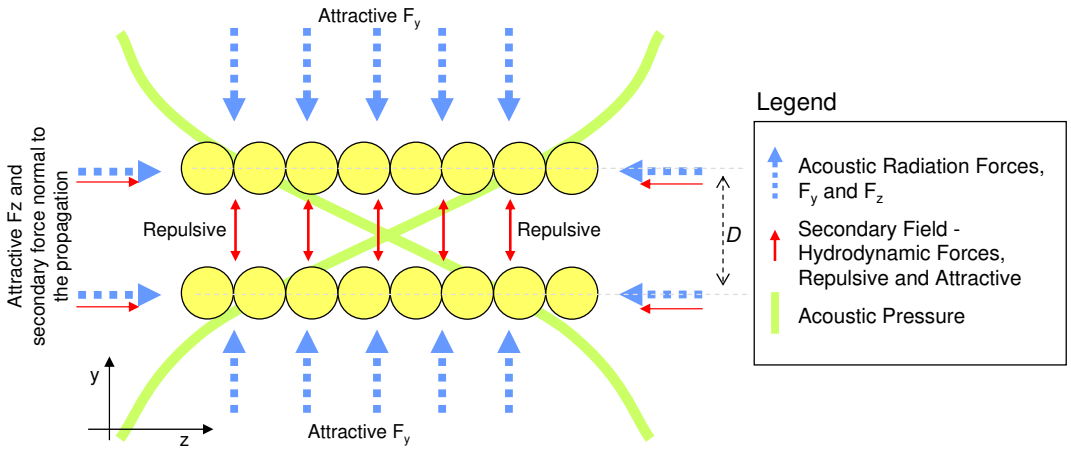

Figure 5.18: While the major acoustic radiation forces given in Equations 5.50 and 5.46 collect particles at pressure nodes, hydrodynamic forces given in 5.61 counterbalances particles aligned with the field. In this case particles form band structures. Number of bands forming depends on the number density of the particles.

beads is shown in Figure 5.19. In most cases, the gap between the bands is observed to be 5-20 μm, in agreement with the analytical result achieved above. For polystyrene beads, band formations are observed mostly below 400 kHz. However, for silica beads, band formations are observed up to 2 MHz regime. One interesting phenomenon recorded during the experiments, as shown as a series of images on the right of Figure 5.19, is that turning on the ultraviolet light for fluorescent imaging tends to increase the gap size. This increase happens in the order of 5 seconds and then reaches a new semi stable state in which some randomized movements are present on the bands. While a clear explanation requires further detailed experiments focusing on this observation, a simple suggestion would be that fluorescent coupling of particles with UV light may in turn lead to microthermal effects which may lead to temperature related viscosity gradients in the fluid in the neighborhood of the particles. In such a case, the effect of secondary forces related to hydrodynamic surrounding of the particles may tend to increase.

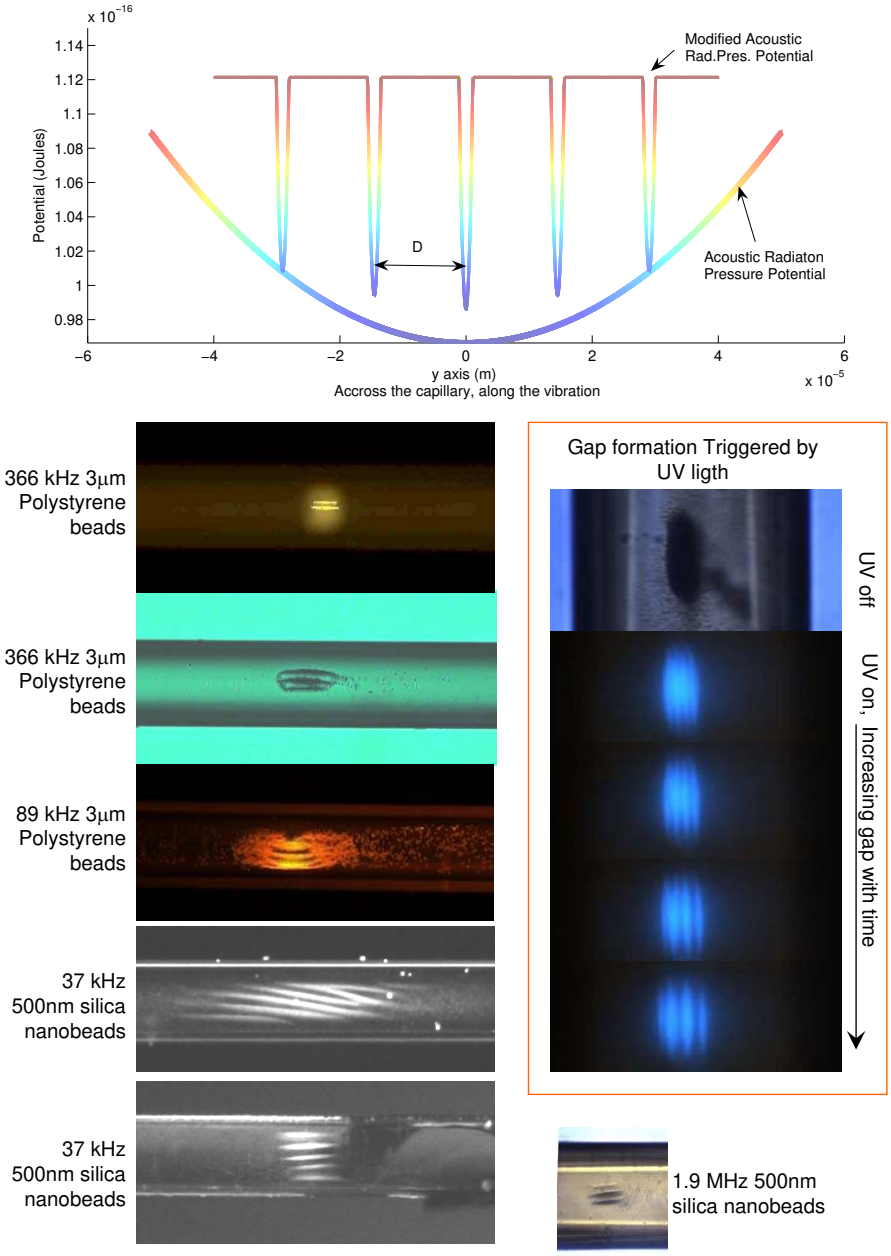

Figure 5.19: Top: Acoustic radiation pressure force field in y direction acts as a harmonic potential, so that particles are collected at the center. However, secondary forces due to inter-particle forces modify the field in a way that a potential well transforms to many number of wells. While the number of wells depends on the particle number density of the particles, the gap between the bands depends on many parameters such as size, density of the particles, frequency, etc. For polystyrene beads, it is observed that turning on the ultraviolet light increases the gap between collection bands. (The capillary diameter is 200μm).

5.3 Acoustic Streaming Effects in a Cylindrical Capillary

Another nonlinear interaction observed in acoustic systems is acoustic streaming. Related to the work presented in this dissertation, acoustic streaming effects are not as influential as acoustic radiation forces. For this reason, acoustic streaming will be briefly touched on for a couple of special related cases. A more comprehensive review of acoustic streaming can be found in [57, 58, 59, 60, 61].

Acoustic streaming is a second order nonlinear phenomenon that results from the attenuation of the sound waves. When acoustic waves are present in a medium, dissipation of the acoustic energy causes a gradient in the momentum flux. Assuming a small fluid volume, the difference in the momentum flux between two faces of the sample unit volume generates the so called Reynolds stress[8] ($\langle \rho_0 v_i v_j \rangle$), leading to the force causing steady streaming. Attenuation of the sound waves happens because of the viscosity of the fluids. Interestingly, while this force is generated because of the viscous properties of the fluid, in most cases, streaming does not depend on the viscosity of the fluid due to the fact that the resistance produced against this streaming flow by the fluid itself is also a result of viscosity.

Attenuation of acoustic energy can happen in two major ways. One happens because of the energy dissipation in the body of the fluid during the propagation of acoustic waves. This dissipation is related to the self viscosity of the fluid medium. As mentioned above, spatial change in the momentum flux leads to an time averaged Reynolds stress value. As in the case of any stress, the gradient of this stress results in a net force in that direction such that,

$$F_i = -\langle \frac{\partial \rho_0 v_i v_j}{\partial x_j} \rangle. \tag{5.67}$$

[8]Where $\vec{v}$ is the acoustic particle velocity and $\langle\rangle$ denotes the time average.

As mentioned above, here, $\vec{v}$ is the first order acoustic particle velocity. This force acts as a body force and can generate a flow. Assuming only the contribution of this force, mean velocity of the fluid due to this motion can be given by the steady state (zero acceleration) solution of equation of motion given in terms of the Navier-Stokes equation,

$$\rho(v_j' \frac{\partial v_i'}{\partial x_j}) = F_i - \frac{\partial \langle p \rangle}{\partial x_j} + \eta \nabla^2 v_j', \tag{5.68}$$

and the continuity equation in acoustic terms [59],

$$\rho_0 \frac{\partial v_i'}{\partial x_j} = -\frac{1}{c^2} \frac{\partial \bar{I}_j}{\partial x_j} \ . \tag{5.69}$$

Here $\vec{v'}$ is the streaming velocity due to the body force F_i given in Equation 5.67, $\langle p \rangle$ is the mean pressure and $\vec{I} = \langle p\vec{v} \rangle$ is the acoustic intensity. In the above equation, viscous terms representing the compressibility are ignored. Solving Equations 5.67, 5.68 and 5.69 for $\vec{v'}$ leads to the solution.

The second and the more common type of attenuation happens at the neighborhood of a stationary boundary. Due to the shear viscous effects, when an acoustic field is generated near a stationary boundary, attenuation occurs near the boundary. Similarly, a stationary fluid on top of an oscillating boundary will result in a similar picture. In fact, acoustic streaming was first observed as a boundary streaming near an oscillating boundary. Savart found that while most of the powder is collected in nodal lines in a Chladni's experiment, fine powders do gather at antinodes where the vibration is maximum. He noted that collections of fine powders at the antinodes were cloudy. Since this unexpected behavior of the fine powder did not happen in vacuum, Faraday, for the first time, concluded that these collections at the antinodes are due to the streaming effects generated by the flexural vibrations of the plate. Later on, Kundt and Dvorak observed that dust particles collect at nodal points of a stationary sound wave excited in a tube. First

the analytical approach to these observations came by –as in the case of many other acoustic phenomena observed before– Rayleigh in 1883 [4]. In his paper, Rayleigh formulated the streaming vortices generated by an flexurally vibrating plate and streaming vortices generated in a tube by the acoustical stationary waves in the tube.

In his famous review, Lighthill [59] concludes that Rayleigh's approach can be also used for the case where a boundary oscillates in a tangential direction where the fluid is stationary. This is because of the fact that in both cases (oscillating fluid-stationary boundary and oscillating boundary-stationary fluid) relative motion between the boundary and fluid generates a frictional dissipative layer at the fluid-structure boundary. This important claim has been experimentally confirmed in the case of a cylinder-fluid system. Streaming vortices generated near a stationary cylinder in an oscillatory flow field [81] are almost identical to the streaming vortices generated near an oscillating cylinder in a stationary fluid medium [82, 83].

In a fluid structure boundary where an oscillatory relative motion exists, due to a no-slip boundary condition and shear viscosity, the first order velocity decays very fast. This change in the velocity generates the second order streaming. Average streaming velocity at the end of boundary layer is called the slip velocity. Confirmed by many other researchers, slip velocity was first calculated by Rayleigh [4] as,

$$v_s = -\frac{3}{4\omega} U(x) \frac{\partial U(x)}{\partial x} \tag{5.70}$$

where $U(x)$ is the amplitude of the relative velocity between fluid and surface and ω is the frequency.

In the next section, in the light of conclusions drawn by Rayleigh and Lighthill, streaming effects in a capillary due to the oscillating capillary walls will be given.

5.3.1 Acoustic Streaming in a Flexurally Vibrating Capillary

In Section 3.2.2, velocity of the fluid particles inside the cylindrical capillary was calculated from boundary conditions. There, in terms of boundary conditions, only the normal velocity at the fluid structure boundary was taken into consideration, since at the time the point of interest was the acoustic pressure at the fluid structure interface and shear viscous effects were ignored. Here, however, the point of interest is the tangential velocities. In a flexurally vibrating capillary, tangential velocities appear in two distinct ways in two planes. In this section, streaming velocities in two planes will be calculated.

5.3.1.1 Streaming Effects in y-z Plane

Since the capillary body is relatively thick, a nonzero tangential velocity at the fluid structure boundary occurs due to the shearing of the capillary walls. This tangential motion parallel to the central axis of the cylinder was calculated in Section 4.1.5. There, analytical results were matching reasonably well with the ANSYS simulation results. Here for simplicity, flexural motion of the capillary in y direction will be taken to be

$$v_r(r,\theta,z)_{wall} = v_0 \sin(k_b z)\sin\theta \ . \tag{5.71}$$

In this case, following up with the same methodology given in Section 4.1.5, tangential velocity becomes approximately

$$v_z(r,\theta,z)_{wall} = v_0 r_1 k_b \cos(k_b z)\sin\theta \ \ . \tag{5.72}$$

In the frequency range 40kHz-1MHz, we have $r_1 k_b \sim 0.1$. Then average slip velocity from Equation 5.70 becomes,

$$v_s = \frac{3v_0^2 r_1^2 k_b^3}{8\omega} \sin(2k_b z) \sin\theta \quad . \tag{5.73}$$

Now we need to find the secondary streaming effects due to this non zero slip velocity at the fluid structure boundary. In reality, this slip velocity exists at about 5δ away from the boundary. This value changes between 8-1μm in the 40kHz-2MHz range. However, since the capillary diameter is higher, for the sake of simplicity, we will consider slip velocity at the boundary $r = r_1$ rather than $r = r_1 - 5\delta$.

Navier-Stokes and continuity equations are given as,

$$\rho[\frac{\partial \mathbf{v}}{\partial t} + (\mathbf{v}\cdot\boldsymbol{\nabla})\mathbf{v}] = -\boldsymbol{\nabla}p + \eta\nabla^2\mathbf{v} + (\zeta + \frac{1}{3}\eta)\boldsymbol{\nabla}(\boldsymbol{\nabla}\cdot\mathbf{v}) \tag{5.74}$$

$$\frac{\partial \rho}{\partial t} + \rho\boldsymbol{\nabla}\cdot\mathbf{v} + \eta\nabla\rho = 0 \tag{5.75}$$

Here, the point of interest is given to the second order acoustic streaming velocities which are small compared to the speed of sound and oscillatory fluid particle velocities. In this case, fluid can be treated as non-compressible, meaning that in 2d cartesian coordinates, the continuity equation reduces to,

$$\rho\boldsymbol{\nabla}\cdot\mathbf{v} = 0 \quad \Rightarrow \quad \frac{\partial v_x}{\partial x} = -\frac{\partial v_y}{\partial y} \tag{5.76}$$

Following this, there exists a function $\boldsymbol{\psi}$ such that

$$\mathbf{v} = \boldsymbol{\nabla}\times\boldsymbol{\psi} \quad . \tag{5.77}$$

Here, $\boldsymbol{\psi}$ is called the stream function. In 2D $\boldsymbol{\psi}$ will have only one component ($\boldsymbol{\psi} = (0, 0, \psi)$), and components of the velocity can be found as

$$v_x = \frac{\partial \psi}{\partial y} \text{ and } \quad v_y = -\frac{\partial \psi}{\partial z} \quad . \tag{5.78}$$

Ignoring the last term (due to the non-compressible case) and taking the curl of Navier-Stokes equation given in Equation 5.74, the curl of the gradient of the pressure is eliminated. Following some vector calculus identities, we have,

$$\frac{\partial(\boldsymbol{\nabla}\times\mathbf{v})}{\partial t}+(\mathbf{v}\cdot\boldsymbol{\nabla})\boldsymbol{\nabla}\times\mathbf{v}-((\boldsymbol{\nabla}\times\mathbf{v})\cdot\boldsymbol{\nabla})\mathbf{v}=\eta\nabla^2\boldsymbol{\nabla}\times\mathbf{v} \tag{5.79}$$

Following Rayleigh [16], since secondary streaming velocities are low, all quadratic second terms can be ignored. Then, in a steady state, all terms in the left hand of above equation are neglected. Plugging in $\mathbf{v}$ from Equation 5.77, the above equation becomes,

$$\nabla^4\psi=0 \quad . \tag{5.80}$$

Here ∇^4 is called the biharmonic operator, which appears in elasticity and stokes creeping flow problems. Apparently, here we have the second case.

Considering the y-z plane of the cylinder, problem can be reduced to two dimensions. Since the acoustic wavelength is much larger than the capillary diameter ($k \ll 2r_1$) and we are seeking an approximate solution, biharmonic equation can be written as [84, 4],

$$\Big(\frac{\partial^2}{\partial y^2}+\frac{\partial^2}{\partial z^2}\Big)^2\psi=0\ . \tag{5.81}$$

The solution of the above equation is expected to be symmetry around the central axis of the cylinder and in z direction it should have the same periodicity as given in Equation 5.73. In this case, taking the center of the capillary as y=0, and the stream function is found to be,

$$\boldsymbol{\psi}(y,z)=(Ay+By^3)\sin(2k_bz) \quad . \tag{5.82}$$

From Equation 5.78, streaming velocities, v_y' and v_z' can be found as,

$$v_y' = -2k_b(Ay+By^3)\cos(2k_bz) \tag{5.83}$$

$$v_z' = (A+3By^2)\sin(2k_bz) \quad . \tag{5.84}$$

Since fluid is bounded by the cylinder at the fluid structure boundary $r = r_1$, the normal velocity v_y has to be zero[9], so $A = -Br_1^2$. At the fluid structure boundary, slip velocity is given in Equation 5.73. Then at $r = r_1$,

$$v_z'(r_1) = B(3y^2 - r_1^2)\sin(2k_b z) = \frac{3v_0^2 r_1^2 k_b^3}{8\omega}\sin(2k_b z) \quad \text{then,} \tag{5.85}$$

$$B = \frac{3v_0^2 k_b^3}{16\omega}\ . \tag{5.86}$$

Finally secondary streaming velocities inside the capillary become

$$v_y'(y,z) = \frac{3v_0^2 k_b^4}{8\omega}(r_1^2 r - r^3)\cos(2k_b z) \tag{5.87}$$

$$v_z'(y,z) = \frac{3v_0^2 k_b^3}{16\omega}(3r^2 - r_1^2)\sin(2k_b z)\ . \tag{5.88}$$

The top schematic in Figure 5.20 shows the normal and tangential velocities during the flexural motion of the capillary.[10] The graph in the middle of same figure shows the plotting of streaming velocities calculated via Equations 5.87 and 5.88. For the capillary structure flexurally oscillating with a vibration velocity ($v_{y\ wall}$) of 1m/s ($v_{y\ wall}$), the slip velocity (v_S) becomes about 10 μm/s. Another streaming which is not shown in this graph is called Schlichting streaming, which happens in the close boundary. This is drawn in the bottom figure. The thickness of this close boundary streaming is very small (5δ). Further information about close boundary streaming can be found in [2]. For capillary or microfluidic systems where cavity dimensions get close to (5δ), Schlichting streaming cannot be ignored and in fact become the dominant streaming effect due to the boundary layer oscillation.

[9]Here, the velocity terms we are talking about are the streaming velocities which are the second order velocities. Motion of the fluid due to the flexural motion of the capillary is not included here; in that case, apparently normal velocity will not be zero but the same as the capillary wall velocity.

[10]For simulation and analytical results regarding this tangential motion, please see Section 4.1.5 in Chapter 4

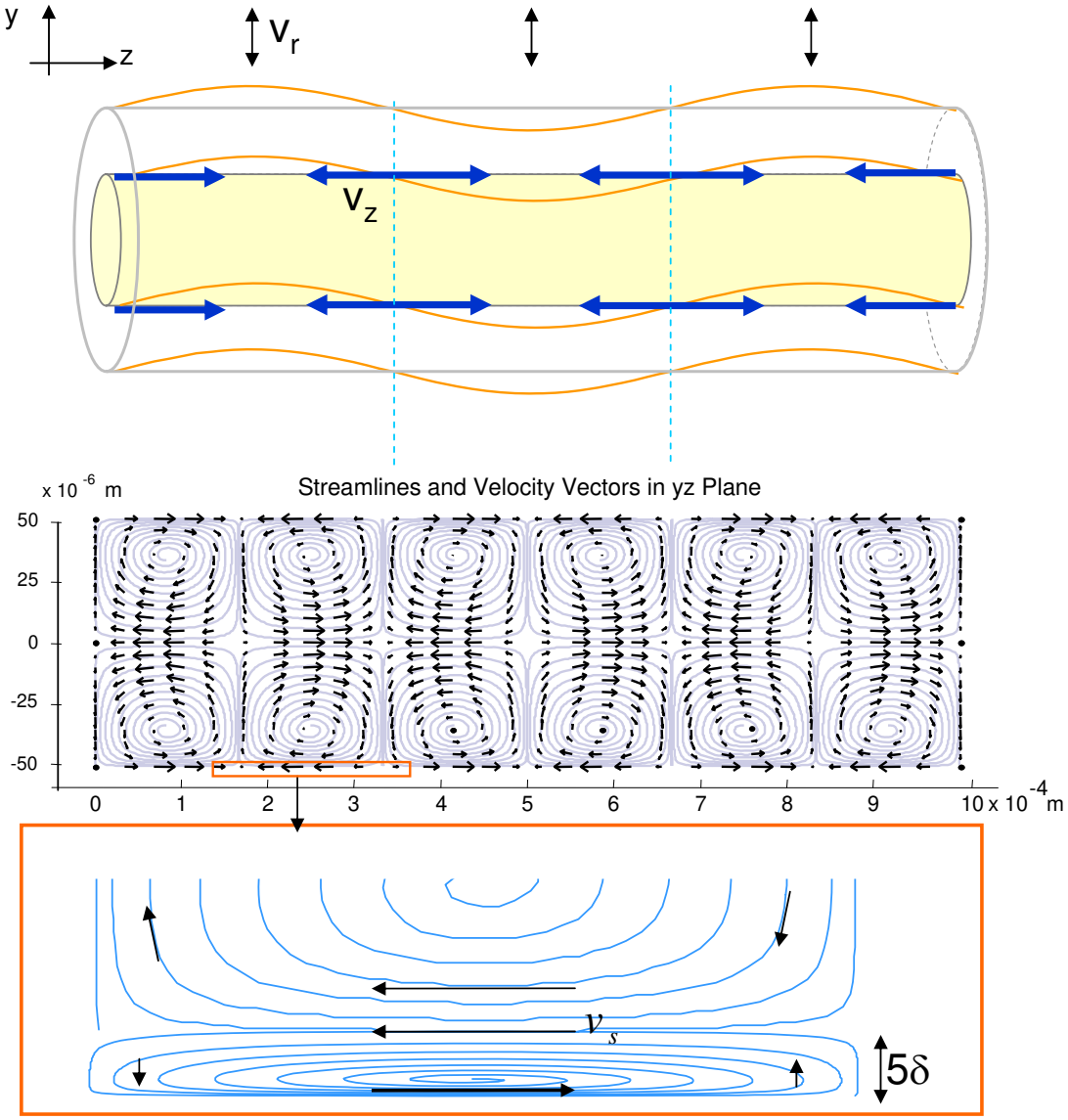

Figure 5.20: Top: Schematic of the normal and tangential velocities at the capillary wall due the flexural motion of the capillary. Middle: Quiver plot of streaming velocities, calculated by Equations 5.87 and 5.88. Bottom: Schematic of Schlichting streaming at the close boundary [2].

5.3.1.2 Streaming Effects in x-z Plane

In this section, streaming effects in x-z plane (capillary cross section) will be introduced. Since in the x-z plane normal and tangential velocities get maximum at vibrational maxima, the streaming effects will be calculated at vibration maxima. As shown in Figure 5.21, for a capillary cross section oscillating up and down with velocity v_0, at points A and C, tangential velocity will be maximum. At these points, normal velocities will be minimum. At points B and D, it will be the opposite. Then at the capillary-fluid boundary, tangential velocity can be written as

$$v_\theta(r_1, \theta) = v_0 \sin\theta \ . \tag{5.89}$$

In this case from Equation 5.70, slip velocity becomes,

$$v_s(r_1, \theta) = \frac{3v_0^2}{4r_1\omega} \sin(2\theta) \ . \tag{5.90}$$

Here, rather than solving the problem, it is possible to make an analogy to the solutions found in the previous part through a curvilinear transformation. In this way, an approximate but a quick solution can be achieved. As shown in Figure 5.21, if we open the oscillating circle from point A, the motion of the boundary looks like a motion of a plate in which flexural and longitudinal modes are coupled in a way that their amplitude is distributed spatially out of phase. Here, the point of interest is tangential velocities. In such an analogy, the relationship between circumference and wavelength becomes $2\pi r_1 = \lambda = 2\pi/k$, which leads to $kz = \theta$ and $kr_1 = 1$. In this case, in replacing all these terms in Equations 5.87 and 5.87,

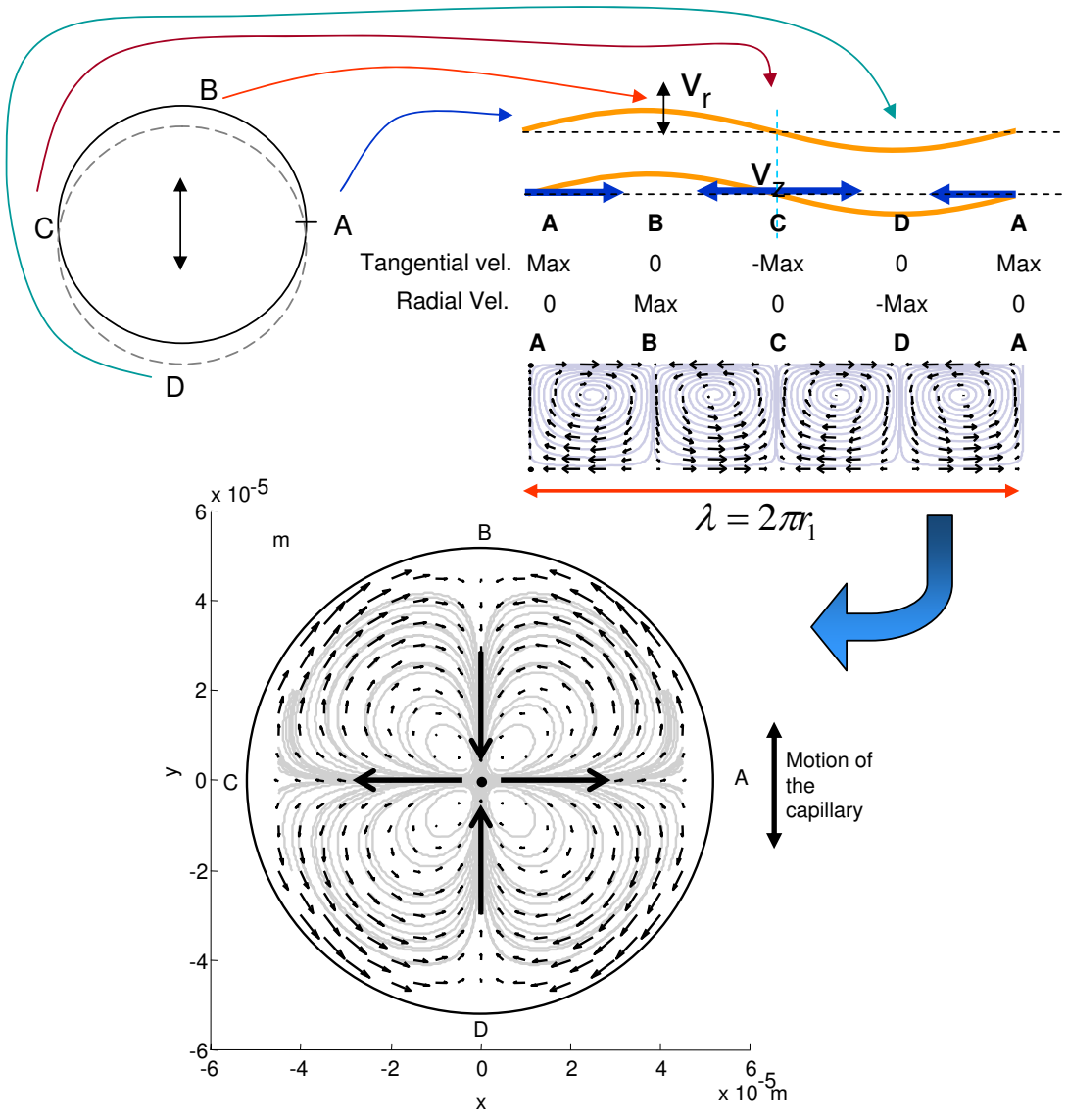

Figure 5.21: Top: Cylinder cross section oscillating in the vertical direction. Opening of the cylinder boundary at point A to a strip, cylinder boundary resembles a plate vibrating in a coupled flexural-longitudinal mode. At points A and C, tangential velocities become maximum which are the point of interest. Just below the strip, steady streamlines due to the motion of the strip are shown. Making a curvilinear transformation, and having $2\pi r_1 = \lambda = 2\pi/k$ lead to $kz = \theta$ and $kr_1 = 1$, it is possible to get the approximate solution. Bottom: Graph showing streaming velocities obtained by Equations 5.91 and 5.92.

we have

$$v_r(r,\theta) = \frac{3v_0^2}{4r_1^4\omega}(r_1^2 r - r^3)\cos(2\theta) \quad (5.91)$$

$$v_\theta(r,\theta) = \frac{3v_0^2}{8r_1^3\omega}(3r^2 - r_1^2)\sin(2\theta)\ . \quad (5.92)$$

Results obtained in the above equations are plotted in the graph given at the bottom of Figure 5.21. Streamlines and orientation of streaming velocity vectors shown in the graph are in agreement with the proposed streamlines by Nyborg [85].

For a capillary oscillating with a velocity of 1m/s at 100 kHz, slip velocity at the boundary is about 10 mm/s. This value is much higher compared to the streaming velocities calculated in the y-z plane. This is because that tangential velocity in x-z plane at a vibration maxima is much higher than the tangential velocities at the vibration minima, which resulted in three orders of magnitude lower streaming slip velocities.

Here, close boundary Schlichting streaming vortices are not included. There will be other streaming vortices in the 5δ neighborhood of the circular cross-section. These vortices, in fact, are the reason behind the nonzero slip velocity as mentioned in the previous section.

Experimental results we obtained show that streaming effects are not influential as long as radiation forces are high enough to capture particles. Streaming effects might be useful for applications where mixing of fluids or samples are desired, and that is another challenging phenomenon due to the laminar flow behavior. Streaming vortices with a speed of 10 mm/s in a microcapillary would trigger fluid mixing in the order of seconds.

CHAPTER 6

EXPERIMENTAL RESULTS AND THE APPLICATIONS

Introduction

Experimental measurements regarding the characterization of the PZT-glass capillary ultrasonic actuator mechanism and the applications in collection and separation of various samples at the microscale will be introduced in this chapter.

In the first part, serving as the characterization of the actuator mechanism: electrical impedance of the PZT plate, interferometric vibration analysis of the capillary, vibration spectrum of the capillary, vibration amplitude versus voltage drive and particle collection and voltage drive linear relationship are introduced.

In the second part, experimental results achieved are presented. These results include the collection of micro and nanoparticles and biological samples such as cells, bacteria and sperm cells; separation of materials with respect to acoustic contrast factor; separation of materials with respect to size; planar centrifugation of the blood; fast and efficient mixing at the laminar flow regime; and utilization and control of oscillating bubbles for particle capture. In the last part, some interesting observations such as a stylish collection mechanism of nanoparticles and observations on the generation of Faraday waves in a microfluid platform have been presented.

6.1 Characterization of the PZT-Glass Capillary Coupled Actuator

The main working principle of the PZT-Glass capillary actuator is the generation of high amplitude acoustic waves in a sub-wavelength size microcapillary. This acoustic excitation inside the capillary is generated by the flexural motion of the capillary, and the flexural motion of the capillary is generated by the coupling of the PZT plate's vibrations. In this sense, designing the device subcomponents in an integrated approach is very important. A superior example would be the ear. The human ear consists of many different acoustical parts made up of different materials and shapes such as the soft material of the outer ear, the channel, membrane, bones suspended in a viscous fluid, the spiral and the nerves; all these components have different characteristics but they combine to provide acoustic to electrochemical transduction in such a superior way that it cannot even be modeled properly in today's information age.

As shown in Figure 6.1, in the case of the PZT-glass capillary actuator mechanism, there also exists a transduction pathway; however, it is *simpler* compared to the case of the ear. Chapters 2, 3, 4, and 5 are dedicated to the modeling of the parts of this transduction cascade. This chapter finalizes the characterization by adding the last loops to the chain. One way to improve the performance of any device depends on the proper characterization of the prototype. In an integrated system in which subcomponents are designed to work in harmony, electrical signal to cavity acoustics coupling may get enhanced. Following these principles, individual subcomponents of the PZT glass capillary actuator, and their coupling with each other will be examined here.

6.1.1 Electrical Impedance

Starting with the PZT plate, Figure 6.2 shows electrical impedance and the phase plots of the PZT plate over the frequency range of 20kHz–2MHz. The spectrum shows many resonance modes where the electrical impedance drops significantly. Since the capillary mass is small compared to the PZT mass, its effect on the electrical impedance of the PZT is not significant for the most of the resonance modes of the PZT. While a finite element modeling of the PZT modes is under investigation by using ANSYS, it will be included in a future reference, but not in this thesis. From an intuitive point of view, it is possible to conclude that, es-

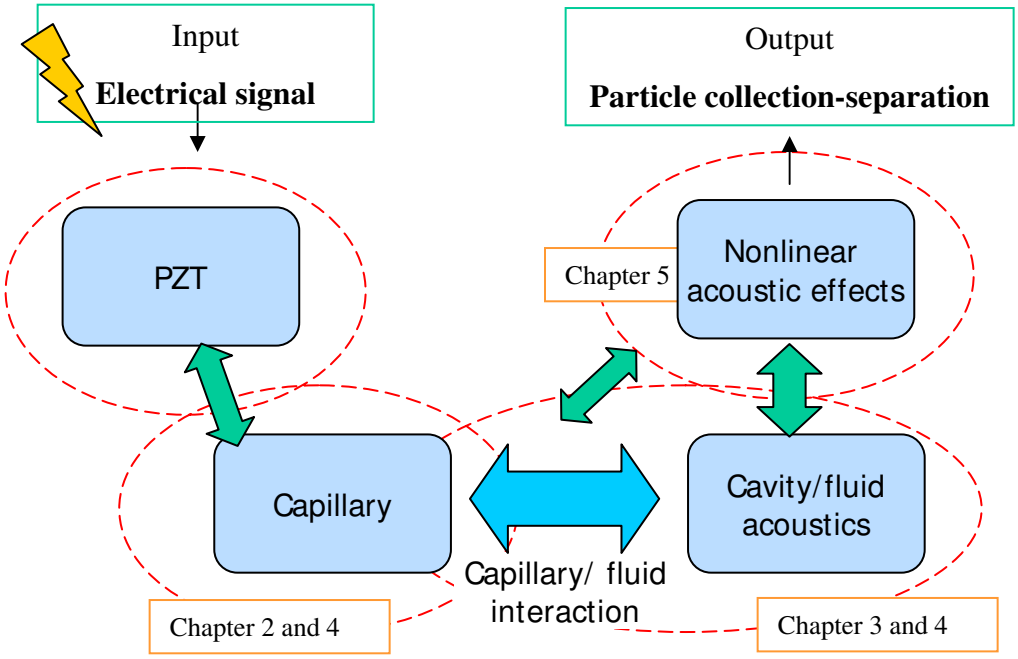

Figure 6.1: Transduction mechanism from electrical signal input to particle manipulation. Electrical signal applied to the PZT, vibrates the PZT. PZT vibrations couple to the capillary and capillary vibrates. Capillary vibrations modify the acoustic field inside the capillary such that, through the nonlinear acoustic interactions particles can be manipulated.

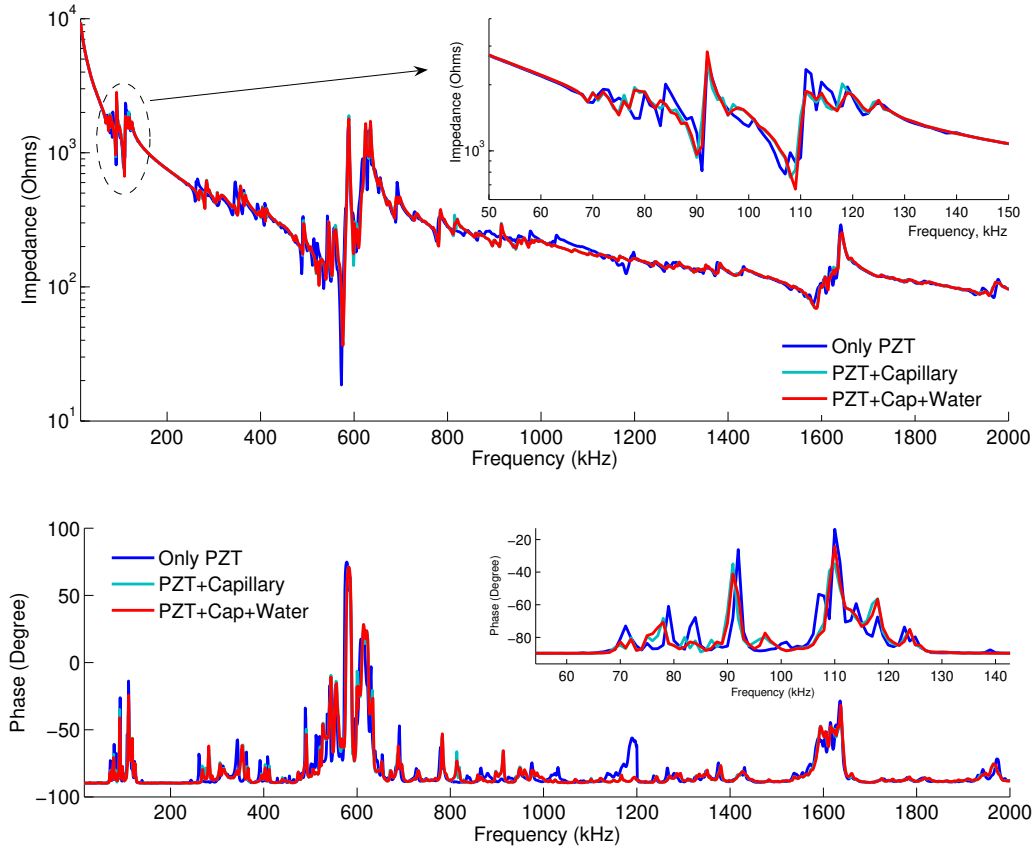

Figure 6.2: Electrical impedance and the phase versus frequency of the PZT-glass capillary actuator. The three curves represent; the PZT plate before the attachment of the capillary; the PZT plate and empty glass capillary; and the PZT plate and the water filled glass capillary. Results show that slight change occurs at some frequencies with the inclusion of the glass capillary.

pecially resonance frequencies of flexural, torsional and shear modes which involve transverse motion, are not heavily influenced by the introduction of the capillary. However extensional modes, especially the ones along the capillary, will be the ones which are influenced. This is why at some resonance modes, resonance or antiresonance frequencies are shifted a little bit. Impedance and phase curves of the water filled PZT-glass capillary system and the empty case are almost identical, which reveals that the addition of water does not influence the rest of the

system at all. This also confirms the intuitive approach presented above. Since the fluid is not clamped, it is free to slide inside the capillary when the capillary is extended due to a extensional mode of the PZT. In this case, it cannot change the total elasticity of the actuator. It only acts as a mass load, and since the mass of the fluid enclosed is small compared to the PZT, the impedance curve of the fluid filled and empty cases is almost identical.

6.1.2 Interferometric Laser Doppler Measurements of the Capillary Flexural Motion

Using a laser Doppler vibrometer is a powerful method for non contact measurement of the surface vibrations. When a laser beam is pointed towards a vibrating surface, a Doppler shift in the reflected beam is generated because of the normal motion of the surface, and it is detected through its interference with the original laser beam. Since this method of measurement is contactless and so does not lead to a mass load or change in the boundary conditions, the measurements are considered to be very accurate. Figure 6.3 shows the interferometric vibrometer scan of the capillary at various frequencies. In this figure the merit is to demonstrate the flexural motion of the capillary, and the amplitude study will be given later in this section. Scans include several harmonics of the flexural modes of the capillary.

In Figure 6.4, vibrational velocity amplitude at the capillary center point is plotted against the frequency for the the empty and fluid filled capillary cases. This is a point scan at the center of the capillary where only odd numbered harmonics could be detected. For all of the even modes, the capillary center is a vibration node and does not reveal any displacement or velocity. Comparing the fluid filled

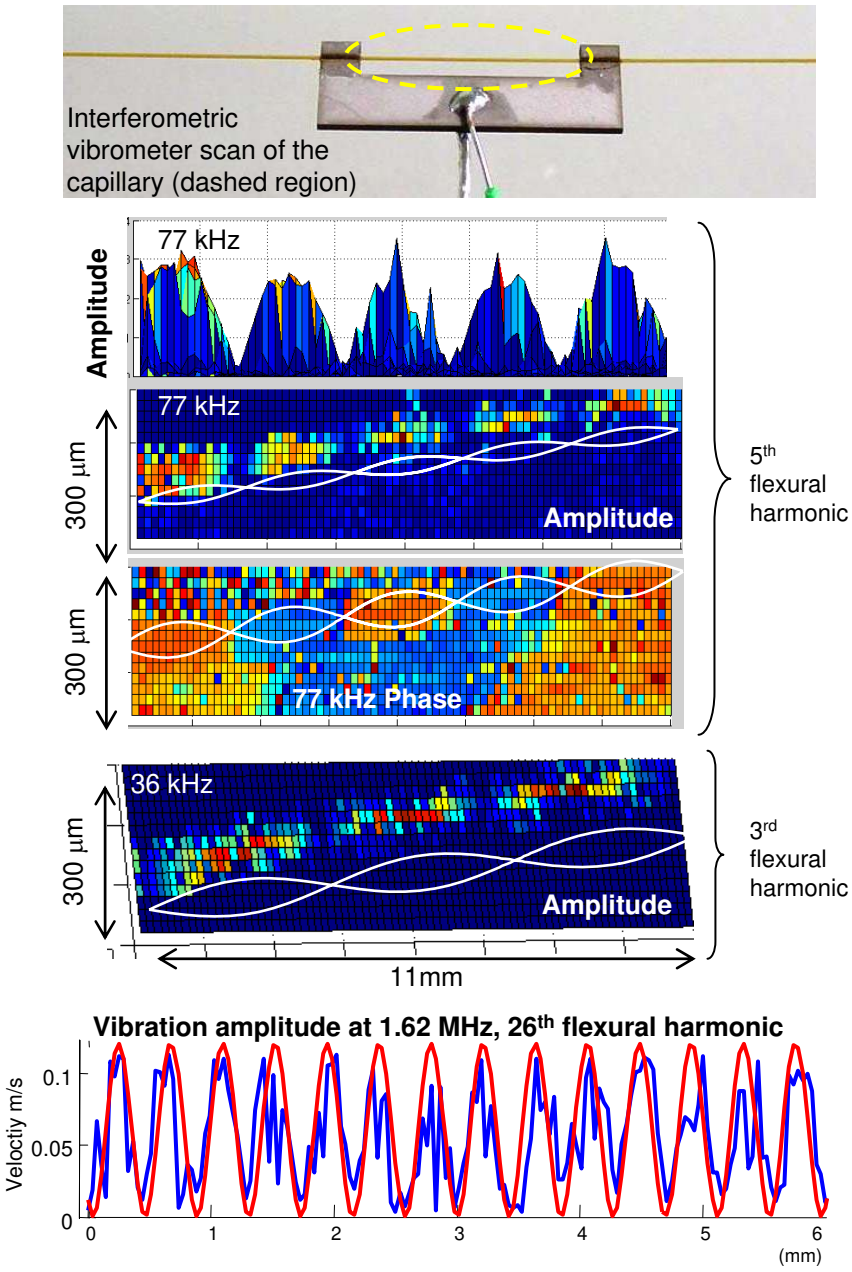

Figure 6.3: Interferometric laser Doppler scan of the resonating capillary regime reveals flexural modes at various frequencies. Here these scans are performed to reveal the mode shapes. A more detailed study on the amplitude analysis will be presented in the next couple of figures. While the top three scans include the whole capillary section shown in the dashed ellipse in the top image, the last scan at 1.6 MHz includes only half of the capillary and shows 13 peaks of 26.

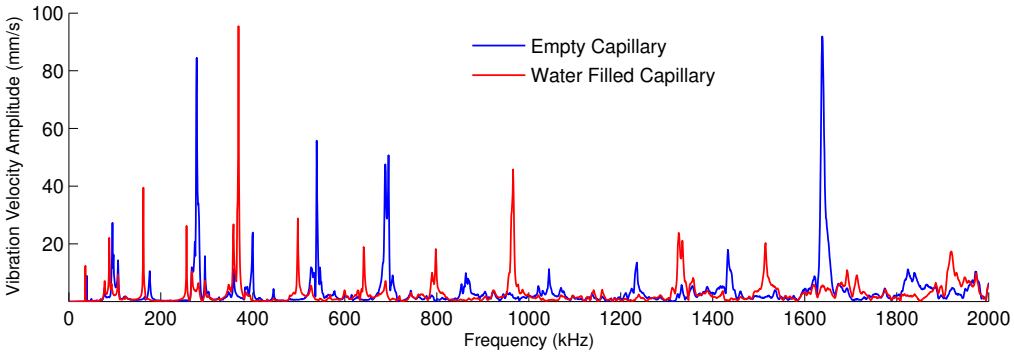

Figure 6.4: Interferometric laser Doppler scan (amplitude spectrum) of the center of the capillary for both empty and fluid filled capillaries. Since the measurements are done at the center of the capillary, peaks only show the odd modes. All even modes are suppressed because the middle point is a node in those cases. Curves reveal that fluid loading changes the frequency of the flexural harmonics significantly

and empty capillary cases, it can be concluded that except for the low frequency regime, there is a significant change in the frequency of the peaks because compared to the mass of the capillary, the mass of the fluid cannot be ignored and causes a significant shift in the peaks. Since the capillary internal radius and the capillary wall has the same length, the addition of the water increases the mass by more than 15%. Since the entire fluid is also pushed and pulled during the motion, in transverse modes, fluid loading shifts the resonance frequencies deliberately.

Plots in Figure 6.5 compare the vibration amplitude of the center of the capillary (in other words, odd numbered harmonics) with the electrical impedance of the PZT. Both the fluid loaded and the empty capillary cases are examined. Vibrational amplitudes are related to the beam mechanics of the capillary, and this is why they do not follow the impedance of the PZT plate. However, especially at frequencies where a flexural harmonic matches a mode of the PZT plate, a huge amplification of the vibrational amplitude can be observed. In experiments, this

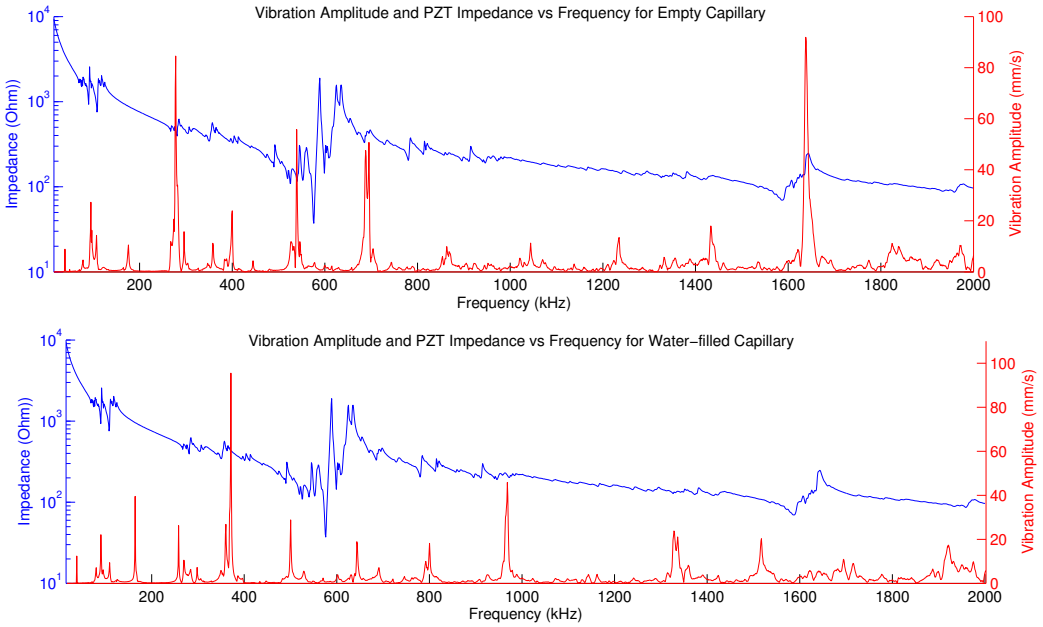

Figure 6.5: The vibration amplitude at the center of the capillary is compared to the electrical impedance of the PZT for fluid loaded and empty capillary cases. Plots show that at flexural harmonics where a PZT mode exists, vibration amplitude is amplified.

matching has also been observed that, while the voltage drive was kept constant, at various frequencies, particle collection happens faster. This is a very important information for device characterization. When designing future devices, enabling some the harmonics of the fluid loaded capillary to match resonance modes of the PZT may further device performance in terms of increasing efficiency during electrical signal to cavity acoustics transduction pathway.

Electrical power is related to the square of the voltage (V^2/R), and the kinetic energy of the flexural beam is related to the square of the velocity (mv_0^2). In this case, voltage drive and the vibration amplitude relationship is expected to be linear. Figure 6.6 shows that amplitude of the vibration increases linearly with the voltage drive. The slope of the curve also defines the conversion efficiency

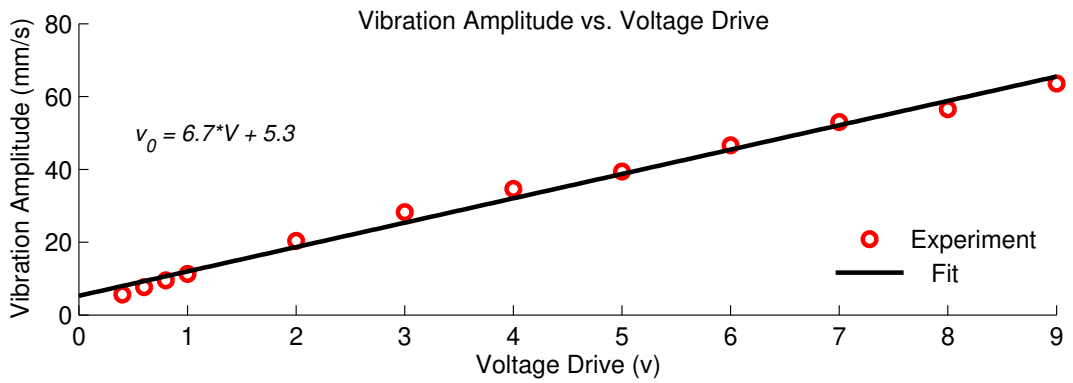

Figure 6.6: Vibration amplitude versus voltage drive. The plot reveals that vibration amplitude linearly increases with the increasing voltage. The slope of the curve is 6.7 mm/s/V.

which in this particular frequency is 6.7mm/s/V. This plot is not produced in one of the fundamental harmonics of the capillary and is just included to reveal the linear behavior in the vibration amplitude-voltage drive relationship. However, this is not the always case, for example, at frequencies such as around 77 kHz, 90 kHz and 300 kHz, PZT has resonance modes which can heavily couple to the capillary flexural modes. In this case, nonlinear oscillations are observed. At these frequencies, amplitude of the oscillation of the capillary varies in the range of 1–60 m/s. This is much higher than the maximum achievable particle velocity in the PZT (5 m/s). Such a case is shown in Figure 6.7. Interestingly, Fast Fourier analysis of these modes reveal that subharmonic modes of the capillary flexural modes are generated.[1] For example, the interferometric scan and experimental results confirm that around 77 kHz, the 5^{th} or sometimes the 3^{rd} flexural harmonics of the capillary is excited. Actual frequency of these mode, however, are around 90 kHz and 36 kHz.

[1]Subharmonic modes mentioned here should not be confused with the subharmonic and subwavelength stationary wave generation inside the capillary cavity mentioned before in the previous chapters. Here only the flexural modes of the capillary are mentioned.

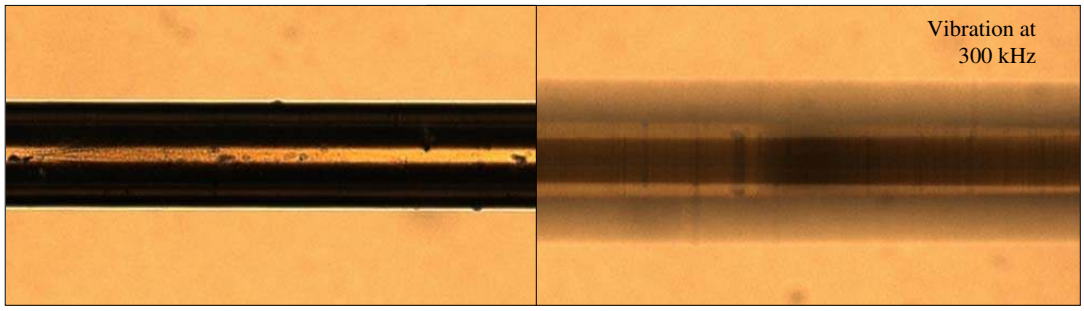

Figure 6.7: Microscope images of the capillary. On the left, actuation is off and the capillary is stationary. On the right, capillary is vibrating during a 300 kHz drive while the mode excited is a lower harmonic mode. Amplitude of the vibrations calculated from the observed displacement gives 1-60 m/s. Capillary diameter is 200μm.

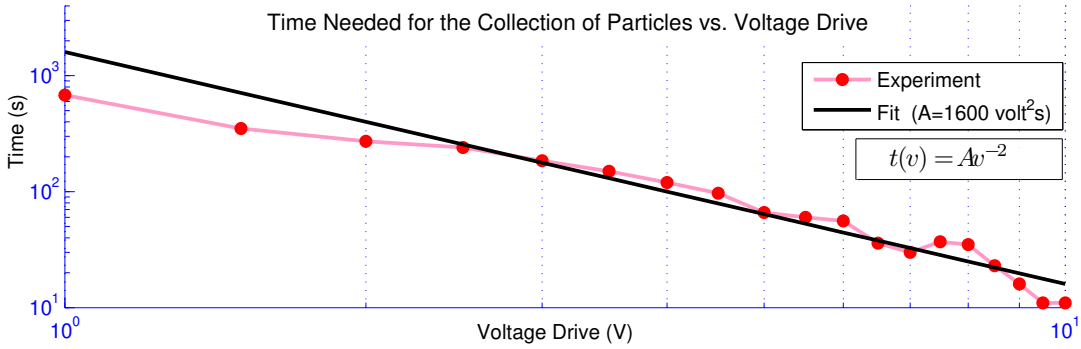

Figure 6.8: Particle collection time versus the voltage drive.

Figure 6.8 shows the collection time versus the voltage drive. It has been shown in the previous sections that collection speed of the particles depends linearly on the acoustic force ($v_s \sim F$) by Stokes law; acoustic force is related to the square of the vibration velocity of the capillary ($F \sim v_0^2$); and velocity of the capillary is linearly related to the voltage. In this case, collection speed of the capillary is expected to depend on the square of the voltage drive ($v_s \sim V^2$). Since the collection time is inversely related to the collection speed, collection time is related

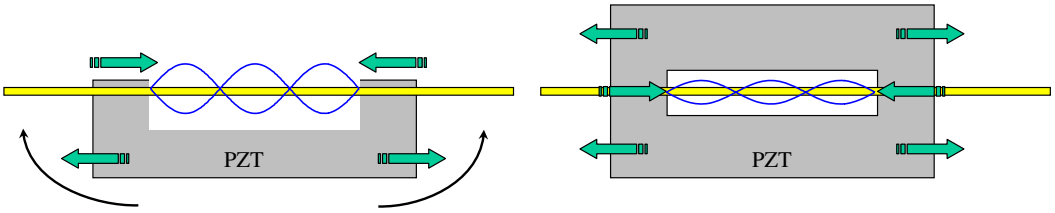

Figure 6.9: Asymmetric loading on the capillary and the relatively free PZT cantilever arrangements possibly increase the amplitude of the flexural vibrations.

to the inverse square of the voltage drive ($t \sim V^{-2}$).

Regarding device characterization, the last part is related to the efficient coupling of the PZT vibrations to the capillary. Figure 6.9 shows two actuator mechanisms. Experiments showed that the device on the right did not perform well in terms of particle collection and separation, which can be attributed to the fact that, free to move PZT cantilever ends and bending load generated by the asymmetric loading increases flexural coupling.

6.2 Applications

Applications of PZT glass capillary actuator in collection and separation of microparticles and biological entities are presented in this section.

6.2.1 Collection of Micro-Nanoparticles

As it was shown in Chapters 4 and 5, flexural vibrations generate subwavelength stationary acoustic pressure fields inside the capillary which lead to the particle

collection. Particles collect at the vibration maxima of the capillary and collection pattern follows the harmonicity of the capillary flexural modes. In Figure 6.10, microscope images (negative) show the collection spots over a broad frequency range. As expected from the theory given in Chapter 2, the wavelength of the flexural modes shows dispersive behavior.

In Figure 6.10, collected particles are 3 μm polystyrene beads, which have a density of 1050 kg/m^3. This is very close to the density of the water. As the acoustic forces are related to the density difference, many materials which have higher density differences than polystyrene–water case can be collected easily. Polystyrene beads are very functional in terms of bioanalytical assay related applications in the microfluidics. In this case, the actuator mechanism presented here may have many other application areas not presented in this study.

One interesting observation included in Figure 6.10 is that, at some frequencies, collection happens at the center of the capillary, while at some frequencies it happens along the capillary. This can be related to the coupling of the acoustic modes generated by the flexural motion and the plane acoustic wave modes along the capillary. Further study is needed for the mechanism of this possible coupling.

While the collection dynamics happen at the micro and nanoscopic regime, due to the high aspect ratio of the capillary (long length), results can be monitored with the naked eye. As shown in Figure 6.11, the collection of 500 nm silica particles are captured with a point and shoot digital camera, which enables monitoring of the system performance even with a simple camera included in a cell phone.

Images on the bottom of Figure 6.11 show the collection behavior of the actuator at different particle size limits. It can be observed that for particle sizes above

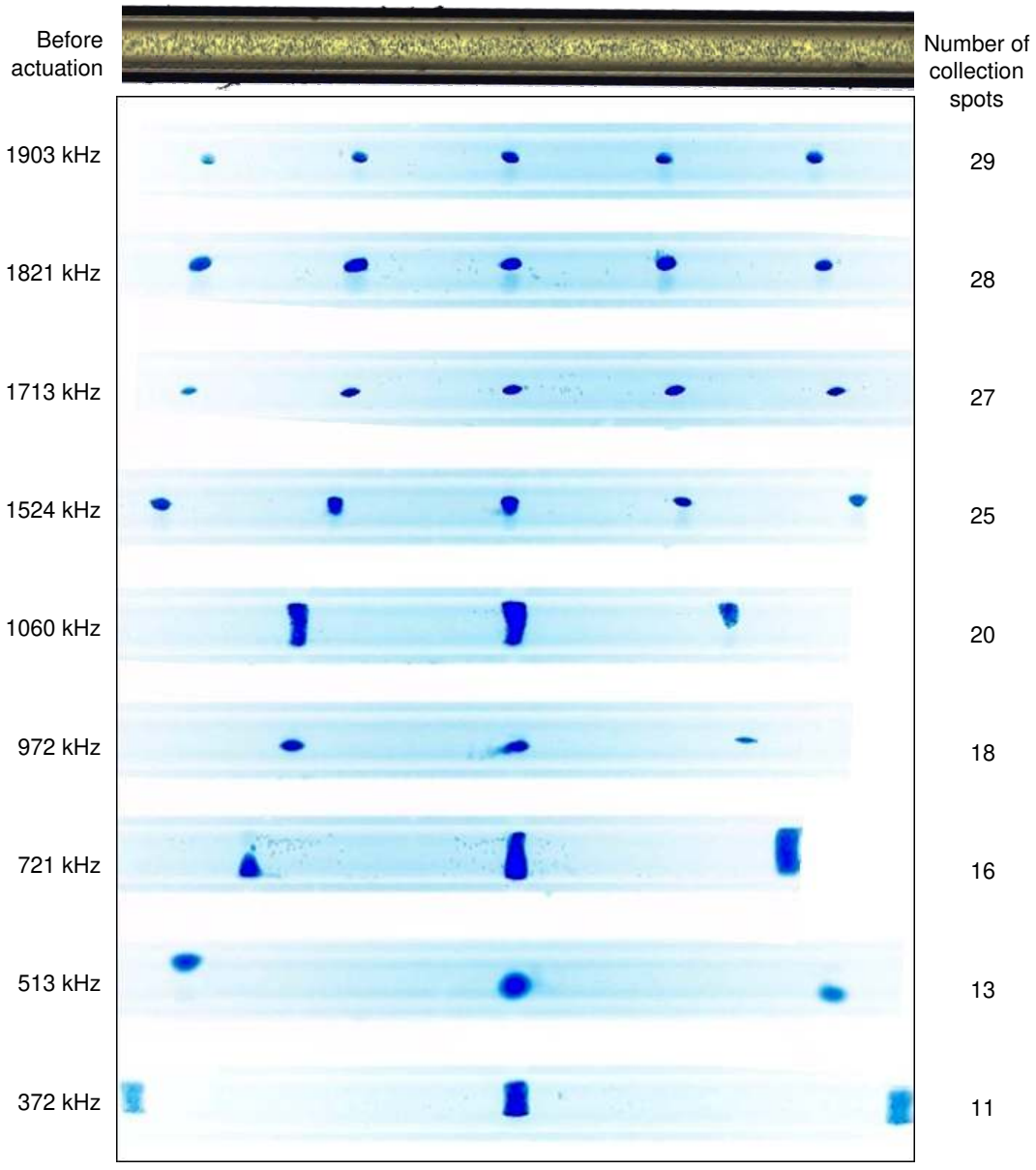

Figure 6.10: Collection of 3 μm fluorescent polystyrene beads at various flexural harmonics of the capillary.

a micrometer, these particles are tightly packed; however, as the particle size gets smaller, the acoustic radiation force decreases, and the collection location become cloudy due to Brownian motion. Still a substantial concentration difference is generated across the capillary which can be observed by the naked eye, as shown in the top images of the same figure.

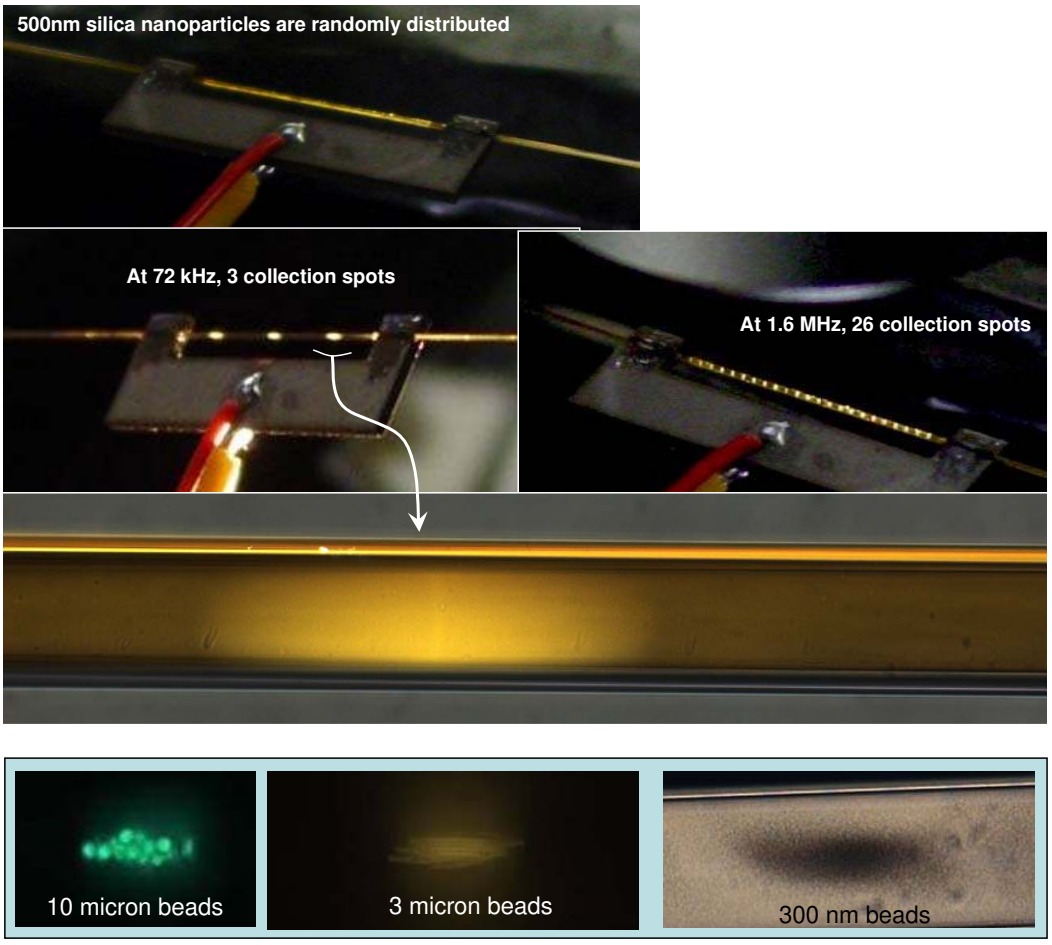

Figure 6.11: On the top, the collection of 500 nm silica nanoparticles under acoustic actuation are shown. The pictures on top are taken with a hand held point and shoot digital camera. The picture in the middle shows the microscope image of collection. The series of pictures on the bottom reveal that as the particles size goes to the submicron regime, a closed packed collection style leaves its place to a cloudy collection.

6.2.2 Collection of Cells and Bacteria

Since all materials have unique material properties which are different than the fluid medium in which they are suspended, acoustic forces can be used to manipulate almost all materials. Biological samples such as bacteria and cells also fall in this wide category. The typical size for the bacteria is in the 2-8 μm range and for the cells it is in the 2-20μm range. This range of particles can be efficiently collected in the PZT-glass capillary actuator.

Figure 6.12 shows the collection of various biological samples. On the top, mice sperm cells (not live) are collected at a vibrational maxima. This method can be used to separate healthy sperm cells from the unhealthy ones. Healthy sperm cells are good swimmers targeted to find the egg cell for fertilizing. After sperm cells are collected, a slow flow can be introduced to the medium and radiation force can be adjusted in a way that good swimmers can statistically run away from the collection spot. In this way while bad swimmers are captured in the acoustic traps, good swimmers can be transported with the flow. The second and the third line of images show collection of Escheria Coli bacteria under ultrasonic actuation in which bacteria concentration at certain locations is drastically increased. The image on the third line shows the increased light scattering from the right section of the capillary due to the collected bacteria. In the food and health industries, detection of bacteria significantly depends on the concentration and detection of very pathogenic bacteria at low concentrations which need treatments to increase the concentration. The actuation mechanism might be helpful in this area.

The images in the fourth and the fifth line of Figure 6.12 show collection and growth of HeLa cells inside the capillary. While this part is under development, by using acoustic radiation forces, three dimensional surface free cell growth might be

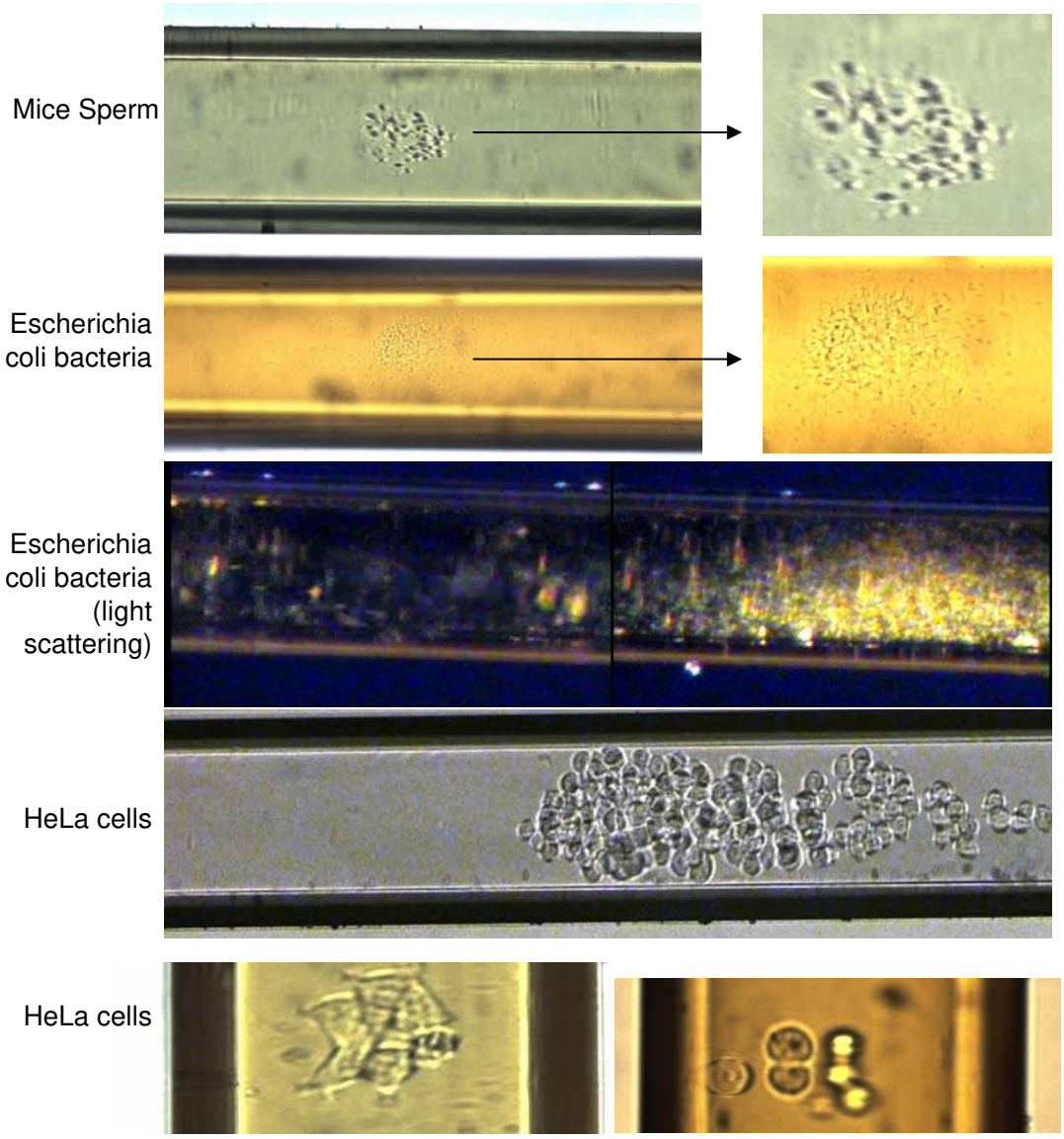

Figure 6.12: Collections of the biological cell samples are presented. On the top, thawed mice sperm cells are collected. Pictures in the second and the third line show the bacteria collection. Bacteria were alive and actively swimming during and after the actuation. Images in the fourth and the sixth lines show HeLa cells collected in a vibrational antinode.

possible. Since stem cells differentiate depending on their community and spatial location, this may have new application possibilities in stem cell research.

6.2.2.1 Safe Zone for the Biological Samples

In microbiology labs acoustic horns are used to damage cells and bacteria so that the proteins and organelles can be released to the fluid in which they are suspended. In the low kHz frequency regime, high amplitude acoustics generate cavitation. Cavitation is a nonlinear phenomenon in which generation of the gaseous bubbles occur due to the high amplitude of the sound. As soon as these bubbles are generated, as shown in Section 6.2.7, they start to oscillate. When they are not confined, they also move. These energetic micron size bubbles can generate enough shear stress in their fluid neighborhood and damage the cell wall.

In our experiments, except for very highly coupled sub 100 kHz frequencies, cavitation has not been observed. In the case of the E.Coli bacteria sample mentioned above, bacterium cells were alive and were swimming even during the actuation.[2] In addition, experiments with cells also revealed that most of the cells continue to grow. One challenge regarding cell growth in a capillary is that cells need nutrition, oxygen and carbon-dioxide to grow. This requires a supply of materials through a continuous flow. In our experiments, a supplement flow was not included. In future cell biology related applications, this flow can be generated by electroosmotic or pressure driven flow.

[2] A video recording showing the collected bacteria while swimming is available from the author upon request.

6.2.3 Separation of Materials with Respect to Acoustic Properties

It was shown in Chapter 5 that the sign of the acoustic radiation force depends on the acoustic factor. As was shown in Figure 5.2, materials which have positive and negative acoustic contrast factors feel forces in the opposite direction, which enables particle separation related to the acoustic contrast factors. Details of this process are given in Section 5.1.3.3. Figure 6.13 shows the separation of air bubbles and 500 nm silica beads under actuation. While 500 nm silica beads collect at the pressure nodes generated at the vibration maxima, air bubbles are collected at vibration nodes. In the images, locations where particles are collected are blurred due to the motion of the capillary, whereas the the image looks sharp at the vibration nodes where bubbles collect. Most of the materials which have creaming

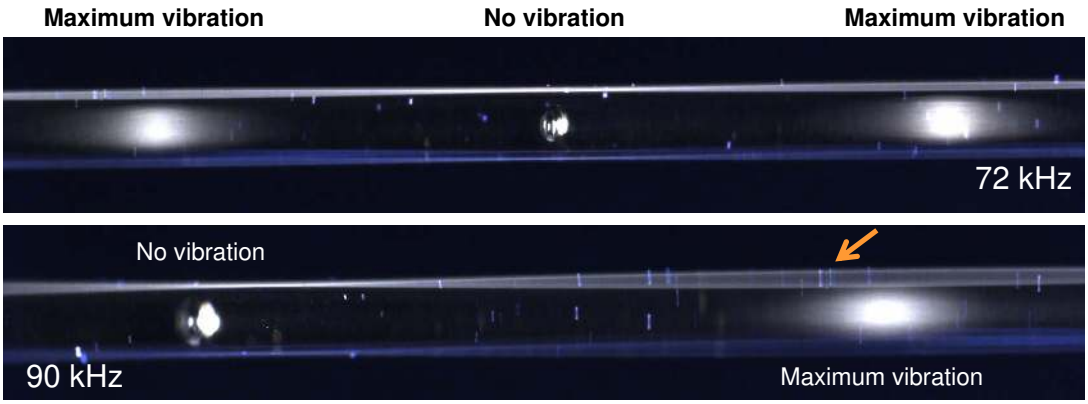

Figure 6.13: Demonstration of separation of materials with respect to the acoustic contrast factor. Here 500 nm silica beads are collected at vibration nodes where acoustic pressure nodes are formed, and air bubbles are collected at vibration nodes. The orange colored arrow points out the motion of a micron size dust particle oscillating with the capillary. (As a scale, the capillary diameter is 200µm.)

effect in the fluid they are suspended in will behave in the same way as the bubble shown here.

6.2.4 Experiments on Blood

As is shown in the previous section, materials can be separated with respect to their acoustic contrast factor. Blood is a very complex fluid. Almost half of its volume is formed by cells of various sizes, and the plasma includes thousands of different proteins, lipids, sugars, or simply whatever the individual ate a few hours ago. Experiments performed with fresh canine blood reveal that as happens in the case of the silica-air bubble mix, red and white blood cells are collected in the vibration maximas, whereas fats and some platelets are most likely collected at the vibration nodes, as shown in Figure 6.14. As in the previous cases, separation bands can be seen with the naked eye and be captured by a point and shoot camera.

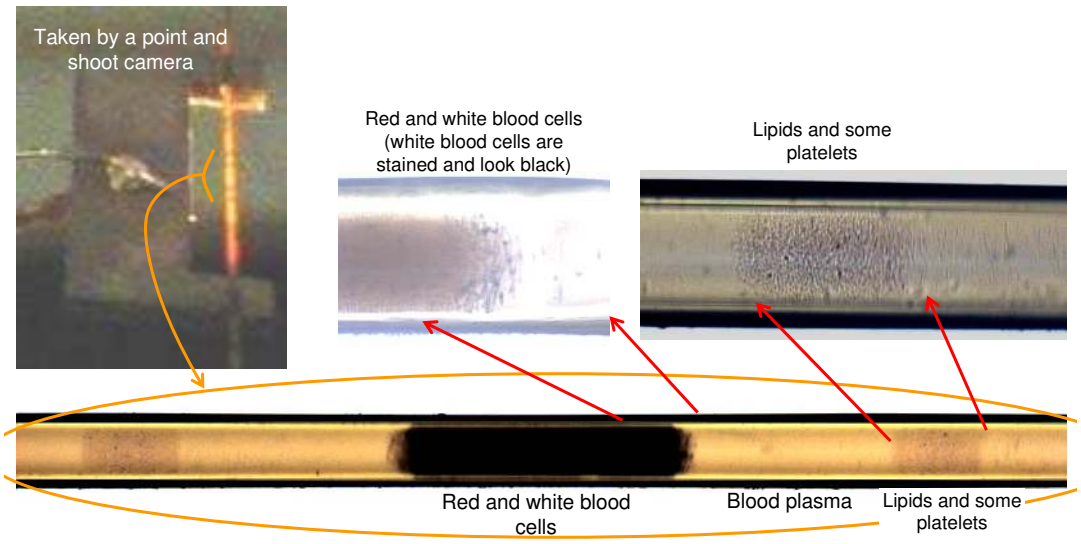

Figure 6.14: Planar chipscale centrifugation of blood components via ultrasonic actuation.

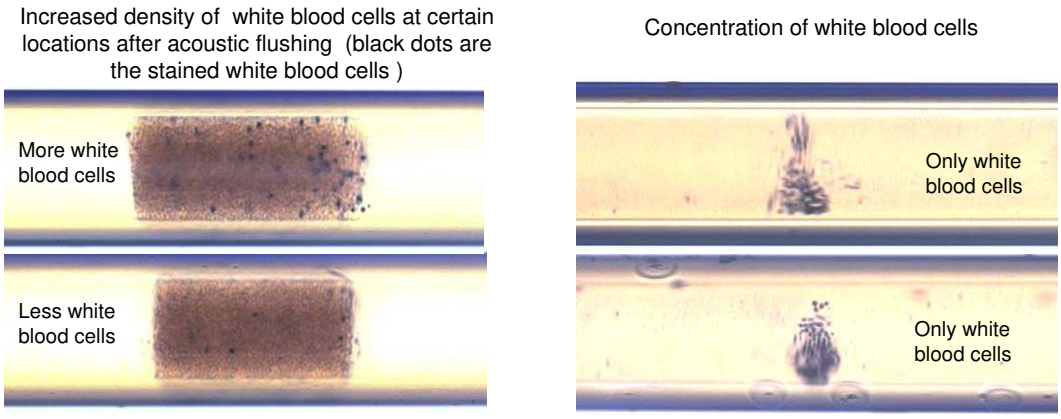

Figure 6.15: The pictures on the left show increased white blood cell number density after a portion of the red blood cells are flushed away. Here, the white blood cells are stained for imaging purposes and appear black. At certain collection spots, collection of only white blood cells can be observed.

The actuator mechanism presented here performs as a chipscale planar centrifuge for the initial separation of blood components. In hematology experiments in which mice is used, blood sampling influences the metabolism of the mice. In order to prevent that, a very small volume of blood sampling is needed requiring small volume bioanalytical equipment. The actuator presented here may help in that area.

One interesting effect that happened during the experiment is that, due to the high amplitude vibrations generated at the free ends of the capillary, some portion of fluid enclosed inside the capillary is acoustically pumped away. During this flow, many of the cells were also flushed out. When the remaining samples were re-concentrated, it was observed that at some collection spots, concentration of the red blood cells were significantly lower. In fact, there were spots where only white blood cells were present. In other words, most of the red blood cells were flushed away so that the concentration of the white blood cells was selectively enhanced.

Resulting pictures showing the concentrated white blood cells after the flush of red blood cells are shown in Figure 6.15. White blood cells are stained with methylene blue, which is why they appear as black colored cells. One explanation for the separation observed here might be as follows: white blood cells are two to three times larger than the red blood cells and the acoustic drag during the flushing of the fluid might have lead to a concentration of white blood cells.

6.2.5 Separation of Microparticles with respect to Size via Mode-switching

As it was shown in the two previous sections, acoustic radiation forces lead to particle separation, depending on the acoustic contrast factor. Another nonlinear acoustic phenomenon that happens near an oscillating surface is acoustic streaming. In a closed cavity, an acoustic streaming effect generates circulating vortices. These streams also capture particles and keep them circulating. Acoustic radiation forces scale with the cube of the particle size, whereas the streaming related Stoke's drag force scales down linearly with particle size. In this case, as the particle size gets smaller, a limit exists in which acoustic radiation forces become smaller than the drag forces. In such a case small particles can be captured in the stream while the bigger particles are held by the radiation force. By this method, as shown in Figure 6.16, an initial mixture of 10 μm blue fluorescent and 3 μm yellow fluorescent polystyrene beads can be separated. At 72 kHz, 10 μm beads collect at the vibration antinodes, whereas 3 μm yellow beads are captured in the stream vortices generated at the vibrational nodes. However, at this frequency (72 kHz), yellow beads span a wide circulation range. To eliminate this, frequency can be shifted to 335 kHz, in this case, the 10th harmonic of flexural mode. In this case,

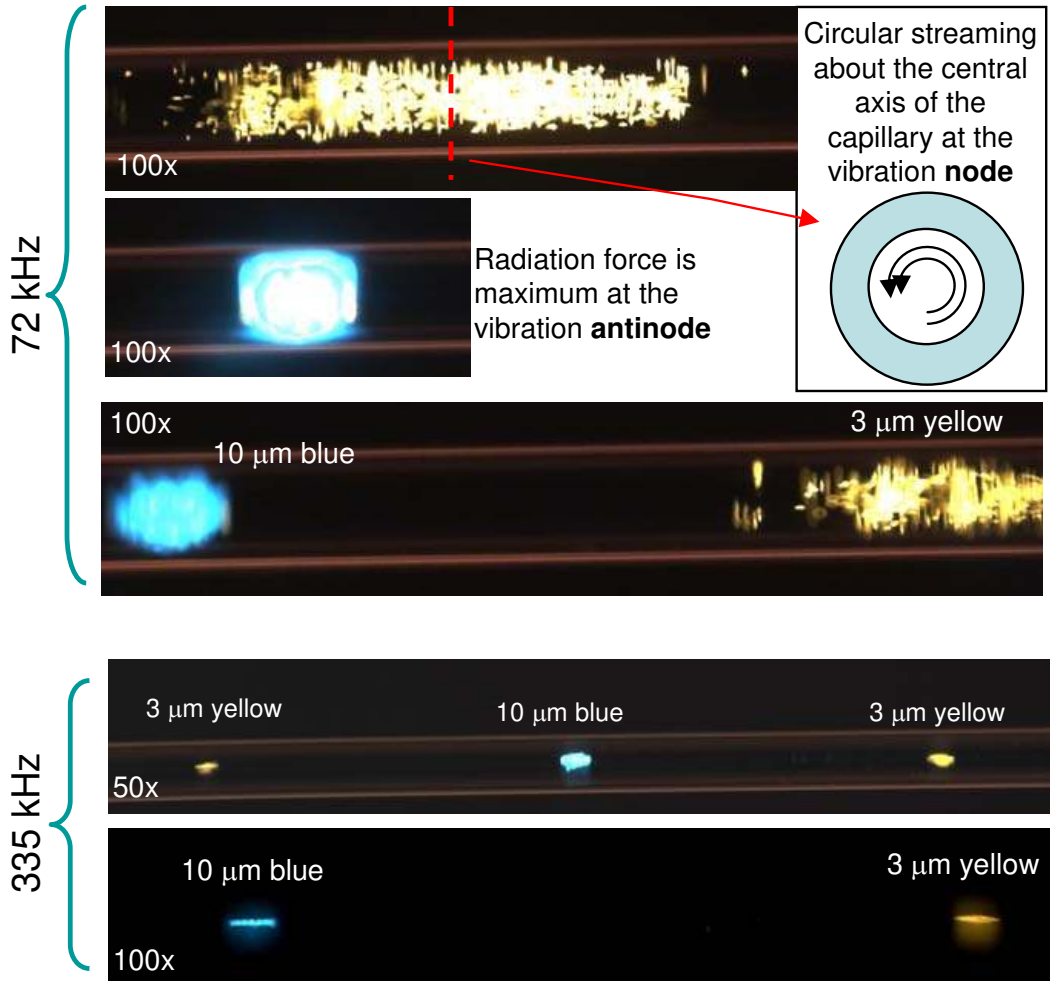

Figure 6.16: Separation of 10μm and 3μm polystyrene beads. At 72 kHz, 10μm beads are captured at vibration antinodes by acoustic radiation forces, whereas 3μm beads are captured in the circulatory acoustic streaming. Switching the resonance frequency to a higher harmonic value of the flexural mode, yellow beads are also captured in a close neighborhood.

a pressure node is generated near the circulatory yellow beads and all beads in the neighborhood are captured. Since the acoustic forces increase with the frequency (Section 5.1.3.2), smaller beads can be captured without any difficulty in a higher harmonic. In this way, beads are localized and separated up to an almost

millimeter apart.

During the separation process mentioned above, blue beads are always stopped by the radiation forces and never captured in the stream. However, in some cases, some portion of yellow beads cannot be fully captured by the stream and get caught by the radiation forces. In this case, locations where yellow beads are captured consist of 100% yellow beads; however; in some experiments, it has been observed that at the spots where blue beads are captured, some yellow beads can be found. However, these beads can still be further separated locally as pictured in Figure 6.17. A fully developed explanation of such a separation needs further investigation but a rough explanation would be as follows: acoustic radiation forces are spring like forces and they become zero at the acoustic pressure nodes. In this case, if a net force is applied to a particle in a certain direction, the particle will move towards that direction until the radiation force gets high enough to balance that applied force. In this case, stokes drag force applied by the slow streaming balances different sizes of particles at different locations which may lead to the observed local separation. Another reason would also be related to the scattering of the primary acoustic field by the large beads collected at the center of the pressure nodes. These scattering effects may modify the net acoustic field such that a secondary minimum can occur in the close neighborhood of the primary minimum.

6.2.6 Mixing

The PZT-Glass capillary actuator presented here can also be used for mixing analytes, beads or fluids which can be a challenge due to the laminar flow governed microfluidics. Figure 6.18 shows the mixing process of the 3μm and 10μm beads

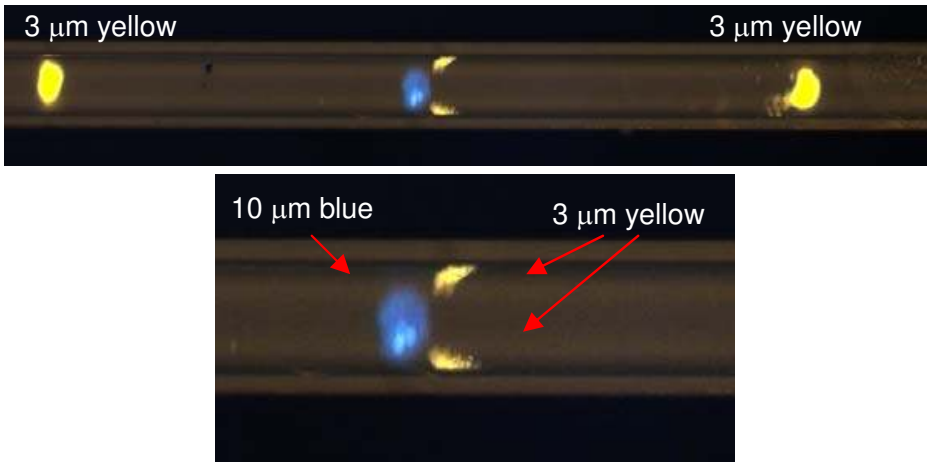

Figure 6.17: While large beads are never captured in the flow field and small beads form 100% pure collections, yellow beads in some experiments get caught by the radiation force so that the acoustic pressure nodes consist of mostly large and some small beads. However, at certain frequencies, these can get further separated locally, as shown here.

which were separated by the methods presented in the previous section.

The greater proportion of this dissertation focuses on the flexural modes of the capillary; however, it is shown in Chapters 2 and 4 that longitudinal and torsinal modes also exist in 20kHz–2MHz frequency regime. In addition, there are frequencies in which no resonance mode of the capillary is found, but due to the PZT resonance, huge amplitude vibrations are coupled to the capillary. This kind of actuation generates propagating waves on the capillary and in the fluid enclosed in the capillary. These interactions lead to statistically semi-controlled motion inside the capillary similar to the process of stirring sugar inside a cup of tea with a spoon. In such a process, while the action and the aim are clear, events taking place are completely chaotic though controllable. In this way, as shown in Figure 6.19, *microstorms* can be generated inside a microscopic cavity which lead

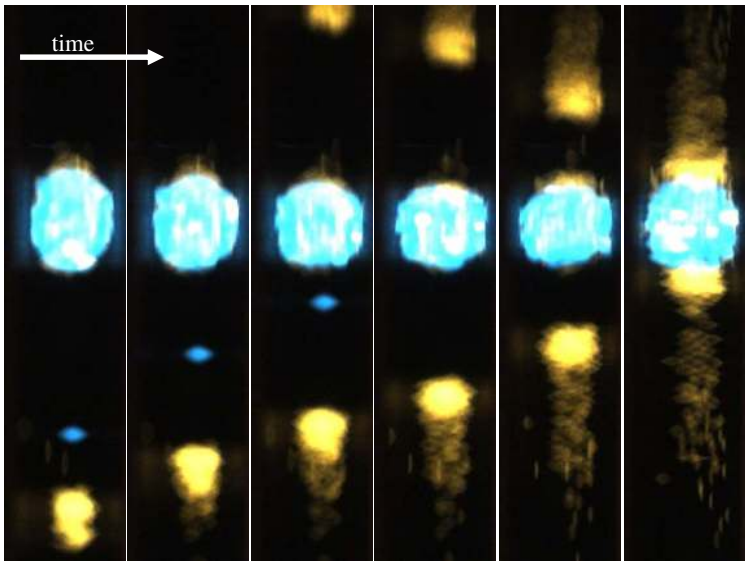

Figure 6.18: Mixing of the 3μm and 10μm polystyrene beads. Beads were previously separated by the acoustical methods presented in the previous section.

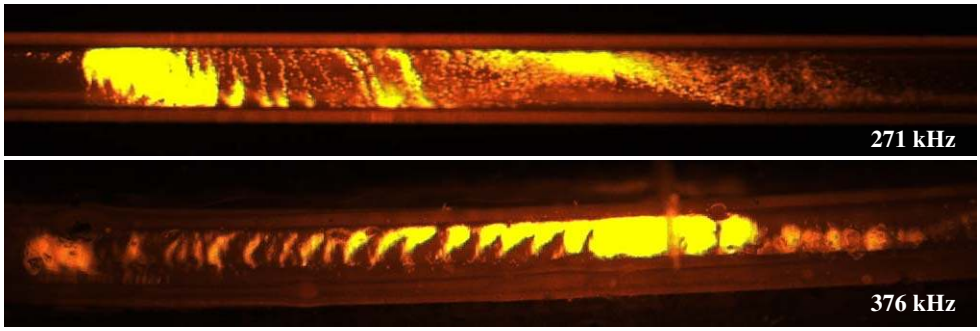

Figure 6.19: Micro"storms" generated inside the capillary can enable fast and efficient mixing in a laminar flow governed regime.

to fast and efficient mixing.

6.2.7 Bubbles

At the resonance modes of the PZT plate, capillary ends suspended freely outside the resonating regime can vibrate rigorously. These very high amplitude oscillations create vibration amplitudes in the order of 10 mm/s or higher. During those vibrations, cavitation effects can be observed and bubbles are introduced into the cavity. These micron size bubbles oscillate at their resonant frequencies and their subharmonics. These high amplitude bubble vibrations generate well-defined streaming jets. As shown in pictures in Figure 6.20, these jets can capture particles randomly suspended in their neighborhood. As illustrated in the top image, there are no particles left in the central zone where two bubbles are oscillating. At the edges, however, freely suspended particles can be observed. Orientation of these fluid jets depends on the vibrational mode of the bubble and so changes with the frequency; a slight change in the drive frequency around the resonance is enough to modify the orientation of the jets. In addition to particle capture, these jets can also be used as a tool to investigate vibrational modes of the bubbles.

The use of oscillating micro-bubbles for microfluidic applications is a another research field which is beyond the scope of this thesis. Here, the method is briefly mentioned as another method to generate and control the bubbles. Since the bubbles are enclosed in a capillary control and monitoring of them can be easier.

Another interesting phenomenon observed during the experiments is that a large bubble is observed to decay in the order of roughly 10-30 seconds. The decay of the bubble was steady, and when the actuation was released the bubble did not appear back. This observation is presented in Figure 6.21.

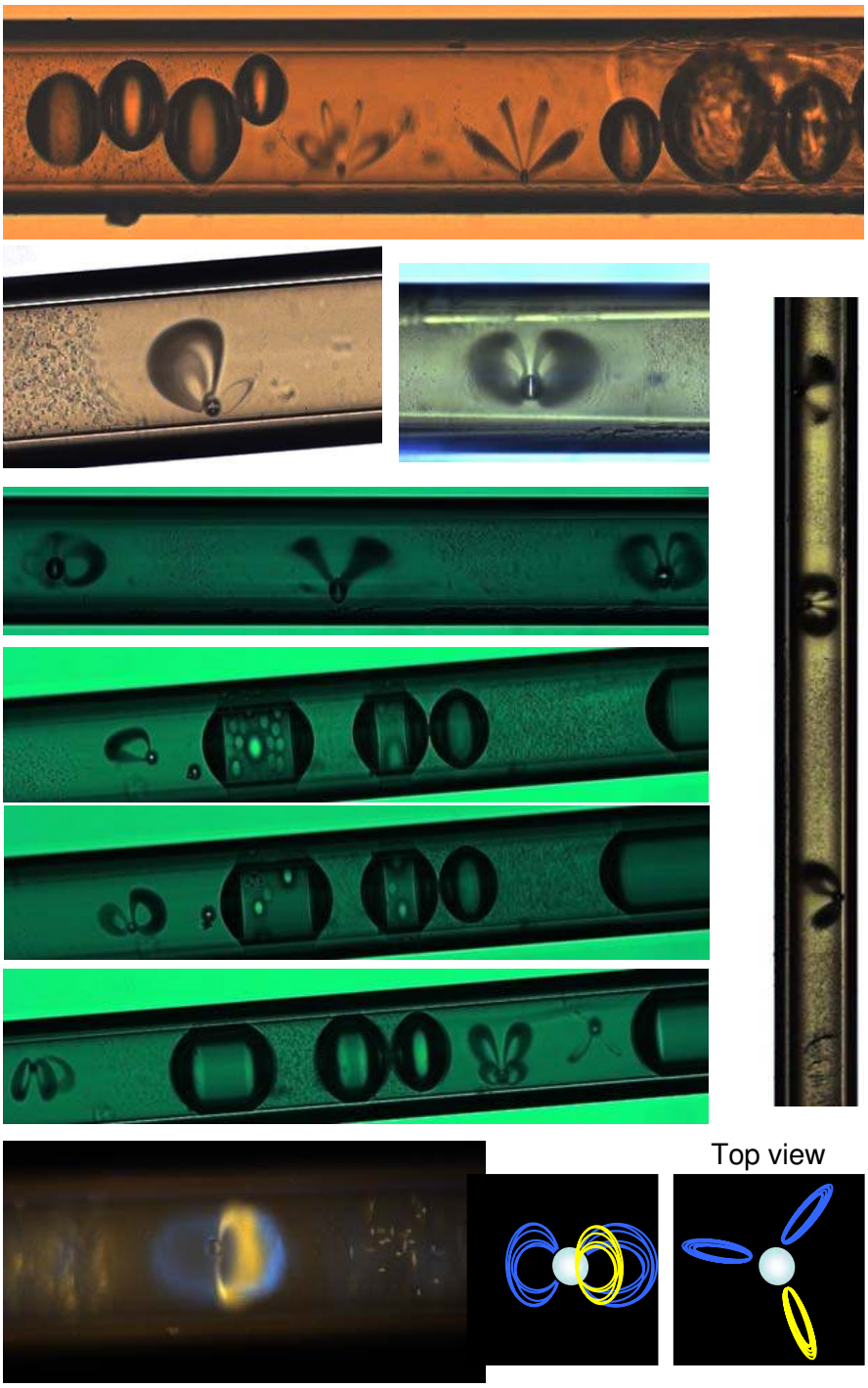

Figure 6.20: Bubbles generated due to cavitation can be forced to oscillate because of the ambient acoustic field. Vibrational modes of the bubbles generate streaming jets in which particles suspended in the neighborhood are captured.

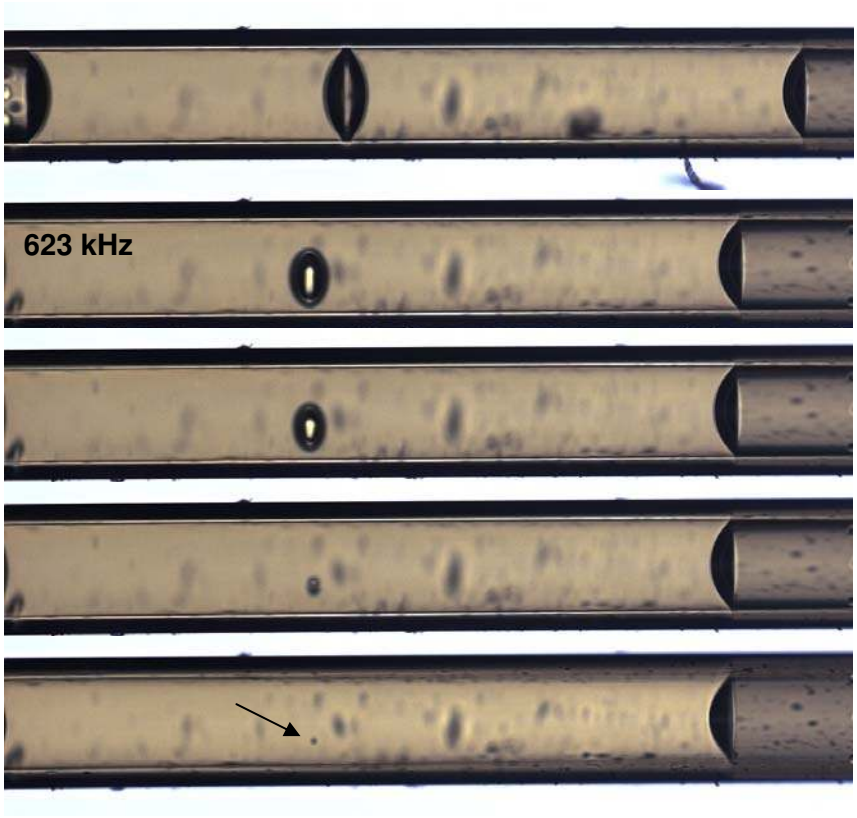

Figure 6.21: Fast decay of a large bubble under ultrasonic actuation. Decay is observed to take place in the order of 10-30 seconds roughly.

6.2.8 Alignment of Asymmetric Microparticles

Until now, most of the particles or biological samples tested in the PZT-glass capillary actuator were round or ellipsoid particles. Here, collection behavior of thin film silicon dioxide (glass) tablet letters is presented. C-O-R-N-E-L tablet letters were fabricated in a way that from C in the beginning to L at the end, particle size goes from biggest to smallest. Few of these letters can be seen in the top picture of Figure 6.22. In the experiments, it is observed that the acoustic field did not regard the letter size difference very much because of the huge asymmetry and high aspect ratios of the particle dimensions. In the acoustic field, these letter

tablets are aligned with respect to the orientation of the acoustic field and can be used as alignment markers helping to find out the orientation and distribution of the acoustic field. The second line of pictures presented in the same figure reveals different angle of orientations at different frequencies. The picture on the right edge also reveals the two sets of collected tablets with a gap comparable to the observations presented in Figures 5.18 and 5.19.

Because glass has strong a density difference (2200 kg/m^3) with water (1000 kg/m^3), it quickly sediments due to gravity. Applying the acoustic forces gradually enables lifting of the structure in a controlled manner. This moment effect may have potential applications in terms of lifting high aspect ratio sedimented particles.

6.3 Other Interesting Observations

6.3.1 Wavy Collection Pattern

As shown in the top picture of Figure 6.23, in most cases, particles are collected at the center of the capillary. However, at some frequencies, these collections are not centered but follow a wavy pattern inside the capillary. This happens in both higher and lower frequencies, but is easier to observe at higher frequencies due to the lower wavelengths. While further investigation is necessary, these secondary effects may stem from coupling of other modes such as capillary longitudinal and torsional modes or acoustical cavity modes, which are the plane modes along the capillary. Another possibility might be the helical wave propagation over the cylinder walls. When an acoustic wave propagates along the cylinder, there are three dimensions

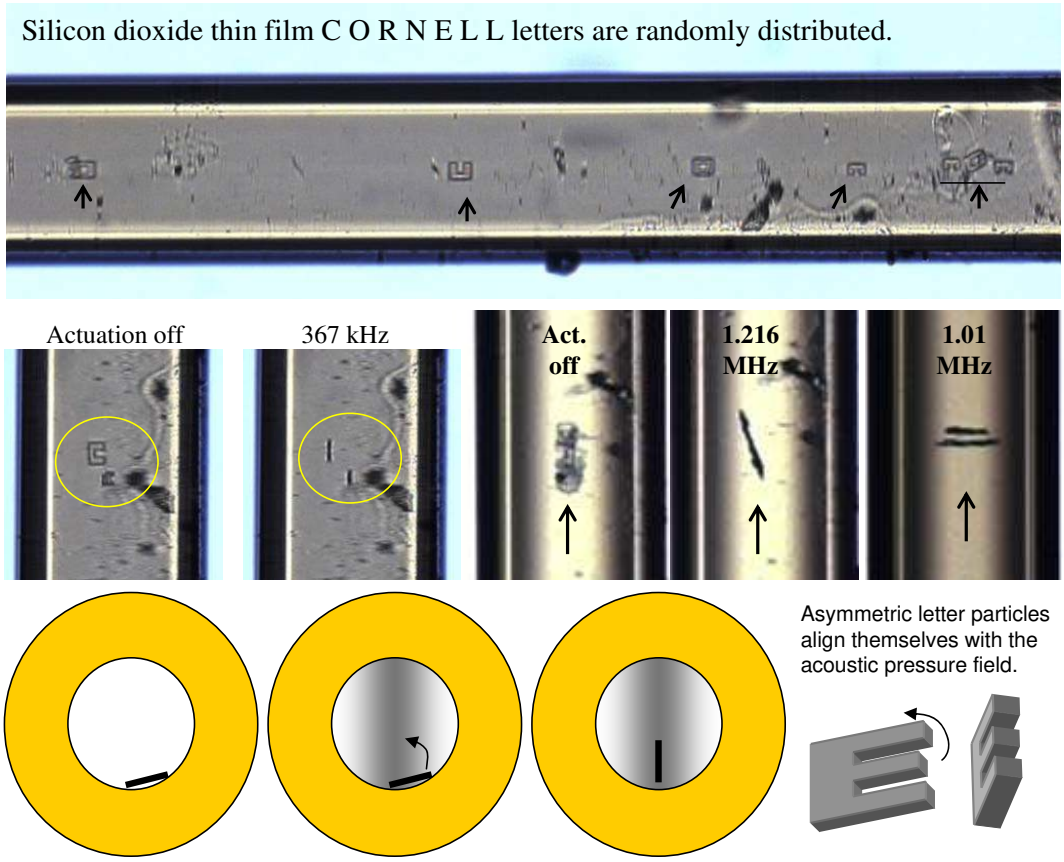

Figure 6.22: Silicon dioxide thin film letter tablets inside the capillary are shown in the top image. Due to the high aspect ratio of the tablet letters, they align themselves with respect to the acoustic field. A gradual increase of the acoustic field generates a moment lifting up the particles sedimented due to the gravity.

it can propagate: radial, angular and along-the-axis directions. The thickness of the capillary in radial direction is very short and resonance frequencies are in much higher frequency regime. And in regular analysis of the flexural modes, only the propagation in the axial (z) direction is considered. However, elastic disturbances can also propagate in the angular directions. When combined with the propagation in the axial direction, waves propagate in a helical manner. Another version of this case was briefly sketched in Figure 4.7. In short, further analysis is needed to

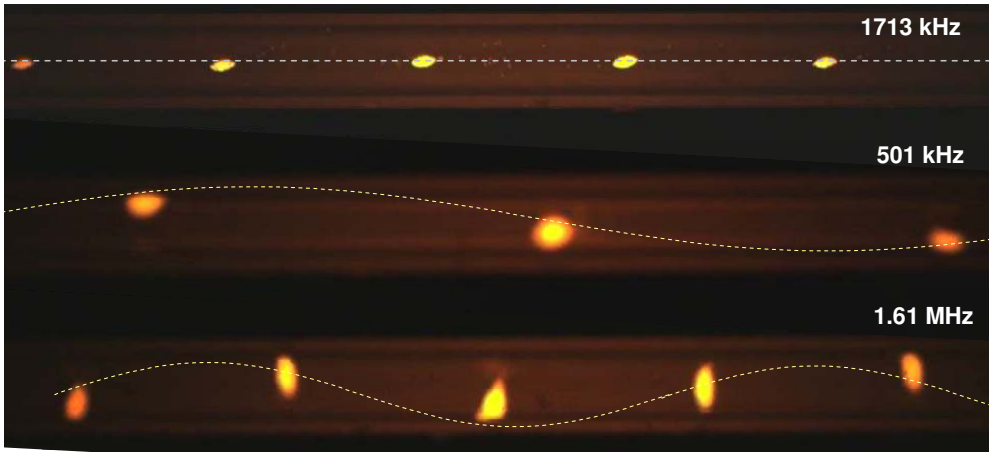

Figure 6.23: In most flexural harmonics, particles collect at the center of the capillary, as shown in the picture on the top. However, at some frequencies, collection locations follow a wavy pattern.

achieve a formal conclusion.

6.3.2 "Designer" Collection of Submicron Particles

At higher frequencies, during the cloudy collection of submicron particles, beautiful shape collection patterns occur. Such collections are shown in Figure 6.24. These splendid artistic patterns may also help to characterize the acoustical microcavity in future studies.

6.3.3 Extreme Slow Waves

When particles are suspended inside the capillary and no actuation is applied, they gradually sediment to the bottom of the capillary. As shown in Figure 6.25,

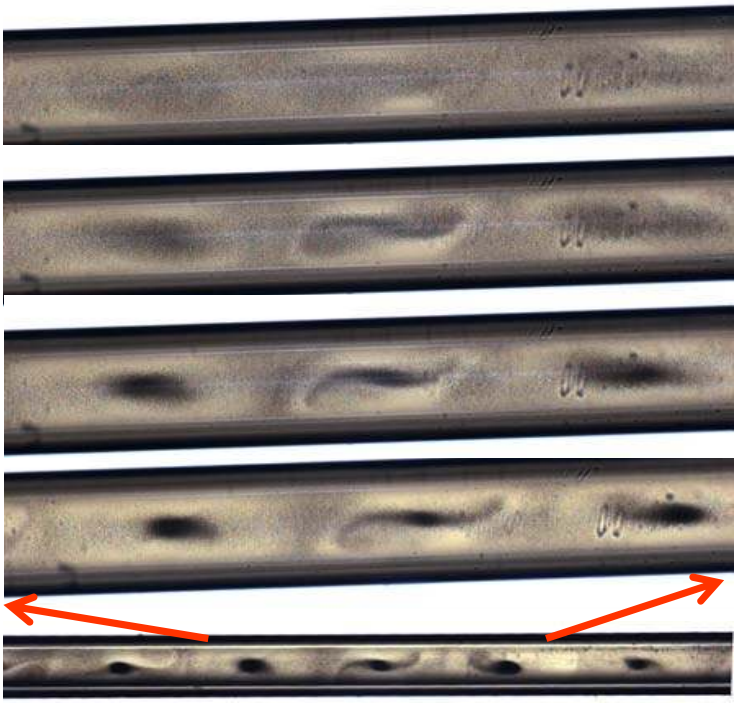

Figure 6.24: Formation of artistic shapes during the collection of submicron particles.

it can be observed that when the particles are at the bottom and in contact with the capillary surface, and the actuation is turned on, they instantaneously form collection patterns with a period of 20-60 μm. These patterns do not form when the particles are suspended. Similar patterns are also generated in another micro actuator mechanism presented in Figure 8.18, which utilizes plane acoustic modes. These periodic formations correspond to a wave speed of 2-10 m/s, an extremely low wave speed to appear in an elastic medium. This is an extremely low wave speed to be appear in an elastic medium. These formations can be related to the striations observed in the Kundt's tube experiments.

In addition, surface waves with similar wavelengths are observed in a water

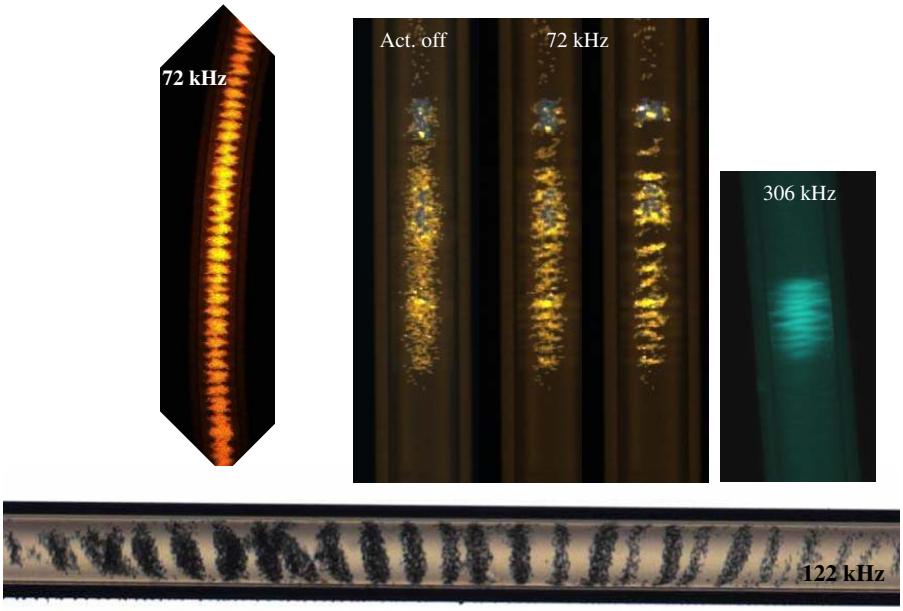

Figure 6.25: When particles sediment to the bottom of the capillary and the actuation is turned on, these particles form periodic collection patterns on the bottom of the surface with wavelengths in the order of 20-50 μm.

Figure 6.26: In a fluid thin layer, generation of Faraday waves is presented.

meniscus left on the capillary walls. When the actuation is on, the periodic wave pattern forms, and that can be seen in Figure 6.26. These waves have wavelength of 60 μm at 79 kHz which result in wave speed of 5 m/s. These waves are possibly the Faraday waves observed at the microscale.

CHAPTER 7

COLLOIDAL DYNAMICS AND MICROACOUSTICS

Introduction

In this chapter, the behavior of charged colloidal suspensions under ultrasonic concentration and their dispersion behaviors after the release of the acoustic forces will be introduced. The results presented here may lead to new bio-analytical techniques at the microscale, which may serve as the microscale alternative to bulky centrifugation systems. The technology can also be used in drug testing.

The typical time line for a drug to be available in the pharmacy takes 12-20 years from the beginning of the project including FDA approval. The total cost of such a development process is in the order of few hundred million dollars [86]. All the necessary tests performed at different stages of development contribute to the increase in the amount of preparation time and the cost of the product such as valuable protein samples. The investment is risky as not all innovative projects pass the necessary stages and become marketable products. In this regard, microfluidic systems are promising for reducing the possibility of fast and accurate characterization of new drugs with low sample use.

This chapter consists of three major sections. In the first section, theoretical and practical background information on colloidal systems is given. Major attractive and repulsive interactions between suspended particles which lead to colloid stability are also introduced in this section.

In the second section, dispersion of colloidal particles after release of acoustic forces is investigated. Before the release of the acoustic forces, particles were

concentrated at preferred locations due to the acoustic forces present. Results prove the generation of a macroscopic electric field, when charged particles are collected at preferred locations. After the release of the acoustic force, this self generated electric field leads to fast dispersion of the particles (few hundred times the rate of regular diffusion). From the dispersion speed and independent zeta potential measurements, the magnitude of the electric field is estimated.

In the third section, characterization of the collective behavior of colloidal systems under acoustic forces is presented. In the first part of this section, zeta potential-particle stability relation is re-demonstrated by use of PZT-glass capillary actuator. In addition, it is shown that PZT-glass capillary actuator can be used to monitor and estimate long term stability of the colloidal systems with relatively short experiments.

The second part of the third section is related to the calibration of acoustic forces against the counterbalancing dispersive forces. While collecting particles at preferred locations, the acoustic force fights against the dispersive electrostatic forces. As the particle concentration increases at the collection points, the electric field reaches a limit to balance the acoustic force. Through the approximate value of the electric field obtained in the second part, the order of magnitude of the acoustic force is obtained. While the acoustic forces can be calculated through first order approximations, strongly nonlinear behavior at some frequency regimes require a measurement-based calibration of the acoustic force. As the actuator mechanism presented here can be potentially used on biological entities, an empirical way of estimating acoustic pressure amplitudes would be helpful so that amplitudes where disruption begins can be strictly prohibited.

7.1 Colloids and Electrochemistry

7.1.1 Colloids: A Short Definitive Introduction

The term colloid can be defined as a system of two substances, in which one substance is distributed evenly in a discrete phase throughout the second substance of continuous phase. The dispersed materials, and the continuous medium they are in may be in gaseous, liquid or solid phases. Macromolecules can also be the dispersed materials. In most cases, dispersed phase substances show colloidal behavior in the size range of 1-1000 nm [87].

Under the umbrella of the above definition, systems such as, fog, smoke, styrofoam, milk, paints, fruit ciders, micro and nanoparticles suspended in fluid, bacteria in water, proteins dissolved in water or other solutions, waste water, shaving cream, drug suspensions, are all colloidal systems. Most available products in the market pass through stages during production in which colloidal interactions became the limiting or the significant factor, which is why developments in the science of colloidal physics and chemistry draw a great deal of attention from very diverse disciplines in academia and industry.

Colloid stability is one of the main subject of interest. For example in paint industry colloidal system of dye particles in the solvent is stabilized enough not to coagulate and also be suitable for mixing (with other colors); however in waste water plant, pollutants need to be precipitated. While the scale is different, colloidal physics and chemistry methods used in a waste water treatment plant to precipitate pollutants and in a biochemistry lab to separate proteins by gradual salt concentration sedimentation, are the same.

While the history of colloidal science dates back to the early 19^{th} century, in nature, colloids and colloidal interactions can be find anywhere and have dominated in importance from the beginning. Blood, skin and milk are examples of very complex and stable colloidal systems. The utilization of colloidal systems and their stabilizing by human beings have also been present for a long time. In many parts of the world, for thousands of years, to prepare good food, people used traditional recipes whose speciality many times relied on colloidal chemistry. One example, Fatma Serhatlioglu, who for many years managed her own vegetable and fruit garden in Elazig, Turkey, used the white soil collected from the hills around her garden, to eliminate the muddy look of the fruit ciders and fruit leathers she prepared from the home grown produce. During the boiling process of the juice, white soil was added to solution, which appeared clear after sedimentation. Careful pouring of supernatant to floured sheets and drying under the sun for a day was the last step before cutting the fruit leathers into single serving pieces. By this method, Serhatlioglu prepared fruit leathers as delicious winter fruit snacks for other family members (including the author). Using her recipe, her dried fruit snacks were always shiny and transparent with an "eat me" look for the kids, rather than a dull and foggy appearance that could spoil their appetite. From a more scientific perspective, her magic white soil was no more than lime carbonate (calcium carbonate) and the process she was following was reducing the acidity and changing the ionic concentration of the solution so that the colloidal fruit particles and fibers start to agglomerate and then precipitate with the added calcium carbonate, so that the supernatant becomes clear. Throughout the history, human kind unknowingly used colloidal chemistry in similar forms and developed experimental experiences which had been transferred from one generation to the next.

In this chapter, among many colloidal systems, the point of interest is on the solid particles dispersed in fluids, particularly their behavior under ultrasonic focusing, and behavior after release of acoustic forces.

7.1.2 Diffusion of Colloidal Dispersions

When a drop of water soluble ink is dropped on the surface of a glass of water, it is observed that ink does not stay where it is dropped but starts to mix with the rest of the water. At the point where ink is introduced to water, the ink concentration is very high and ink diffuses from high concentration region to low concentration region. In 1855, A. Fick [88] formulated the law of diffusion. In his first law, he related the flux $J(z,t)$ of the material passing through at point z to the spatial gradient of concentration ($n(z,t)$), so two quantities are related to each other through a constant called diffusion coefficient (D).

$$J(z,t) = -D\frac{\partial n(z,t)}{\partial z} \tag{7.1}$$

From his first law, assuming the concentration is changing in time due to particle flux, he also derived the second law of diffusion, which relates concentration change in time to the change in the behavior of the flux in spatial coordinates. Assuming the diffusion constant D is the same for everywhere in the solution, the second law of diffusion is given by,

$$\frac{\partial n(z,t)}{\partial t} = D\,\frac{\partial^2 n(z,t)}{\partial z^2}. \tag{7.2}$$

While Fick's formulation through macroscopic observations was very successful in terms of explaining general diffusion behavior, a microscopic explanation became clear afterwards.

The microscopic explanation of diffusion is related to molecular dynamics. Flu-

ids consist of molecules and these molecules have velocities whose average is related to temperature. Velocities of these molecules have a distribution and this distribution had been modeled by the Maxwell-Boltzmann distribution [89]. Micro and nanoparticles suspended in a fluid are subject to collisions of fluid molecules moving with certain velocities. Each colliding fluid molecule transfers some amount of momentum to the particle. Since velocities of these hitting molecules have a distribution, most of the time net momentum transfer to the particle is not zero, but rather has a random net value and direction. This random momentum transfers result in short time jiggling motions and cause a statistical average displacement of the particle. This phenomenon is known as Brownian motion after Robert Brown, due to his early observations on random displacements of plant pollens under the microscope [90](1827). In fact, random motion of particles in fluids and gases was observed much earlier by many other researchers, Jan Ingenhousz on the random motion of coal dust particles in alcohol solution [91]. However, Brown was the first to make systematic experiments and conclude that these movements are not due to bubbles, interactions among particles, nor the particles themselves. While a strong debate was active for the following 50 years about the cause of these random motions, with the development of the molecular theory, in 1877, Delsaulx suggested motion is due to random impact of liquid molecules [92]. After him, many theoretical approaches including relating the motion to temperature have been published. In early 1900s, independently, Smoluchowski and Einstein published articles giving a more complete theoretical approach. While its area of interest is primarily electrical noise, beginning section of article published by Abbott et al. [93] gives the brief history and references of this phenomenon. In his work, Einstein used the fact that in equilibrium, free energy should be zero and he calculated the equilibrium dynamics due to concentration change and osmotic pressure [94]. Relating the flux

of particles passing an area to diffusion constant, he found the diffusion constant for a particle given as[1]

$$D = \frac{kT}{6\pi\eta a} \tag{7.3}$$

where k is the Boltzmann constant, T is the temperature in Kelvin scale, η is the viscosity of the fluid and a is the radius of the particle [94]. For a particle having size of 500 nm, suspended in water, at room temperature, the diffusion constant is expected to be around 0.85 $\mu m^2/s$ which is in the order of experimentally obtained values given in the literature [95].

Assuming N_0 is the initial concentration of noninteracting molecules or colloidal particles introduced to a solution at $z = z_0$ at $t = 0$, the solution of Fick's second law of diffusion for the concentration in one dimension gives

$$n(z,t) = \frac{N_0}{\sqrt{4\pi Dt}} e^{(z-z_0)^2/4Dt} \quad . \tag{7.4}$$

If there is only one particle, then the above formula simply gives the probability distribution of finding the particle at a particular location. The mean displacement of the particle or distribution of particles can be found from the distribution function. Since this function is a Gaussian distribution, the mean displacement will be given as

$$\lambda_z = \sqrt{2Dt}. \tag{7.5}$$

As seen, the mean displacement is related to the square root of the time.

As an example, assuming 1000 silica particles (d=300 nm) are introduced to the solution at $z = 0$ point, at $t = 0$, the change in the concentration distribution is given in Figure 7.1. In this plot, total area under the each curve gives the total particle number (1000).

[1]Since the derivation can be found in many sources such as [94], it is skipped here.

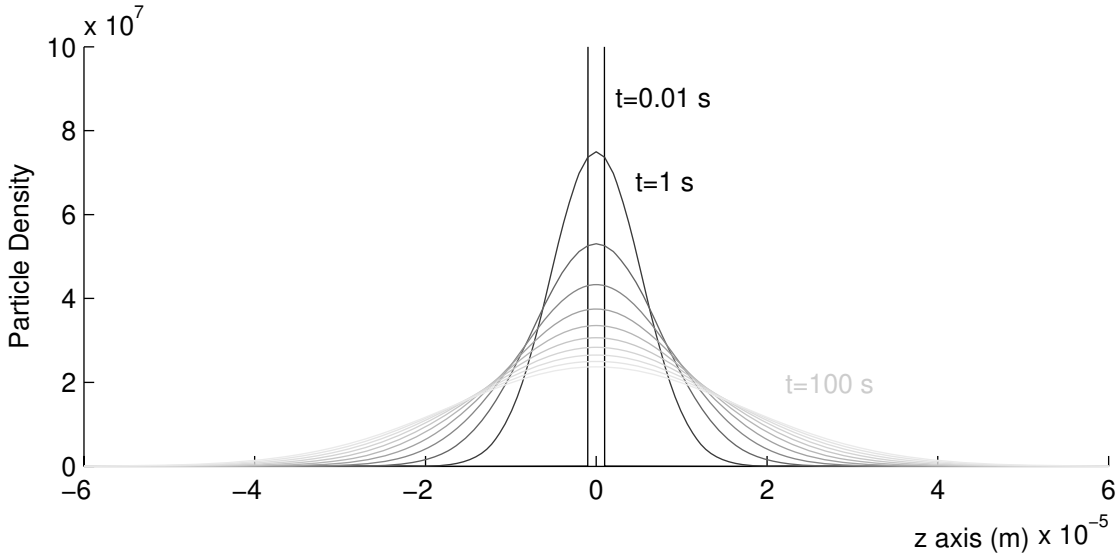

Figure 7.1: Diffusion of 1000 non interacting particles. Since particles assumed to be noninteracting, at $t = 0$, particle density at $z = 0$ is infinite (Dirac-delta function). As time passes, distribution function takes the form of a Gaussian distribution. Here, particle size is 500 nm and solution is water at room temperature. While the mean displacement increases with square root of time, the tail of the distribution moves faster. In a system of interacting particles, like silica beads, particle density distribution cannot be infinite due to the exclusion principle. For such cases, particle distribution at t=0 can be approximated as a step function or a Gaussian in which t is replaced by $(t + t_0)$ where $t_0 > 0$.

7.1.3 Inter-particle Forces in Colloidal Dispersions and the Colloidal Stability

7.1.3.1 DLVO Theory and van der Waals Interactions

Particles suspended in a fluid medium are subject to many different interactions. Some of these interactions can be listed as van der Waals, electrostatic, hydration interactions. Depending on the electrolytic or steric conditions, this list can be

expanded. Assuming no steric interactions are present due to the absence of any absorbed micellar or polymer layers, van der Waals and electrostatic interactions have more significant influence compared to other forces listed above. The theory developed by Derjaguin, Landau, Verwey and Overbeek[2] has been known as DLVO theory for more than half a century. Although it has been known that DLVO theory fails at certain ranges such as low colloidal and salt concentrations, or high salt concentrations and colloidal crystallization, it remains as the fundamental first order approach in terms of characterization of colloid stability. DLVO theory predicts the interaction energy between two particles to be the sum of van der Waals (U_v) and electrostatic forces (U_e),

$$U = U_v + U_e \tag{7.6}$$

van der Waals interactions are always attractive and for short gaps in the order of particle size, interaction energy between two identical spherical particles due to van der Waals effect is given as [96]

$$U_v = -\frac{A_{12}a}{6h} \tag{7.7}$$

where a is the particle radius, h is the gap between the particles, and A_{12} is the Hamaker constant, named after H.C. Hamaker [97].

Before introducing electrostatic interactions of colloidal particles suspended in fluid, it is necessary to investigate further the electrochemistry of the system.

7.1.4 Electrochemistry of Dispersions and Zeta Potential

Many particles bear surface charges when they are suspended inside a fluidic medium. Usually this phenomenon stems from capturing of ions present inside

[2]Derjaguin and Landau, and Verwey and Overbeek had developed this theory independently.

the fluid, or losing some surface ions present on the particle or both. Due to this ionic exchange, as shown in Figure 7.2 an electrical double layer forms in the fluid particle boundary region. Inner ions in the double layer are strongly attached to the particle surface and move with it, and they form the Stern layer [98]. Outside of the Stern layer, remaining counter ions form a diffuse region which defines the shear layer in which particle moves with respect to the stationary fluid molecules. The electric potential at this layer is called zeta potential (ζ) which defines the electrokinetic properties of the particle. Being the only measurable quantity related to the charge information of the particle inside the fluid, zeta potential is used in place of surface potential in analytical calculations.

Zeta potential, ζ is an experimental quantity and can be obtained from electrophoretic mobility of the particles by the formula

$$\zeta = \frac{3\eta\upsilon}{2\varepsilon E f(\kappa a)} \tag{7.8}$$

where η is the viscosity of the fluid, υ is the particle velocity with respect to stationary fluid, E is the applied electric field, ε is the dielectric constant of the material, and $f(\kappa a)$ is a constant number related to Debye length, and a the radius of the particle; in this case $f(\kappa a)$ is 1.5 [98]. Zetasizer Nano Z series by Malvern Instruments [3] is used to characterize zeta potential of the particle samples. As shown in Figure 7.3, the idea behind the measurement is as follows: as particles are accelerated in a fluidic channel by the electrical potential applied at the ends,[3] their velocity is measured by laser particle image velocimetry. As the limit velocity of the particle depends on the limit where the Stokes drag force balances the force due to the electric field, zeta potential can be extracted as long as other parameters are known.

[3]This phenomenon is known as electrophoresis.

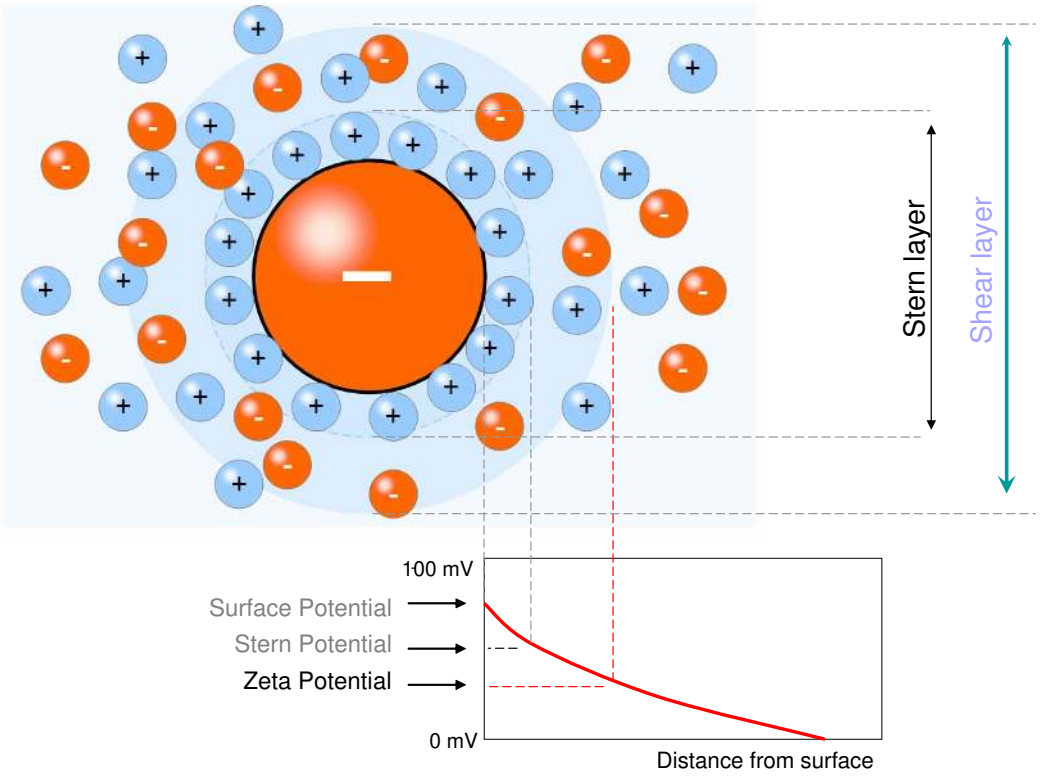

Figure 7.2: Particle in a fluid, surrounding double layer, stern layer and potential. Zeta potential with respect to distance is sketched after [3].

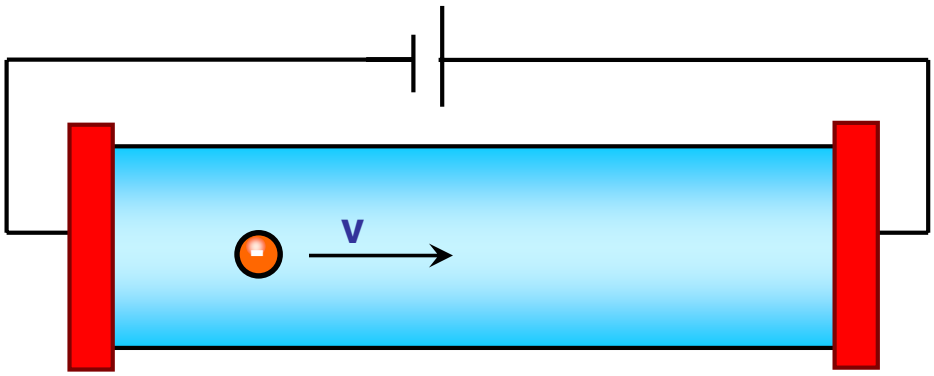

Figure 7.3: Particle suspended inside the fluid moves due to the electric field. From the speed of the particle, its electrical mobility can be extracted, which leads to Zeta potential through Equation 7.8.

Another method used to characterize zeta potential of the colloids is the electroacoustic method, in which vibration of the colloid due to acoustic waves generates an oscillating electric field. Since the size of the colloidal particle is much bigger than the molecules of the fluid or the ions dissolved in it, particle vibrates in the acoustic field while diffusing shear layer remains stationary. This changes the local neutrality and generates an oscillating electric field. Through the correlation of the acoustic wave frequency and electric field or current measurement, zeta potential can be extracted. The reverse is also possible, in which acoustic waves generated by the applied oscillating electric field are detected. From the correlation, zeta potential can be extracted [99, 100]. While electrophoretic measurements are used widely, due to the limitation of light scattering at high colloidal concentrations, the electroacoustic method is preferred for dense dispersions.

In colloidal science, Zeta potential is one of the most crucial parameters from which colloidal stability is predicted. Zeta potential and colloidal stability are affected in the similar way by various factors. One important variable on the Zeta potential is the pH of the solution in which particles are dispersed. A typical variation of the Zeta potential of a negatively charged silica particle would look like the graph given in Figure 7.4. A qualitative explanation to this variation can be given as follows: negative particle suspended in water attracts positive hydrogen ions to form a surrounding double layer. As the acidity increases, concentration of the hydrogen ions gets higher so that the potential at the diffuse layer initially decreases and then starts to get positive values at higher pH values. The point where zeta potential gets its zero value is the isoelectric point. At the isoelectric point, electrostatic forces between particles gets minimal and particles do not respond to the external electric field. Proteins can be separated with respect to their isoelectric point. Since each protein has a unique amino acid chain format,

its isoelectric point is also unique; in this case, target protein can be separated through precipitation by changing the pH of the solution accordingly.

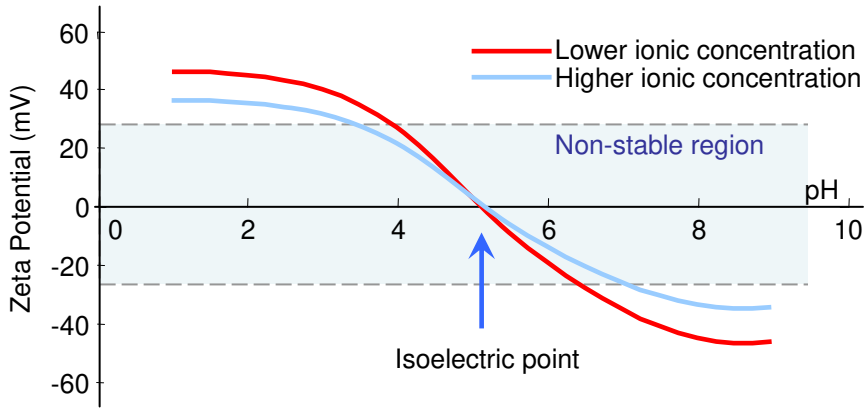

Figure 7.4: A typical variation of zeta potential for silica particles suspended in fluid at various pH values. For below 30 mV or above -30 mV, colloidal system is not stable and coagulation followed by precipitation or creaming is expected. This colloidal system is not expected to be stable between pH values 4 and 6.5.

Another parameter which affects zeta potential is the ionic concentration of the solution. The presence of ions dissolved in the solution affects the length of the diffuse layer (also known as Debye-Huckel length). Diffuse layer thickness, κ^{-1}, is related to the ionic strength of the solution through the formula

$$\kappa^{-1} = \sqrt{\frac{\varepsilon kT}{e^2 I}} \tag{7.9}$$

where ε is the dielectric permittivity of the fluid, e is the electric charge and I is the ionic concentration. Entering ε, kT and e parameters for water at 25 °C, the above formula is reduced to

$$\kappa^{-1} = \frac{1}{3.29\sqrt{I}} \quad . \tag{7.10}$$

We can deduce from the above relationship that when the ionic concentration increases, thickness of the diffuse layer decreases; this causes a faster potential

drop from the surface of the particle and results in a decrease in the zeta potential. The typical variation of zeta potential in the case of increased ionic concentration is shown in Figure 7.4.

While calculating the net interaction energy between two particles suspended in the fluid through the DLVO theory in the previous section, electrostatic interactions were left untouched. Here now that will be completed. In the case of colloidal particles suspended inside the fluid, instead of the surface charges and surface potential, charge density at the diffuse layer and correspondingly zeta potential become the determining factor. In this case, the interaction energy between two particles surrounded by the diffuse layers can be written as [96],

$$U_e = \pi\varepsilon\zeta^2 a e^{-\kappa h} \quad . \tag{7.11}$$

From Equations 7.6 and 7.7, total interaction energy between two spherical particles predicted by the DLVO theory is found to be

$$U = -\frac{A_{12}a}{12h} + \pi\varepsilon\zeta^2 a e^{-\kappa h} \quad . \tag{7.12}$$

Now it is possible to find the total interaction energy predicted by the DLVO theory for silica beads suspended in water. For silica in water, A_{12} is 0.82 10^{-20} J [96]; diameter of the silica beads is 500 nm; at pH 7, zeta potential would be around 30 mV and assuming slight salt concentration, typical κ would be 1/3 nm^{-1}. For these given parameters, interaction energy of two colloidal silica particles are given in Figure 7.5. In the same figure, it is observed that when the zeta potential is around 30 mV, two particles at a long distance are in a negative energy state and they will attract each other. However, as they come closer, electrostatic repulsion will start to increase exponentially. For example, in this case, they will observe an energy barrier of $100kT$. If only a force field pushes them harder than this barrier,

they can coagulate. In the same plot, total energy at 15 mV Zeta potential is also plotted. In this case, electrostatic repulsion is not strong enough to generate an energy barrier, and particles will keep attracting each other until they stick and flocculate. At higher Zeta potential and κ values, the effect of the electrostatic pushing would span much longer distances up to several microns.

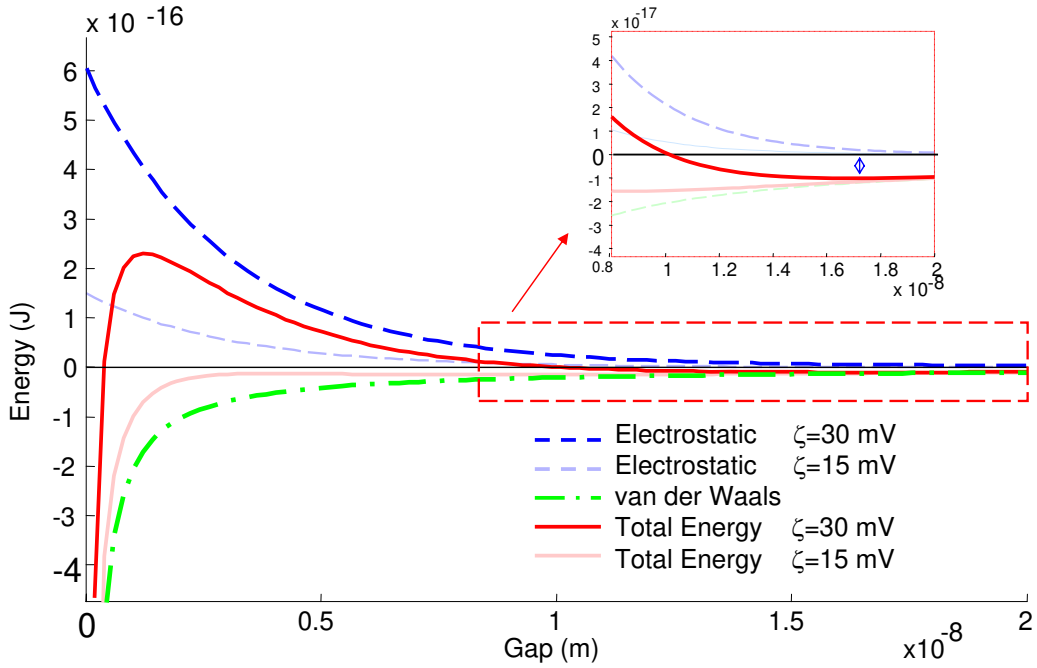

Figure 7.5: Energy diagram of two interacting spherical charged particles. While the van der Waals attraction pulls particles to each other, electrostatic interactions push them away from each other. When particles have zeta potential of 30 mV, electrostatic repulsion generates an energy barrier. When zeta potential is lower, electrostatic repulsion is not high enough to generate a barrier. In this case, particles eventually collapse to each other. Even in the presence of an energy barrier, depending on the conditions, the electrostatic field may decay faster than van der Waals interactions (zoomed in sub-figure). Then particles will be stable in such a distance.

Before concluding this section, it is also noteworthy to highlight that the change in the ionic concentration not only affects the diffuse layer length but also the Zeta

potential, which was mentioned before. In this case, for a constant surface charge (σ), and thin diffuse layer ($\kappa a \gg 1$), it is possible to have an approximate relation between κ and zeta potential;

$$\zeta = \frac{\sigma}{\varepsilon\kappa} \quad . \tag{7.13}$$

From this relationship, we can conclude that as the thickness of the diffuse layer (κ^{-1}) increases, zeta potential increases. However, for very low ionic concentrations, diffuse layer may get comparable to or even larger than the particle size, in which case the above approximation may not give accurate results.

7.1.5 Sedimentation Potential

In colloidal systems, when the homogeneity of the fluid particle density is altered with external effects like gravity or centrifugation, a macroscopic electric field forms inside the solution parallel to the concentration gradient [101]. This macroscopic field can be measured with careful experiments. Magnitude of the electrical potential is usually in the order of 1-10 mV. This field also causes equilibrium distribution profile to deviate strongly from a predicted barometric profile [102].

The equation for sedimentation potential under a gravitational force field was calculated by Ohshima et al. [101] as

$$V_{sed} = -\frac{\varepsilon\zeta h(\kappa d) g \Delta\rho\phi}{\eta\chi} \tag{7.14}$$

where g is the gravity, ϕ is the total volume fraction of particles, d is the distance between high particle density and low particle density points, and χ is the conductivity of the suspension. $h(\kappa a)$ is a known dimensionless function [103]. In the equation, the ($g\Delta\rho V_p$) phrase represents the gravitational force. The electric field,

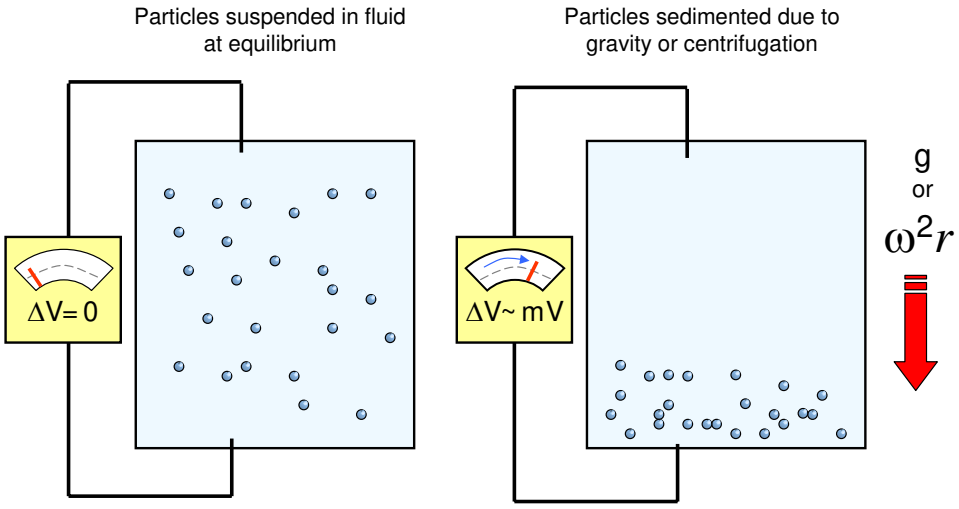

Figure 7.6: Sedimentation potential is generated when the distribution of the colloidal particles changes due to the external force fields such as gravity or centrifugal acceleration.

E_{sed}, due to the sedimentation potential, can also be approximated as

$$E_{sed} = \frac{V_{sed}}{d} \quad . \tag{7.15}$$

It has been known that internal electric field due to sedimentation leads to an equilibrium density profile of sedimentation in ultracentrifugation experiments.

7.2 Dispersion of Colloids Concentrated under Acoustic Radiation Force

Since acoustic forces only depend on the density and the elastic properties of the materials, they can be used to investigate other properties of the colloidal system, such as diffusive, electrokinetical, or hydrodynamic properties.

By using the actuator mechanism defined in this thesis, it is possible to concentrate dispersed colloidal particles to a very small volume. As it was shown in Chapter 6, focusing of dispersed micron size or larger particles is in the order of seconds. Since acoustic radiation force is related to the third order of the particle radius, some drop in collection time is expected.

Faraday found that colloidal particles causes scattering of incident light [104]. His clever comments on the experiments guided J. Tyndall to further develop the method[4]. Today this phenomenon is known as Tyndall effect. Lord Rayleigh further formulated the scattering theory for the case particle sizes are smaller than the wavelength of the light beam (and this is known as Rayleigh scattering). By using this scattering principle it is possible to monitor concentration change before or after actuation. Experimental setup is shown in Figure 7.7. As sketched on top of the given figure, external light source is projected onto the capillary with an angle so that, only some portion of the light scattered from the colloidal dispersion enclosed inside the capillary can be collected in the microscope objective.

Hand held camera images show that results are visible without any magnification. Before actuation, a continuous illumination from the capillary is observed. After actuation light is scattered only at locations where silica particles are focused. As expected from theory, at 30 kHz, 3 collection points are observed, and at 1.625 MHz, 25 collection points are observed.

[4]Being a very successful experimenter full of intuitive capabilities, for Faraday this was not the only case. Some history books comment that his mathematical training level was not more than basic trigonometry and he did not have a proper calculus training. However, many experimental results and clever conclusions reported by him led many other scientists, who have a good mathematical training and intuition, to further develop theories. Two important examples would be; his early observations and notes on relation of electricity and magnetism led Maxwell to develop the electromagnetic theory (this topic later led to the development of the field theory); his early experiments on the displacement of particles in a standing sound field led Rayleigh to develop streaming effects. The "controlling microparticles with acoustical effects" theme of this dissertation also dates back to Faraday's early observations.

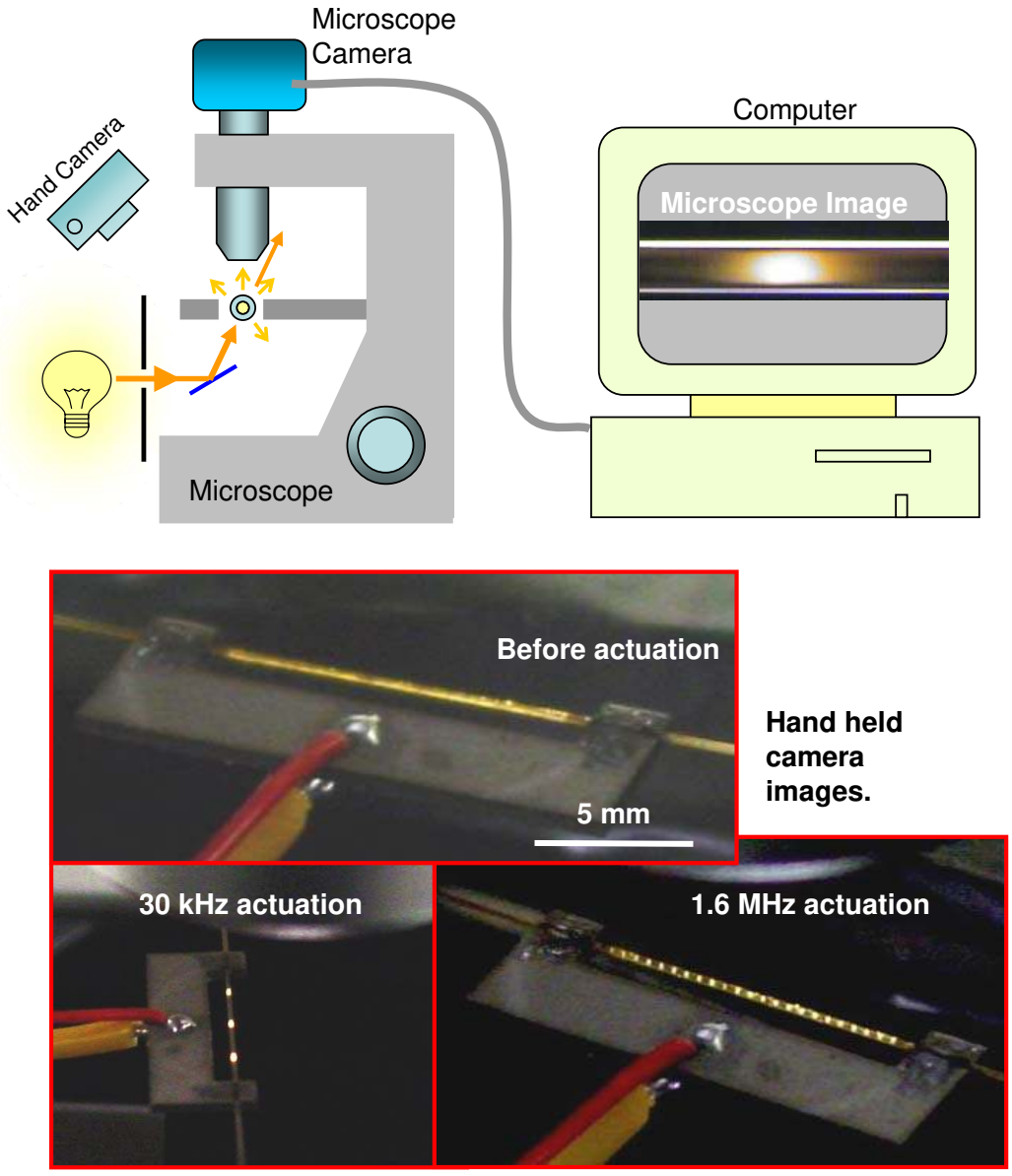

Figure 7.7: Top schematics show the experimental setup related to the imaging. Part of the light scattered from the colloidal particles inside the capillary is collected at the microscope objective and transferred to the computer through the microscope digital camera. As seen from the pictures, results are visible to the naked eye. Pictures shown here are taken with a regular digital camera. The picture taken before the actuation shows a constant scattering along the capillary. After actuation, collection of particles changes the distribution of the scattered light. In this configuration, dispersion can be monitored with a hand held digital camera (not shown here).

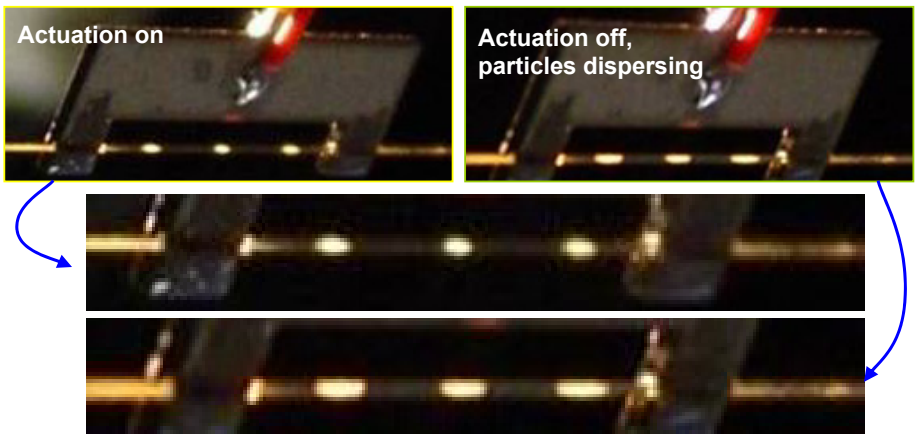

Figure 7.8: Hand held, point and shoot digital camera images show the dispersion of collected particles after the release of acoustic actuation. Results are visible to the naked eye and dispersion can be monitored without a microscope.

Pictures shown in Figure 7.8 are taken by a point and shoot digital camera. These pictures showing the dispersion of silica particles, demonstrate that dispersion of nanoparticles can be observed with a regular digital camera which eliminates the need of a microscope.

In the following sections, dispersive behavior of the colloidal particles will be investigated with the help of acoustic focusing in a PZT-capillary coupled actuator.

7.2.1 Silica Nanoparticles Dispersed in Water

The image shown on top of Figure 7.9 shows the 500 nm silica nanoparticles dispersed inside the capillary. Silica nanoparticles were obtained from Kisker-Biotech with a particle concentration of 50mg/ml from which volume fraction was calculated to be 0.11. While particles had red fluorescent dye at their core, fluorescence

property is not used in this experiment.[5] The second image from top shows the capillary and focused particles, after 3 minutes of actuation at a resonance frequency. Here, the 5th flexural mode is excited around 90 kHz with a voltage drive of 17 Vpp. Keeping the actuation time (∼5 min) longer, it is possible to have similar focusing volume at much lower voltages like 5 Vpp. Voltage dependent collection efficiency will be investigated in Section 7.3.3; in this section we are more interested in dispersive behavior of particles after the actuation is turned off.

As mentioned in Section 7.1, particles tend to spread due to diffusion and electrostatic interactions. The series of images taken at different times after the acoustic actuation is turned off is given in the middle section of Figure 7.9. Intensity data are obtained from these images by use of ImageJ freeware [105]. For each image, intensity through the central axis is extracted. To be able to reduce the fluctuations and monitor the broad variation of the concentration, data are smoothed through taking the moving average of each data point with its neighbors. While this process did not have a significant effect on most of the images, it also smoothed out the saturation observed at the focal volume locations in the figures. Surface plot shown in the bottom of Figure 7.9 shows the variation of the intensity of the light scattered along the central axis of the fluid column enclosed in the capillary over time.

It has been shown that the intensity of the light scattered from colloidal suspensions depends on the concentration. In bulk solutions, this is valid for a very low concentration regime. However, the fluid column width in our case is only $100\mu m$, and intensity saturation is observed in much higher concentrations. As a first order approximation, we assumed concentration is linearly dependent on

[5] In fact, instead of light scattering, light intensity due to fluorescence emission could also be used. One reason this is not preferred over the static light scattering is that intensity of fluorescent emission decreases over time due to the phot-bleaching effect.

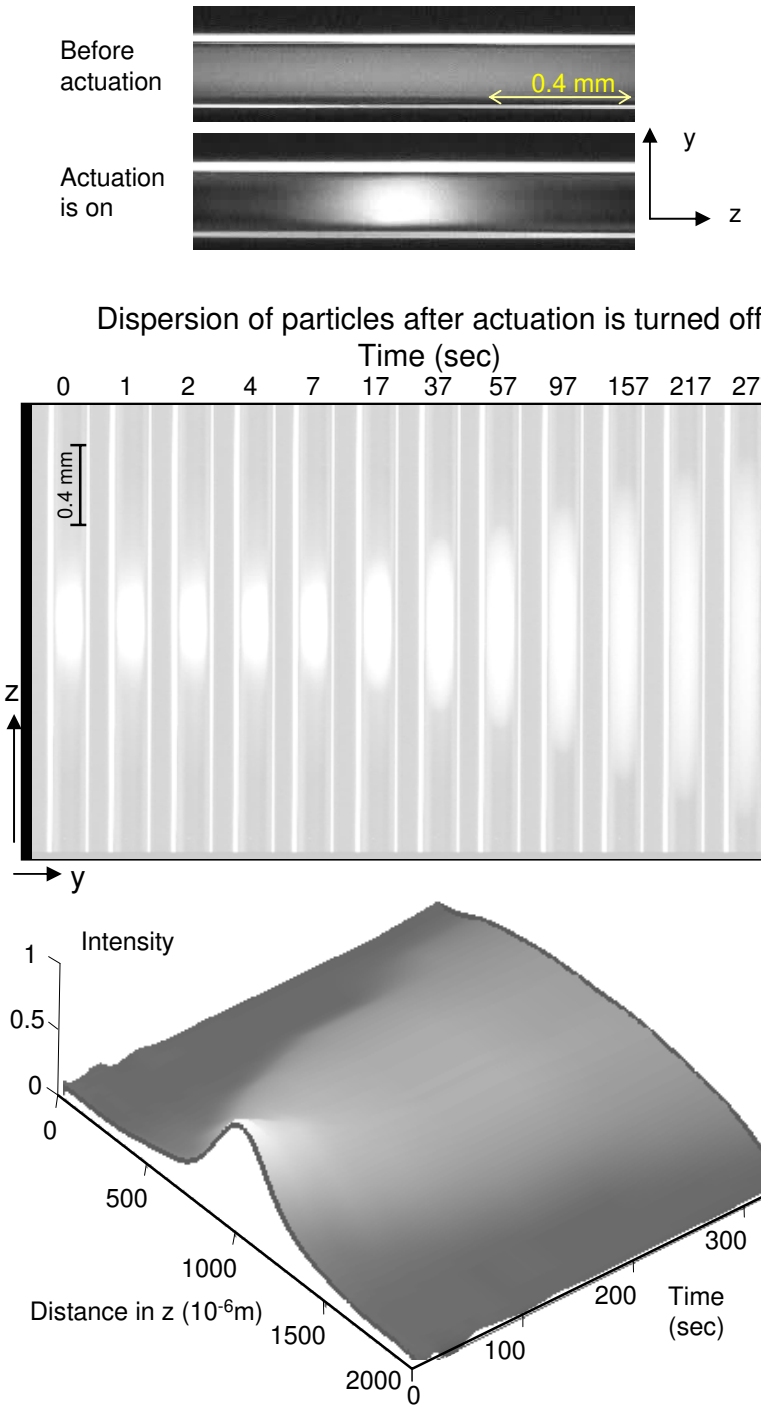

Figure 7.9: Particles randomly distributed inside the capillary are focused by the acoustic forces. As soon as actuation is turned off, particles start to disperse from the concentrated region. Concentration distribution is correlated with the intensity of the scattered light.

the capillary structure. In this case, total area under each curve should result in the same value. This is because the total number of particles does not change over time. While values of total area under each curve were in the same range, a consistent drop was observed as the focal volume decreases (in other words local concentration increases). This observation is in agreement with the limitation mentioned for the high concentration cases. To fix this ambiguity, a first order approximation is modified by normalizing each curve so that the area under each curve gives the same value. During the normalization process, most spread cases were taken as the reference since the intensity-concentration relation is more valid in lower concentrations.

As mentioned in the beginning of this section, the particle volume fraction is 0.11. When particles are focused due to acoustic forces at the 5th flexural mode, all particles dispersed inside the capillary in a range of 2.2 mm are focused to a range of less than 400 μm. This collection raises particle volume fraction to around 0.6 at the focal point, which is very close to the close-packed structure of the particles. In a close-packed crystal structure (cubic or hexagonal), particle volume ratio gets its highest value of 0.74.[6] In this case, at the focal point, particles are squeezed very close to each other and further investigation of any crystallization behavior may give interesting results. Confocal microscopy techniques would be helpful for such an investigation.

Utilizing the above assumptions, we find the volume fraction distribution of particles along the capillary at different times. Results are plotted in Figure 7.10.

[6]This is known as Kepler Conjecture, proposed by Johannes Kepler in 1611. Kepler came to this conclusion based on the results of Thomas Harriot, on the problem of maximizing the number of cannon balls to be stacked in the ship decks. Much later Hariot's model became the basis for the modern atomic theory. With his conjecture, Kepler did not include a proof and only 2 centuries later, Gauss came with a proof for the periodic lattice case. 120 pages long formal proof for the general case of Kepler Conjecture -based on computational calculations- was published recently in 2005 by Hales [106].

The highest and also the narrowest distribution shows the volume fraction distribution when the acoustic actuation is just turned off. All the other distributions show the spreading of particles. While initial distributions seem like Gaussian distributions, later distributions are different. Zooming in to the area where there are slopes, we observe particles disperse in a different way compared to the Gaussian distribution shown in Figure 7.1. In a Gaussian distribution, the slope at the variance value decreases with time. In this case, there is a a change in the slope, however it is not distinguishable since the its spatial location moves much faster compared to the change in the slope value. This suggests that, in the spreading of particles in this case, effects other than diffusion are more dominant.

Figure 7.11 shows the first derivative of the volume fraction with respect to the central axis of the capillary. Curves plotted here show that the magnitude of the maximum slope decays in time, and this decay is comparable to the decay expected by the diffusion of the beads. However, the location of the maximum slope moves with a different and higher rate. The dots in Figure 7.12 show the location of the maximum value of the slope, z'_{bound}, with respect to time. The fitted black line on the data shows a square root relation given as

$$z'_{bound} = \alpha\sqrt{t} \tag{7.16}$$

where α is found to be $6 \times 10^5 \mu/s^{1/2}$. This relationship shows that the diffuse layer where particle volume fraction change is maximal, moves at a rate of the square-root of time. In fact, this relationship is analogous to the mean displacement of diffusion given in Equation 7.5. Defining $\alpha = \sqrt{2D_f}$ and rephrasing the above equation accordingly, we get for the fit function

$$z'_{bound} = \sqrt{2D_f t} \tag{7.17}$$

where *expansion coefficient* D_f is found to be $550\mu m^2/s$.

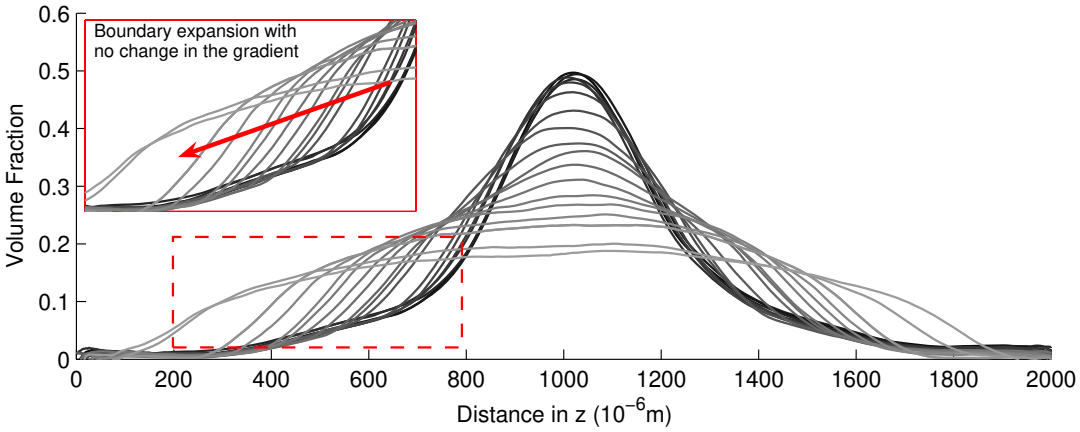

Figure 7.10: Concentration distribution (in terms of volume ratio) of the 500 nm silica particles. The darkest curve represents the distribution at t=0, while the lightest one represents t=337 seconds. Other curves represent distributions at (t= 1, 2, 4, 7, 17, 37, 57, 97, 157, 217, 277, 337 seconds). It is observed from the zoomed in section, that the boundary moves in a way and with a speed that are not predicted by the pure diffusion (Figure 7.1).

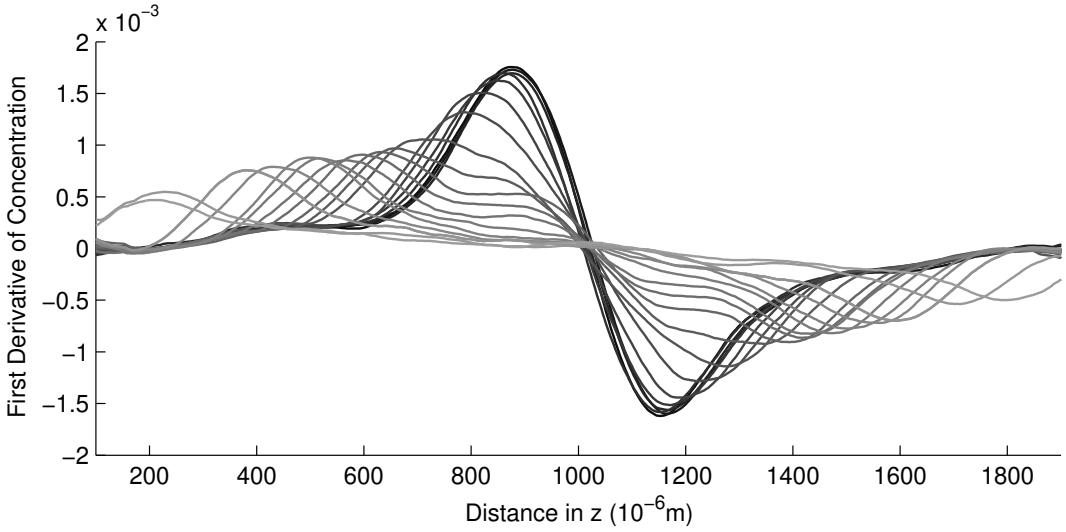

Figure 7.11: Derivative of the concentration distribution with respect to the z axis. The darkest colored curve represents the data at (t=0) and the lightest at t=337 seconds. The change in the amplitude and the spatial location of the peaks carry information about the self spreading characteristic of the concentrated colloidal system.

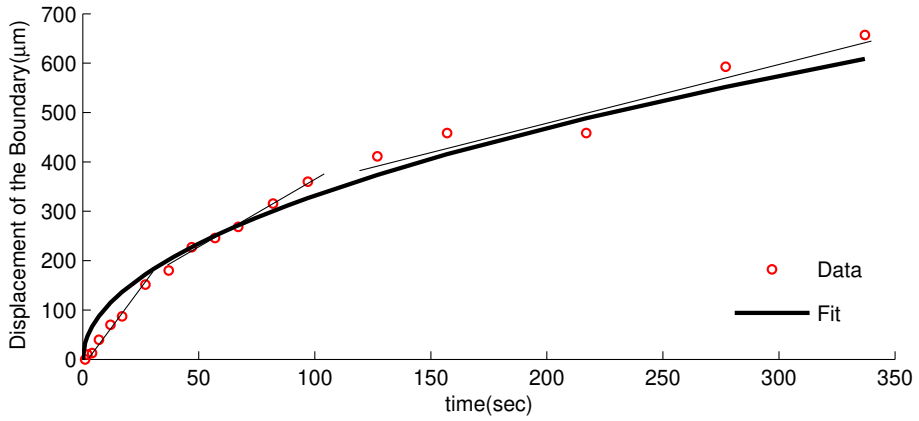

Figure 7.12: Displacement of the peaks given in in Figure 7.11. In other words displacement of the boundary versus time.

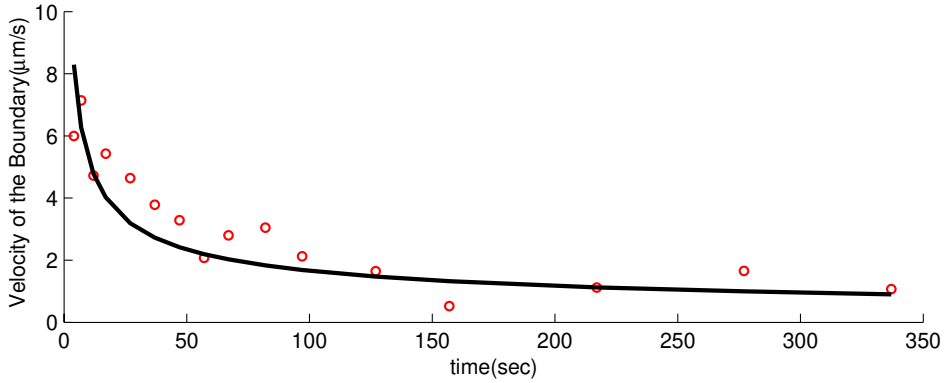

Figure 7.13: Speed of the movement of the peaks plotted in Figure 7.11

Figure 7.13 shows the dispersion velocity where the concentration gradient is maximal. It is observed that in the beginning, concentration spreads with velocities in the order of 5−6 μm/s. Later on the velocity of the boundary exponentially decays down to 1−2 μm/s with time as the concentration decreases due to spreading. This suggests that the force responsible for the spreading should be a function of concentration or concentration gradient.

In colloidal systems, dispersive effects occur due to; diffusion; build up of osmotic pressure due to concentration change; and electrostatic interactions. The

possible contribution of these effects will be examined in order.

7.2.1.1 Contribution of the Diffusion

An expansion coefficient with a value of 550 $\mu m^2/s$ is about 650 times larger than the diffusion constant of 0.85 $\mu m^2/s$ for 500 nm silica particles at room temperature. This result shows that particles spread with a velocity 650 times larger than they would spread just with pure diffusion. The boundary spreads with velocities around 5 $\mu m/s$ in the beginning and decreases to 1.5 $\mu m/s$ around 300 seconds. If particles would spread just with the influence of diffusion, then the concentration distribution expected at $t = 300$ seconds would be identical to the concentration distribution observed at $t = 1$ second. Since two curves are almost identical, sketching is skipped here. In summary, the contribution of diffusion to the spreading observed is very minimal and can be ignored. It is, in fact, lower than the experimental measurement errors in this case.

7.2.1.2 Contribution of Osmotic Pressure

One may argue that the fast dispersion observed in experiments is due to the osmotic pressure built from the dense collection of colloids. Osmotic pressure $P_\phi(z)$ for the colloids can be found through the Carnahan-Starling formula [107]:

$$P_\phi(z) = \frac{3kT}{4\pi r^3}\phi(z)\Big(\frac{1+\phi(z)+\phi^2(z)-\phi^3(z)}{(1-\phi(z))^3}\Big) \tag{7.18}$$

where k is the Boltzmann Constant, T is the temperature, r is the particle radius, and $\phi(z)$ is the particle volume fraction as a function of z. Osmotic pressure values calculated for increasing time measurements are shown in Figure 7.14.

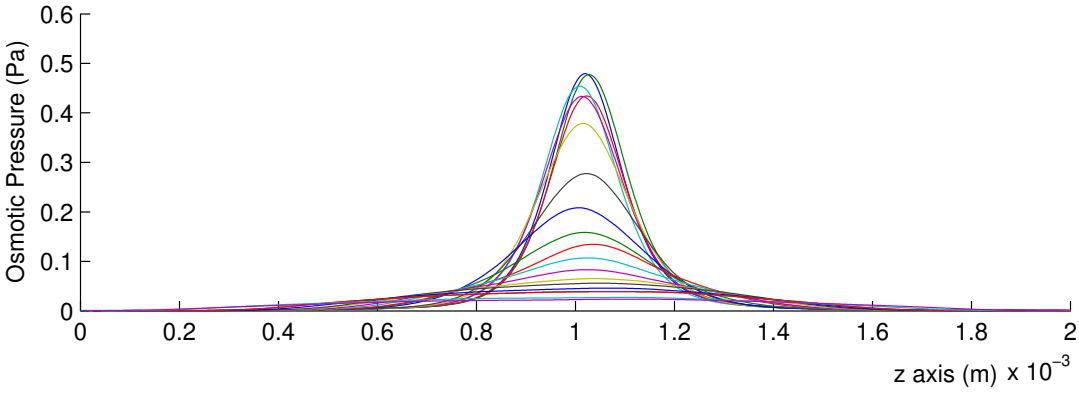

Figure 7.14: Spatial distribution of the osmotic pressure due to the concentration distribution of the particles. When external forces are not present, particles will be pushed away from a high pressure region to a low pressure region. However, this push is expected to be very low due to the low peak value of the osmotic pressure. This is due to the microscopic size of the colloidal particles. (Value of osmotic pressure is inversely related to the cube of the radius of the particles and can reach significant levels, for example, in the case of ions.)

In a pressure gradient, net force on a particle can be calculated approximately as

$$f(z) = \frac{\partial P_\phi(z)}{\partial z} dz A_p \tag{7.19}$$

where $f(z)$ is the force on the particle and dz the change in z, and A_p is the cross sectional area of the particle (this formula is obtained simply from equation of motion; the difference between force due to the pressure from one side and force due to the pressure from the other side is the net force acting on the particle). Since, here, particle sizes are small compared to the length of the capillary (nm$\ll$mm), we can approximate dz as the particle diameter; then the formula becomes

$$f(z) = \frac{\partial P_\phi(z)}{\partial z} V_p \tag{7.20}$$

where V_p is the particle volume.

This force will be limited by the Stokes drag force [94] due to the viscosity of the water. Stokes drag force is given as

$$f_s = -bv_l \tag{7.21}$$

where v_l is the particle limit velocity and b is the drag coefficient given by

$$b = 6\pi\eta r \tag{7.22}$$

where η is the viscosity of the fluid (1 mPa·s for water).

In this case, due to the osmotic pressure, limit velocity of the particles is found to be

$$v_l = \frac{V_p}{6\pi\nu r}\frac{\partial P_\phi(z)}{\partial z} \tag{7.23}$$

where $P_\phi(z)$ is given by Equation 7.18. Limit velocity due to the osmotic pressure built by the concentration variation of the particles is plotted in Figure 7.15. Magnitude of the velocities obtained due to osmotic pressure is highest when the concentration gradient is the highest; this is just after turning off the actuation. Even the highest velocity value (about 5-6 nm/s) due to osmotic pressure is three orders of magnitude lower than the velocity of the dispersion observed in the experiment. Following this, it is possible to conclude that osmotic pressure built up due to the high particle concentration gradients cannot be the reason behind the fast spreading of the 500 nm particles.

For the case of the charged particles, the radius of the particle used to calculate osmotic pressure in Equation 7.18 should be modified to include the diffuse layer around the particle. This increase in the radius will further lower the osmotic pressure and its effect on spreading.

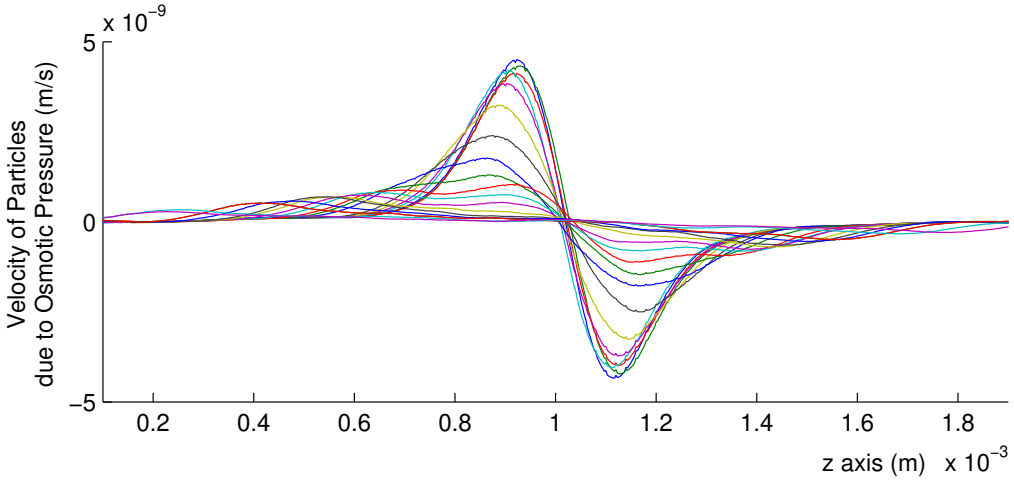

Figure 7.15: Velocity of the particles due to the osmotic pressure gradient. 500 nm particles are still large compared to water molecules and so the influence is negligible.

7.2.1.3 Contribution of Electrostatic Interactions

In Section 7.1.5, it was mentioned that when the concentration distribution of colloidal dispersions is changed due to external forces such as gravity or centrifugation, a voltage difference is generated between high and low concentration regions. This difference in the electrical potential is known as sedimentation potential.

In the case of concentrating colloids at particular locations inside the capillary, the same phenomenon occurs. At locations defined by the flexural modes of the capillary, colloidal particles are concentrated close to their close packed structure. Due to this concentration effect, build up of an electric field is expected. When the actuation is turned off particles start to disperse due to this self built electric field by their concentration at specific locations. By using the electrophoresis phenomenon mentioned in Section 7.1.4, build up of an electric field can be calculated from the measured dispersion velocity of the particles. Since velocities due

to osmotic pressure and diffusion are negligible, it is assumed that the observed high velocity spreading of the particles is due to the self generated electric field. Modifying Equation 7.8 to relate the electric field with the particle velocities, we have

$$E = \frac{3\eta}{2\varepsilon\zeta f(\kappa a)}\upsilon \tag{7.24}$$

where $f(\kappa a) = 1.5$. Applying this relationship to the velocity values shown in Figure 7.13 for the expanding boundary locations, we find the electric field values depending on time. Results are plotted in Figure 7.16. In this case, electric field values in the order of $200V/m$ can be responsible for the fast dispersion of the particles. This is a really macroscopic voltage difference and electric field for a microscale experiment. As shown in Figure 7.17, such an electric field would give voltage differences around 100 mV in 0.5 mm. In macroscopic sedimentation potential measurement experiments, values obtained are usually in the order of 1-10 mV.

7.2.2 Silica Nanoparticles Dispersed in Alcohol

Performing a similar experiment for a different sample of 500 nm silica nanoparticles suspended in ethyl alcohol, we obtain similar fast dispersion characteristics. Silica nanoparticles used in these experiments were obtained from the research group of Prof. Ulrich Wiesner. In this case, particle concentration is much lower compared to the previous case in which the 300 nm silica particles were suspended in water. One advantage of the low concentration is that data related to short time spreading can be extracted more clearly. As shown in the series of pictures given on top of Figure 7.18, particles collected under ultrasonic force at $t = 0$ start to disperse as the actuation is turned off. Two graphs in Figure 7.18 show the

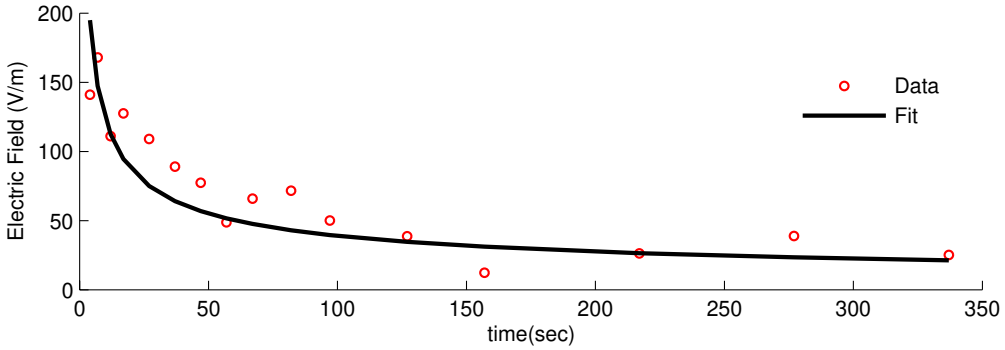

Figure 7.16: Decay of the electric field with time is plotted. At time zero, since particles are very concentrated at focal points, amount of electric field gets the highest level. As the particles spread total electric field sensed at the boundary decreases.

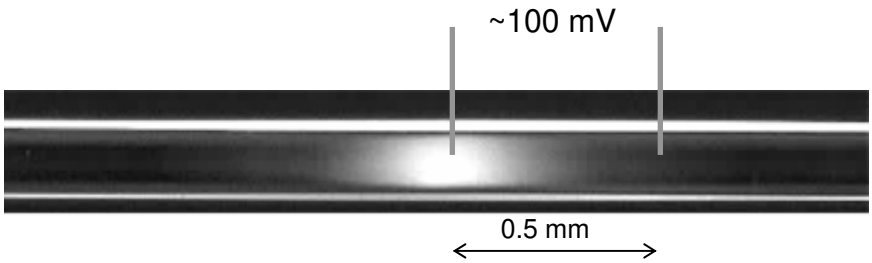

Figure 7.17: Voltage difference between two locations inside the capillary, due to the generated electric field by the concentration of the particles.

displacement and velocity of the concentration boundary versus time. From the displacement curve, fitting data to Equation 7.17, we find D_f to be 270 $\mu m^2/s$. The diffusion coefficient for non interacting silica particles of 500 nm is 0.8 $\mu m^2/s$. Here again, it is observed that the boundary of the concentration moves 350 times faster than it would move with regular diffusion.

As given in the plot of velocity versus time in Figure 7.18, at the beginning particles at the boundary move with speeds around 25 $\mu m/s$. This high speed dispersion suggests the existence of a significant electric field in the concentration

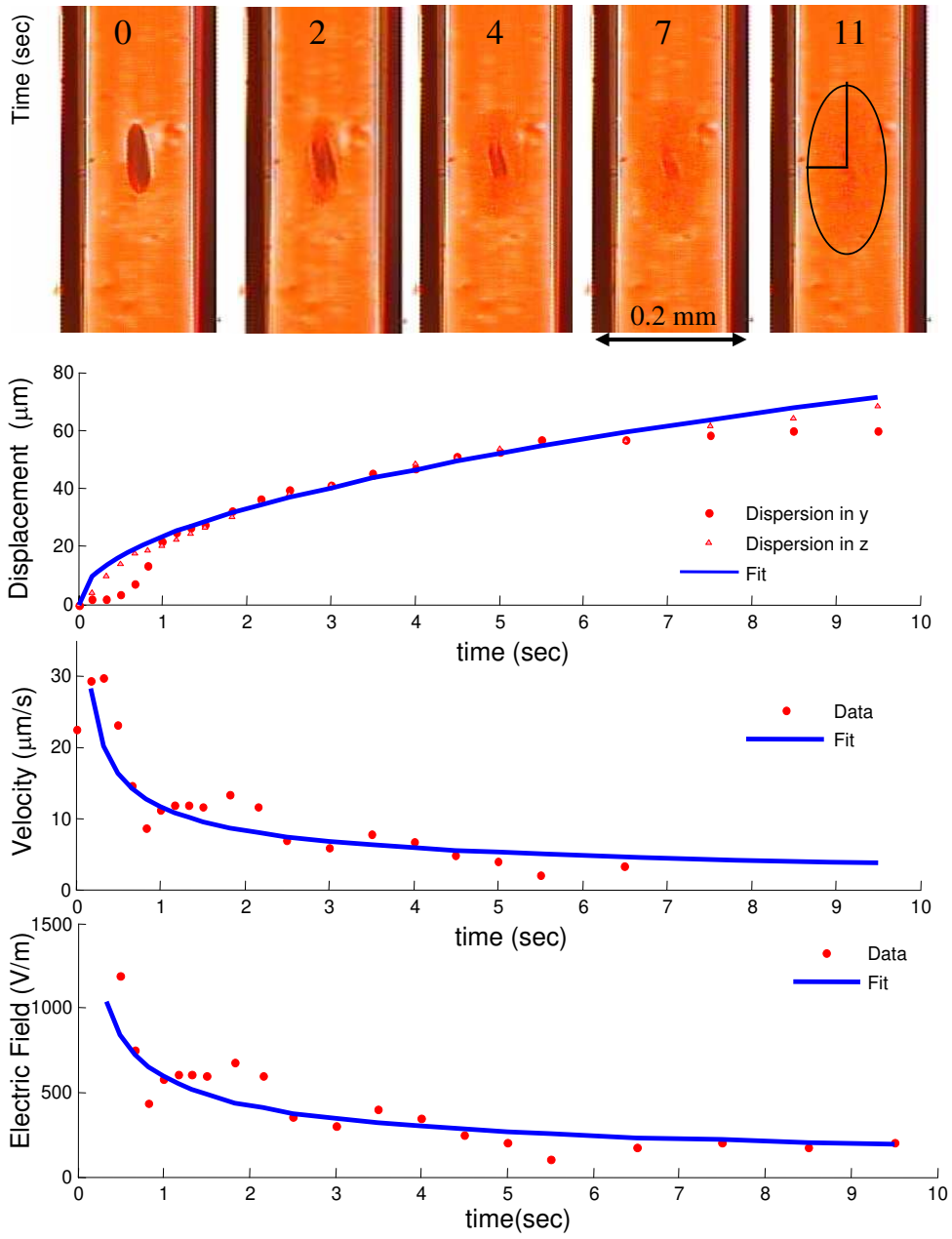

Figure 7.18: Dispersion of collected particles suspended in ethyl alcohol. Imaging is done with the transmitted light, so that any location where particles exist look darker. Plots below the pictures are the mean displacement and the velocity of the boundary of the particle gradient. The bottom plot shows the estimated electric field at the boundary.

regime.

The electric field generated due to the collection particles can be calculated by using Equation 7.24. The viscosity of the ethyl alcohol is 1.1 mPa.s and the relative permittivity at room temperature is 24.3 [108]. Pure ethanol does not have electrolytic properties as much as water does. Due to the lack of any ions present in solution, zeta potential can be approximated to the surface potential. In the literature, it is reported that silica nanoparticles suspended in ethanol have zeta potential values between negative 100-200 mV [109, 110, 111]. Assuming zeta potential of 100 mV, electric field values are found to be in the order of 1000 V/m. In the case of the upper limit, if zeta potential is 200 mV, then electric field values decrease to 500 V/m, which is still considerably significant and much higher than the electric field values observed in a DI water suspension. This is due to the presence of H^+ and OH^- ions in DI water.

Since the size of the particles (500nm) are larger compared to the 300 nm particles mentioned in the previous section, due to Equation 7.18, the effect of osmotic pressure will be much lower and will not have any effect. Results obtained by the dispersion of silica nanoparticles suspended in alcohol strongly suggests the presence of a significant electric field at the microregime.

7.2.3 Summary

In this section, the build up of a macroscopic electric field has been shown due to concentration of particles under ultrasonic forces at microscale. 500 nm size silica particles show good enough collection behavior under ultrasonic forces. In addition, in this size range, osmotic pressure values generated due to high concentration

gradients are negligibly low. This factor enables more accurate observance of effects due to the electric field generated by the collection or sedimentation of particles. In the literature, it can be found that similar experiments are performed for 22 nm particles by use of ultracentrifugation [102, 112]. These experiments require bulky equipments such as ultracentrifuge tools and long centrifuge times up to a week.

Using the PZT-glass capillary actuator presented here, experiments to obtain the above presented results can take less than 5 minutes. Considering the portability and low power needs of the device, the actuator mechanism introduced here may lead to a new method to analyze and characterize colloidal dispersions. Due to the high aspect ratio of the capillary, dispersion of the colloids inside the capillary can be monitored even with a regular digital hand held camera and a simple light source setup (a cheap diode laser) which can even eliminate the need to use a microscope.

7.3 Acoustic Focusing of Colloidal Particles and Calibration of Acoustic Field against Electrokinetic Effects

In this section, the behavior of colloidal nanoparticles under ultrasonic radiation forces will be investigated briefly. When acoustic radiation is present, to collect particles at the preferred locations, radiation force has to overcome dispersive forces. In the previous section, amplitude of dispersive forces was examined. Out of diffusive, osmotic pressure and electrostatic interactions related forces, electrostatic

interactions were the dominant dispersive forces. In colloidal systems, electrostatic interactions highly depend on the parameters related to the electrochemistry of the system. As mentioned in Section 7.1.4, zeta potential is one of the major parameters defining electrokinetic particle behavior.

In the first part, experimental results related to the effect of zeta potential (related to pH of the solution) on the collection behavior is mentioned. In the second part of this section, a method to calculate acoustic radiation forces by use of these counterbalancing dispersive forces is introduced.

7.3.1 Acoustic Focusing of Colloidal Particles Dispersed in Solutions of Various pH Values

As mentioned in Section 7.1.4, concentration of ions in the solution has a great effect on the thickness of the diffuse layer around the particle. Figure 7.4 shows a typical pH dependence of zeta potential around the silica particles. When the zeta potential is low, electrostatic repulsion between the charged particles are screened with the shrunk diffuse layer and particles flocculate and then start to coagulate. This can also be seen in the total energy diagram shown in Figure 7.5 obtained from DLVO theory. The flocculation process can be slow if only van der Waals interactions are present. However, flocculation can happen much faster in the presence of external attractive forces.

Figure 7.19 shows the actual zeta potential measurements of 300 nm and 500 nm silica nanoparticles suspended in solutions having various pH values. Measurements are performed in Zetasizer Nano by Malvern instruments [3]. It is observed that as the acidity of the solution increases (decreasing pH), zeta potential around

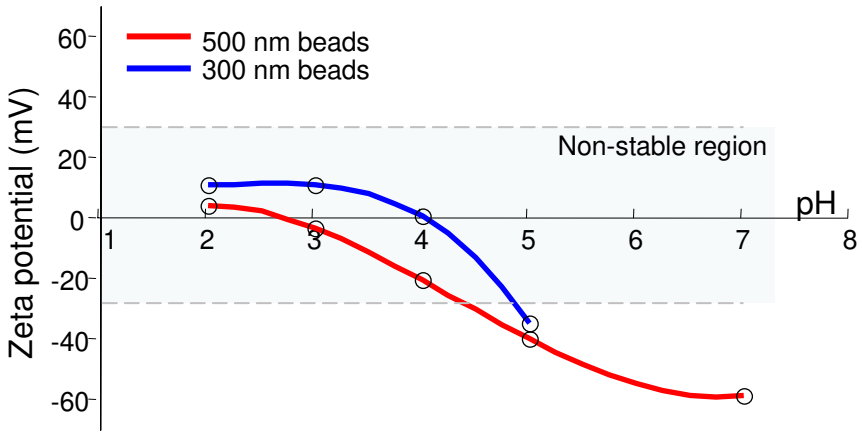

Figure 7.19: Zeta potential measurement of 300 nm and 500 nm silica beads suspended in aqueous solution of different pH.

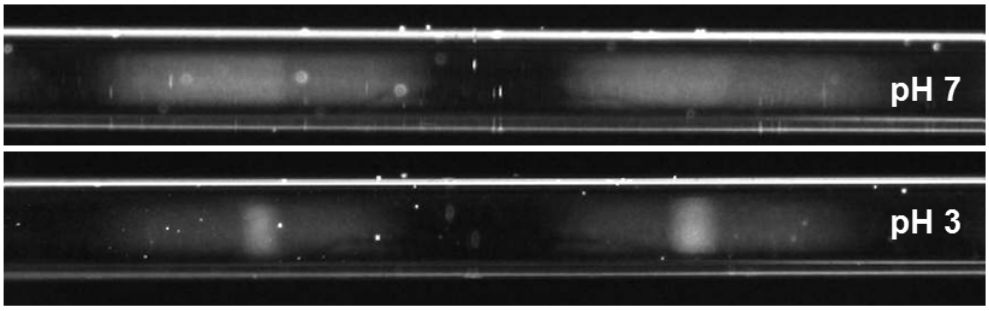

Figure 7.20: Collection of 300 nm particles. The top image shows the particles suspended in a pH 7 solution. The bottom image shows particles suspended in a pH 3 solution.

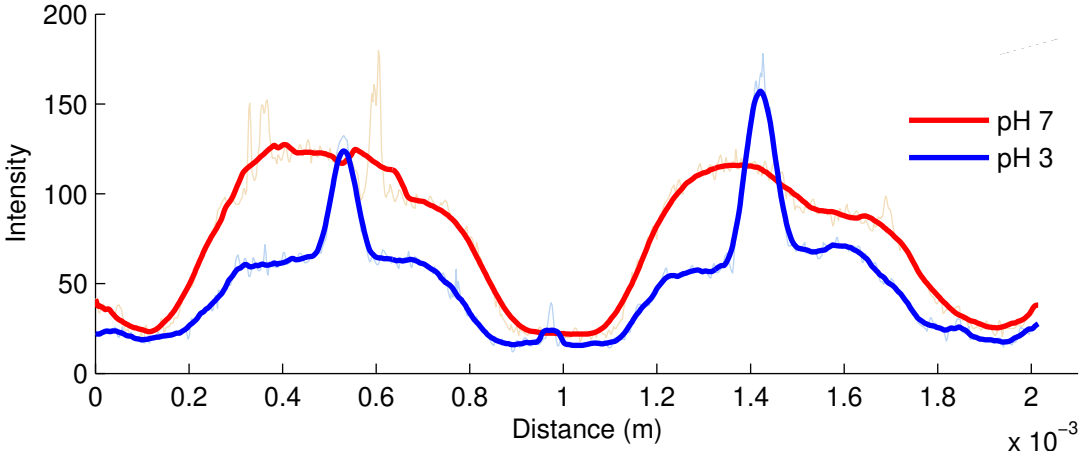

Figure 7.21: Intensity of the scattered light measured at the central axis along the z direction.

the particle starts to decrease. This is due to the collection of H^+ ions around the negatively charged particles. At pH levels below 4, concentration of H^+ ions are high enough to reverse the polarity of the zeta potential at the diffuse layer. Zeta potential measurement is a good indicator of particle stability [113]. It has been known that when zeta potential is between -30 mV and 30 mV, electrostatic repulsion between the particles can not balance attractive forces and particles tend to flocculate. In pH values above 5, silica colloids tested would be stable since the zeta potential is lower than -30mV. For pH values below 5, flocculation is expected. Particle size measurements confirm these expectations. For example at pH 7, particle size distribution peaks are around 300 nm and 530 nm for 300 nm and 500 nm, respectively. However, at pH 3, location and width of the peaks change. Due to the low zeta potential at lower pH values, particles flocculate and measurements show peaks at larger values such as 700 nm, 1200 nm, and 1800 nm. This change can also be observed in the PZT-glass capillary coupled actuator. Figure 7.20 shows an image of the collection of the same silica nanoparticles suspended in solutions having different pH values. Frequency of the actuation is 503 kHz, which represents the 11^{th} flexural mode of the capillary. While a uniform cloudy collection is observed at pH 7, consistent brighter spots appeared at the center of the focal points at pH 3. Figure 7.21 shows the intensity of the scattered light, which can also be associated with the concentration of particles. As particles stick and move together, the effect of acoustic radiation force increases, leading to a better collection. This is similar to the sedimentation experiments performed under centrifugation where larger particles settle to the bottom. Here, larger particles are collected at the center.

At pH 3, all particles go under flocculation, which can be observed clearly in Figure 7.22. In this figure, at pH 7, collection seems to be more cloudy since particle

sizes are around 300 nm. However at pH 3, individual particles are distinguishable; the mixture is not cloudy and a more condensed collection is observed.

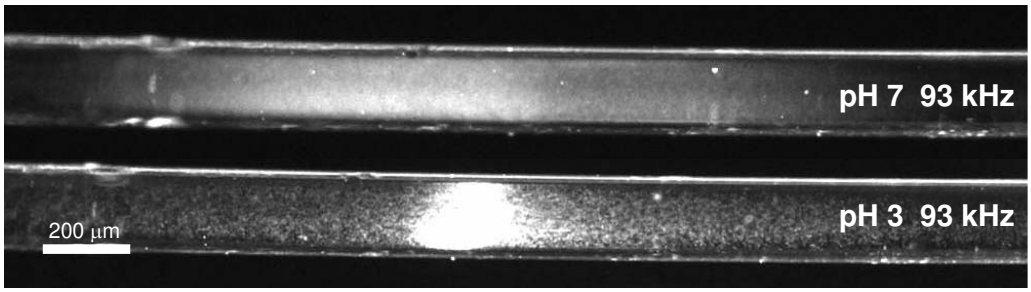

Figure 7.22: At a low voltage drive, at pH 7, a cloudy collection occurs. This is due to the electrostatic repulsion and small particle size. At lower pH values, due to the small zeta potential value, particles flocculate under ultrasonic forces. In this case, a clearer collection is observed. In fact, individual particles can be easily resolved in this magnification, which confirms the particle size is higher than 300 nm because some particles become stuck to each other and then move together.

All results mentioned above suggest that the PZT-glass capillary coupled actuator mechanism can be used to estimate long term stability of particles with performing short term experiments. Due to the low sample volume need and low power actuation, actuator may increase the efficiency and decrease the cost and time needed for the production of materials in which colloidal stability is important.

7.3.2 Collection Behavior of Silica Nanobeads under Acoustic Radiation Forces

In Section 7.2.1, after release of acoustic actuation, dispersion of silica nanoparticles from preferred concentrated regions were examined. Investigation led to finding the

existence of a macroscopic electric field generation due to the concentration of the charged particles. In this section, the collective behavior of colloidal nanoparticles is investigated.

A series of pictures given on top of the Figure 7.23 shows the collection of silica nanopartiicles under ultrasonic actuation. Graphs placed in the middle and on the bottom of the same figure show the intensity variation of the scattered light along the central axis in z direction, versus time. In Section 7.2, it was mentioned that the intensity of the scattered light can be correlated with the spatial concentration distribution of the colloid.

At the beginning, silica nanoparticles were concentrated under acoustic forces. Then, they were let to disperse as the actuation was turned off (more than five minutes). The state of the concentration distribution at t=0 shows these dispersed particles. Observations on the series of pictures and data extracted from these show that after the acoustic actuation is turned on at $t = 0$, a drastically fast change occurs on the axial concentration distribution of the capillary. This change occurs in the first 30 miliseconds. A particle at the concentration boundary moves with a drastic speed of 5 mm/s for about 30 milliseconds. After 1 second, we observe that change in the distribution of the concentration slows down dramatically. Still, in just 60, seconds concentration distribution takes its new stable form under acoustic forces.

Four possible explanations exist for the very fast change of concentration distribution in the first 30 milliseconds. Validity of these possibilities will be argued here briefly. First, when the actuation is turned on acoustic forces are present both in y and z directions. While the acoustic forces in z direction act to focus particles at preferred locations along the z axis, forces in y direction do the same in y direction

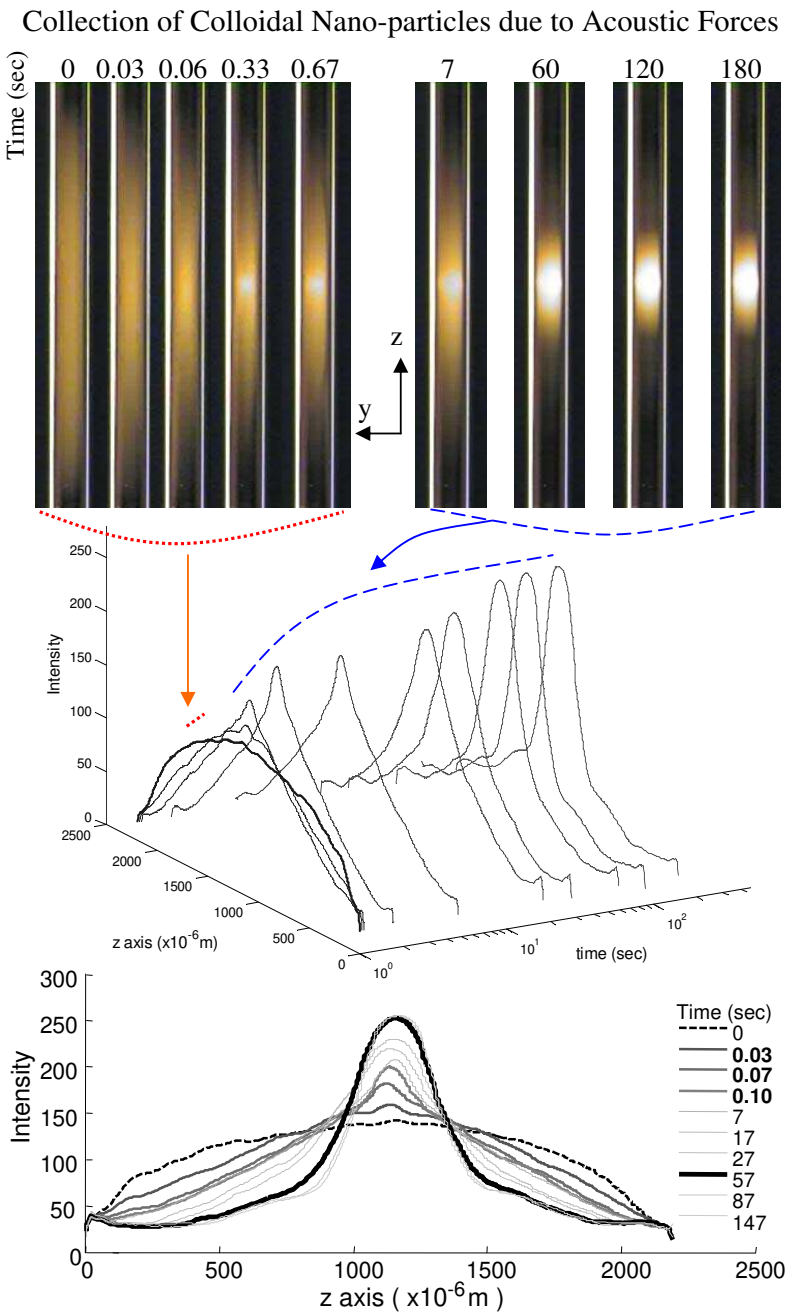

Figure 7.23: Focusing of 500 nm particles at pH 7, under ultrasonic actuation. Voltage drive supplied to the PZT plate is 17 Vpp. As soon as actuation is turned on, concentration distribution of the particles changes to a new state within 30 milliseconds. After 30 milliseconds, the change rate slows down to order of seconds. At about 60 seconds, the particles reach their new stable concentrated state. At this point, the electric field generated by the condensation of particles counterbalance the acoustic forces.

to focus particles at the center. Since the capillary width is much smaller than its length, displacement of particles in y direction becomes much faster and results a major change in the axial concentration distribution. However, from the intensity distribution along the capillary in z and y directions, it is possible to conclude that this cannot be the major single reason.

The second explanation is the contribution of the generated electric field. While in the beginning, particles were dispersed freely, the initial concentration increases due to the instant appearance of acoustic forces. However, as soon as particle concentration starts to change, the electric field generated slows down the push of the acoustic forces. However, because the velocity of the particles are in the order of 5 mm/s, forces on the particles to generate this speed will be really high and not very feasible.

The third explanation is through acoustic streaming. Here, it is argued that both acoustic streaming and acoustic radiation forces contribute to the collection of the particles. Then, the claim is as follows: when the actuation is turned on, high amplitude streaming effects cause an initial change in the distribution of the particles. This streaming is not a steady state streaming but just happens when the actuation is turned on. This kind of streaming has been observed in some other experiments; however, further observations are required in order to make more comments.

The fourth possible reason is the change in the effective acoustic field due to the concentration of particles. When particles start to come together, their effect in the internal acoustic pressure distribution will be more dominant. This may lead to a decrease in the amplitude of acoustic forces on the particles.

Out of these four explanations for the slowing down of initial sudden change, finding individual contributions requires further investigation. However, following the concentration change at the tails of the concentration change, we conclude that the effect of a self generated electric field and the change in the distribution of the acoustic field would be more dominant due to the particle collection.

Another observation is that dispersion behavior of the colloidal silica after turning off the actuation (Figure 7.10) is not the same as the collection behavior of the colloidal silica (Figure 7.23). This is expected since the spatial distribution of the acoustic radiation forces is different than the spatial distribution of the electric field. During the dispersion, electrostatic interactions are the only effective force source. However, during the collection, two forces act together, acoustic collective forces and electrostatic repulsive forces. During the collection, as the collection concentration increases, forces due to the generated electric field increases. At a certain limit electrostatic repulsion gets high enough to balance the acoustic push. In the experiment given above, this limit is reached at around 60 seconds. From the images and plots shown in Figure 7.23, it can be seen that no major change occurs after 60 seconds. In the next section, this limit will be used to estimate acoustic forces.

7.3.3 Calibration of Acoustic Radiation Forces through Counteracting Electrokinetic Dynamics

In Chapter 3, we had calculated the amplitude of the acoustic radiation forces on particles due to the acoustic pressure waves generated by the flexural motion of the capillary. Methods used to derive these forces are mostly first order approxi-

mations. In the capillary structure, depending on the voltage drive, the amplitude of flexural vibrations may reach high values so that nonlinear approaches should also be considered. Since these devices are aimed for delicate samples, a better empirical understanding is needed for the distribution of the radiation forces inside the capillary actuator. Use of hydrophones to quantify the acoustic field is not straightforward due to dimensional limitations; therefore, an alternative method is needed to measure the radiation force directly.

In the previous sections, we already mentioned that the collection behavior of the colloidal nanoparticles under acoustic forces is heavily affected by the electric field generated due to the increase in the concentration of the particles. It was also mentioned that concentration distribution reaches a new stable state as the amount of electric field increases to the limit to counterbalance acoustic net forces. When collection of particles reaches a stable limit and the actuation is turned off, particles start to disperse due to the electric field. A stable limit during the actuation suggests that the acoustic force counterbalances the electric field. In this case, the motion of the particle after turning off the actuation can be associated with the acoustic force. When the actuation is on, the net force on a particle at the concentration gradient boundary is given as

$$F_{ac} - F_e = 0 \tag{7.25}$$

where F_{ac} is the acoustic net force and F_e is the force due to the electric field. Since there is no net displacement, the Stokes drag force is zero. Just after turning off the actuation, equation of motion becomes

$$F_s - F_e = 0 \tag{7.26}$$

where F_s is the Stokes drag given in Equation 7.21, which can be calculated from experimental observation of the expansion velocity of the boundary due to the

electric field. For the time region just before and after turning off the actuation, the force on the particle due to the electric field F_e will not change instantly, then the acoustic force can be approximated as

$$F_{ac} = F_s \ . \tag{7.27}$$

It is important to note that this relationship is only valid just around the time when the actuation is turned off.

As shown in Figure 7.12, at the beginning, the velocity of the particles at the boundary is around $7\mu m/s$. In this case, we find the drag force on a particle at the boundary from Equation 7.21 as, 2×10^{-14} Newton, which is also equal to the acoustic force on a particle at the concentration gradient boundary after all particles are collected.

Since the acoustic force here is associated with the drag force, one may ask what the contribution is of the zeta potential of the particles. Zeta potential affects the concentration distribution. In other words, when the zeta potential is higher, the concentrated volume of the particles will be higher and the concentration will be less dense. Then, the electric field will reach the limit in a more disperse phase to balance acoustic forces. When zeta potential is lower, then the particles will form a more dense concentration and the electric field will reach the same limit at a more dense concentration. In both cases, the limit value of the electric field will be the same; however, spatial distribution will be different. So as long as zeta potential is high enough to give enough push, it should not matter. However, if it is lower than a threshold value, then the electric field cannot reach the limit to counterbalance acoustic forces and floccillation might happen.

If the particles were not charged at all, they would collapse under acoustic actuation and the concentration gradient at the boundary would be a steeper line.

In addition, particles would not disperse as fast and measurements would not be possible.

7.3.4 Collection Efficiency versus Power Drive

In this section, relationship between collection efficiency and the voltage drive supplied to the PZT will be briefly mentioned.

In Page 6.1.2, it was shown that amplitude of acoustic forces on the particles increases with the square of the voltage drive. During the experiments, it was observed that collection speed and voltage drive are related. Estimate relation based on empirical relations is given as

$$v_{collection} \sim (Vpp)^2 \ . \tag{7.28}$$

More detailed analysis will be presented in a future reference. Here it will be only mentioned that the stable collected state of colloidal particles can be reached in a minute with 17 Vpp drive. It has been experimentally verified that collection time reduces to few seconds with some slight amplification at 30-40 Vpp drive regime. Under these higher drive conditions, it has been verified that acoustic radiation forces are high enough to hold 500 nm beads, during a consistent sample flow through the capillary.

7.4 Conclusion and Future Studies

Possible use of PZT-glass capillary actuator for the characterization of the colloidal systems is introduced in this chapter. The actuator presented here may replace

bulky centrifugal systems because it is small, easy and cheap to fabricate. In addition results can be obtained very fast with low sample volume requirement (0.6 microliters). The actuator mechanism presented here may be a great contribution to drug design and development. Since the amount of power consumed by the actuator is very low, portable battery operated hand held devices are also possible. Another advantage of the capillary actuator is that, even the internal diameter of the capillary is 100 micrometers, results are observable to the naked eye and can be monitored in detail with a regular hand held digital camera or a document scanner.

The capillary used is the standard fused silica capillary and the actuator presented here can be integrated with wide range of other larger or same size bio analytical tools such as HPLC or other microfluidic systems.

It is demonstrated in Section 7.3.1 that device can be used to monitor behavior of the colloids, at various pH values. In the analysis of the colloidal systems, since the theory can deviate from experimental results especially in high salt concentrations or acidity, direct experimental observation is always performed in product development. In this regard, PZT-glass capillary actuator may be a cheap, fast and accurate characterization device for the colloidal stability.

Results presented in this chapter suggest that device can be used to collect agglomerating proteins at their isoelectric values.

Since effect of power drive on the collective acoustic forces increases with more than a linear relation, with some amplification collection and study of smaller particles would also be possible.

CHAPTER 8

OTHER MICROSCALE ULTRASONIC ACTUATORS

Introduction

The major foci of this chapter are the new actuator mechanisms inspired by the PZT-glass capillary actuator. In the first section, the silicon bulk microfabricated actuator will be introduced. Some introductory approaches related to the characterization of the actuator are given. Similar to the PZT-glass capillary actuator, the collection and separation results obtained in the new microfabricated actuator are presented. The bulk-PZT actuation provides high electromechanical coupling and the microfabricated silicon part constitutes a general purpose platform for different fluidic capabilities.

In the second section, the design and the fabrication of the 10-100 μm diameter microfabricated capillary actuator is described. Details of the microfabrication steps and preliminary characterization results are introduced.

In the third section, the Kundt's tube is revisited. A capillary serving as a microcavity is actuated by another microcapillary serving as a piston. As a result, particle collection under standing pressure plane waves are demonstrated. The major drawback of this actuator is because the end locations of the fluid column define the boundary condition, experiment to experiment variations cannot be controlled, which makes the actuator a device to be perfected in the future.

The last section of this chapter deals with some possible minor advancements to the PZT-glass capillary actuator.

8.1 Silicon Bulk Microfabricated Actuator

8.1.1 Introduction

For many bioassays, it is necessary to separate an incoming sample into its components, which can be antibody-coated-beads or cells. By separating the components by size in two dimensions, optical detection can be used to implement assays. In previous chapters it, was demonstrated that commercial glass capillaries can be used for acoustic chromatography at microscopic levels. In contrast, here, the radiation forces are used to manipulate particles in two dimensions on a planar surface, a major advance for practical devices. The new device process brings the advantage of silicon fabrication techniques, which enable addition of more features like optically thin silicon nitride layers for easy optical imaging, poly-resistors for temperature control of the fluid enclosed by the channel, and a stress-strain sensing mechanism for the characterization of the wave propagation within the bulk silicon walls.

The device consists of two layers of bulk micromachined silicon layers bonded together, forming the body of the actuator and a laser-cut PZT (Lead-Zirconate-Titanate-Oxide) plate as the source of bulk ultrasonic actuation. The silicon bulk-micromachined microfluidic ultrasonic actuator allows two dimensional ultrasonic standing waves on an optically transparent silicon nitride membrane. The frequency of selective standing waves can control the radiation pattern to hold and separate particles of different sizes, forming traps similar to a two-dimensional array of optical tweezers. By changing the drive frequency, particles can be brought together for reactions, and can also be brought apart for interrogation. This device enables focusing and/or separation of microparticles of different sizes under

a low voltage drive (0.5-20 Vpp), which may lead to portable, battery operated diagnostic devices. Silicon-nitride layers on top and on the bottom of the channel enable optical and UV-fluorescence imaging while coupling the vibrational motion into fluid. Complete electrical isolation of the fluid inside the channel, no specific pH or ionic solution requirement (as it is for electrical property based separations), and easy integration with other microfluidic devices are the main advantages of the device.

8.1.2 Fabrication

The fabrication process, which is sketched in detail in Figure 8.1, starts with LPCVD deposition of 1 μm thick low stress silicon-nitride and 0.8 μm thick poly-silicon layers on the silicon wafer consecutively. After the top poly layer has been doped via ion implantation and patterned by reactive ion etching (RIE), a thermal oxide layer of 360 nm has been grown (b). Before the aluminum sputtering (c), the oxide layer is patterned for the contact holes. Later, the top and the bottom nitride layers are patterned via RIE for the anisotropic bulk etching of the silicon in tetra-methyl ammonium hydroxide (TMAH) solution without attacking the aluminum (d) [114]. After the etching (e), two symmetric patterned layers are bonded together with epoxy, where the middle etched cavities form the channel (f). Grommets for the fluid transfer, and the PZT plate to actuate the silicon body are adhesively bonded (Figure 8.1 and Figure 8.3).

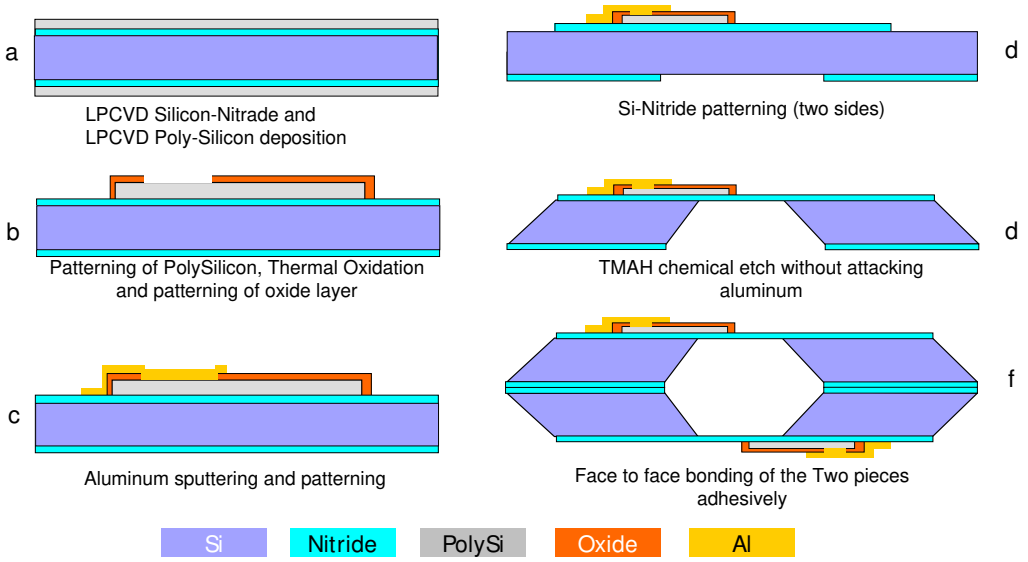

Figure 8.1: Microfabrication steps for the silicon microfluidic actuator.

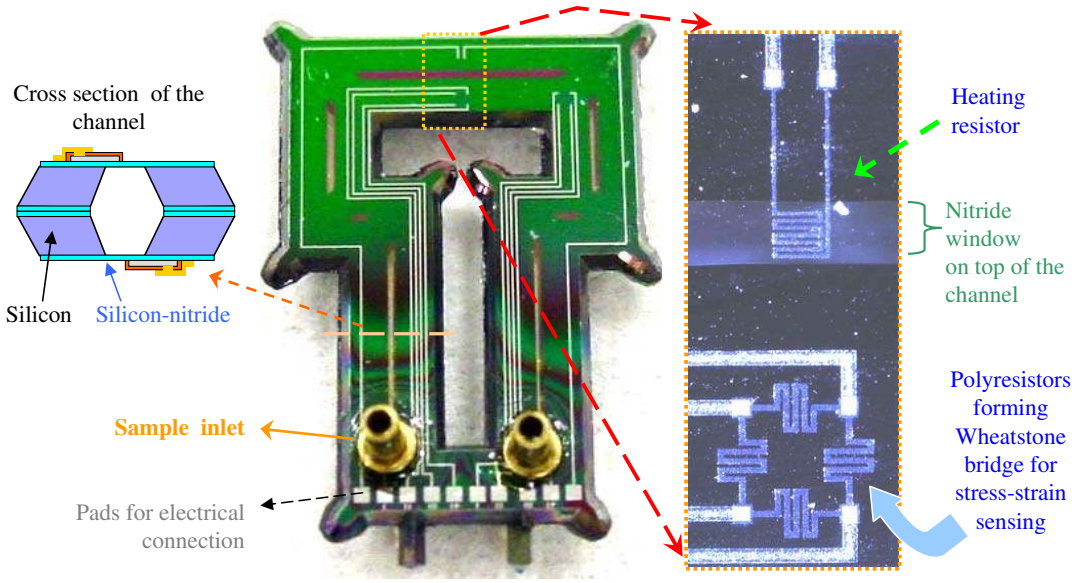

Figure 8.2: Details of a fabricated actuator. The PZT plate has not been attached in this device.

8.1.3 Experimental Results

After bonding the PZT plate to the silicon structure, the hybrid actuator is driven with a function generator. Separation and manipulation processes take place between a 50 kHz to 2 MHz drive frequency.

In the small actuator volume, within the frequency drive range, various different wave dynamics with different phase speeds are present. Vibrations of the PZT plate can excite many different modes matching to the spectrum of the drive signal. The vibrational modes of the different device parts can be listed as bulk, quasi-longitudinal, flexural and shear modes on the silicon cavity walls; flexural plate and membrane modes of the silicon-nitride membranes; and acoustic cavity modes in the enclosed fluid volume. It is also known that in silicon, due to its anisotropic crystalline structure, propagation speeds of waves depend on the propagation direction [115]. The difference in the propagation speed of different modes result in different wavelengths. Acoustic streaming and force field related to the dynamics of particles are a combination of all these different modes. The nodes and antinodes of these fields, tunable by the drive frequency, result in particle collection and/or separation at some frequencies obtained through experimental trials.

While this richness of various wave speeds brings flexibility to the device, when combined with the adhesive layer and the PZT, analytical modeling of the actuator mechanism becomes a problem of many unknowns. A laser interferometric Doppler scan (using a PolyTec^{TM} vibrometer) of the vibrating surface helps to identify specific modes. For example, the surface plot on the right side of Figure 8.3 shows interferometric scan of dashed area at 1.6 MHz and 1 Vpp drive. Scan reveals high amplitude transverse oscillations in silicon-nitride membrane and the silicon body.

Due to the difference material properties and dimensions, vibrations of nitride membrane and silicon body will have different wavelengths at the same frequency, which can be used to produce controlled acoustic traps for particle collection and separation.

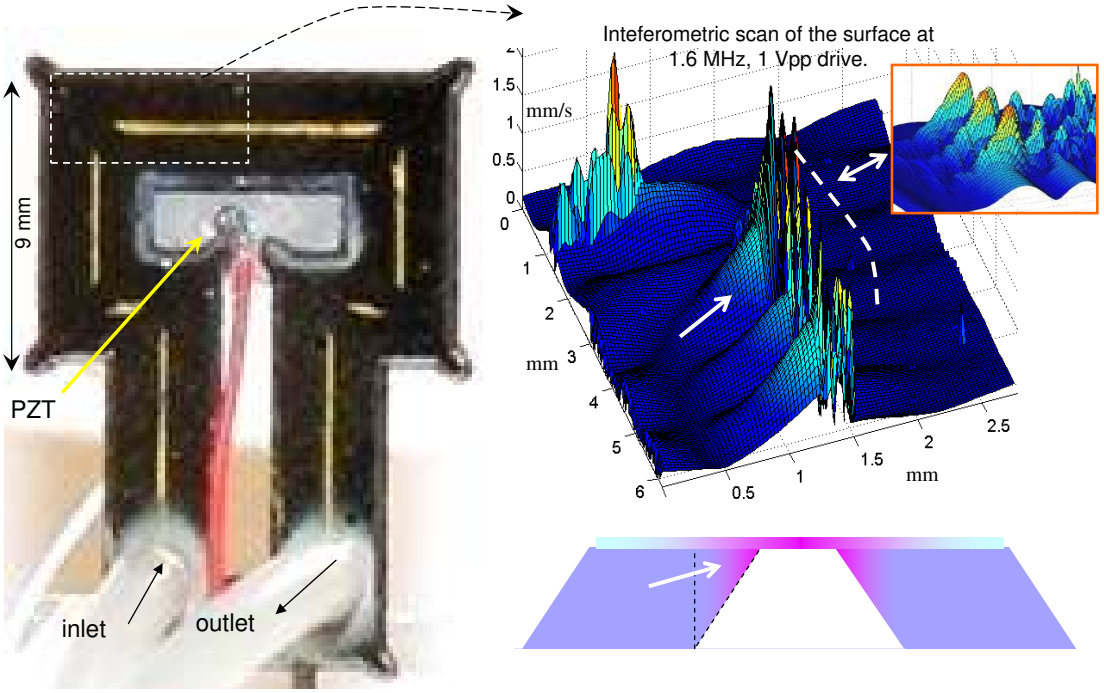

Figure 8.3: Left: Silicon microfluidic actuator with PZT plate attached. Right: Interferometric scan of the area shown on the picture of the actuator. Amplitude of the vibrations are maximal on the silicon-nitride plate. Waves on the silicon body get mechanically amplified due to the triangular cross section. This can be seen on the interferometric scan (along the arrow amplitude of vibration increases).

Nitride membrane has high aspect ratios, about 1/100. In this case, vibrational modes which are related to the transverse motion will be mostly dominant. When a transverse vibration is present in a boundary, fluid loading significantly effects the wave dynamics. This is because, when the structure moves in normal direction to the boundary, significant amount of fluid mass has to be pushed or pulled. For

cases in which wavelength on the elastic structure or plate is less than the acoustic (sonic) wavelength, fluid acts as a mass load. In this subsonic case, disturbances in the fluid can not propagate and evanescently remain close to the boundary [50]. In the reverse supersonic case however, fluid acts as a spring and disturbances generated at the boundary propagates as acoustic waves into the fluid. Due to the coupled propagation, in the second case a great portion of the elastic energy in the structure is coupled to the fluid.

Figure 8.4 shows the collection of particles due to transverse vibrations of the silicon-nitride membrane. The images displayed are captured by an up-right epi-fluorescent microscope (Zeiss-AxioPlanII). A picture of focused 3 micron polystyrene beads at 609 kHz and 440 kHz having the cluster size of tens of microns was taken under regular light transmission, which also demonstrates optical top to bottom transparency. Particles collect at the vibration antinodes. Two types of transverse vibrations can be generated in a membrane, flexural vibrations due to the flexural rigidity of the plate and membrane vibrations due to the tension on the membrane. To be able to understand what type of vibration is responsible for the particle collection, wavelength of the modes are extracted from particle collection images by placing imaginary nodal lines between the collection spots as shown in series of images on the right side of Figure 8.4.

From wavelength data, phase speed of the transverse membrane waves can be estimated ($c = \lambda f$). Phase speeds found from these figures are plotted in Figure 8.5. Top line in this figure shows the fit to the experimental data which remains almost constant around 200 m/s. At the same graph, theoretical values for flexural waves in a silicon nitride plate (in vacuum and liquid loaded cases) are plotted.

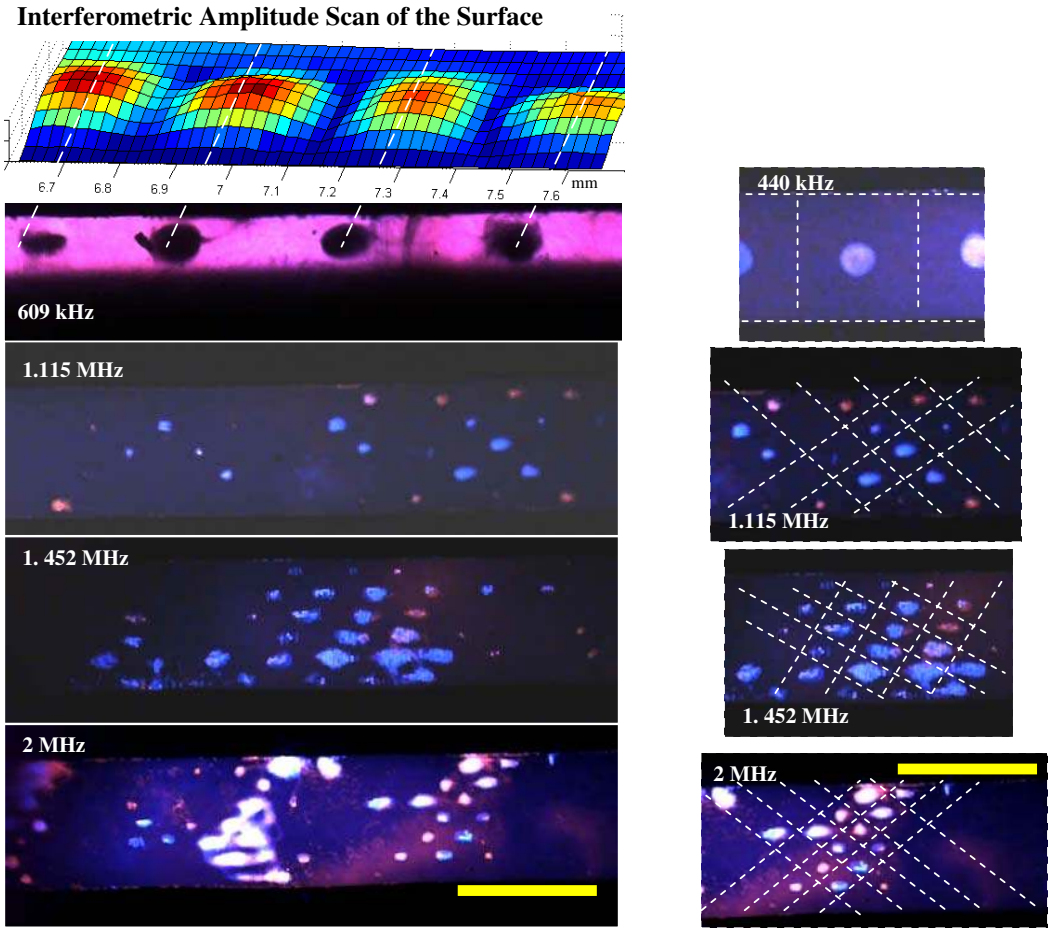

Figure 8.4: Left: Collection of 3μm (red) and 10μm (blue) polystyrene beads due to transverse motion of the silicon nitride membrane. Interferometric amplitude scan of the membrane area matches the location of particle collections. At higher frequencies, smaller particles tend to collect at the edges as the red spots in 1.115 MHz case. Right: Imaginary lines showing the possible nodal planes of the transverse vibrations. Particles collect at the displacement antinodes.

Phase speed for flexural waves is given by [50]

$$c_f = \sqrt{\omega}\left(\frac{Eh^2}{12(1-\nu^2)\rho}\right)^{1/4} \tag{8.1}$$

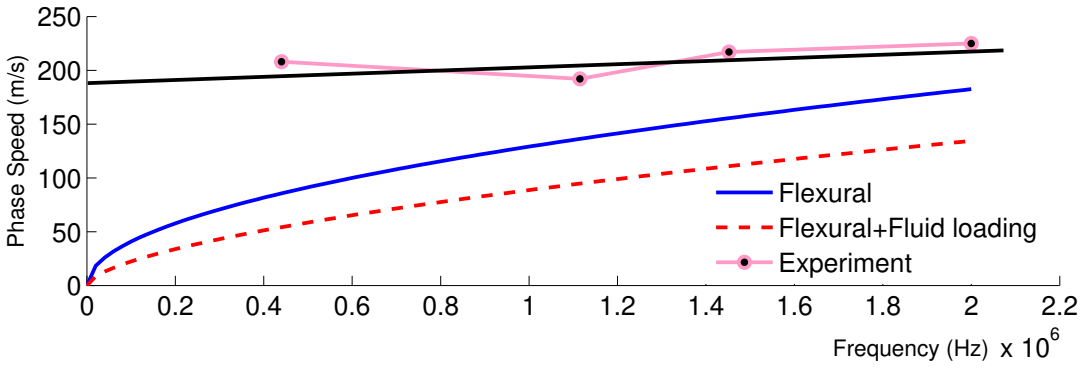

Figure 8.5: Graph of phase speed versus frequency. Flexural vibrations show dispersive behavior and experimental data shows that vibrations are not flexural modes but membrane modes.

and for liquid loaded case,

$$c_f = \left(\omega^3 \frac{Eh^3}{12\rho_0(1-\nu^2)}\right)^{1/5} \tag{8.2}$$

where E is the Young's modulus, ν is the Poisson's ratio, ρ is the density of the plate, ρ_0 is the density of the fluid, h is the thickness of the plate and the ω is the angular drive frequency. For the silicon nitride (E ~250GPa, ν =0.24, ρ=3290 kg/m^3, h=1 m) in 400kHz–2MHz regime, speed of the flexural waves varies between 50 m/s and 150 m/s. Experimentally obtained phase speed shows only a very slight variation versus frequency and it is almost constant around 200 m/s. It is known that phase speed for the membrane waves is not dispersive and given by [116]

$$c_f = \sqrt{\frac{\tau}{\rho}} \tag{8.3}$$

where τ is the tensile stress keeping the membrane taut over the silicon etched substrate. Since flexural and membrane wave motion is almost identical, effect of fluid loading will be very similar. In this case similar to the flexural case, assuming fluid loading causes 1/3 reduction in the phase speed, stress over the membrane can be estimated to be around 270MPa, within the range of the residual stress value in LPCVD low stress silicon nitride.

Assuming a sinusoidal membrane motion and solving the Helmhotz's equation with fluid-structure boundary conditions [116], one may get the pressure distribution across the channel as,

$$p = -(\frac{jA\rho_0 ck}{k_z})cos(k_x x)sin(k_y y)(e^{-k_z z} + e^{k_z(z-g)}) \tag{8.4}$$

where g is the distance between the two nitride membranes, A is the amplitude of the oscillation, k_x and k_y are the wave vectors on the membrane and k is the wave vector in liquid and the net cavity wave vector k_z is given by

$$k = \sqrt{(k_x^2 + k_y^2 - k^2)} \ . \tag{8.5}$$

With a phase speed of 200 m/s -lower than speed of sound in water (1450 m/s)- membrane modes are always subsonic and k is real, which means pressure coupling is evanescent. Equation 8.4 is plotted for various frequencies against z axis in Figure 8.6. It can be concluded from this plot that, at low frequencies, due to the low k value, acoustic pressure penetrates more into the cavity. This also explains the small slope in the fit on the phase speed data in Figure 8.5. (At low frequencies, membrane ends up pushing more fluid). It is observed that, for frequencies higher than 200 kHz, acoustic pressure variation happens only in the close boundary (less than 200 μm). In this case, acoustic radiation pressure forces do not play a major role in collection of particles. As shown in Figure 8.7, acoustic streaming generated by the transverse motion of the membrane collects particles at the vibration antinodes.

From the interferometric scan of the bulk silicon walls, elastic wave speeds in the silicon walls are observed to be between 3000-8000 m/s. Since these values are higher than the speed of the acoustic waves in water (1450m/s), in other words supersonic, normal displacements generated by these vibrations strongly couple

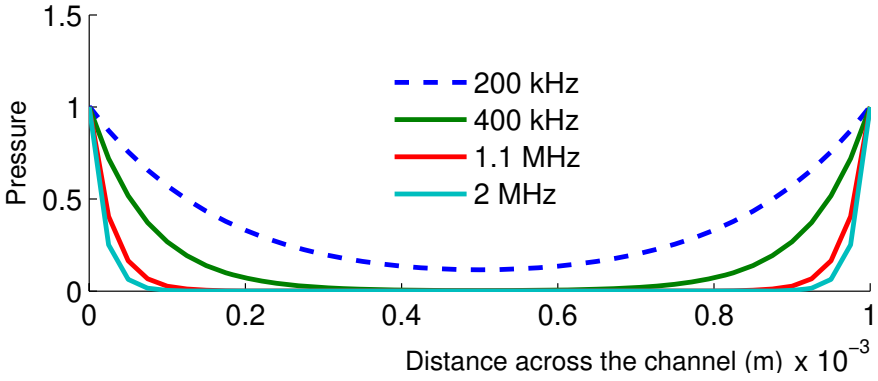

Figure 8.6: Pressure across the channel due to the vibration of the silicon nitride membrane.

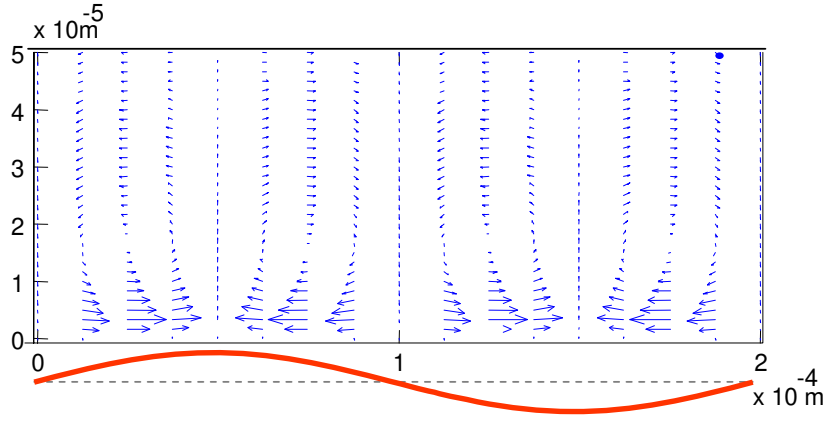

Figure 8.7: Acoustic streaming (outside the viscous boundary) generated by the transverse motion of the capillary. Calculated from [4].

into the fluid cavity (k in Equation 8.5 becomes imaginary). In this case, acoustic radiation pressure gradients with pressure nodes can be generated which enables capture of particles by acoustic radiation forces. Since acoustic radiation forces are related to the cube of the particle size [58], larger particles feel this force much higher; whereas small particles are more prone to the streaming effects. As shown in Figure 8.8, for example at 1.488 MHz, by generating streaming effects and radiation force field at the same time with some distance, particles can be

separated with respect to their size. Figure 8.9 shows the series of images showing the separation of mixed 3μm yellow and 10μm blue[1] beads at 1.488 MHz, further localization of separated beads by switching to 600 kHz (mode shown on the top of Figure 8.4), and mixing of the separated beads again at 1.766 MHz by exciting a mode where radiation force field and streaming effects are generated at the same spot.

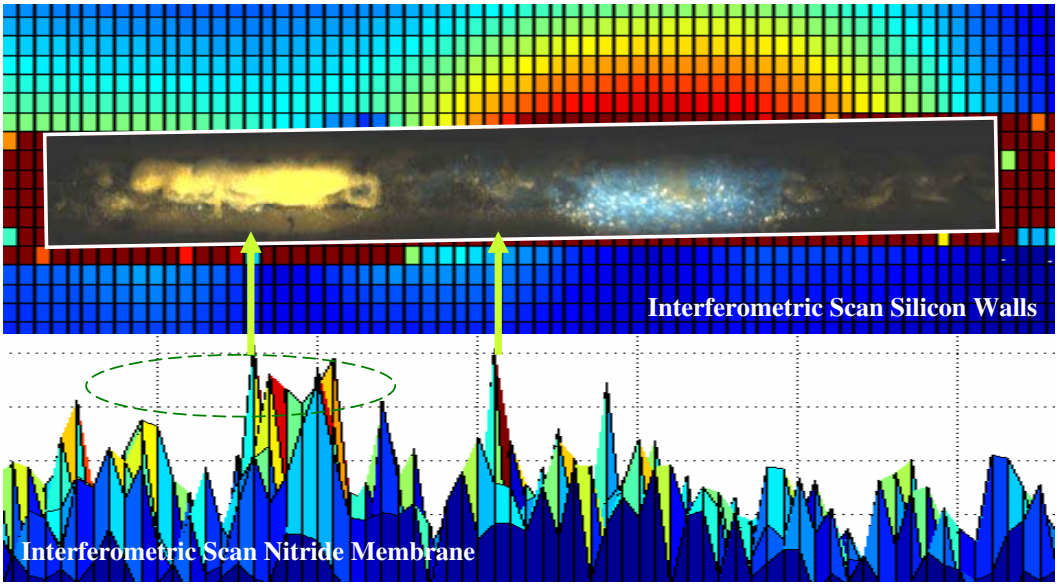

Figure 8.8: Interferometric scan of the silicon walls reveals that 10μm blue particles are collected at the vibrational maximum of the silicon walls, whereas 3μm yellow particles are captured in the streaming generated due to the high amplitude vibrations of the silicon-nitride membrane.

All these experiments mentioned above are performed with few volts peak to peak drive. Since the losses in the single crystal silicon are low, the vibration transferred to silicon from PZT generates a considerable amount of vibration. Some experiments, unfortunately, ended earlier than planned because of the shattering

[1]In fact, fluorescent dyes in these beads are red and green, instead of yellow and blue. However, due to the optical filters used, the captured images gave false colors. Here, colors recorded by the microscope digital camera are used to identify beads.

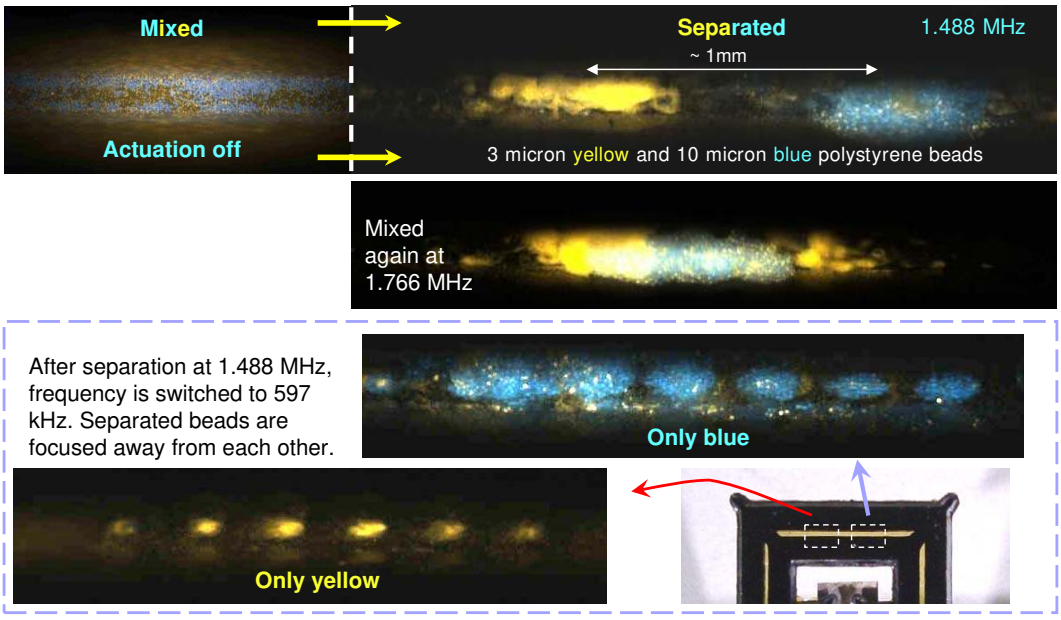

Figure 8.9: Separation of 3 micrometer yellow and 10 micrometer blue polystyrene beads. Beads were mixed before actuation, and by frequency hopping clusters of beads can be separated up to millimeters. Separated microparticles can be combined again through switching to another frequency. After the particles are separated into two main clusters, by switching the frequency to 597 kHz, they can be localized at the closest possible collective location.

Figure 8.10: Shattered silicon-nitride membrane due to the high amplitude mechanical vibrations coupled from the silicon. This particular case occurred at 495 kHz with few volts peak to peak drive where a resonance of the whole pzt-silicon actuator exist.

of the silicon nitride membrane due to the high amplitude of vibrations even at few volts peak to peak. Figure 8.10 shows the cracks on the silicon-nitride membrane,

the fragments of which are often ejected from the devices.

8.1.4 Conclusion

A new PZT driven silicon bulk micromachined microfluidic actuator that couples bulk silicon motion to silicon nitride membrane is presented. Membrane and bulk modes on the nitride membrane and the silicon body form frequency selected standing waves producing two dimensional arrays of traps. By changing the frequency, particles of different sizes can be brought together or separated under a CMOS compatible low voltage drive. Chromatography in a micro-platform with a separation of 500 μm between 3 μm and 10 μm beads was achieved. Work on capturing cells and studying cell growth at elevated temperatures using the integrated heaters and stress sensors for the resonance feedback in the presented actuator remain as future work.

8.2 Silicon Nitride Microcapillary Actuator

8.2.1 Introduction

In this section, fabrication and characterization of suspended optically transparent microfluidic channels for ultrasonic actuation are presented. This new device may enable focusing and detection of smaller structures in a submicron regime and has the advantage of integrability with other lab-on-chip microfluidic systems, lower voltage drive, better controlled boundary conditions, and better coupling with respect to the previous models and devices where the construction includes hand

assembly.

In the previous chapters, CMOS compatible, low voltage ultrasonic actuation of microfluidic capillaries had been demonstrated as an efficient way of manipulating microbeads and biological entities at the micro-scale. Devices were consisted of commercially available silica capillary tubing attached to the laser cut PZT plate becoming the source of the actuation. During this actuation, the main vibrational modes excited were bending modes. With the previous system, microparticles down to 300 nm were successfully collected and also particles of different sizes were separated in fluid. Here, a new approach enables precise control of the optically transparent suspended channels with diameters in the order of few μm to 10 μm.

8.2.2 Fabrication

The fabrication process is a modified version of a process available in the literature [3]. The steps followed are given in Figure 8.11. Fabrication started with growing thermal oxide on <100> silicon wafers and patterning the oxide by RIE etching. The silicon substrate was etched anisotropically by DRIE etching by use of Bosch® process. Etching is followed by a thinner layer of thermal oxide growth (b) and RIE etching of this layer at flat surfaces. After removing of the oxide from the bottom of the trench, an isotropic plasma etch of silicon was performed, which formed the template cavity for the channel (c). Removal of all oxide layers by wet etching (HF solution) followed by deposition of low stress LPCVD silicon nitride until the channels are sealed from the top (d). Later, the nitride on the top and bottom surfaces were patterned (e) and the exposed silicon parts were anisotropically etched in hot KOH solution, releasing the suspended channels (f).

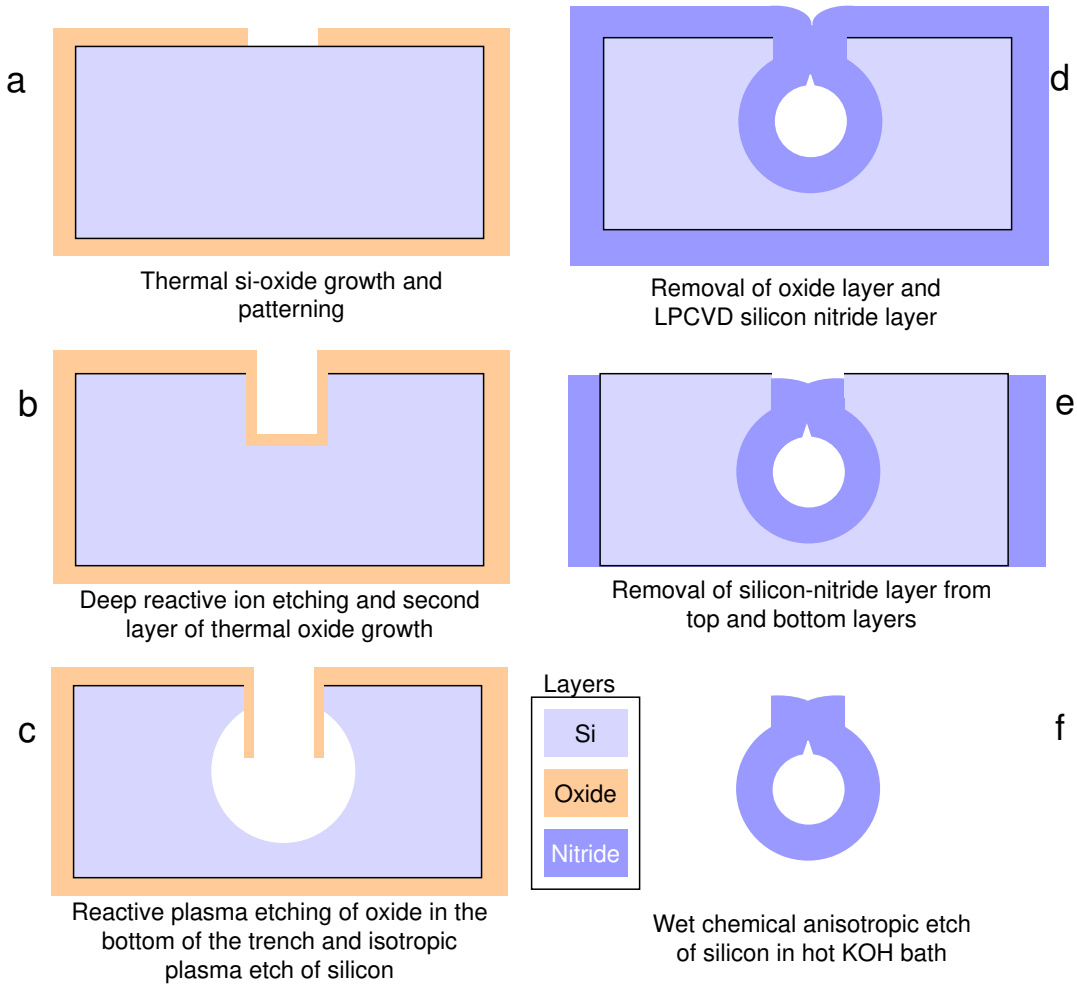

Figure 8.11: Steps for the microfabrication of silicon-nitride suspended capillaries.

After the silicon die including suspended nitride capillaries is ready, it is adhesively bonded to the PZT plate cut with a dicing saw.

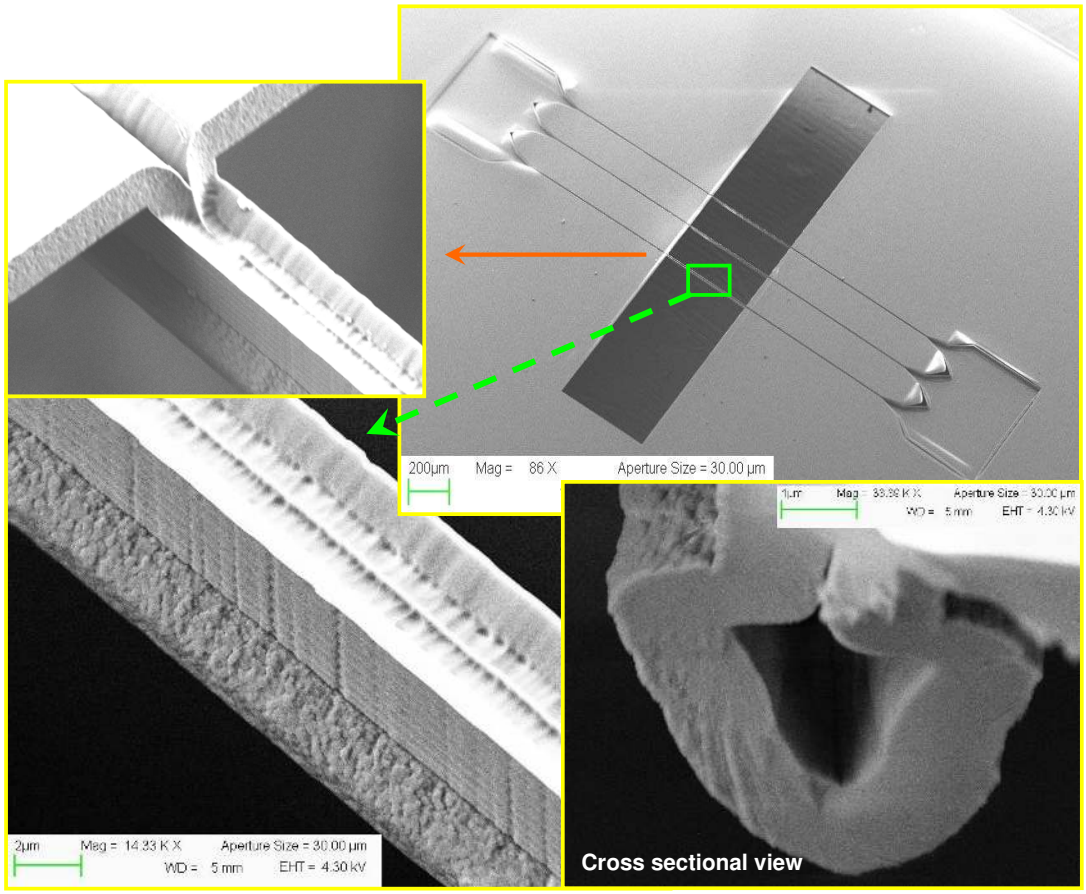

Figure 8.12: In the electron microscope images of the silicon-nitride capillaries, details of the capillary structure, cross section, inlets and outlets are shown.

8.2.3 Preliminary Results

In a suspended or clamped-clamped tubing, one can excite many vibrational modes depending on the channel inner and outer radius ratio, material type, the channel length, and any other geometrical features. Because the aim here is to excite the capillary flexural modes similar to the PZT-glass capillary hybrid actuator presented in Chapters 2 and 3, the channel radius and the wall thickness are designed accordingly. As for optical detection, thermal silicon oxide or LPCVD

nitride are good candidates with conformal coating capability; LPCVD nitride, due to its low stress, is used to demonstrate the preliminary devices. The SEM image of the fabricated device with inlets and outlets, a closer look at a 10 μm size nitride suspended channel, and a cross section image of another channel are shown in Figure 8.12. The lengths of the suspended channels vary from 100 μm to 500 μm.

The final PZT-driven device is shown in Figure 8.13. For the mechanical testing of the device, the PZT plate is driven with a regular function generator. An interferometric scan of the nitride capillaries is performed both spatially and in a wide frequency range (500 kHz-7 MHz). Since the interferometer is sensitive mostly to normal displacements, flexural modes can be identified more easily. In the given frequency regime, modes extracted from the interferometric scan are plotted in Figure 8.14. In the plot, two distinct dispersion curves are identified. Flexural motion of the capillary can be in two dimensions. When the cylinder is symmetric around the axis, two resonant states will be degenerate. However, when the structure is not symmetric, as is the case here, then the frequency values for the n^{th} mode in two dimensions will be different. When the structure is not symmetric, flexural rigidity around different axes will be different. Here, since all material properties are the same, the difference between two curves stems from different area moment of inertia, I_i, values. In this case, from the curves fit to the data, the ratio of the area moments of inertia around two different is extracted to be 2.27. Testing of the device with fluid samples is left as future work.

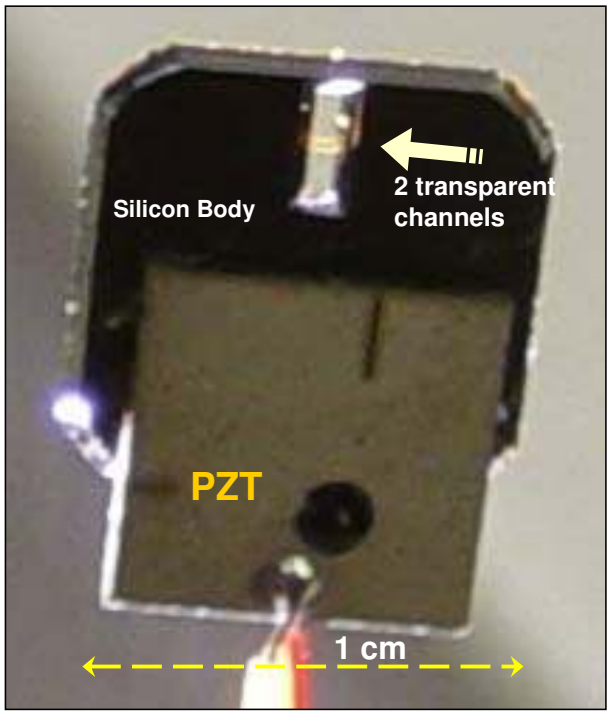

Figure 8.13: Silicon dye with PZT plate is attached. Two capillaries can be seen as they scatter the incident light beam on them.

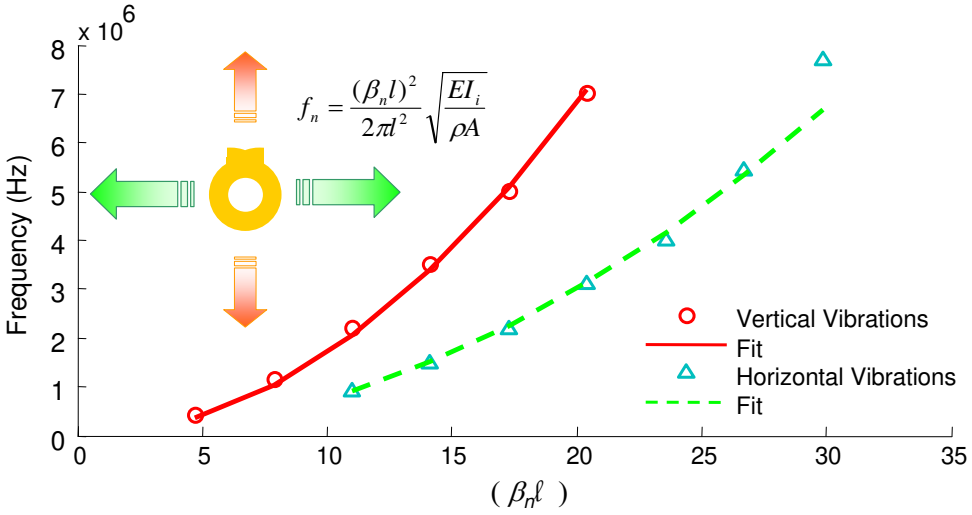

Figure 8.14: Dispersion curves for the modes detected from an interferometric scan. Two distinct quadratic relationships stem from the asymmetric cross section of the capillary structure. Due to the asymmetry, area moment of inertias around two orthogonal axes defining cross section are different.

8.2.4 Conclusions

Silicon-nitride suspended capillaries are produced through silicon microfabrication techniques. It has been verified from the optical interferometry scan results that for the frequency regime actuator is run, flexural modes are the main modes excited. For microfluidic applications, this enables the familiar working principle with the PZT-glass capillary actuator.

8.3 Excitation of P-Waves in the Capillary

8.3.1 Introduction

Introduced in this section is the particle collection due to the standing pressure waves formed along the fluid column enclosed by a cylindrical capillary. As shown in Figure 8.15, the silica capillary having a 200 μm outer and 100 μm inner diameter is filled with 3M instant glue and adhesively bonded to a rectangular PZT plate. Another capillary having an inner diameter of 320 μm and outer diameter of 435 μm is filled with fluid (DI water) with suspended sample microparticles. Then, a thinner cylinder attached to the PZT is carefully inserted into the larger capillary, which includes the sample. In this configuration, the thin capillary acts as a piston inside the larger capillary, which enables selective excitation of cavity modes in terms of pressure waves because the coupling is directly between the capillary acting as the piston, and the fluid enclosed by the larger capillary. Similar to the other experiments, the PZT plate is driven with a function generator.

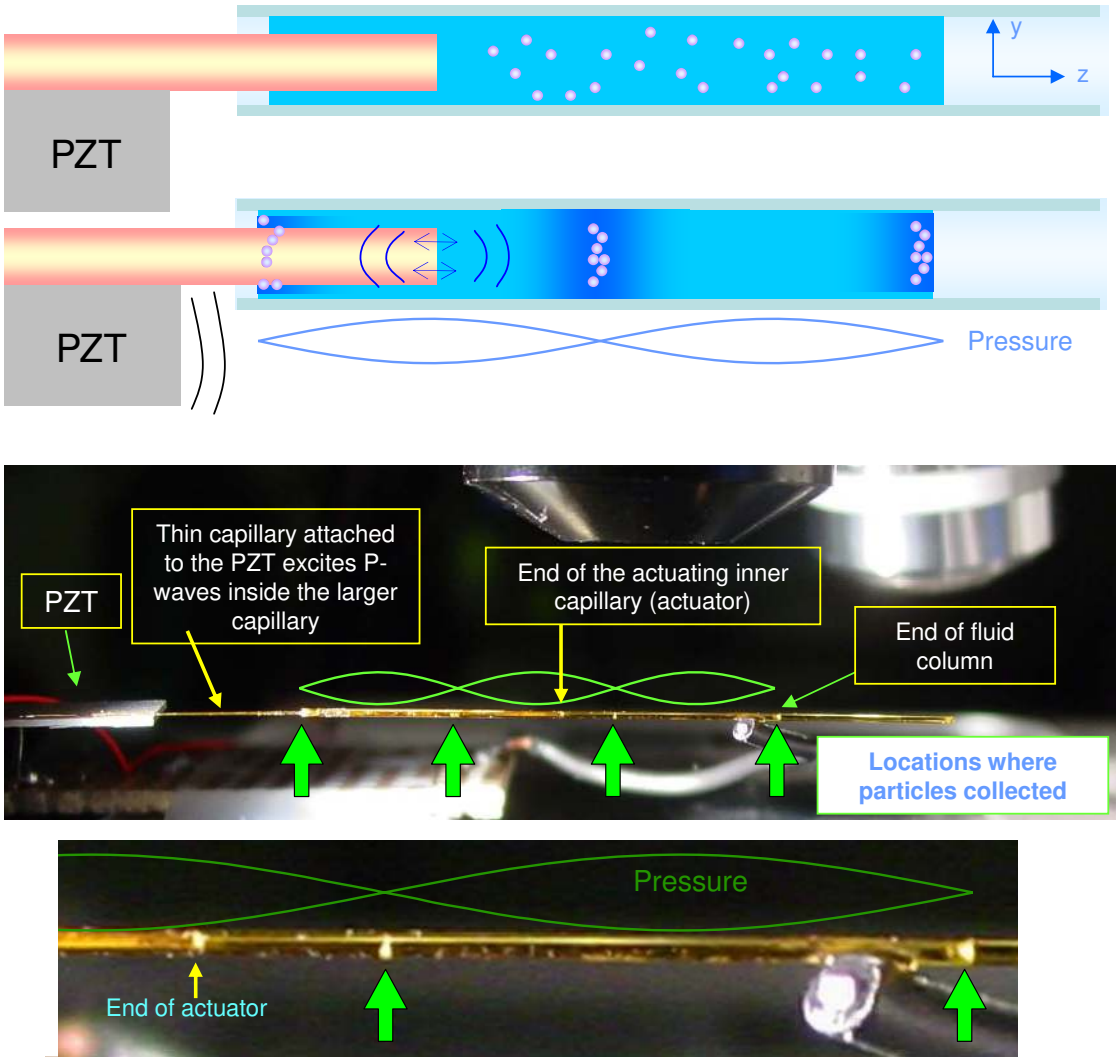

Figure 8.15: Top: Schematic for the exclusive excitation of p-waves in a column of fluid, enclosed in a microfluidic capillary. Internal excitation is enabled by a second thinner capillary attached to the PZT plate. The picture in the middle shows the PZT plate, the thin capillary (actuator) attached to the PZT plate, the capillary enclosing the fluid column and the sample, and the collection of the particles. The bottom picture shows a magnified version of the above image.

8.3.2 Results and Discussion

As shown in the pictures included in Figure 8.15, particle collection can be monitored without a microscope. Images shown in this figure were captured with a point and shoot, hand held digital camera. Here, actuation frequency is 62 kHz. Wavelength can be measured from the distance between the collection points, in this case, the speed of the wave inside the capillary is found to be 1450 m/s. This is, in fact, higher than the theoretical expectation of 1330 m/s calculated through the method given in Appendix A.

Collection results confirm that the length of the fluid column is the only important parameter defining the resonance frequencies. In this case, resonance frequencies can be find from the equation

$$f_n = \frac{c_p}{\lambda_n} = \frac{c_p}{2l} n \tag{8.6}$$

where c_p is the speed of waves, λ_n is the wavelength of the n^{th} mode, and l is the length of the fluid column.

Figure 8.16 shows the collection of 10 μm particles due to the standing pressure wave fields at various frequencies. Wavelengths obtained from the distance between the collection locations result are used to calculate the speed of the waves as 1450 m/s. As shown in Section 3.1.2, below the cut off frequencies of the radial and angular modes, the distribution of the pressure waves only depends on the z axis; these are plane wave modes. The shape of the collection of particles looks like a disk aligned in the normal direction to the central axis of the capillary. This observation proves that variation in pressure values exist only along the cylinder.

After particles are collected at a resonance frequency, a small shift in the frequency results in a change in the angular alignment of the collected particles. This

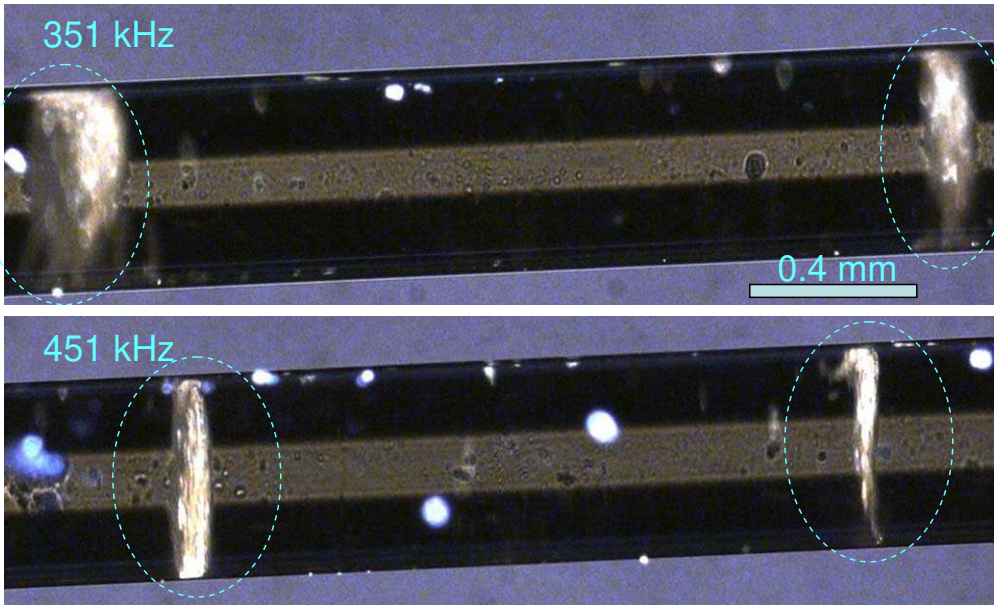

Figure 8.16: Particle collection at two different resonance frequencies. Frequencies of the modes are dependent on the length of the fluid column. When the frequency is lower than the first cut off frequency for the radial modes, P-waves do not have any radial or angular dependence, so the collection forms a disc shape, aligned normally to the central axis of the cylindrical capillary.

effect is shown in Figure 8.17. In this way, the packing structure of the microparticles can be observed. In the same figure, the crystalline packing structure of the 10 μm particles can be observed. This method reveals that microparticles can be aligned and packed in a crystalline structure under acoustic forces.

In a Kundt's tube experiment, when sand particles are collected primarily at pressure node locations, fine structures were observed on the bulk collections. These striations have been observed in many experiments and their periodicity cannot be associated with a wave speed. In cavity mode experiments performed here, similar to the PZT-glass capillary actuator, striations have been observed. In this configuration, the periodic distance between two fine collections is about

Figure 8.17: After particles are collected at a pressure node, their alignment with the central axis can be changed by a slight frequency shift. This alignment change reveals the crystalline packing structure of the particles collected under acoustic radiation pressure forces.

60 μm. This value at 62 kHz corresponds to a wave speed of 7 m/s. Since no form of wave propagation is known for these values, it can be concluded that these striations do not follow the periodicity of any P-wave propagation. As shown in [117], these striations are related to the possible secondary effects, particularly the streaming vortices occurring inside the cavity.

8.3.3 Conclusion

In this section, exclusive excitation of acoustic cavity modes for p-waves has been demonstrated. Experimental results show that microparticles are captured at pressure nodes. The location of the pressure nodes and also the capture of the particles by the acoustic radiation forces in a standing pressure field are found to be in agreement with theoretical expectations. The value of the phase speed of sound waves calculated from experiments are higher compared to the theoretical value obtained

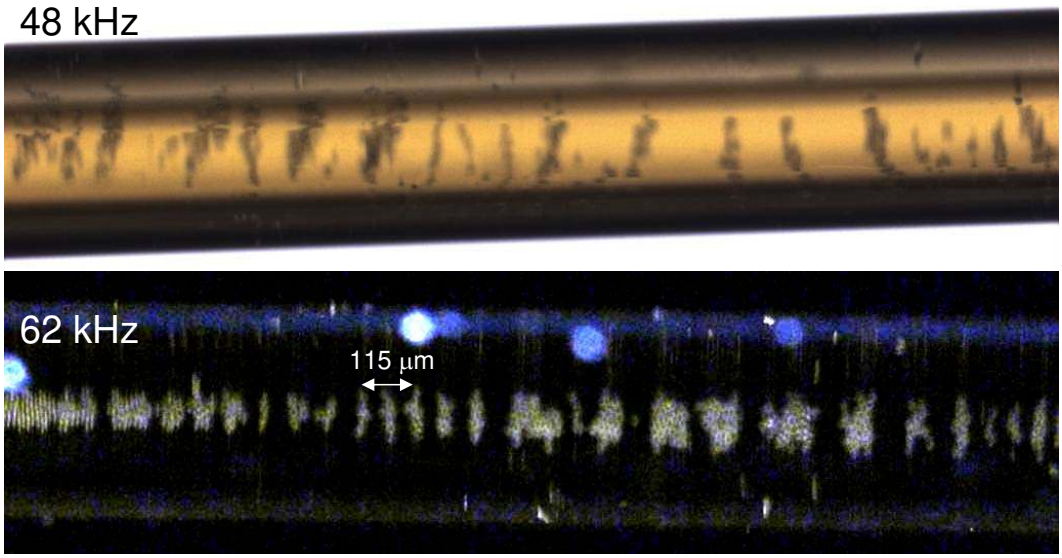

Figure 8.18: Striations observed in Kundt's tube experiments show their existence in microfluidic cavities as well. If the periodicity of the fine collections are associated with a wave dynamics, then the speed of such a wave is found to be 7 m/s. This is not possible and it is argued that these striations might be related to the circular streaming effects. Observation of striations only happen when particles were initially waited to sediment to the bottom of the capillary and then the actuation is turned on.

by the method given in Appendix A.

While this actuator enables investigation of pressure and force field distributions, and works as a proof of the concept, the feasibility for general applications is questionable because resonance frequencies depend on the length of the fluid column. Since this a highly varying parameter from experiment to experiment and even during the experiment due to factors such as evaporation, the characterization of the actuator is not straightforward. In addition, considering possible integration with other microfluidic sytems, unknown boundary conditions limit the use of the actuator. In this regard, the PZT-glass capillary coupled actuator, which

was presented in earlier chapters, eliminates this problem. Since the frequencies of the flexural modes defined by the length of the capillary, characterization of the device, and integrability with other microfluidic systems are more straightforward.

APPENDIX A

CORRECTION FOR THE SPEED OF SOUND WAVES IN A THICK HOLLOW CYLINDER

In this section, the derivation of the speed of sound waves in a thick cylindrical tube is shown. We followed a similar pattern that was mentioned in [46]. Information about the theory of elasticity can be found in many books such as [18, 21, 118]. We will skip the details and start with the equation of motion. In tensor notation,

$$(\lambda + \mu)s_{ij,j} + \mu s_{i,jj} + \rho f_i = \rho \ddot{s}_i \tag{A.1}$$

and in vector notation

$$(\lambda + \mu)\vec{\nabla} \cdot \vec{\nabla} \cdot \mathbf{s} + \mu \nabla^2 \mathbf{s} + \vec{\nabla} f = \rho \ddot{\mathbf{s}} \tag{A.2}$$

where $\mathbf{s}$ is the displacement and λ and μ are known as Lamé constants, which define elastic properties of materials.

In cylindrical coordinates, divergence operator ($\vec{\nabla}$) is given as

$$\vec{\nabla} \cdot \mathbf{A} = \frac{1}{r}\frac{\partial (rA_r)}{\partial r} + \frac{1}{r}\frac{\partial A_\theta}{\partial \theta} + \frac{\partial A_z}{\partial z} \tag{A.3}$$

where $\mathbf{A}$ is a random vector in 3D.

Hooke's general formula relating strain to stress is given as

$$\tau_{ij} = \lambda \epsilon_{kk} \sigma_{ij} + 2\mu \epsilon_{ij} \tag{A.4}$$

where strain elements are given by the general formula,

$$\epsilon_{ij} = \frac{1}{2}(s_{i,j} + s_{j,i}) \ . \tag{A.5}$$

It is possible to write displacement vector $\mathbf{s}$ in Equation A.2 in terms of scalar and vector potentials, Φ and $\mathbf{H}$ such that

$$\mathbf{s} = \vec{\nabla}\Phi + \vec{\nabla} \times \mathbf{H} \tag{A.6}$$

satisfying wave equation

$$\nabla^2\Phi = \frac{1}{c_1^2}\frac{\partial^2\Phi}{\partial t^2} \qquad \text{and} \qquad \nabla^2\mathbf{H} = \frac{1}{c_2^2}\frac{\partial^2\mathbf{H}}{\partial t^2} \ . \tag{A.7}$$

Assuming a fluid cylinder, the general solution of the equation for the scalar field is given as

$$\Phi(r,\theta,z,t) = AJ_n(\alpha r)\cos n\theta e^{i(\xi z-\omega t)} \tag{A.8}$$

From Equation A.7 we find

$$s_r = \frac{\partial\Phi}{\partial r} \tag{A.9}$$

giving

$$s_r = A\alpha J_{n+1}(\alpha r)\cos n\theta \ . \tag{A.10}$$

At low frequencies, such as in our case for $n = 0$,

$$J_1(\alpha r) = \frac{\alpha r}{2} \tag{A.11}$$

then

$$s_r(r) = A\alpha r \tag{A.12}$$

which can be written in terms of its boundary value at r_1 as

$$s_r(r) = \frac{s_r(r_1)}{r_1} r \ . \tag{A.13}$$

In fluids, the relationship between pressure and displacement was derived in section 3.1.1 as

$$p = \lambda_1\frac{\delta\rho}{\rho_0} = \lambda_1\frac{\Delta V}{V} = \lambda\vec{\nabla}\cdot\mathbf{s} \tag{A.14}$$

where λ_1 is the Lame constant for the fluid and equal to the bulk modulus given in section 3.1.1 as ß. Assuming no angular (θ) dependence for the low frequency regime (long wavelengths compared to the cylindrical radius), we have

$$p(r,z) = \lambda_1\Big(\frac{\partial s_z}{\partial z} + \frac{\partial s_r}{\partial r} + \frac{s_r}{r}\Big) \tag{A.15}$$

$$p(r_1,z) = \lambda_1\Big(\frac{\partial s_z}{\partial z} + 2\frac{s_r(r_1)}{r_1}\Big) \qquad \text{at } r = r_1 \ . \tag{A.16}$$

To further proceed for the wave equation, we need to know more about the $s_r(r_1)$ term in Equation A.16. We expect to have pressure dependence in this value; as the pressure increases, displacement of the capillary fluid boundary will increase. In this case we need to look to the capillary body.

Assuming only r dependence in the solid structure, we have $\vec{\nabla} \times \mathbf{s} = 0$, and using vector identity

$$\nabla \times \mathbf{A} = \nabla(\nabla \cdot \mathbf{A}) - \nabla^2 \mathbf{A} \tag{A.17}$$

Equation A.2 becomes

$$(\lambda_2 + 2\mu_2)\nabla^2 \mathbf{s} = 0 \tag{A.18}$$

$$(\lambda_2 + 2\mu_2)\left(\frac{1}{r}\frac{\partial}{\partial r}\left(r\frac{\partial s_r}{\partial r}\right) + \frac{s_r}{r^2}\right) = 0 \tag{A.19}$$

where λ_2 and μ_2 are the Lame constants for the solid cylinder. The solution of Equation A.19 gives the radial displacement s_r for the solid cylinder,

$$s_r(r) = Ar + \frac{B}{r} \tag{A.20}$$

where A and B are constants to be found from boundary conditions. At interfaces, pressure and displacement in $\mathbf{r}$ direction have to be continuous for equilibrium; having pressure p at $(r = r_1)$ and 0 at $(r = r_2)$ we have

$$\tau_{rr}(r_1) = -p \tag{A.21}$$

$$\tau_{rr}(r_2) = 0 \tag{A.22}$$

$$s_r(r_1)_{fluid} = s_r(r_1)_{solid}\ . \tag{A.23}$$

From Equation A.4 we have

$$\tau_{rr}(r) = \lambda_2 \vec{\nabla}\mathbf{s} + 2\mu\epsilon_{rr} \tag{A.24}$$

where ϵ_{rr} can be found from Equation A.5 as

$$\epsilon_{rr}(r) = A - \frac{B}{r^2}\ . \tag{A.25}$$

Inserting Equations A.20 and A.25 in Equation A.24, and solving for boundary conditions given in Equation A.21, we find constants A and B as

$$A = \frac{r_1^2}{2(\lambda_2+\mu_2)(r_2^2-r_1^2)}p \tag{A.26}$$

$$B = \frac{r_1^2 r_2^2}{2\mu_2(r_2^2-r_1^2)}p \ . \tag{A.27}$$

As expected we find the radial displacement (s_r) as a function of internal pressure (p). For the solid cylinder at the fluid-solid boundary we can write

$$\frac{s_r(r_1)}{r_1} = \Bigg(\underbrace{\frac{r_1^2}{2(\lambda_2+\mu_2)(r_2^2-r_1^2)} + \frac{r_2^2}{2\mu_2(r_2^2-r_1^2)}}_{M} \Bigg) p \tag{A.28}$$

where we use M for the phrase in parenthesis. Using the boundary condition given in Equation A.23, we can insert Equation A.28 into Equation A.16. Then at the interface we find

$$p = -\lambda_1 \Big(\frac{\partial s_z}{\partial z} + 2Mp \Big) \tag{A.29}$$

Solving the above equation for pressure, p, taking partial derivative with respect to z we have

$$p = -\lambda_1 \Big(\frac{\partial s_z}{\partial z} + 2Mp \Big) \tag{A.30}$$

$$\frac{\partial p}{\partial z} = -\Big(\frac{\lambda_1}{2M\lambda_1 + 1} \Big) \frac{\partial^2 s_z}{\partial z^2} \ . \tag{A.31}$$

From the conservation of momentum for a fluid element given in Equation 3.8, we know that

$$\frac{\partial(\rho \mathbf{u})}{\partial t} = -\vec{\nabla} p \tag{A.32}$$

since the velocity ($\mathbf{u}$) is the time derivative of displacement ($\mathbf{s}$) we have

$$\rho \frac{\partial^2(\mathbf{s})}{\partial t^2} = -\vec{\nabla} p \ . \tag{A.33}$$

We are expecting variation in pressure to be mostly in $\mathbf{z}$ direction. For $\mathbf{z}$ direction we have

$$\rho \frac{\partial^2 s_z}{\partial t^2} = -\frac{\partial p}{\partial z} \ . \tag{A.34}$$

Using the identity above in A.31 we find

$$\frac{\partial^2 s_z}{\partial t^2} = -\Big(\frac{\lambda_1}{\rho(2M\lambda_1 + 1)}\Big)\frac{\partial^2 s_z}{\partial z^2} \tag{A.35}$$

which is the wave equation

$$\frac{\partial^2 s_z}{\partial t^2} = c_p^2 \frac{\partial^2 s_z}{\partial z^2} \tag{A.36}$$

where

$$c_p = \sqrt{\frac{\lambda_1}{\rho}\frac{1}{(1 + 2M\lambda_1)}} \tag{A.37}$$

or

$$c_p \;=\; c\;\frac{1}{\sqrt{1 + 2M\lambda_1}} \tag{A.38}$$

where $c = \sqrt{\lambda_1/\rho}$ is the speed of sound in bulk fluid and M is given by

$$M = \frac{r_1^2}{2(\lambda_2 + \mu_2)(r_2^2 - r_1^2)} + \frac{r_2^2}{2\mu_2(r_2^2 - r_1^2)}\ . \tag{A.39}$$

What Equation A.38 tells us is that the speed of a propagating wave in a thick cylindrical tube (in low frequency regime) is reduced related to a parameter which depends on the radius and thickness of the tube and elastic properties of the fluid and the tube.

BIBLIOGRAPHY

[1] S.H. Crandall, D.C. Karnopp, and E.F. Kurtz. *Dynamics of Mechanical and Electromechanical Systems*. McGraw-Hill, 1968.

[2] H. Schlichting. *Boundary-Layer Theory*. McGraw-Hill, 1979.

[3] http://www.malvern.com/zetasizer.

[4] Lord Rayleigh (J.W. Strutt). On the circulation of air observed in kundt's tubes, and on some allied acoustical problems. *Philosophical Transactions of the Royal Society of London*, 175:1–21, 1884.

[5] T.M. Squires and S.R. Quake. Microfluidics: Fluid physics at the nanoliter scale. *Rev. Mod. Phys.*, 7(3):977–1026, July 2005.

[6] G.M. Whitesides. The origins and the future of microfluidics. *Nature*, 442:368–373, 2006.

[7] D.B. Weibel, W.R. DiLuzio, and G.M. Whitesides. Microfabrication meets microbiology. *Nature Reviews Microbiology*, 5:209–218, 2007.

[8] C.E. Bradley and R.M. White. Acoustically driven flow in flexural plate wave devices: Theory and experiment. *Proc. IEEE Ultrasonics Symp*, pages 593–597, 1994.

[9] V. Kaajakari, A. Sathaye, and A. Lal. An acoustic vortex particle concentrator. *Proceedings of the microTAS Conference, Monterey, CA*, pages 185–187, 2001.

[10] S. Hardt and F. Schoenfeld. *Microfluidic technologies for miniaturized analysis systems (Chapter 9: Ultrasonic Particle Manipulation, by M.Hill and N.R. Harris)*. Springer Verlag, 2007.

[11] A. Nilsson, F. Petersson, H. Jonsson, and T. Laurell. Acoustic control of suspended particles in micro fluidic chips. *Lab on a Chip*, 4:131–135, 2004.

[12] P.H. Brodeur. Acoustic separation in a laminar flow. *Proc. IEEE Ultrasonics Symp.*, 3:1359–1362, 1994.

[13] C.H. Lee and A. Lal. Low-voltage high-speed ultrasonic chromatography for microfluidic assays. *Proceedings of the Solid State Sensor and Actuator Workshop, Hilton Head Island, South Carolina*, pages 206–209, 2002.

[14] A. Lal. *Micromachined Silicon Ultrasonic Longitudinal Mode Actuators: Theory and Applications to Surgery, Pumping and Atomization*. PhD thesis, University of California, Berkeley, 1996.

[15] P. Yager, T. Edwards, E. Fu, K. Helton, K. Nelson, M.R. Tam, and B.H. Weigl. Microfluidic diagnostic technologies for global public health. *Nature*, 442:412–418, 2006.

[16] Lord Rayleigh (J.W. Strutt). *The Theory of Sound*. Dover Publications, 1945.

[17] S.P. Timoshenko. On the correction for shear of the differential equation for transverse vibrations of prismatic bars. *Philosophical Magazine*, 41:744746, 1921.

[18] K.F. Graff. *Wave Motion in Elastic Solids*. Dover Publications, New York, 1991.

[19] L. Pochammer. Über die fortpflanzungsgeschwindigkeiten kleiner schwingungen in einem unbegrenzten isotropen kreisylinder. *Zeitschrift für Reine und Angewandte Mathematik*, 81:324–326, 1876.

[20] C. Chree. The equations of an isotropic elastic solid in polar and cylindrical coordinates, their solutions and applications. *Transactions of the Cambridge Philosophical Society Math. Phys. Sci*, 14:250 – 369, 1889.

[21] A.E.H. Love. *A Treatise on the Mathematical Theory of Elasticity*. Cambridge University Press, Cambridge, 1952.

[22] H. Kolsky. *Stress waves in solids*. Clarendon Press, Oxford, 1953.

[23] C.T. Loy and K.Y. Lam. Vibration of thick cylindrical shells on the basis of three-dimensional theory of elasticity. *Journal of Sound and Vibration*, 226(4):719–737, 1999.

[24] I. Mirsky and G. Herrmann. Axially symmetric motions of thick cylindrical shells. *Journal of Applied Mechanics*, 25:97 – 102, 1958.

[25] I. Mirsky and G. Herrmann. Non-axially symmetric motions of cylindrical shells. *Journal of Acoustics Society of America*, 29:1116 – 1123, 1957.

[26] D.C. Gazis. Exact analysis of the plane-strain vibrations of thick-walled hollow cylinders. *J. Acoust. Soc. Am.*, 30(8):786–794, 1958.

[27] J.E. Greenspon. Flexural vibrations of a thick-walled cylinder according to the exact theory of elasticity. *Journal of Aerospace Sciences*, 27:1365–1373, 1957.

[28] D.C. Gazis. Three-dimensional investigation of the propagation of waves in hollow circular cylinders. I. Analytical Foundation. *Journal of the Acoustical Society of America*, 31:568–573, 1959.

[29] D.C. Gazis. Three-dimensional investigation of the propagation of waves in hollow circular cylinders. II. Numerical Results. *Journal of the Acoustical Society of America*, 31:573–578, 1959.

[30] A.E. Armenekas, D.S. Gazis, and G. Herrmann. *Free Vibrations of Circular Cylindrical Shells*. Pergamon Press, Oxford, 1969.

[31] R.K. Singal and K. Williams. Theoretical and experimental study of vibrations of thick circular cylindrical shells and rings. *Journal of Vibration, Acoustics, Stress, and Reliability in Design*, 110(4):533 – 537, 1988.

[32] A.E. Armenakas. On the accuracy of some dynamic shell theories. *Journal of the Engineering Mechanics Division, Proceedings of the American Society of Civil Engineers*, 93(EM5): 95–109, 1967.

[33] G.E. Greenspon. Vibration of a Thick-Walled Cylindrical Shell-Comparison of the Exact Theory with Approximate Theories. *Journal of the Acoustical Society of America*, 32: 571–578, 1960.

[34] M.R. Mofakhami, H.H. Toudeshky, and Sh.H. Hashemi. Finite cylinder vibrations with different end boundary conditions. *Journal of Sound and Vibration*, 297(1-2):293 – 314, 2006.

[35] T.C. Lin and G.W. Morgan. Study of axisymmetric vibrations of cylindrical shells as affected by rotary inertia and transverse shear. *Journal of Applied Mechanics*, 23:255–261, 1956.

[36] L.M. Brekhovskikh and V. Goncharow. *Mechanics of Continua and Wave Dynamics*. Springer-Verlag, 1994.

[37] H. Goldstein. *Classical Mechanics*. Addison-Wesley, 1997.

[38] Y.C. Fung. *Foundations of solid mechanics*. Prentice-Hall, 1965.

[39] J.R. Hutchinson. Shear coefficients for timoshenko beam theory. *Journal of Applied Mechanics*, 68:87–92, January 2001.

[40] J. Miklowitz. *The Theory of Elastic Waves and Waveguides*. North-Holland Series in Applied Mathematics and Mechanics, 1979.

[41] T. Ikehara, J. Lu, M. Konno, R. Maeda, and T. Mihara. A high quality-factor silicon cantilever for a low detection-limit resonant mass sensor operated in air. *Journal of Micromechanics and Microengineering*, 17(12):2491–2494, 2007.

[42] M.G. Wertheim. Mmoire sur la vitesse du son dans les liquides. *Annales de Chimie et de Physique*, T23:434, 1848.

[43] H. Helmholtz. Bericht uber die theoretische akustik betreffenden arbeiten vom jahre 1848 und 1849 (report on theoretical acoustics concerning works of the years 1848 and 1849). *Wissenschaftliche Abhandlungen von Hermann Helmholtz (Treatises by Hermann Helmholtz), Leipzig, J.A. Barth*, pages 233–255, 1882.

[44] V.D.J. Korteweg. Ueber die fortpflanzungsgeschwindigkeit des schalles in elastischen rohren. *Annalen der Physik, (Wied. Ann)*, T5:526, 1878.

[45] H. Lamb. On the velocity of sound in a tube, as affected by the elasticity of the walls. *Manchester Memoirs*, 42,10:116, 1898.

[46] A. Kaufman and A.L. Levshin. *Acoustic And Elastic Wave Fields in Geophysics, III*. Elsevier, 2005.

[47] D.T. Blackstock. *Fundamentals of Physical Acoustics*. John Wiley and Sons, 2000.

[48] J.D. Jackson. *Classical Electrodynamics*. John Wiley and Sons, 1998.

[49] E.G. Williams. *Fourier Acoustics, Sound Radiation and Nearfield Acoustical Holography*. Academic Press, 1999.

[50] F. Fahy and P. Gardonio. *Sound and Structural Vibration, Radiaton, Transmission and Response*. Academic Press, 2007.

[51] L. Cremer, M. Hungar, and E.E. Ungar. *Structure Borne Sound*. Springer-Verlag, 1988.

[52] E.G. Williams. On greens functions for a cylindrical cavity. *J. Acoust. Soc. Am. 102 (6), December*, 102(6):3300–3307, 1997.

[53] J. Wolfe, J. Smith, J. Tann, and N.H. Fletcher. Acoustic impedance spectra of classical and modern flutes . *Journal of Sound and Vibration*, 243:127–144, 2001.

[54] M.S. Howe. *Acoustics of Fluid-Structure Interactions*. Cambridge University Press, 1988.

[55] *ANSYS Reference Guide, Version 11.*

[56] R.T. Beyer. Radiation pressure-the history of a mislabeled tensor. *J. Acoust. Soc. Am.*, 63(4):1025–1030, 1978.

[57] R.T. Beyer. *Nonlinear Acoustics*. Naval Sea Systems, 1974.

[58] M.F. Hamilton and D.T. Blackstock. *Nonlinear Acoustics*. Academic Press, 1997.

[59] J. Lightill. Acoustic streaming. *Journal of Sound and Vibration*, 61(3):391–418, 1978.

[60] W.L. Nyborg. Acoustic streaming. *Physical Acoustics*, IIB:265–331, 1965.

[61] S. Boluriaan and P.J. Morris. Acoustic streaming: from rayleigh to today. *Aeroacoustics*, 2(3-4):255–292, 2003.

[62] D.T. Blackstock M.F. Hamilton, editor. *Nonlinear Acoustics, (Chapter 6, by T.G. Wang and C.P.Lee)*. Academic Press, 1997.

[63] A. Kundt. Ueber eine neue art akustischer staubfiguren und ber die anwendung derselben zur bestimmung der shallgeschwindigkeit in festen krpern

und gasen. *Annalen der Physik (Leipzig: J. C. Poggendorff)*, 127(4):497–523, 1866.

[64] L.V. King. On the acoustic radiation pressure on spheres. *Proceedings of the Royal Society of London. Series A, Mathematical and Physical Sciences*, 147(865):212–240, 1934.

[65] J. Rudnick and M. Barmatz. Measurements of the acoustic radiation pressure on a sphere in a standing wave field. *J. Acoust. Soc. Am.*, 62:20–22, 1977.

[66] E. Leung, N. Jacobi, and T. Wang. Acoustic radiation force on a rigid sphere in a resonance chamber. *J. Acoust. Soc. Am.*, 70:1762–1767, 1981.

[67] K. Yosioka and Y. Kawasima. Acoustic radiation pressure on a compressible sphere. *Acustica*, 5:167173, 1955.

[68] L.P. Gor'kov. On the forces acting on a small particle in an acoustical field in an ideal fluid. *Soviet Physics-Doklady*, 6:773–775, 1962.

[69] P.J. Westervelt. The theory of steady forces caused by sound waves. *J. Acoust. Soc. Am.*, 23(4):312–315, 1951.

[70] P.J. Westervelt. Errata: The theory of steady forces caused by sound waves [j. acoust. soc. am. 23, 312 (1951)]. *J. Acoust. Soc. Am.*, 26(6):719, 1951.

[71] A. Doinikov. Acoustic radiation force on a spherical particle in a viscous heat-conducting fluid. I. General formula. *J. Acoust. Soc. Am.*, 101(2):713–721, 1997.

[72] A. Doinikov. Acoustic radiation force on a spherical particle in a viscous heat-conducting fluid. II. Force on a rigid sphere. *J. Acoust. Soc. Am.*, 101(2):722–730, 1997.

[73] A. Doinikov. Acoustic radiation force on a spherical particle in a viscous heat-conducting fluid. III. Force on a liquid drop. *J. Acoust. Soc. Am.*, 101(2):731–740, 1997.

[74] S.D. Danilov and M.A. Mironov. Mean force on a small sphere in a sound field in a viscous fluid. *J. Acoust. Soc. Am.*, 107(1):143–153, 2000.

[75] K. Yasuda and T. Kamakura. Acoustic radiation force on ficrometer-size particles. *Appl. Phys. Lett.*, 71(13):1771–1773, 1997.

[76] F.K. Bjerknes. *Fields of Force*. Columbia U.P., 1906.

[77] L.A. Crum. Bjerknes forces on bubbles in a stationary sound field. *J. Acoust. Soc. Am.*, 57(6):1363–1370, 1975.

[78] M.A.H. Weiser and R.E. Apfel. Interparticle forces on red cells in a standing wave field. *Acustica*, 56:114–119, 1984.

[79] X. Zheng and R.E. Apfel. Acoustic interaction forces between two fluid spheres in an acoustic field. *J. Accoust. Soc. Am.*, 97:22182226, 1995.

[80] D.J. Bell and P. Dunnil. Mechanisms for the acoustic conditioning of protein precipitates to improve their separation by centrifugation. *Biotechnology and Bioengineering*, 26:691–698, 1984.

[81] J. Holtsmark, I. Johnsen, T. Sikkeland, and S. Skavlem. Boundary layer flow near a cylindrical obstacle in an oscillating, incompressible fluid. *J. Acoust. Soc. Am.*, 26(1):26–39, 1954.

[82] C.Y. Wang. The flow field induced by an oscillating sphere. *Journal of Sound and Vibration*, 2(3):257–269, 1965.

[83] M. Tatsuno. Circulatory streaming around an oscillating circular cylinder at low reynolds numbers. *J. Phys. SOC. Japan*, 35:915–920, 1973.

[84] L.D. Landau and E.M. Lifshitz. *Fluid Mechanics*. Pergamon Press, 1987.

[85] W.L. Nyborg. Acoustic streaming near a boundary. *J. Acoust. Soc. Am.*, 30(4):329–339, 1958.

[86] M. Arkin. Sedimentation for success. *Modern Drug Discovery*, 7(11):45–47, 2004.

[87] D. Myers. *Surfaces, Interfaces, and Colloids: Principles and Applications*. Wiley-VCH, 1999.

[88] A. Fick. On liquid diffusion. *Philosophical Magazine*, 10:30, 1855.

[89] J.W. Rohlf. *Modern Physics from Alpha to Zeta*. John Wiley & Sons, 1994.

[90] R. Brown. A brief account of microscopical observations made in the months of June, July and Aug. 1827, on the particles contained in the pollen of plants;

and on the general existence of active molecules in organic and inorganic bodies. *Philosophical Magazine*, 4(21):161–173, 1828.

[91] J. Ingenhousz. Vermichte schriften physisch medicinischen inhalts. *Wapler, Vienna*, 2:123–126, 1877.

[92] J. Delsaulx. Thermo-dynamic origin of the brownian motion. *The Monthly Microscopical Jounal*, 18:1–7, 1877.

[93] D. Abbott, B.R. Davis, N.J. Phillips, and K. Eshraghian. Simple derivation of the thermal noise formula using window-limited fourier transforms and other conundrums. *IEEE Transactions on Education*, 39(1):1–13, 1996.

[94] A. Einstein. *Investigations on the Theory of the Brownian Movement*. Dover Publications, 1956.

[95] B. Rieger, H.R.C. Dietrich, L.R. van den Doel, and L.J. van Vliet. Diffusion of microspheres in sealed and open microarrays. *Microscopy Resarch and Tech*, 65:218–225, 2004.

[96] J. Gregory. *Particles in Water*. IWA Publishing, 2006.

[97] H.C. Hamaker. The london van der waals attraction between spherical particles. *Physica*, 4(10):10581072, 1937.

[98] I.D. Morrison and S. Ross. *Colloidal Dispersions: Suspensions, Emulsions and Foams*. Wiley Interscience, 2002.

[99] R.J. Hunter. Recent developments in the electroacoustic characterization of colloidal suspensions and emulsions. *Colloids and Surfaces*, 141:37–65, 1998.

[100] A.S. Dukhin and P.J. Goetz. *Ultrasound for Characterizing Colloids*. Elsevier, 2002.

[101] H. Ohshima, T.W. Healy, and L.R. White. Sedimentation velocity and potential in a dilute suspension of charged spherical colloidal particles. *J.Chem.Soc, Faraday Trans. 2*, 80:1299–1317, 1984.

[102] M. Rasa, B.H. Erne, B. Zoetekouw, R. van Roij, and A.P. Philipse. Macroscopic electric field and osmotic pressure in ultracentrifugal sedimentation-diffusion equilibria of charged colloids. *J.Phys.:Cond. Matter*, 17:2293–2314, 2005.

[103] T.G.M. van de Ven. *Colloidal Hydrodynamics*. Academic Press, 1989.

[104] F. Moreno, J.M. Saiz, and F. Gonzales. Backscatter. *Encyclopedia of Optical Engineering By Ronald G. Driggers. CRC Press*, pages 142–150, 2003.

[105] M.D. Abramof, P.J. Magelhaes, and S.J. Ram. Image processing with imagej. *Biophotonics International*, 11(7):36–42, 2004.

[106] T.C. Thomas. A proof of the kepler conjecture. *Annals of Mathematics. Second Series*, 162(3):10651185, 2005.

[107] N.F. Carnahan and K.E. Starling. Equation of state for nonattracting rigid spheres. *Journal of Chemical Physics*, 51:635–636, 1969.

[108] C.H. Hamann, A. Hamnett, and W. Vielstich. *Electrochemistry*. Wiley-VCH Verlag GmbH, 1998.

[109] A.P. Philipse and A. Vrij. Non-aqueous silica dispersions. charged particle interactions studied by scattering of light. *Trends in Colloid and Interface Science III*, 79:270–271, 1989.

[110] M. Kosmulski and E. Matijevic. Zeta potentials of silica in water-alcohol mixtures. *Langmuir*, 8(4):10601064, 1992.

[111] B.J. Maranzano and N.J. Wagner. Surface charge of 3-(trimethoxysilyl) propyl methacrylate (tpm) coated stober silica colloids by zeta-phase analysis light scattering and small angle neutron scattering. *Langmuir*, 16:10556–10558, 2000.

[112] M. Rasa and A. Philipse. Evidence for a macroscopic electric field in the sedimentation profiles of charged colloids. *Nature*, 429:857–860, 2004.

[113] Malvern Instruments. *Zetasizer Nano User Manual*.

[114] E.H. Klaassen, R.J. Reay, and G.T.A. Kovacs. Diode-based thermal r.m.s. converter with on-chip circuitry fabricated using cmos technology. *Sensors and Actuatros A*, 52:33–40, 1996.

[115] K.Y. Kim, W. Sachse, and A. G. Every. On the determination of sound speeds in cubic crystals and isotropic media using a broadband ultrasonic point-source/point-receiver method. *J. Acoust. Soc. Am.*, 93:1393–1406, 1993.

[116] T.D. Rossing and N.H. Fletcher. *Principles of Vibration and Sound*. Springer, 2004.

[117] E. N. da C. Andrade. On the groupings and general behaviour of solid particles under the influence of air vibrations in tubes. *Phil. Trans. R. Soc. Lond. A*, 230:413–445, 1932.

[118] B.A. Auld. *Acoustic Fields and Waves in Solids*. John Wiley and Sons, 1973.